

BIOINSPIRED IRON MODELS: FROM DIIRON COMPLEXES TO SUPRAMOLECULAR FUNCTIONALIZED METALLOCAVITANDS

Diego Vidal Sánchez

Per citar o enllaçar aquest document:
Para citar o enlazar este documento:
Use this url to cite or link to this publication:
<http://hdl.handle.net/10803/668200>

ADVERTIMENT. L'accés als continguts d'aquesta tesi doctoral i la seva utilització ha de respectar els drets de la persona autora. Pot ser utilitzada per a consulta o estudi personal, així com en activitats o materials d'investigació i docència en els termes establerts a l'art. 32 del Text Refós de la Llei de Propietat Intel·lectual (RDL 1/1996). Per altres utilitzacions es requereix l'autorització prèvia i expressa de la persona autora. En qualsevol cas, en la utilització dels seus continguts caldrà indicar de forma clara el nom i cognoms de la persona autora i el títol de la tesi doctoral. No s'autoritza la seva reproducció o altres formes d'explotació efectuades amb finalitats de lucre ni la seva comunicació pública des d'un lloc aliè al servei TDX. Tampoc s'autoritza la presentació del seu contingut en una finestra o marc aliè a TDX (framing). Aquesta reserva de drets afecta tant als continguts de la tesi com als seus resums i índexs.

ADVERTENCIA. El acceso a los contenidos de esta tesis doctoral y su utilización debe respetar los derechos de la persona autora. Puede ser utilizada para consulta o estudio personal, así como en actividades o materiales de investigación y docencia en los términos establecidos en el art. 32 del Texto Refundido de la Ley de Propiedad Intelectual (RDL 1/1996). Para otros usos se requiere la autorización previa y expresa de la persona autora. En cualquier caso, en la utilización de sus contenidos se deberá indicar de forma clara el nombre y apellidos de la persona autora y el título de la tesis doctoral. No se autoriza su reproducción u otras formas de explotación efectuadas con fines lucrativos ni su comunicación pública desde un sitio ajeno al servicio TDR. Tampoco se autoriza la presentación de su contenido en una ventana o marco ajeno a TDR (framing). Esta reserva de derechos afecta tanto al contenido de la tesis como a sus resúmenes e índices.

WARNING. Access to the contents of this doctoral thesis and its use must respect the rights of the author. It can be used for reference or private study, as well as research and learning activities or materials in the terms established by the 32nd article of the Spanish Consolidated Copyright Act (RDL 1/1996). Express and previous authorization of the author is required for any other uses. In any case, when using its content, full name of the author and title of the thesis must be clearly indicated. Reproduction or other forms of for profit use or public communication from outside TDX service is not allowed. Presentation of its content in a window or frame external to TDX (framing) is not authorized either. These rights affect both the content of the thesis and its abstracts and indexes.



Doctoral Thesis

Bioinspired iron models: From diiron complexes to
supramolecular functionalized metallocavitands

Diego Vidal Sánchez

2019

Doctoral programme in Chemistry

Supervised by: Dr. Miquel Costas Salgueiro

Tutor: Dr. Miquel Costas Salgueiro

**Presented in partial fulfilment of the requirements for a doctoral
degree from the University of Girona**



Dr Miquel Costas Salgueiro, from Universitat de Girona

I DECLARE:

That the thesis entitled “Bioinspired iron models: From diiron complexes to supramolecular functionalized metallocavitands”, presented by Diego Vidal Sánchez to obtain a doctoral degree, has been completed under my supervision.

For all intents and purposes, I hereby sign this document.

Dr. Miquel Costas Salgueiro

Girona, 4th March 2019

“- Fantasy has no limits...

- *That is not true, you lie!*

- Silly child, you know nothing about the Fantasy story.
It is the world of human fantasies. Each part, each creature,
belongs to the world of the dreams and hopes of humanity.
Consequently, there are no limits for Fantasy...

- *And why is it dying then...?*

-Because humans are losing their hopes and forgetting
their dreams. This is how Nothing becomes stronger.

- *What is the Nothing?*

- It is the remaining vacuum, the desolation that destroys this
world and my entrustment is to help the Nothing.

- *Why?*

- Because the human without hopes is easy to control
and whoever has control, will have the Power.”

Michael Ende. The neverending story.

*Dedicado especialmente a mis padres, por todo su
esfuerzo y dedicación, por hacerme ser quien soy.*

A Valeria, por tener siempre espacio para una sonrisa y quitar las nubes.

FULL LIST OF PUBLICATIONS

Publications derived from this thesis:

FROM CHAPTERS IV AND V

“A Deep Cavitand Receptor Functionalized with Fe (II) and Mn (II) Aminopyridine Complexes for Bioinspired Oxidation Catalysis” Vidal, D., Costas, M., Lledó, A., *ACS Catal.*, **2018**, 8, 3667-3672.

Work from Chapter III is ongoing and will be published in the future.

Publications not included in this thesis:

“C-H Bond Oxidation Catalyzed by an Imine-Based Iron Complex: A Mechanistic Insight” Olivo, G., Nardi, M., Vidal, D., Barbieri, A., Lapi, A., Gómez, L., Lanzalunga, O., Costas, M., Di Stefano, S., *Inorg. Chem.*, **2015**, 54, 10141-10152.

“Controlling Selectivity in Aliphatic C-H Oxidation through Supramolecular Recognition” Vidal, D., Olivo, G., Costas, M., *Chem. Eur. J.*, **2018**, 24, 5042-5054.

LIST OF ABBREVIATIONS

(HCOH)_n = paraformaldehyde.

Δ^9D = Δ^9 stearoyl-acyl carrier desaturase.

Δ^9Dox = oxidized state Δ^9 -D.

Δ^9Dred = reduced state Δ^9 -D.

°C = Celsius degrees

¹³C-NMR = carbon nuclear magnetic resonance

¹H-NMR = proton nuclear magnetic resonance

AcOH = acetic acid.

ADO = aldehyde deformylating oxygenase.

azpy = 2-(phenylazo)pyridine.

BDE = bond dissociation energy.

BMM = bacterial multicomponent monooxygenase.

BPO = benzoyl peroxide.

CF₃SO₃⁻ = triflate anion.

CH₂Cl₂ = dichloromethane.

CH₃CN = acetonitrile.

CHD = cyclohexadiene.

cis-DMCH = *cis*-1,2-dimethylcyclohexane.

CytP450 = cytochrome P450.

DHA = 9,10-dihydroanthracene.

DNA = deoxyribonucleic acid.

EBpytacn = 1,2-bis(4-methyl-7-(pyridin-2-ylmethyl)-1,4,7-triazonan-1-yl)ethane.

ET = electron-transfer.

Et₂O = diethyl ether.

EtOH = ethanol.

Fe²⁺/Fe^{II} = iron(II).

Fe³⁺/Fe^{III} = iron(III).

Fe⁴⁺/Fe^{IV}/FerryI = iron (IV).

H₂SO₄ = sulfuric acid.

HAT = hydrogen atom transfer.

hDOHH = human deoxyhyupsine hydroxylase.

HERFD XAS = K α high-energy-resolution fluorescence-detected X-ray absorption spectroscopy.

His = histidine.

HMePytacn = 1-methyl-4-(pyridin-2-ylmethyl)-1,4,7-triazacyclononane.

Hr = hemerythrin.

K_2CO_3 = potassium carbonate.

MCD = magnetic circular dichroism.

MeOH = methanol.

MMO_{ox} or Ox = oxidized state sMMO.

MMO_{red} or Red = reduced state sMMO.

MOF = metal organic framework.

Na_2SO_4 = sodium sulfate anhydrous.

$NaBH(OAc)_3$ = sodium triacetoxyborohydride.

NaOH = sodium hydroxide.

NBS = N-Bromosuccinimide.

$NBu_4^+IO_4^-$ = tetrabutylammonium periodate.

NH_3 = ammonia.

O_2 = oxygen.

PH = pheno hydroxylase.

PNPCC = *p*-nitrophenyl choline carbonate.

Q = bis(μ -oxo) $Fe_2(IV)$ intermediate.

RNR R2_{ox} = oxidized state RNR R2.

RNR R2_{red} = reduced state RNR R2.

RNRs = ribonucleotide reductases.

S = superoxo intermediate from Toluene-4-monooxygenase.

SbF_6^- = hexafluoro antimoniate anion.

sMMO = soluble methane monooxygenase.

T4MOH = toluene-4-monooxygenase.

Tacn = 1,4,7-triazacyclononane.

TBAIO₄ = tetrabutylammonium periodate.

TBAPI = tetrabutylammonium periodate.

THF = tetrahydrofuran.

ToMOH = toluene monooxygenase.

TON = turnover number.

trans-DMCH = *trans*-1,2-dimethylcyclohexane.

Ts₃tacn = 1,4,7-tritosyl-1,4,7-triazacyclononane.

TsMePytacn = 1-methyl-4-(pyridin-2-ylmethyl)-7-tosyl-1,4,7-triazacyclononane.

TsPytacn = 1-(pyridin-2-ylmethyl)-4-tosyl-1,4,7-triazacyclononane.

Tstacn = 1-tosyl-1,4,7-triazacyclononane.

X = (μ -oxo)Fe₂(III,IV) intermediate.

XAS = X-ray absorption spectroscopy.

XRD = X-ray diffraction.

α -KG = α -ketoglutarate.

δ = chemical shift.

LIST OF FIGURES

- Figure I.1.** Heme and non heme iron dependent enzymes involved in O₂ metabolism. (p. 10)
- Figure I.2.** Structure of cytochrome P450 enzyme. (p. 11)
- Figure I.3.** Structure of non-heme mononuclear iron enzyme. (p. 11)
- Figure I.4.** Synthetic model complex approach for the mimic of enzymes. (p. 14)
- Figure I.5.** Selected model complexes for mononuclear non-heme enzymes. (p. 15)
- Figure I.6.** Examples of Synthetic high-valent mononuclear Fe(IV)=O complexes. (p. 16)
- Figure I.7.** Structures of Ligands used to mimic sMMO. (p. 19)
- Figure I.8.** DHA oxidation rates by high-valent diiron complexes supported by TPA* ligand at -80 °C. Blue bars indicate S = 1 Fe^{IV} center, red bars indicate S = 2 Fe^{IV} center. 9F and 9OMe are the same as 9 where an OH ligand is replaced for F or OMe respectively. (p. 25)
- Figure I.9.** 3D model representing the enzyme active site. Blue color represents the binding sites, red color the catalytic site and black the substrate. Image adapted from: Thomas Shafee, Enzyme structure, CC BY 4.0. (p. 26)
- Figure I.10.** Supramolecular approach to build artificial enzymes. (p. 27)
- Figure I.11.** Structures of supramolecular receptors used to mimic enzyme reactivity. (p. 28)
- Figure I.12.** Two strategies used to design supramolecular catalysts. (p. 31)
- Figure I.13.** Breslow's supramolecular Catalyst (left) and schematic model of catalyst-substrate binding. (p. 32)
- Figure I.14.** Zn(Salen)-Cavitand developed by Richeter and Rebek. Ref 130. (p.34)
- Figure I.15.** Schematic structure of *trans*-Ru^{II}(tpy)(azpy)(OH)₂ metallocavitand (left) and 3D model of the host-guest adduct formed with alkylammonium styrene substrate **4** (right). Ref 131. (p. 35)
- Figure I.16.** Hybrid organic-inorganic iron supramolecular systems reported from Olivia Reinaud (A, ref 134) and Richard Hooley (B, ref 135). (p. 36)
- Figure III.1.** Schematic structure of two reported mononucleating ligands: Pytacn and MePy₂tacn and their novel dinucleating versions studied in this thesis: EBPytacn and Py₄btacn. (p. 46)
- Figure III.2.** ¹H NMR spectra of EBPytacn ligand in CDCl₃ at 298K. (p. 48)
- Figure III.3.** X-Ray structures of **1**, **2**, **2**-SbF₆ and **2**-Zn. Hydrogen atoms are omitted for clarity. (p. 50)
- Figure III.4.** *d*-orbital distribution in octahedral III complexes and high spin and low spin configuration in Fe²⁺ complexes. (p. 54)
- Figure III.5.** X-Ray structure of **2**-SbF₆ measured at 130 K and 275 K. Hydrogen atoms are omitted for clarity. (p. 55)
- Figure III.6.** ¹H NMR spectra of **1**, [Fe^{II}₂(EBPytacn)(CH₃CN)₄](CF₃SO₃)₄, in acetone-*d*₆ at 298K. (p. 56)

Figure III.7. Enlargement of the diamagnetic region of the ^1H NMR spectra of **2**, in CD_3CN Top, red spectra: ^1H NMR spectra of **2** at 298 K. Bottom, blue spectra: ^1H NMR spectra of **2** in CD_3CN at 235 K. (p. 57)

Figure III.8. ^1H NMR spectra of **1** (bottom) and **2** (top) in acetone- d_6 at 235 K. Top spectra: Enlargement of the diamagnetic region of the ^1H NMR spectra of **2**. Bottom spectra: ^1H NMR spectra of **1**. (p. 58)

Figure III.9. UV-vis spectra of **2** in acetone at different temperatures, ranging from 298 K (red spectra), to 198 K (blue spectra). Top right: inset of the plot ϵ Vs T, corresponding to changes of 380 nm band upon cooling. (p. 59)

Figure III.9b. Molecular orbitals simplified diagram for a d-d transition in an octahedral d^6 transition metal. (p. 60)

Figure III.10. UV-vis spectra of **2** in CH_3CN at different temperatures, ranging from 298 K (red spectra), to 238 K (blue spectra). Top right: inset plot ϵ Vs T, corresponding to changes of 395 nm band upon cooling. (p. 61)

Figure III.10b. UV-vis spectra of **2** in CH_3CN at different temperatures, ranging from 298 K (red spectra), to 238 K (blue spectra). Top right: inset plot ϵ Vs T, corresponding to changes of 395 nm band upon cooling. (p. 62)

Figure III.11. UV-vis spectra of changes of **1** (blue line) and $\mathbf{1}^{\text{IV}}=\mathbf{O}$ (red line). Grey lines show the progressive formation of $\mathbf{1}^{\text{IV}}=\mathbf{O}$ upon addition of 2 equiv oxidant to **1** in CH_3CN at 273 K. The inset show the kinetic traces for the formation of $\mathbf{1}^{\text{IV}}=\mathbf{O}$ on its maximum of absorbance band at 744 nm. (p. 64)

Figure III.12. UV-vis spectra of synthetic bis-oxo complexes changes $\mathbf{1}^{\text{IV}}=\mathbf{O}$ (red line) and $\mathbf{2}^{\text{IV}}=\mathbf{O}$ (green line) in acetonitrile at 273 K. (p. 65)

Figure III.13. High resolution ESI-MS spectra of complex $\mathbf{2}^{\text{IV}}=\mathbf{O}$ in acetonitrile with sPhIO. Inset of the simulated species contributing to the experimental peak at 545.1019 m/z. (p. 66)

Figure III.14. High resolution ESI-MS spectra of complex $\mathbf{1}^{\text{IV}}=\mathbf{O}$ in acetonitrile with TBAIO₄. Top right: inset of the simulated species contributing to the experimental peak at 468.0642 m/z. (p. 67)

Figure III.15. UV-vis spectrum of the decay of the $\mathbf{2}^{\text{IV}}=\mathbf{O}$ band (green) upon addition of 100 eq of thioanisole at 298 K to form the initial species **2**. inset shows the kinetic traces following an exponential decay. (p. 67)

Figure III.16. UV-vis spectrum of the decay of the $\mathbf{2}^{\text{IV}}=\mathbf{O}$ band (green) upon addition of 100 eq of triphenylmethane at 298 K. inset shows the kinetic traces of following an exponential decay. (p. 71)

Figure III.17. Plot of the pseudo-first order rate constants k_{obs} vs substrate concentration to obtain the second order rate constants k_2 for the reaction of $\mathbf{2}^{\text{IV}}=\mathbf{O}$ with C-H bonds in acetonitrile at 298 K. (p. 72)

Figure III.18. Plot of $\log(k_2')$ vs BDE $\mathbf{2}^{\text{IV}}=\mathbf{O}$. k_2 values were normalized by the number of H available on the substrate to obtain the corresponding k_2' . (p. 74)

Figure IV.1. Selected regions and assignment of the ^1H NMR spectrum of **2** (400 MHz, acetone- d_6). Multiplicity edited ^1H - ^{13}C HSQC spectrum of **2** (400 MHz, acetone- d_6 , 298K). Assignment made with the help of the corresponding COSY spectrum. (p. 81)

Figure IV.2. Solid state structure (left) and schematic drawing (right) of the 2-Chloromethylpyridine cavitand derivative **6** and metallocavitand $2 \cdot \text{Fe}_2\text{Cl}_4\text{O}$. Hydrogen atoms and amide groups of cavitand walls are omitted for clarity. (p. 83)

Figure IV.4. ^1H -NMR spectra of **2** upon titration with $\text{Zn}(\text{OTf})_2$. (p. 84)

Figure IV.5. ^1H NMR spectra of **2** and $2 \cdot \text{Zn}(\text{OTf})_2$ in different solvents; inset of the methine region. (p. 85)

Figure IV.6 ^1H NMR spectrum of $2 \cdot \text{Fe}(\text{OTf})_2$ in CD_3CN (400 MHz, 298 K); inset of the methine region. (p. 86)

Figure IV.7 ^1H NMR spectrum of $7\text{b} \cdot \text{Fe}(\text{OTf})_2$ in CD_3CN with paramagnetic parameters (400 MHz, 298 K). (p. 86)

Figure IV.8. Top: ^1H NMR spectra (full sweep width) of various host guest complexes with $2 \cdot \text{M}(\text{OTf})_2$ with the methine region highlighted (in some cases overlapped with resonances of the unbound guest). (p. 88)

Figure IV.9. Right: Upfield regions taken from the full ^1H NMR spectra of figure IV.8. Left: Upfield region of the ^1H NMR spectra of $8\text{c} \subset 2 \cdot \text{Fe}(\text{OTf})_2$ at 298 K (top) and 240 K (bottom). (p. 89)

Figure IV.10. Multiplicity edited ^1H - ^{13}C HSQC (400 MHz, CD_3CN , 240 K) of $8\text{c} \subset 2 \cdot \text{Fe}(\text{OTf})_2$. Red CH/ CH_3 , blue CH_2 . (p. 90)

Figure V.1. Bioinspired alkane and alkene oxidations with Fe and Mn metallocavitands. (p. 93)

Figure V.2. HRMS of the reaction mixture just after finishing the reaction. Inset corresponding to the experimental and simulated peak of the detected species. (p. 95)

Figure V.3. Formation of an Fe(IV) oxo species $[2 \cdot \text{Fe}(\text{O})]^{2+}$. Evolution of the UV-vis spectra upon treatment of $2 \cdot \text{Fe}(\text{OTf})_2$ with TBAIO_4 at 0 °C. Inset: ESI-MS spectrum of the same reaction mixture. (p. 98)

Figure V.4. Evolution of the UV-Vis spectra of $2 \cdot \text{Fe}(\text{OTf})_2$ (1 mM, CH_3CN): a) blue, start; b) red, after addition of TBAIO_4 ; c) green: after addition of thioanisole. Inset: evolution of the Fe(IV) oxo band at $\lambda=747$ nm. (p. 100)

Figure VII.1. Side and top views of the X-ray diffraction structure of **6**. Ellipsoids are shown at 50% probability (gray: C, blue: N, red: O, green: Cl). Solvent molecules (MeOH) occupying the cavity are shown in space filling representation. (p.123)

Figure VII.2. X-ray diffraction structure of $2 \cdot \text{Fe}_2\text{Cl}_4\text{O}$: unit cell (left), side view (center) and top view (right). Ellipsoids are shown at 50% probability (gray: C, blue: N, red: O, green: Cl, orange: Fe). Disordered solvent molecules in the cavity not shown. (p.125)

Figure VII.3. Upfield regions in the ^1H NMR spectra of $8\text{c} \subset 2 \cdot \text{Fe}(\text{OTf})_2$ (top) and $10 \subset 2 \cdot \text{Fe}(\text{OTf})_2$ (bottom), showing the resonances of the cyclohexyl moiety buried in the aromatic pocket of the cavitand (blue). (p. 127)

LIST OF TABLES

Table III.1. Selected Bond Lengths (Å) and Angles (°) for **1**, **2**, **2**-SbF₆ and **2**-Zn complexes. (p. 52)

Table III.2. Rate constants (k_2') obtained for C-H oxidation by **2**^{IV}=O. (p. 71)

Table III.3. Crystal data for **2** and **2**-Zn binuclear complexes. (p. 115)

Table III.4. Crystal data for **2**-SbF₆ and **1** binuclear complexes. (p. 116)

Table IV.1 Comparison of guest-binding in octaamide cavitand **1** and metallocavitands **2**·M(OTf)₂. Amide groups of cavitand walls are omitted for clarity. (p. 87)

Table V.1. Catalytic epoxidation reaction with Mn catalysts **2**·Mn(OTf)₂ and **7b**·Mn(OTf)₂ for a 1:1 mixture of substrates. Conditions: catalyst (1 mol %), H₂O₂ (2.0 eq), AcOH (17 eq.), MeCN, 0 °C, 30 min. (p. 97)

Table VII.1. Crystal data and structure refinement for **6**. (p. 124)

Table VII.2. Crystal data and structure refinement for **2**·Fe₂Cl₃O. (p. 125)

Table VII.3. Analytical method for ee measurement of epoxide products in C=C oxidation. (p. 161)

LIST OF SCHEMES

- Scheme I.1.** O₂ activation mechanism by heme and non-heme iron enzymes. (p. 12)
- Scheme I.2.** Schematic representation of the resting state of non-heme diiron enzyme sMMO (left) and methane oxidation mechanism (right). (p. 13)
- Scheme I.3.** Oxidation reactions mediated by high-valent non-heme iron(IV)-oxo complexes. (p. 17)
- Scheme I.4.** Two approaches for the preparation of dimeric iron complexes. (p. 18)
- Scheme I.5.** Generation of different synthetic intermediates relevant to sMMO. (p. 20)
- Scheme I.6.** Peroxodiferric intermediate formed upon O₂ activation of the iron(II) precursor. (p. 21)
- Scheme I.7.** Different complex electrophilicity in C-H bond oxidation by peroxodiferric or high-valent diiron(IV)-oxo intermediates. (p. 21)
- Scheme I.8.** Synthetic high-valent diiron(IV)-oxo intermediates with closed or open cores obtained from the one electron reduced diiron(III) precursors. Red oxygens represent incorporation of oxygen atoms from the oxidant to the intermediate. (p. 22)
- Scheme I.9.** Reversible O₂ bond scission to form a diiron (IV)-oxo and its *syn-to-anti* transformation. Blue color indicates high-spin S = 2 iron(IV)-oxo. (p.23)
- Scheme I.10.** Library of diiron(IV)-oxo complexes obtained from a diiron(III) common precursor. Green indicates low spin S = 1 and blue high spin S = 2 Fe(IV) center. (p. 24)
- Scheme I.11.** Enzyme-like mechanism for the intermolecular ring opening of epoxyalcohols. From ref 118. (p. 30)
- Scheme I.12** Schematic representation of the Olivo, Di Stefano and Costas supramolecular catalyst and its selective catalytic C-H oxidation reaction. (p. 33)
- Scheme II.1.** Tetradentate (bottom) and pentadentate (top) dinucleating ligands and their related iron(II) complexes as platform to generate dioxodiiron(IV) intermediate species. (p. 42)
- Scheme II.2.** Schematic representation of the preparation of hybrid inorganic/organic metallocavitands. (p. 42)
- Scheme II.3.** Reactivity of the metallocavitands as catalyst towards C-H and C=C (left). Iron(IV)=O generated in a cavitand and its reactivity towards sulfides (right). (p. 42)
- Scheme III.1.** Synthetic procedure scheme of the EBPytacn ligand. (p. 47)
- Scheme III.2.** Chemical synthesis to prepare **1**^(IV)=O and **2**^(IV)=O from its iron (II) precursors **1** and **2**, respectively. (p. 63)
- Scheme III.3.** Proposed mechanism for the OAT to sulfides for diiron(IV)-oxo complexes. (p. 69)
- Scheme III.4.** Proposed mechanisms for the oxidation of C-H bonds following a HAT mechanism with rebound or diffusion of the radical. (p. 71)
- Scheme III.5.** Proposed mechanism for the HAT reactivity towards C-H bonds with iron(IV)-oxo complexes with diffusion of the carbon center radical to form desaturation products. (p. 73)

Scheme IV.1. General schematic synthesis of the new functionalized metallocavitands. (p. 77)

Scheme IV.2. Schematic synthesis of **4**. (p. 78)

Scheme IV.3. Schematic synthesis of cavitand **2**. (p. 78)

Scheme IV.4. Exploration of cavitand **2** coordination chemistry different metal ions. Amide groups of cavitand walls are omitted for clarity. (p. 80)

Scheme V.1. Catalytic oxidations with Fe catalyst. a) **2**·Fe(OTf)₂ (3 mol %), H₂O₂ (2.5 eq), AcOH (1.5 eq.), MeCN, 0 °C, 30 min. (p. 94)

Scheme V.2. Catalytic oxidations with Fe and Mn catalysts for substrates that bind inside the cavitand. a) **2**·Fe(OTf)₂ (3 mol %), H₂O₂ (2.5 eq), AcOH (1.5 eq.), MeCN, 0 °C, 30 min. b) **2**·Mn(OTf)₂ (1 mol %), H₂O₂ (2.0 eq), AcOH (17 eq.), MeCN, 0 °C, 30 min. (p. 96)

Scheme VII.1. Schematic synthesis of the EBPytacn ligand. (p. 110)

Scheme VII.2. Schematic synthesis of diiron(II) **1** and **2** complexes. (p. 112)

Scheme VII.3. Schematic synthesis for the obtention of synthon **4**. (p. 118)

Scheme VII.4. Schematic synthesis for the obtention of cavitand **2**. (p. 119)

Scheme VII.5. Catalytic oxidations with Fe catalysts. a) **2**·Fe(OTf)₂ (3 mol %), H₂O₂ (2.5 eq), AcOH (1.5 eq.), MeCN, 0 °C, 30 min. (p. 159)

Scheme VII.6. Catalytic olefin epoxidations with Fe catalysts. a) **2**·Fe(OTf)₂ (3 mol %), H₂O₂ (2.5 eq), AcOH (1.5 eq.), MeCN, 0 °C, 30 min. (p. 160)

Scheme VII.7. Catalytic oxidations with Fe and Mn catalysts for substrates that bind inside the cavitand. a) **2**·Fe(OTf)₂ (3 mol %), H₂O₂ (2.5 eq), AcOH (1.5 eq.), MeCN, 0 °C, 30 min. b) **2**·Mn(OTf)₂ (1 mol %), H₂O₂ (2.0 eq), AcOH (17 eq.), MeCN, 0 °C, 30 min. (p. 161)

AGRACEDIMIENTOS

Aquí se acaba una etapa (oficialmente) que ha sido crucial en mi vida, sin duda la de mayor crecimiento profesional, pero también personal. No podría finalizar esta gran etapa sin dedicar un momento a todas aquellas personas que han formado parte de ella, porque sin ellos/-as Esta historia no se habría escrito.

Primero de todo, a mi director y supervisor Miquel Costas, el cual un día, te abre las puertas del QBis Y te da la oportunidad de subirte al barco. Muchísimas gracias Miquel, por darme tal oportunidad, por tu pasión contagiosa por la química, por todos los conocimientos, la guía y la paciencia. Sin todo esto esta historia ni siquiera habría comenzado. Gràcias Anna I Xavi, los Lords del QBis 4, por todo el tiempo dedicado, la ayuda y los Buenos momentos. A Alicia, la nueva jefa del QBis 4, vales mucho, gracias por la sinceridad, la objetividad y los buenos momentos. Te deseo lo mejor en lo que viene y en lo que vendrá! Gracias Raquel por tu papel fundamental en el QBis, que seríamos sin tu "arte gitano" para los negocios!

Gracias a todos los miembros del QBis, cada uno de vosotros ha tenido un papel fundamental en esta historia. Gracias Michela, compañera de vitrina y de fatigas, de risas y llantos, por toda la ayuda sin condicionantes. Has sido como una madre para mí. Giorgio, gracias por todo lo que me has enseñado desde el principio, por tu sabiduría. Por "aguantar" todas las preguntas en cualquier momento, por tu apoyo, y por ver juego de tronos en tu casa! Marco, pisellone, gracias por acompañarme en esta aventura, por tu empatía, por los desahogos, por las tonterías y las risas y buenos momentos juntos. Gràcies Sabenya, per haver donat el millor de tu, pots dir mil vegades que "no t'agrada la gent", però jo t'he calat fins al fons. Has sigut una persona fonamental per poder tirar endavant amb tot això i ets un gran amic. Gràcies per les classes particulars de Català correcte, capsigrany! Joan, ets un crack, una Excel·lent persona i un bon jueguista! No canviis! Carles, siempre al pie del cañon, sonriente y dispuesto a darte la mano. Lorena, espero que no pierdas esa risa y esas ganas de fiesta! Ori, gracias por haberme aguantado, por tus buenos consejos y las paridas sin fin. Olaf, me ha gustado mucho conocerte más a fondo, gracias por tu sinceridad. Cris, de las más veteranas en el QBis, muchísima suerte en tu nueva etapa! A Todos los miembros que implantaron el "wine club", las cenas, noches de jarana (que no son pocas) y todas las risas, anécdotas y momentos que nunca olvidaré. A todos mis compañeros con los que he tenido la oportunidad de compartir esto y a todos los que empezáis o habéis empezado hace poco el doctorado, que tengáis toda la suerte del mundo y le saquéis todo el jugo que tiene. Andrea, estoy muy feliz de que hayas entrado en esta familia, eres una bellísima persona, te deseo lo mejor.

También quiero agradecer y dedicar unas líneas con cariño para el team “Cal Mico”, Carla, Brenda, Ernest, Pau, Nil. Hay un dicho que dice: “nunca es tarde si la dicha es buena”. Gracias por haber compartido y compartir esta afición conmigo con la misma pasión que yo, por las charlas entre vías y por las birras post-entreno. Amun, sempre amunt!

Gracias a los amigos de una vida, los que habéis estado ahí desde el principio. Fito, casi desde que nacimos hemos estado juntos, inseparables, aunque pasen meses, y espero que no cambie. Infinitas gracias por todo, absolutamente todo. Mario y Niki, que os voy a decir, hemos vivido todo juntos. Hemos compartido y cumplido sueños y en gran parte habéis sido mis maestros. Gracias por vuestra incondicionalidad ante todo, por demostrarme que la distancia no significa nada si la amistad es una como la vuestra. Por hacer como si el tiempo no hubiera pasado cada vez que nos vemos. Gracias por aguantarme y apoyarme en esta aventura y espero que siga así para toda la vida. Especial dedicación para todos los integrantes del cafesssstttt! Gracias por hacer cada reencuentro único, por hacerme sentir en el hogar cada vez que volvemos. Porque nos sigamos uniendo siempre y siempre sea igual de bueno. Por las risas infinitas. Gracias, de corazón.

Gracias a mis padres. Lo sois todo para mí. Mis referentes, mis consejeros, mis amigos y mis maestros. Gracias por todo el apoyo incondicional siempre, en la salud y en la enfermedad, en la riqueza y en la pobreza, No puedo describir con palabras la suerte que tengo de que seáis mis padres. Habéis vivido el doctorado conmigo como si lo hubierais hecho vosotros. Gracias, gracias y millones de gracias.

Por supuesto, no podrías faltar tú. Qué te voy a contar, si todo lo que escribo aquí ya lo sabes. Has aguantado la época más dura de esta travesía. Has apagado todos los fuegos sin quemarte lo más mínimo. Has sido compañera, consejera, amiga. Eres mi válvula de sobrepresión, siempre haciendo que mis nervios más explosivos encontraran su vía de escape. Esta historia también las has escrito tú, Valeria, y espero que no pares de escribirla, pero siempre con esa sonrisa imborrable.

ACKNOWLEDGEMENTS

This work would not have been possible without the following collaborations:

- Serveis tècnics de Recerca (STR) from Universitat de Girona for technical support, with special remark to Laura Gómez and Anna Costa for their help with mass spectrometry.
- Dr. Agustí Lledó, from the DiMoCaT group in the Universitat de Girona (UDG) for all the support and knowledge contributed in the collaborative project with Dr. Miquel Costas about bioinspired catalysis employing cavitand receptors.

- Financial support by:

Spanish Ministry of Economy, Competitivity and Industry (MINECO, CTQ2015-70795-P).

ICREA (ICREA Academia award to MC).

GRAPHICAL ABSTRACT

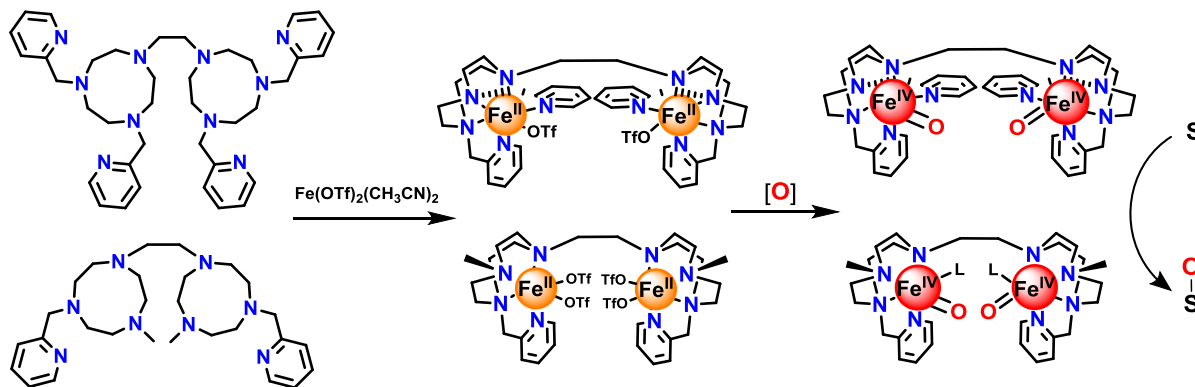
Summary (p. 1)

Chapter I. General Introduction (p. 7)

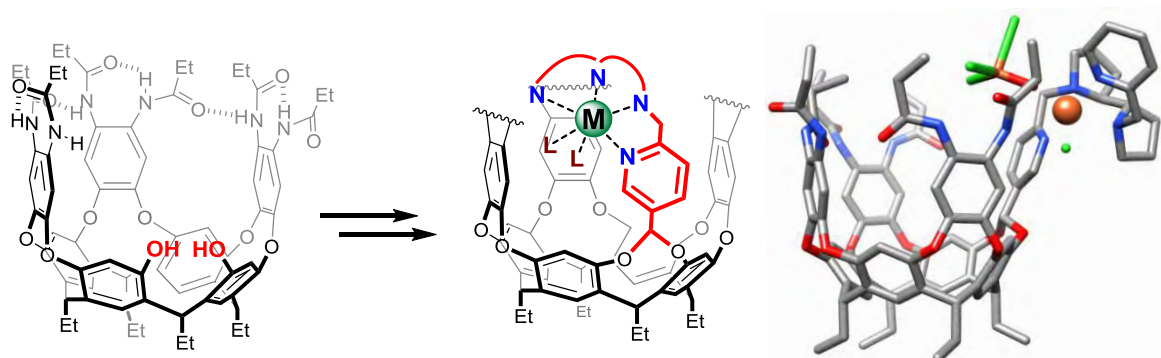
Chapter II. Objectives (p. 39)

Chapters III, IV and V. Results and discussion (p. 43)

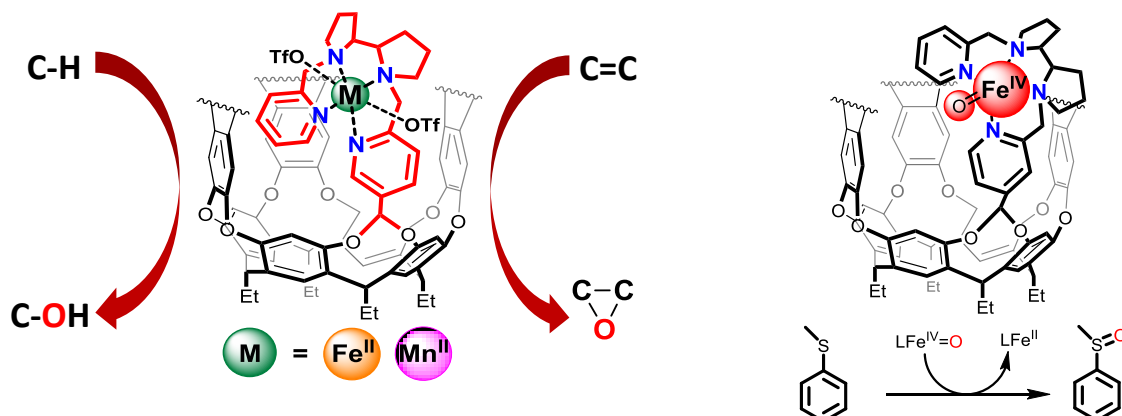
III.1 Synthesis, characterization and reactivity of diiron complexes with dinucleating bis-tacn-based ligands (p. 41)



IV.1 Synthesis and characterization of a new functionalized metallocavitand (p. 77)



V.1 Reactivity studies of metallocavitands (p. 93)



Chapter VI. General conclusions (p. 103)

Chapter VII. Experimental section (p. 107)

Annex (p. 131)

References (p. 163)

Summary	1
Resumen	3
Resum	5
Chapter I. General introduction	7
I.1. Oxygenases in biological systems.....	9
I.2. Biological role of iron-containing enzymes.....	10
I.3. Synthetic non-heme bioinspired model complexes.....	14
I.3.1 Mononuclear non-heme iron model complexes.....	14
I.3.1.1. High valent non-heme iron(IV)-oxo model complexes.....	16
I.3.2. Binuclear non-heme iron model complexes.....	18
I.3.2.1. Non-heme Peroxodiiron model complexes.....	20
I.3.2.2 Binuclear High-valent iron(IV)-oxo intermediates.....	21
I.4 Rising complexity in bioinspired model complexes.....	26
I.4.1. Supramolecular tool as approach for enzyme mimics.....	27
I.4.1.1. Artificial enzymes. From stoichiometric to catalysis.....	28
I.4.1.2. Supramolecular metal complex catalysts.....	31
I.4.2. Cavitands as platform for enzyme-like reactions.....	34
Chapter II. Main objectives	39
Chapters III, IV and V. Results and discussion	43
III.1. Synthesis, characterization and reactivity of diiron complexes with dinucleating bis-tacn-based ligand	45
III.1.1 Synthesis and characterization of two novel dinucleating ligands based on the tacn scaffold and their related iron complexes.....	45
III.1.1.1. Synthesis and characterization of the dinucleating ligands EBPytacn and Py ₄ btacn.....	46
III.1.1.2. Synthesis and characterization of the dinucleating complexes 1 and 2	49
III.1.1.2.1 Solid state structures.....	51
III.1.1.2.2. Solution behavior.....	55
III.1.1.2.2.1. ¹ H NMR spectroscopy.....	55
III.1.1.2.2.2. UV-vis spectroscopy.....	59
III.1.2. Trapping and characterizing diiron(IV)-oxo intermediate species.....	63
III.1.3. Reactivity studies of the diiron(IV)-oxo species.....	68

III.1.3.1. Reactivity studies of 2^{IV=O} in OAT towards sulfides.....	68
III.1.3.2. Reactivity studies of 2^{IV=O} in HAT towards C-H bonds.....	71
III.2. Concluding remarks.....	74
IV.1. Synthesis and characterization of a new functionalized metallocavitand.....	77
IV.1.1. Synthesis of a novel cavitand platform functionalized with a chelating ligand scaffold and their bioinspired Fe(II), Mn(II) and Zn(II) complexes.....	77
IV.1.1.1 Synthesis of a functionalized cavitand with an aminopyridine ligand scaffold.....	77
IV.1.1.2. Synthesis of the Fe(II), Mn(II) and Zn(II) coordination complexes.....	80
IV.1.2. Characterization studies of the new cavitand and its metal complexes.....	81
IV.1.2.1. Structural characterization of 2 and its metal complexes.....	81
IV.1.3. Host-Guest studies.....	87
IV.2. Concluding remarks.....	91
V.1. Reactivity studies of metallocavitands.....	93
V.1.1. Catalytic studies employing 2 .Fe(OTf) ₂ and 2 .Mn(OTf) ₂ metallocavitands.....	94
V.1.2. Intermediate species and reactivity.....	98
V.1.2.1. Generation and characterization of high-valent iron(IV)-oxo species in a metallocavitand platform.....	98
V.1.2.2. Reactivity of high-valent iron(IV)-oxo species in oxygen atom transfer to sulfides in a cavitand platform.....	99
V.2. Concluding remarks.....	101
Chapter VI. General conclusions.....	103
Chapter VII. Experimental section.....	107
VII.1. Experimental section chapter III.....	109
VII.1.1. Materials and methods.....	109
VII.1.2. Experimental protocols.....	110
VII.1.2.1. Synthesis of ligands.....	110
VII.1.2.2. Synthesis of the complexes.....	113
VII.1.2.2. General procedure for the generation and reactivity of the Fe(IV)-oxo species.....	114
VII.1.2.3.1. Generation of the Fe(IV)-oxo intermediates.....	114

VII.1.2.3.2. Reactivity studies of the Fe(IV)-oxo intermediates towards OAT/ HAT.....	114
VII.1.3. X-ray diffraction data.....	115
VII.2. Experimental section chapter IV.....	117
VII.2.1. Materials and methods.....	117
VII.2.2. Experimental protocols.....	117
VII.2.2.1. Synthetic procedures.....	117
VII.2.2.1.1. Synthesis of guests 8-11.....	122
VII.2.3 X-ray diffraction data.....	123
VI.2.2.3. Host-Guest studies.....	127
VI.2.2.3.1. Standard protocol for ¹ H NMR Host-Guest studies.....	127
VII.3. Experimental section chapter V.....	128
VII.3.1. Materials and methods.....	128
VII.3.2. Experimental protocols.....	129
VII.3.2.1. Catalytic oxidation reactions.....	129
VII.3.2.1.1. General procedure for catalytic oxidations.....	129
VII.3.2.1.2. Generation and reactivity of the cavitand-Fe(IV) oxo species [2•Fe ^{IV} (O)] ²⁺	129
Annex.....	131
Annex chapter III.....	133
Annex chapter IV.....	140
Annex chapter V.....	159
References.....	163

Summary

In nature, enzymes are the responsible for important organic transformations, including the oxidation of organic molecules. Hydrocarbons are difficult targets, due to their high and iso energetic bonds, for which enzymes display an outstanding selectivity. The active center of these enzymes is composed by first row transition metals such as iron, forming in many cases high-valent iron(IV)-oxo species. These intermediate species have been trapped and characterized in natural systems in their oxidation reactions. So, there is a need to study the mechanism of these enzymes in detail, in order to be able to replicate the chemistry performed by them. One of the most used approaches consists in the design and synthesis of bioinspired complexes, imitating the metal center with simple chelating ligands. Mononuclear metal systems have been widely studied, due to their simple structure, but there is a lack in the study of binuclear systems, where both metals can cooperate or bridge between them. On the other hand, there are few examples of more complex systems, replicating not only the active center, but also the binding pocket that accommodate the substrate in the enzyme and drive the reaction through specific pathways. Supramolecular chemistry is one of the approaches used to imitate this selectivity of enzymes, which for model complexes is a difficult task. This doctoral dissertation is focused on this two less explored topics: in one hand the design and synthesis of simple binuclear iron models bearing the triazacyclononane moiety and the study of their reactivity. On the other hand, the design and synthesis of more complex systems to imitate the environment in the active center of an enzyme is approached using cavitands as supramolecular platform.

In first place, two new dinucleating ligands and its binuclear Iron(II) complexes have been synthesized and characterized. From them, it has been able to prepare and characterize two new diiron(IV)-oxo species and study their reactivity towards well established substrates, as are oxygen atom transfer (OAT) to thioanisoles or hydrogen atom abstraction (HAT) to benzylic C-H bonds. This diiron(IV)-oxo core has been identified as intermediate in the formation and breaking of the O-O bond, which has been found in the soluble methane monooxygenase (sMMO) that hydroxylates CH_4 to CH_3OH .

In the second part, it has been synthesized and characterized a cavitand functionalized with a tetraaminopyridine ligand for the coordination of first row transition metals as Fe(II), Mn(II) and Zn(II). This system consists in a well-defined and active coordination complex anchored to a confined space suitable for substrate binding, mimicking the enzyme-like structure. The resulting Mn(II) and

Fe(II) complexes are competent catalysts for bioinorganic transformations as the oxidation of C-H and C=C bonds with hydrogen peroxide under mild conditions.

Non-heme oxoiron (IV) complexes are highly reactive species which readily engage in C-H oxidation and oxygen transfer reactions, and their high reactivity is usually non compatible with elaborated supramolecular scaffolds. From the iron(II) supramolecular platform it was achieved the clean formation, stabilization and reactivity (towards OAT reagents) of an iron(IV)-oxo intermediate.

Resumen

En la naturaleza, las enzimas son las responsables de importantes transformaciones orgánicas, incluida la oxidación de las moléculas orgánicas. Los hidrocarburos son objetivos difíciles, debido a una alta energía de sus enlaces, además de ser estos isoenergéticos, para los cuales las enzimas muestran una selectividad única. El centro activo de estas enzimas está compuesto por metales de la primera serie de transición, como el hierro, que en muchos casos forman especies de alto estado de oxidación, tales como el hierro(IV)-oxo. Estas especies intermedias han sido observadas y caracterizadas en sistemas naturales en sus reacciones de oxidación. Por lo tanto, es necesario estudiar en detalle el mecanismo de estas enzimas, para poder replicar la química realizada por ellas a nivel sintético de laboratorio. Una de las estrategias más utilizadas consiste en el diseño y la síntesis de complejos bioinspirados, imitando el centro metálico con ligandos quelantes simples. Los sistemas de complejos metálicos mononucleares han sido ampliamente estudiados, debido a su estructura simple, pero hay una carencia de estudios referentes a sistemas binucleares, donde ambos metales pueden cooperar o unirse entre ellos. Por otro lado, hay algunos ejemplos de sistemas más complejos, que no solo reproducen el centro activo, sino también el sitio de reconocimiento que aloja el sustrato en la enzima y conduce la reacción a través de vías específicas. La química supramolecular es uno de los enfoques utilizados para imitar el sitio de reconocimiento de las enzimas, que para los complejos simples que imitan solo el centro activo es una tarea difícil. Esta tesis doctoral se centra en estos dos temas menos explorados: por un lado, el diseño y la síntesis de complejos modelo simples binucleares de hierro utilizando como base el quelante macrocíclico triazaciclono-nano y el estudio de su reactividad. Por otro lado, el diseño y la síntesis de sistemas más complejos para imitar el sitio de reconocimiento de un enzima, en el que a la vez se encuentre un centro activo capaz de llevar a cabo la reactividad. Este último proyecto se ha llevado a cabo utilizando cavitandos como plataforma supramolecular.

En primer lugar, se sintetizaron y caracterizaron dos nuevos ligandos binucleares y sus complejos diméricos de hierro (II). A partir de ellos, se ha podido preparar y caracterizar dos nuevas especies binucleares de alto estado de oxidación hierro(IV)-oxo, para los cuales se ha podido estudiar su reactividad con algunos sustratos, como lo son la transferencia de átomo de oxígeno (OAT) a tioanisoles o la oxidación de enlaces C-H bencílicos mediante un proceso de abstracción de hidrógeno (HAT). Esta especie activa binuclear de hierro(IV)-oxo se ha identificado como intermedio en la formación y rotura del enlace O-O que se ha encontrado en la enzima metano monooxigenasa (sMMO) que hidroxila CH_4 a CH_3OH .

En la segunda parte, se ha sintetizado y caracterizado un cavitando funcionalizado con un ligando de tetraaminopiridina para la coordinación de metales de la primera serie de transición, tales como Fe (II), Mn (II) y Zn (II). Este sistema consiste en un complejo de coordinación activo y bien definido anclado a un espacio confinado donde pueden unirse moléculas orgánicas más pequeñas (sustratos), que simula la estructura similar a la enzima. Los complejos de Mn (II) y Fe (II) resultantes son catalizadores competentes para transformaciones bioinorgánicas, ya que son capaces de oxidar enlaces C-H y C = C con peróxido de hidrógeno en condiciones suaves.

Los complejos de alto estado de oxidación como los descritos anteriormente (hierro(IV)-oxo) son especies altamente reactivas que están involucradas en las reacciones de oxidación, y su alta reactividad generalmente no es compatible con estructuras supramoleculares elaborados, ya que pueden ser degradadas por las especies altamente reactivas. Sin embargo, a partir del complejo de hierro(II) anclado al cavitando, se logró la formación limpia, la estabilización y la reactividad (tipo OAT) de un intermedio de hierro(IV)-oxo anclado a la cavidad supramolecular.

Resum

En la naturalesa, els enzims són els responsables d'importantes transformacions orgàniques, inclosa l'oxidació de molècules orgàniques. Els hidrocarburs són objectius difícils, a causa d'una alta energia dels seus enllaços, a més de ser aquests isoenergètics, per als quals els enzims mostren una selectivitat única. El centre actiu d'aquests enzims està compost per metalls de la primera sèrie de transició, com el ferro, que en molts casos formen espècies d'alt estat d'oxidació, com es el cas del ferro(IV)-oxo. Aquestes espècies intermèdies han estat observades i caracteritzades en sistemes naturals en les seves reaccions d'oxidació. Per tant, cal estudiar en detall el mecanisme d'aquests enzims, per poder replicar la química realitzada per elles a nivell sintètic de laboratori. Una de les estratègies més utilitzades consisteix en el disseny i la síntesi de complexos bioinspirats, imitant el centre metàl·lic amb lligands quelants simples. Els sistemes de complexos metàl·lics mononuclears han estat àmpliament estudiats, per la seva estructura simple, però hi ha una manca d'estudis referents a sistemes binuclears, on tots dos metalls poden cooperar o unir-se entre ells. D'altra banda, hi ha alguns exemples de sistemes més complexos, que no només reproduïen el centre actiu, sinó també el lloc de reconeixement que allotja el substrat dins l'enzim i condueix la reacció a través de vies específiques. La química supramolecular és una de les eines més utilitzades per imitar el lloc de reconeixement dels enzims, cosa que pels complexos simples que imiten només el centre actiu és una tasca difícil. Aquesta tesi doctoral es centra en aquests dos temes menys explorats: d'una banda, el disseny i la síntesi de complexos model simples binuclears de ferro utilitzant com a base el quelant macrocíclic triazacilononà i l'estudi de la seva reactivitat. D'altra banda, el disseny i la síntesi de sistemes més complexos per imitar el lloc de reconeixement d'un enzim, al que alhora es trobi un centre actiu capaç de dur a terme la reactivitat. Aquest últim tema s'ha dut a terme fent servir cavitands com a plataforma supramolecular.

En primer lloc, s'han sintetitzat i caracteritzat dos nous lligands binuclears i els seus complexos dimèrics de ferro (II). A partir d'ells, s'ha pogut preparar i caracteritzar dues noves espècies binuclears d'alt estat d'oxidació ferro(IV)-oxo, per als quals s'ha pogut estudiar la seva reactivitat amb alguns substrats, com ho són la transferència d'àtom d'oxigen (OAT) a tioansoles o l'oxidació de enllaços C-H benzílics mitjançant un procés d'abstracció de hidrògen (HAT). Aquesta espècie activa binuclear de ferro(IV)-oxo s'ha identificat com intermedi en la formació i trencament de l'enllaç O-O que s'ha trobat en el enzim metano monooxigenasa (sMMO) que hidroxila CH_4 a CH_3OH .

A la segona part, s'ha sintetitzat i caracteritzat un cavitand funcionalitzat amb un lligant de tetraaminopiridina per a la coordinació de metalls de la primera sèrie de transició, com Fe (II), Mn (II) i Zn (II). Aquest sistema consisteix en un complex de coordinació actiu i ben definit ancorat a un espai confinat on poden unir-se molècules orgàniques més petites (substrats), que simula l'estructura similar a l'enzim. Els complexos de Mn (II) i Fe (II) resultants són catalitzadors competents per a transformacions bioinorgàniques, ja que són capaços d'oxidar enllaços C-H i C = C amb peròxid d'hidrogen en condicions suaus.

Els complexos d'alt estat d'oxidació com els descrits anteriorment (ferro(IV)-oxo) són espècies altament reactives que estan involucrades en les reaccions d'oxidació, i la seva alta reactivitat generalment no és compatible amb estructures supramoleculares elaborades, ja que poden ser degradades per les espècies altament reactives. No obstant això, a partir del complex de ferro (II) ancorat al cavitand, es va aconseguir la formació neta, l'estabilització i la reactivitat (tipus OAT) d'un intermedi de ferro(IV)-oxo ancorat a la cavitat supramolecular.

CHAPTER I

GENERAL INTRODUCTION

I.1 Oxygenases in biological systems.

Selective and mild alkane oxidation reactions are of interest because they generate valuable molecules for organic synthesis from widely available feedstocks.¹⁻² This is strongly related with the production of fine chemicals, which are important alkane-based molecules, that in many cases require a selective oxidation step in their synthesis,³ . However, harsh reaction conditions (high pressure, high temperatures, long reactions times, etc.) and hazardous oxidizing reagents (Chloramines, chromates, permanganates) are often required, producing large quantities of non-desired waste products. There has been a growing interest in developing new, more efficient methodologies, especially catalytic processes that avoid the use of stoichiometric quantities of hazard materials and at the same time reducing the waste production.⁴⁻⁶

In this regard, dioxygen is the greenest reagent to perform oxidation reactions, being one of the most important molecules in nature that plays a critical role in biology, ranging from nutrient metabolism to the synthesis of various important biomolecules such as amino acids, hormones, neurotransmitters, etc.⁷ But dioxygen is present in nature as an inert molecule due to its triplet ground state that makes the direct reaction with singlet molecules a forbidden process. Nature can overcome this problem activating dioxygen by means of enzymes containing first row transition metals such as iron, manganese and copper.⁸⁻⁹ The active metal center is capable to react directly with triplet oxygen making it reactive, thanks to the ability of these enzymes to support different oxidation states.¹⁰⁻¹² At the same time, enzymes are not only able to enable cleavage of strong bonds, but also to drive reactions through a specific pathway due to delicate weak interactions between the second coordination sphere (the protein structure surrounding the metal center) and the substrate. In addition, the second coordination sphere defines the space available in the proximity of the metal. These features define a confined space where the substrate is isolated from bulk medium and exposed to direct contact with appropriate functional groups, restricting its approach to the metal center to specific paths. As a consequence of this “selective” positioning, highly efficient and selective processes (in terms of stereo, regio and chemoselectivity) take place under mild conditions.¹³ This unique behavior displayed by enzymes is especially remarkable when multiple bonds with similar energies are present in the substrate, a situation that represents a big challenge for conventional organic synthesis.

I.2 Biological role of iron-containing enzymes.

Oxygenases can contain chemically very diverse active sites, and display a wide array of

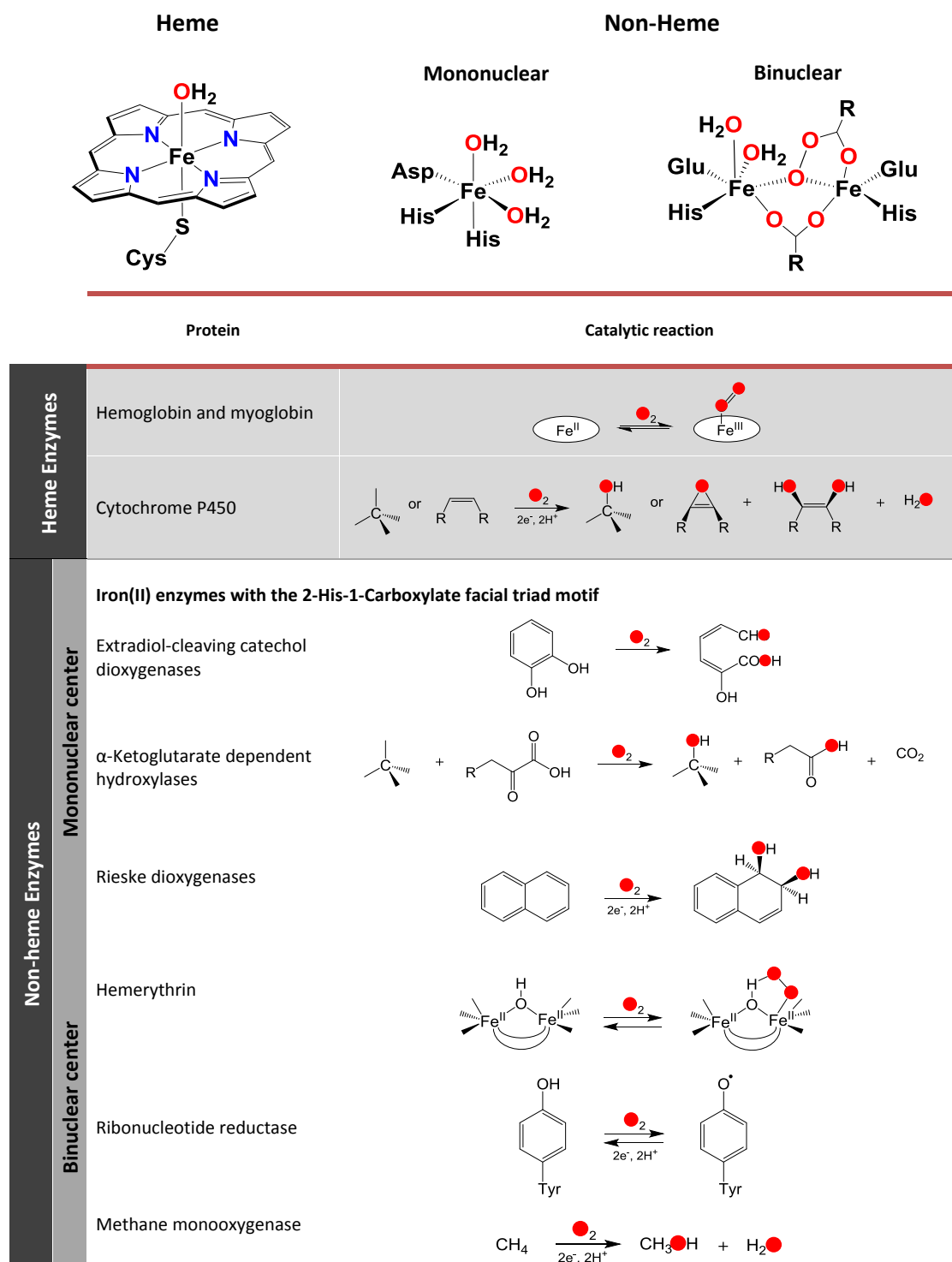


Figure I.1. Heme and non heme iron dependent enzymes involved in O₂ metabolism.

transformations. Iron is usually the metal present in their active site, being the main responsible for

their reactivity (figure I.1). In the active sites, iron is usually coordinated to nitrogen and oxygen based donating ligands. There are two main classes of enzymes depending on the type of ligand chelating the metal: heme and non-heme. Heme proteins refer to those where the metal is

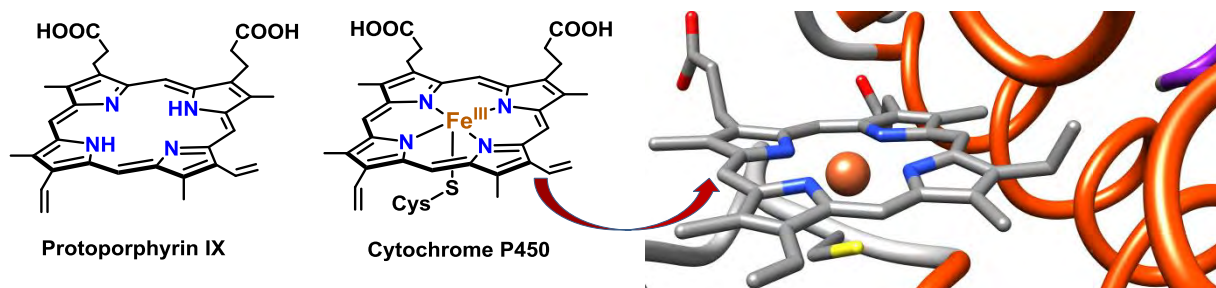


Figure I.2. Structure of cytochrome P450 enzyme.

coordinated to a protoporphyrin macrocycle with cysteine or histidine as an axial ligand (Figure I.2).¹⁴⁻¹⁵ The cytochrome P450 (CytP450) family of enzymes is the prototype of heme oxygenase and peroxidase enzymes. On the other hand, non-heme enzymes (figure I.3) are not supported by a macrocycle ligand, but by amino acid residues, especially histidine (imidazole) and aspartic/glutamic (carboxylic acid containing amino acids).¹⁶ There is a wide range of non-heme enzymes, so they are classified depending on the transformation (Figure I.1). At the same time, non-heme enzymes can be

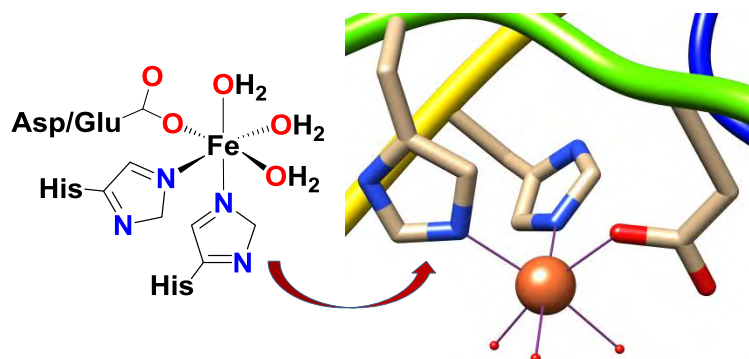
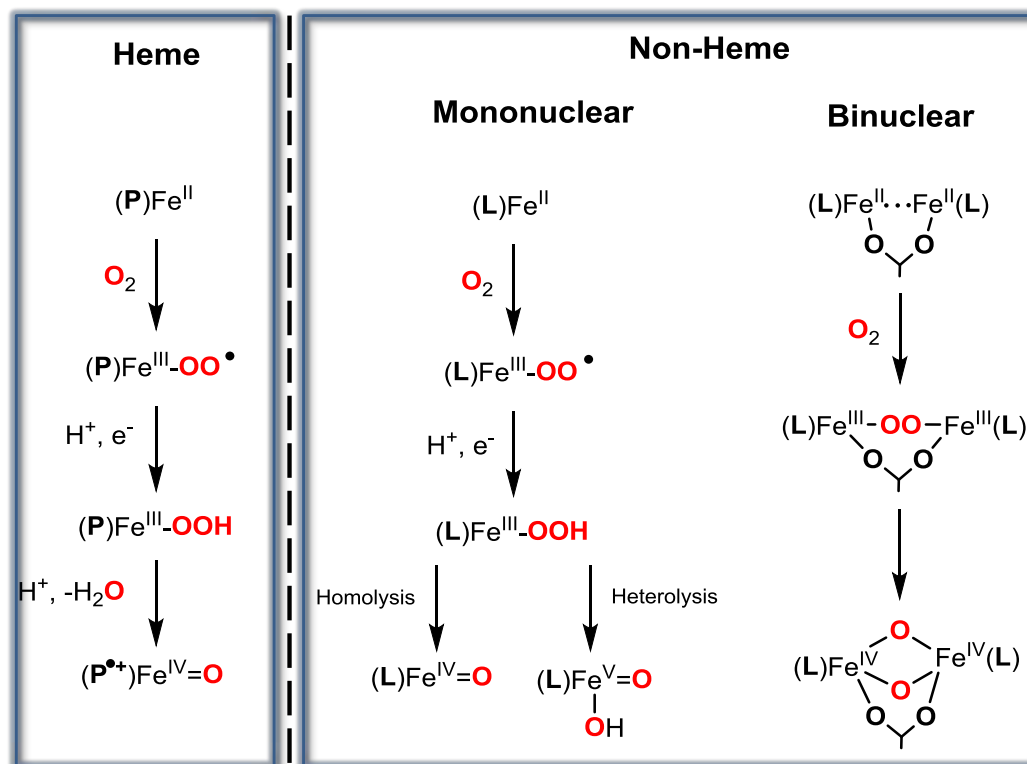


Figure I.3. Structure of non-heme mononuclear iron enzyme.

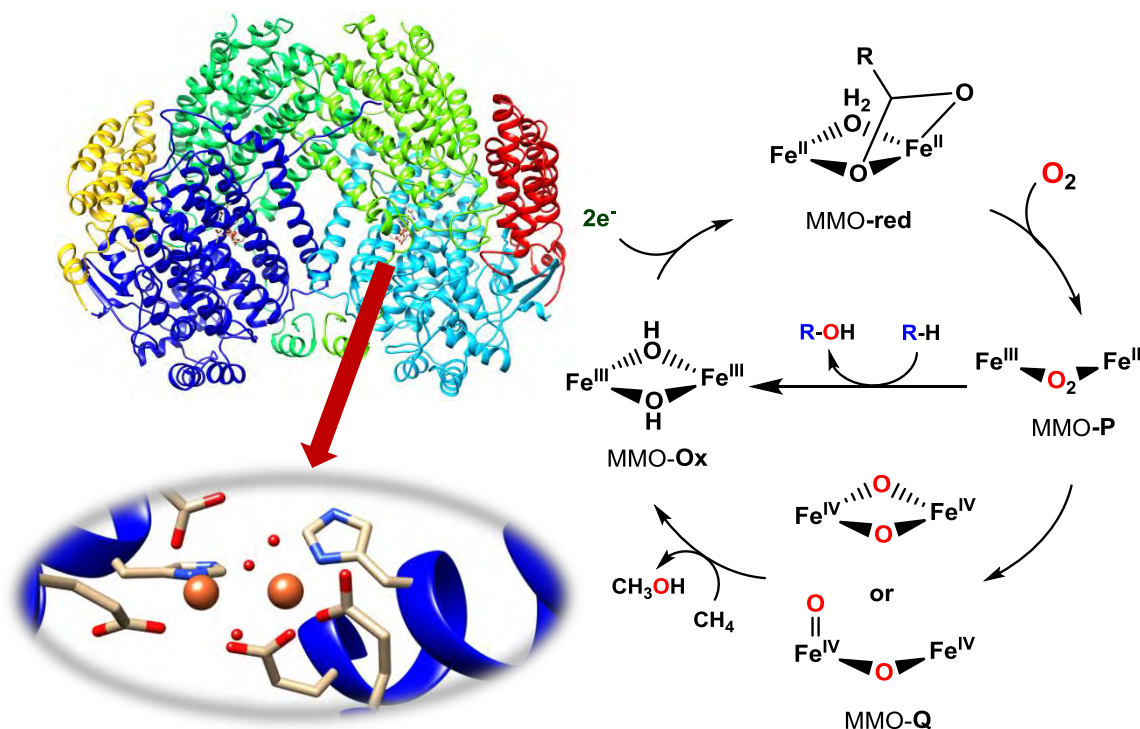
divided in two classes depending on its nuclearity: mononuclear iron enzymes (figure I.3), with most representative examples being Rieske and α -KG-dependent oxygenases. On the other hand, enzymes bearing a binuclear iron center are gaining interest in the last few years (scheme I.1, right; scheme I.2).¹⁷⁻²⁰ The most remarkably diiron enzyme is soluble methane monooxygenase (sMMO), being the only natural system able to oxidize methane to methanol. (scheme I.2).

General introduction



Scheme I.1. O₂ activation mechanism by heme and non-heme iron enzymes

Understanding the action mechanism of both heme and non-heme systems may provide ideas to scientists of how to reproduce their function with artificial systems. (Scheme I.1).⁹ Generally for both type of enzymes, the oxygen molecule binds to an iron(II) metal center, that is oxidized to form iron(III)-superoxo and/or iron(III)-peroxo species.²¹ In these later species, O-O bond can be cleaved, producing the formation of high-valent iron-oxo species, which are more powerful oxidants than the previous ones. For heme enzymes, the species formed upon O-O bond cleavage is formulated as a radical (P•⁺)iron(IV)-oxo (formally an iron(V)-oxo),²² proposed in 1970s by J.T. Groves et al,²³⁻²⁴ and experimentally demonstrated in 2010 by Green et al, where the active species iron(IV)-oxo cation radical, compound I, was trapped and characterized in the natural enzyme.²⁵ For non-heme iron oxygenases, the most evoked species is the iron(IV)-oxo,^{7, 25-33} which trap and characterization has been successfully accomplished by Bollinger and Krebs.¹² The first high-valent iron(IV)-oxo in a non-heme natural system was observed in the mononuclear iron enzyme TauD (α -KG dependent enzyme).²⁸ A similar situation is found in diiron enzymes, where from a diiron(II) reduced form, oxygen is coordinated to the metal to form Fe-OO-Fe peroxo complexes, that upon O-O bond cleavage give place to the high valent diiron(IV)-oxo species (scheme I.1)



Scheme 1.2. Schematic representation of the resting state of non-heme diiron enzyme sMMO (left) and methane oxidation mechanism (right).

Binuclear iron enzymes, which models are the objective of chapter III of this thesis, have been less studied due to their higher complexity compared with mononuclear ones and have been reviewed recently by L. Que and coworkers.³⁴ During the last years, the most studied systems regarding binuclear non-heme iron enzymes have been hemerythrin, soluble methane monooxygenase (sMMO) and ribonucleotide reductase (RNR), due to their biological implication in oxygen transport, oxidation of methane to methanol and implication in synthesis of DNA, respectively. One of the most studied, and reference for this thesis is the sMMO, with special focus on the high valent species called intermediate **Q** (scheme 1.2), formulated as a bis(μ -oxo)Fe₂(IV) diamond closed core. This species have been postulated during the years and demonstrated by Lipscomb and co-workers in 2015 employing time-resolved resonance Raman (TR³) spectroscopy aided by labelling studies.³⁵ The data reveal a bis(μ -oxo)Fe₂(IV) diamond closed core structure.³⁶⁻³⁸ However very recently, the structure of **Q** has been reanalyzed by DeBeer and co-workers by K α high-energy-resolution fluorescence-detected X-ray absorption spectroscopy (HERFD XAS). The data favors an open core for the structure of **Q**, which is in disagreement with the EXAFS analysis from 1997 and with the results obtained by Lipscomb by TR³. Moreover, there is also a debate regarding if the diamond core closed structure is reactive enough to perform hydrogen atom abstraction (HAT) from unactivated C-H bonds based on the higher reactivity found for model complexes upon opening

General introduction

the diamond core,³⁹ proposing a closed to open isomerization to gain enough reactivity prior to the HAT.

I.3. Synthetic non-heme bioinspired model complexes.

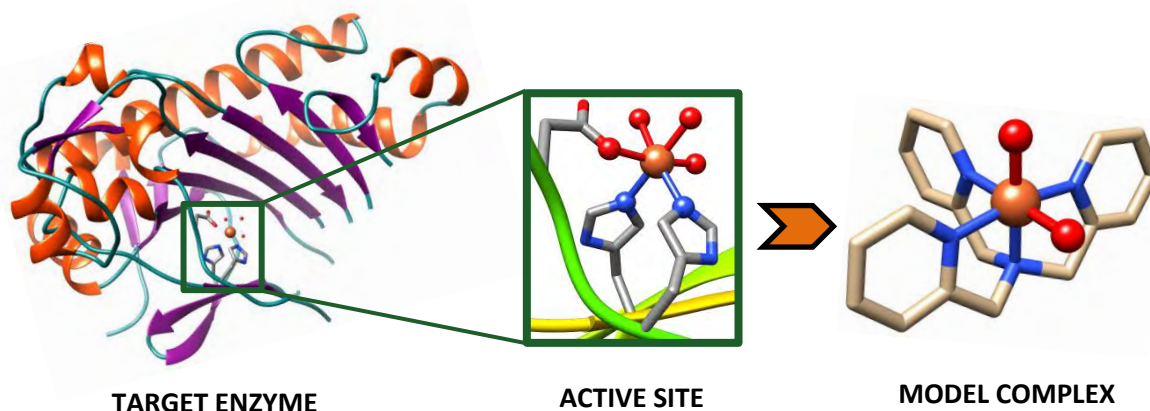


Figure I.4. Synthetic model complex approach for the mimic of enzymes.

To study metalloproteins is challenging, usually because the active metal center represents a very small part of the whole enzyme, which purification and isolation may be tedious and difficult because of its complex structure. The development of synthetic model complexes is a very useful tool in order to reproduce non-heme enzymes in a simple manner, copying the structure and function of the first coordination sphere of the metal center (figure I.4). Characterization methods such as spectroscopic techniques (UV-Vis, Mössbauer, EPR, etc.) can be applied much easier to bioinspired model complexes because of their much simpler structure. Also, the properties and parameters of metastable species can be studied much more easily in these kind of model complexes and compared with those of the natural enzyme to gain insight in the mechanistic details. To reproduce the first coordination sphere of non-heme iron oxygenases, N-donor ligands to mimic histidines and O-donor as carboxylate and alkoxide ligands to mimic glutamate and aspartate residues are usually the choice. These ligands are relatively easy to tune and so electronics, sterics or coordination effects affecting the metal can be studied systematically and correlate them with reactivity features.

I.3.1. Mononuclear non-heme iron model complexes.

A large range of complexes have been prepared in order to mimic both structure and function of these enzymes. A remarkable starting point in this field was reported by Que and coworkers back in

1997 with the TPA system,⁴⁰ a nitrogen-based tetradentate ligand bearing an amine group bonded to 2 methylenepyridine groups that chelates the iron center leaving two free cis-labile coordination sites, $[\text{Fe}^{\text{II}}(\text{TPA})(\text{CH}_3\text{CN})_2]^{2+}$ (figure I.5), which represents the first example of a well-defined non-heme mononuclear iron(II) complex able to perform the stereospecific oxidation of unactivated C-H bonds. Since then, several iron(II) systems have been described with a similar chelating motif,

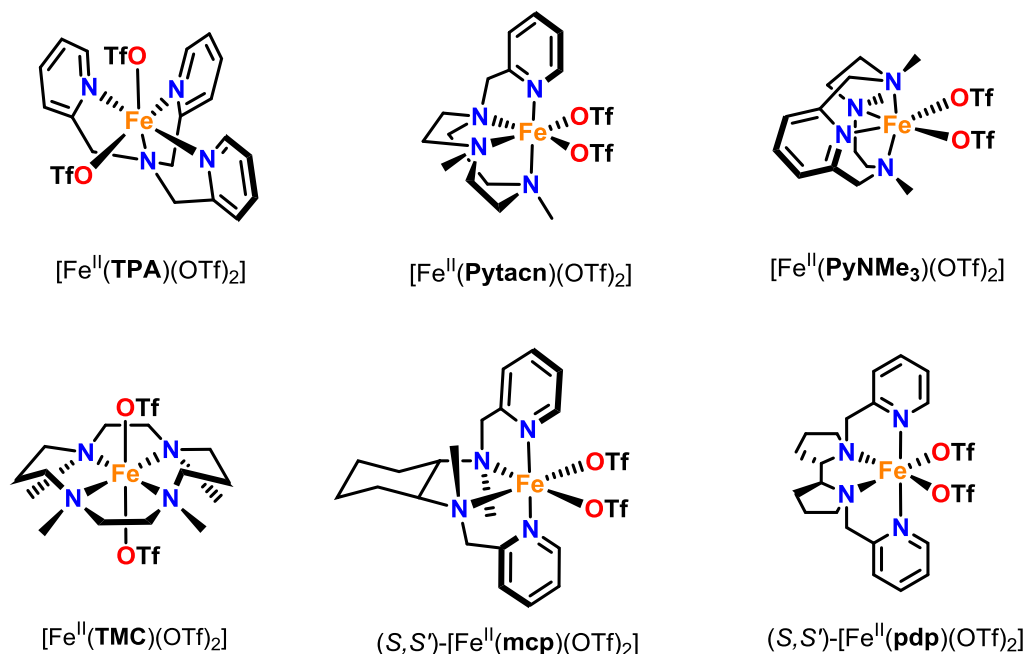


Figure I.5. Selected model complexes for mononuclear non-heme enzymes.

demonstrating to be good functional models for these enzymes,^{16, 41-46} The model complexes depicted in figure I.5 represents just a small group of the very wide variety reported in the last years, such the examples from Gebbink,^{16, 47} Burzlaff⁴⁸ or Chi-Ming Che,⁴⁹ among others. At the same time, is of relevant importance the nature of the species responsible of this special reactivity. Some of the complexes depicted in figure I.5 have been used also as platforms to obtain intermediate species, metastable species responsible of the reactivity, but difficult to detect directly in natural systems. These species can be generated in synthetic model complexes and compared with the ones of the enzymes. The species generated in model complexes are easier to surrogate to kinetic or spectroscopic studies, simplifying its study and characterization in comparison with natural systems. . The most evoked intermediate for non-heme iron enzymes have been the high-valent iron(IV)-oxo species, being the intermediates finally responsible of substrate oxidation. In the next section synthetic iron(IV)-oxo intermediate species will be described briefly.

I.3.1.1. High valent non-heme iron(IV)-oxo model complexes

Several efforts have been devoted to the study, isolation and characterization of high-valent iron-oxo complexes to get more insight into spectroscopic and chemical properties of these species. Is of special relevance the iron(IV)-oxo intermediate, present in most of non-heme enzymes and being a really powerful oxidant that can react with strong C-H bonds. Regarding non-heme mononuclear iron enzymes, a high-valent iron(IV)-oxo species was first observed in TauD, an α -ketoglutarate dependent enzyme, which iron center could be assigned as a high-spin $S = 2$ with the help of spectroscopic techniques. This intermediate has been subsequently observed in several non-heme iron enzymes.

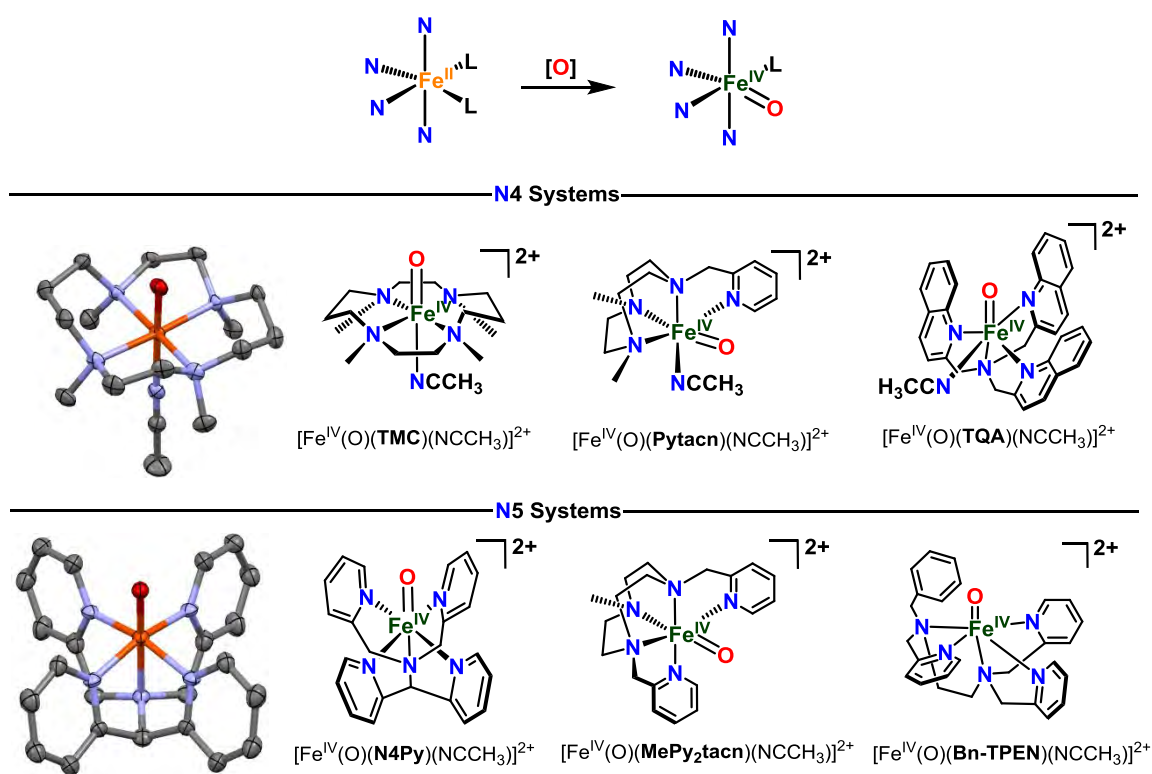
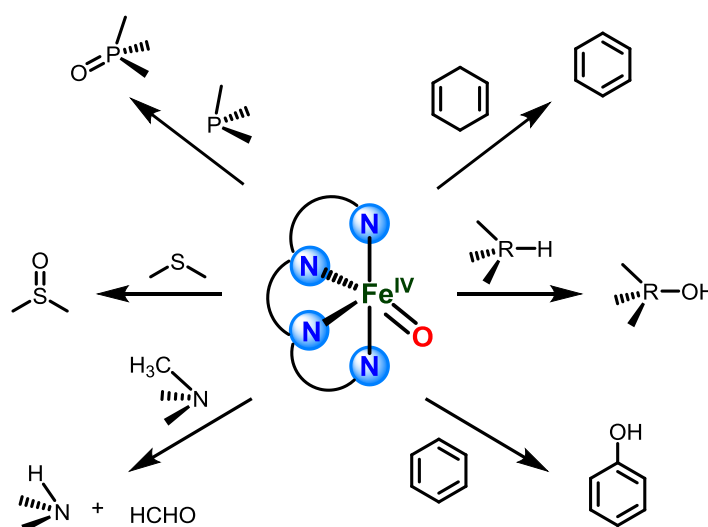


Figure I.6. Examples of Synthetic high-valent mononuclear Fe(IV)=O complexes.

In 2000, the first evidence for a mononuclear non-heme Fe(IV)=O was reported by Wieghardt et al. despite in low yield.⁵⁰ However, there was no structural information available for this species due to its instability. But in 2003, the first crystal structure of a synthetic Fe(IV)=O in high-yield was reported by Que and coworkers with the **TMC** system,⁵¹ thanks to the great stability of the $[\text{Fe}^{\text{IV}}(\text{O})(\text{TMC})(\text{NCCH}_3)](\text{OTf})_2$ complex, allowing its crystallization and resolution of the crystal structure (figure I.6, top left). Since then, several iron(IV)-oxo complexes have been synthesized and

characterized with a big variety of ligands (figure I.6) and even more crystal structures appeared during the years.^{42, 46, 52-54} Not only tetradentate ligands have been used, but also pentadentate ones⁵⁵⁻⁶⁰ that usually favour the stabilization of this intermediate species as is the case of the **N4Py** system, allowing also its crystallization⁶¹ (figure I.6, bottom left), or **MePy₂tacn** system⁵⁶ (figure I.6), which is the pentadentate version of the **Pytacn**, changing a methyl for an extra pyridine. A very nice perspective about iron(IV)-oxo complexes have been recently reviewed by Lawrence Que Jr.⁶² Synthetic iron(IV)-oxo intermediates are generated employing oxygen atom transfer agents from the Fe(II) precursor, typically PhIO, NBu₄(IO₄), mCPBA or peracetic acid as schematized in figure I.6, top.

One of the most intriguing aspects relies on the spin state and reactivity of the high-valent Fe(IV)=O. In nature, enzymes possess a high-spin $S = 2$ iron(IV)-oxo metal center¹² which is able to oxidize high BDE substrates with high reaction rates.^{8, 63} These species have a highly-reactive nature, performing reactions as OAT towards sulfides and phosphines or the more challenging HAT from strong C-H bonds as cyclohexane among others (Scheme I.3).⁶³⁻⁶⁴ In contrast, most synthetic high-



Scheme I.3. Oxidation reactions mediated by high-valent non-heme iron(IV)-oxo complexes

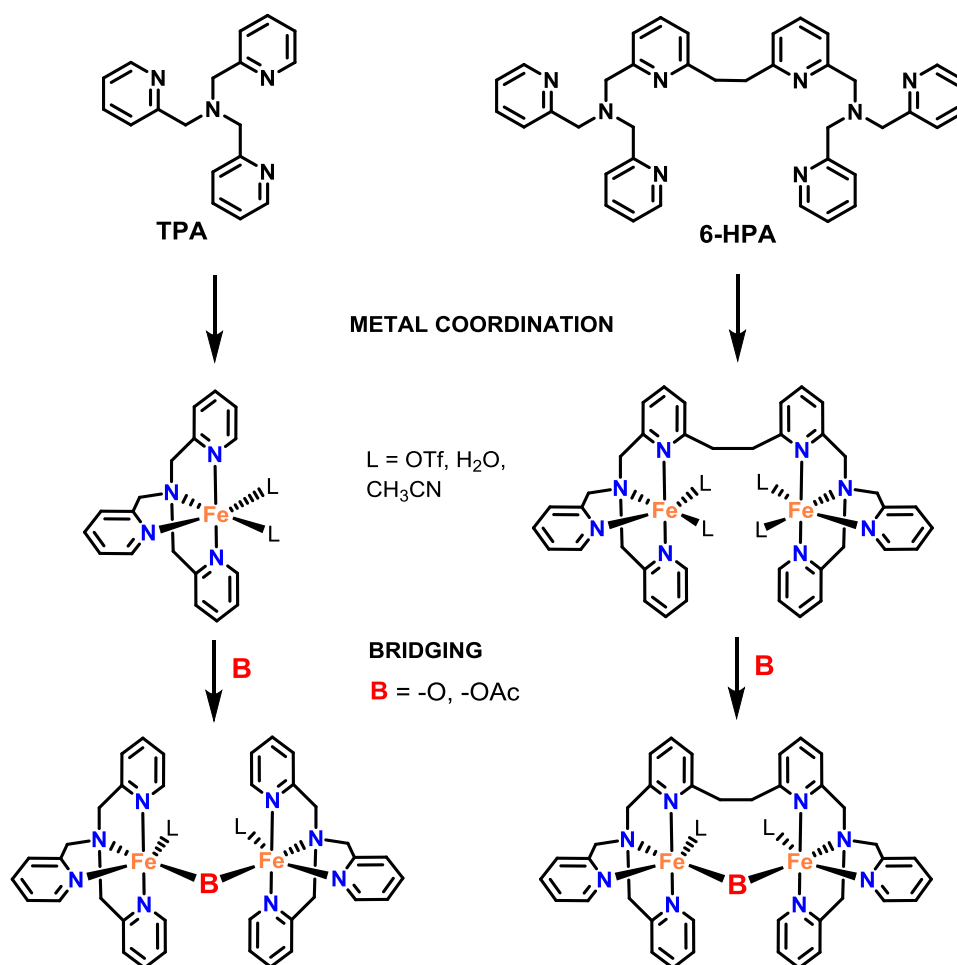
valent Fe(IV)=O complexes present a low spin $S = 1$ configuration and usually are sluggish oxidants,⁶⁵ presenting low reaction rates compared with natural systems or even no reaction with strong C-H bonds. Few examples of synthetic $S = 2$ Fe(IV)=O complexes have been reported showing a similar behavior as enzymes. This is the case of the **TQA** system, reported recently by Que and coworkers.⁶⁶ The $[\text{Fe}^{\text{IV}}(\text{O})(\text{TQA})(\text{NCCH}_3)]^{2+}$ complex (figure I.6) shows the fastest rate for the oxidation of cyclohexane for a Fe(IV)=O, only overcome by the spectroscopically trapped Fe(V)=O

General introduction

$[\text{Fe}^{\text{V}}(\text{O})(\text{OAc})(\text{PyNMe}_3)]^{2+}$.⁶⁷ The **TQA** Fe(IV)=O intermediate also exhibits the closest spectroscopic parameters and reactivity rates comparing with the natural enzyme TauD-J.

Mononuclear iron(IV)-oxo intermediates have been extensively studied, but there is a big lack of models for binuclear iron enzymes. Only few reports for synthetic high-valent diiron(IV)-oxo intermediates that will be discussed in chapter III have been reported.

I.3.2. Binuclear non-heme iron model complexes.



Scheme I.4. Two approaches for the preparation of dimeric iron complexes.

Efforts for modelling iron dependent O₂ activating enzymes have been principally devoted towards monoiron examples and models for diiron oxygenases are scarce. As mentioned in section I.3, synthetic models generally employ neutral rich N-donor ligands, usually lacking the carboxylate-rich environment in the first coordination sphere of diiron enzymes, thus not reproducing exactly the structure environment,⁶⁸ but providing key properties for reproducing their chemistry, intermediate

species and/or their spectroscopic features. Scheme I.4 summarizes two strategies mainly used to model diiron enzymes. One is the use of a mononucleating ligand used to generate monometallic complexes that can dimerize to form a diiron complex through an oxo, hydroxo or carboxylate bridge, as is the case of the monometallic **TPA** system reported by Que and coworkers (scheme I.4, left).⁶⁹ The second approach relies in the use of a dinucleating ligand with two chelating sites for two metal ions, forcing the both iron centers to generate a dimeric unit, as the **6-HPA** system developed by Kodera and coworkers (scheme I.4, right). The advantage of using this last strategy is that no external ligands are needed to put together both iron centers and just upon coordination of the metal directly to the ligand, the bimetallic structure can be obtained. Moreover, diiron(II) complexes bearing carboxylates, oxo or hydroxo bridging ligands are usually pretty susceptible of oxidation, meanwhile the absence of bridging moieties in dinucleating ligands makes diiron(II) complexes less susceptible.

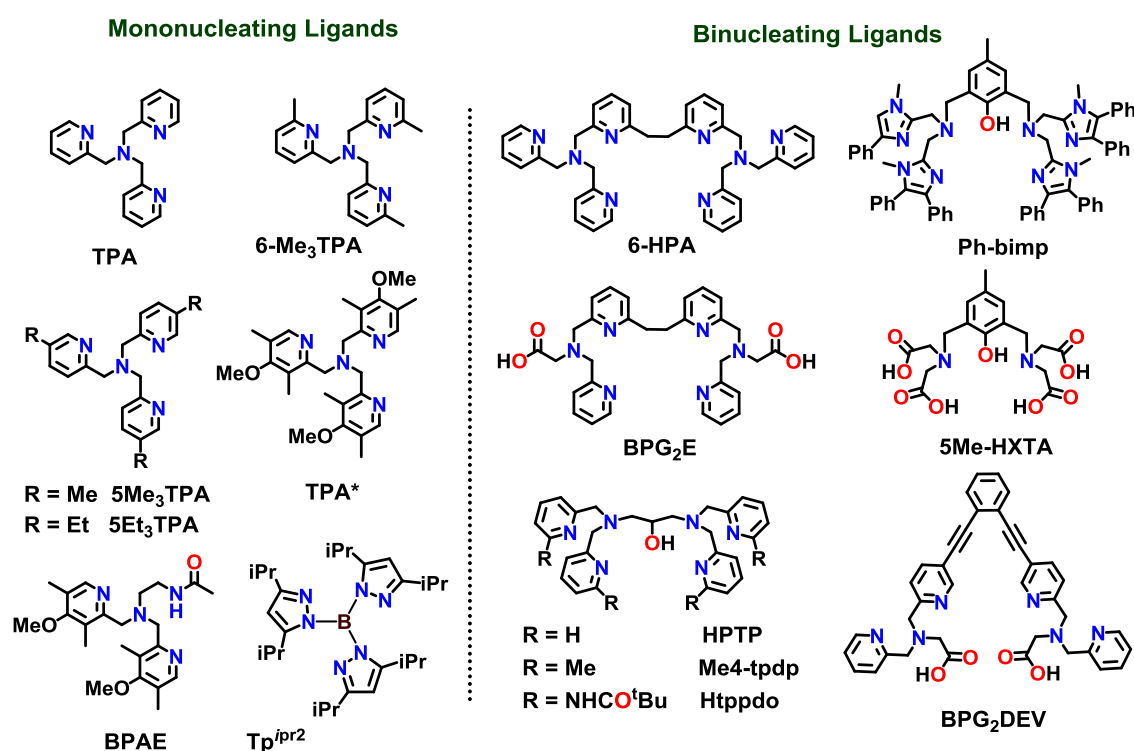
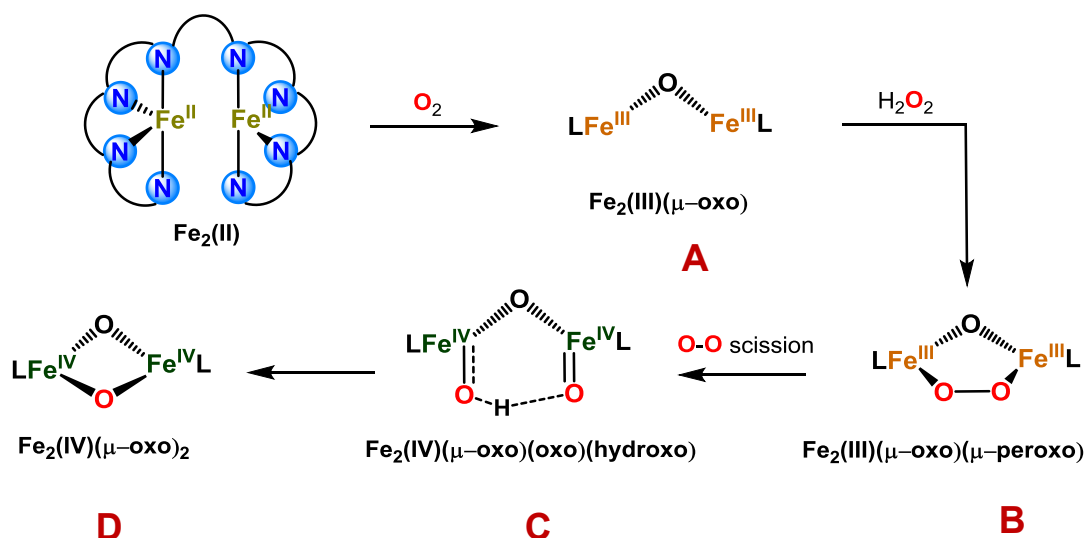


Figure I.7. Structures of Ligands used to mimic sMMO.

The final goal of these models is to mimic the reactivity and structure of intermediate **Q** from sMMO, capable of oxidizing the highly energetic C-H bond of 105 kcal/mol of methane. Not only this, but is also selective towards methanol as product, avoiding overoxidations and working under mild conditions. As described in section I.2.2.3, high-valent diiron(IV) intermediate **Q** in MMO is formed from a diiron(III)-peroxo precursor **P** after O-O bond scission, so it is also important to mimic **P**. The

General introduction



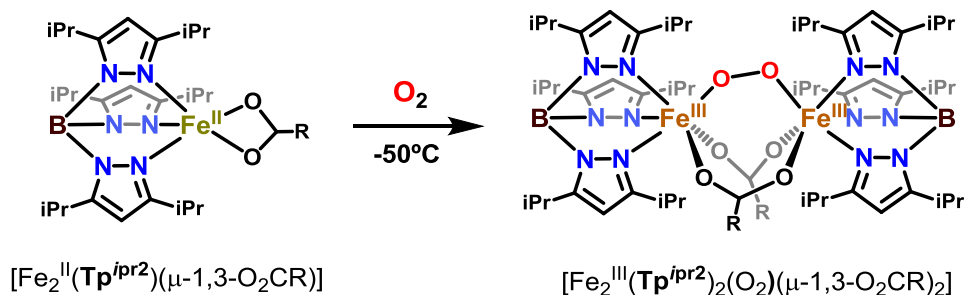
Scheme I.5. Generation of different synthetic intermediates relevant to sMMO.

ideal goal for model complexes is depicted in scheme I.5: starting from a diiron(II) precursor, to promote a first oxidation to an iron(III)-oxo, that upon treatment with a peroxide reagent could be converted to an iron(III)-peroxo (resembling **P**), that upon O-O bond scission could evolve to a high-valent diiron(IV)-oxo intermediate, resembling **Q**.

A wide variety of ligands have been synthesized to obtain binuclear iron complexes that could rise to relevant intermediates to **P** and above all to **Q** and some of them are summarized in figure I.7. In the next section synthetic peroxodiferric intermediates and high-valent diiron(IV)-oxo intermediates will be discussed.

I.3.2.1. Non-heme Peroxodiiron model complexes.

Peroxodiiron model complexes are important in order to gain more insight about the nature of **Q**, its formation and structure. They are also competent oxidants to react with electron-rich substrates, but not the strong C-H bonds of methane, for which only **Q** is a competent oxidant. Two single strategies can be applied to obtain them: by bubbling O_2 into a solution of a diferrous complex (scheme I.5, first step, scheme I.6) or reacting a diiron(III) precursor with H_2O_2 (scheme I.5, second step). Around 30 synthetic peroxo complexes have been characterized.⁷⁰⁻⁷⁹ XRD or XAS analysis has been useful to gain structural insight and Mössbauer, resonance Raman and UV-Vis spectroscopy for further characterization. The most distinctive of the peroxo complexes is the one reported with $\text{Tp}^{\text{ipr}2}$ system (scheme I.6), $[(\text{Tp}^{\text{ipr}2})_2\text{Fe}^{\text{III}}_2(\text{O}_2)(\mu\text{-}1,3\text{-O}_2\text{CR})_2]$, first characterized by Kitajama⁷⁷ and subsequently crystallized by Kim and Lippard.⁷² Mössbauer parameters, resonance Raman and UV-Vis features of this complex are the closest ones resembling intermediate **P** of sMMO. This complex



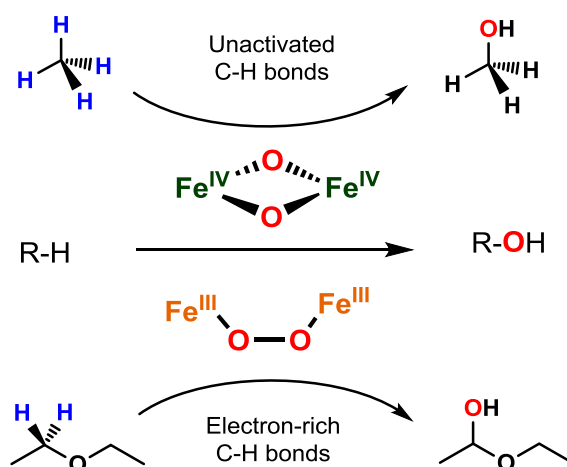
Scheme I.6. Peroxodiferric intermediate formed upon O_2 activation of the iron(II) precursor.

presents a *cis*- μ -1,2-peroxo binding mode, the same one found for \mathbf{X}^{80} and postulated for \mathbf{P} by spectroscopic and kinetic measurements.

For comparison with other diferric peroxo complexes it can be observed that the metal center is very sensitive to changes on its structure. The use of similar mononucleating ligands, **6-Me₃TPA**,⁸¹ **Ph-bimp**,⁷⁴ **BPG₂DEV**,⁷⁹ **6-HPA**,⁷⁸ and **BPG₂E**,⁸² also achieved peroxo intermediates comparable to those of \mathbf{P} . These peroxo complexes are in some cases able to react directly with electron-rich substrates (scheme I.7, bottom), as a paragon of \mathbf{P} ,⁸³ no needing the high-valent diiron(IV)-oxo powerful oxidant.

I.3.2.2. Binuclear High-valent iron(IV)-oxo intermediates

For the most relevant diiron enzyme sMMO the peroxo intermediates undergoes O-O bond cleavage to form binuclear high-valent $\text{Fe}_2(\text{IV})$ -bis(oxo) \mathbf{Q} . This intermediate is able to oxidize aerobically methane (scheme I.7, top) under mild conditions and ambient pressure.⁸⁴ This is a very

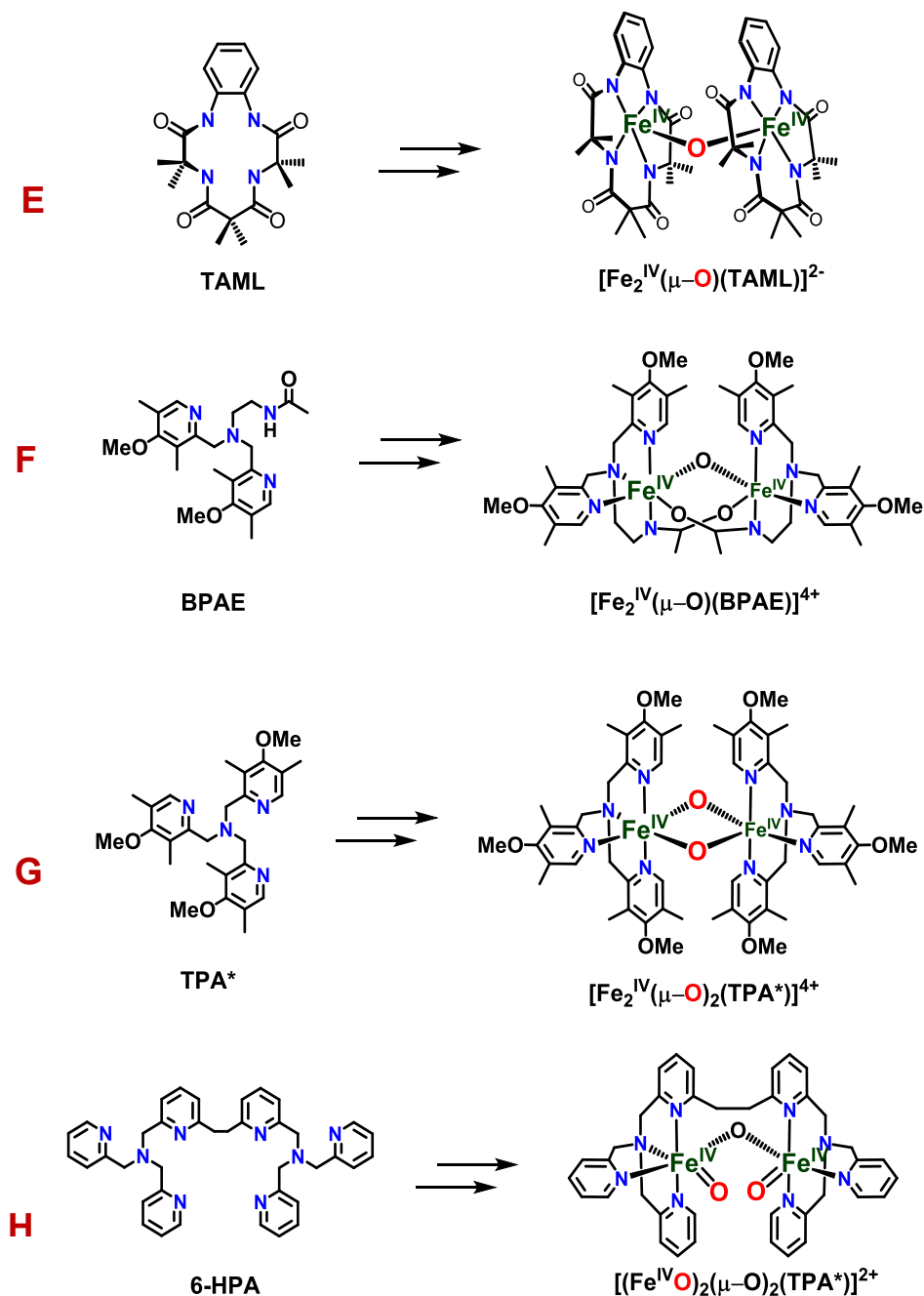


Scheme I.7. Different complex electrophilicity in C-H bond oxidation by peroxodiferric or high-valent diiron(IV)-oxo intermediates.

General introduction

remarkable reaction from the industrial point of view, which development could unlock many synthetic transformations and allow carrying out greener processes.

Despite the large number of peroxodiferric complexes synthesized and characterized, only four systems are capable of reproducing to some extent the high-valent diiron(IV)-oxo structure of

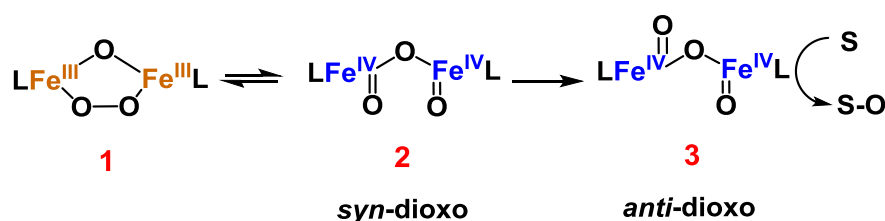


Scheme I.8. Synthetic high-valent diiron(IV)-oxo intermediates with closed or open cores obtained from the one electron reduced diiron(III) precursors. Red oxygens represent incorporation of oxygen atoms from the oxidant to the intermediate.

intermediate **Q** (scheme I.8): The **TAML** system from Collins et al., able to generate a $[\text{Fe}_2^{\text{IV}}(\mu\text{-O})(\text{TAML})]^{2-}$ intermediate (E, Scheme I.8),⁸⁵ being the only crystallographically characterized complex with a $(\mu\text{-O})$ diiron(IV) structure. However, is not as reactive as intermediate **Q** from sMMO and is only able to perform HAT from alcohol weak C-H bonds to form aldehydes and OAT to phosphines. Its low reactivity is solved by the **BPAE** system (F, Scheme I.8) from Que and coworkers, that could generate a high-valent diiron complex $[\text{Fe}_2^{\text{IV}}(\mu\text{-O})(\text{BPAE})_2]^{4+}$ (F, Scheme I.8).⁸⁶ One peculiarity of this system is the employment of a pentadentate ligand, intentionally used to stabilize intermediate species, but sacrificing their oxidizing ability. However in this case, the high-valent diiron(IV) intermediate is able to attack at 10 °C strong C-H bonds from cyclohexane or acetonitrile, similarly to the monomeric $[\text{Fe}^{\text{IV}}(\text{N4Py})(\text{NCCH}_3)]^{4+}$ system, or strong O-H bonds as methanol and *t*-butanol,⁸⁶ demonstrating that this high-valent species are species strong enough to oxidize inactivated C-H bonds.

From a mechanistic point of view, one of the most remarkable systems is the **6-HPA** (H, Scheme I.8) reported by Kodera et al.⁷⁸ The studies start with the μ -oxo-diiron(III) precursor, that upon the addition of H_2O_2 (1.2 eq) and Et_3N (2 eq), converts to a novel species with characteristic chromophores in the UV-Vis spectra, assigned to a μ -oxo- μ -peroxodiiron(III) intermediate (**1**, Scheme I.9)⁸⁷ by similarity to those observed for **6-Me₃TPA** complexes.⁸⁸ The **6-HPA** system was able to epoxidize *trans*- β -methylstyrene. a remarkable observation because usually iron-peroxo intermediates are not electrophilic enough to attack these bonds.

This apparent inconsistency was explained by analogy of **P** to **Q** conversion, where the peroxodiiron intermediate undergoes O-O bond cleavage to afford intermediate **Q**, interconverting to a higher electrophilic μ -oxo-dioxodiiron(IV) active species, able to attack these bonds. Kodera has accumulated evidence for the existence of an equilibrium between the peroxodiiron(III) **1** and dioxoiron(IV) **2** by reversible O-O bond cleavage (Scheme I.9). Moreover, this intermediate could be isolated as solid, and its Mössbauer analysis demonstrates this reversibility as the temperature

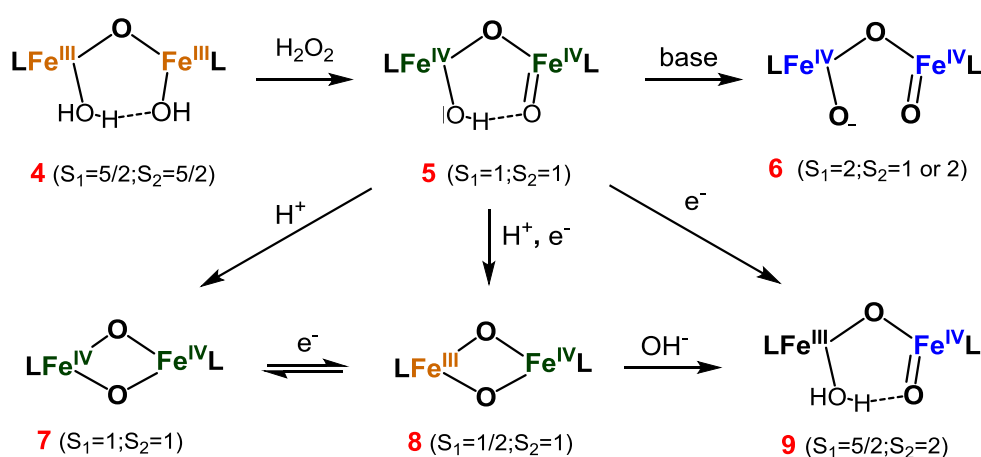


Scheme I.9. Reversible O_2 bond scission to form a diiron (IV)-oxo and its syn-to-anti transformation. Blue color indicates high-spin $S = 2$ iron(IV)-oxo.

General introduction

changes between 23 and 295K, where **1** shows parameters typical for μ -oxo-(μ -1,2-peroxo)diiron(III) and **2** to a high-spin $S = 2$ iron(IV)-oxo species resembling those of intermediate **Q** of sMMO. The reactivity of this intermediate was also explored in C-H oxidation of hydrocarbon substrates as cyclohexane, 1,2-dimethylcyclohexane, adamantane, toluene, ethylbenzene and cumene.⁸⁹ Remarkably, this compound is able to work under catalytic conditions and the authors propose a *syn*-to-*anti* isomerization of the diiron(IV)-oxo previous to the substrate oxidation based on kinetic measurements, $^{18}\text{O}_2$ labelling studies, KIE measurements and DFT studies, where the *anti*-form seems to react faster than the *syn* one due to lower steric hindrance.

Another important system has been the **TPA** (tris(2-pyridylmethyl)amine) from L. Que and coworkers. With a family of ligands based in the electron-rich version of the **TPA**, **TPA*** (tris(4-



Scheme I.10. Library of diiron(IV)-oxo complexes obtained from a diiron(III) common precursor. Green indicates low spin $S = 1$ and blue high spin $S = 2$ Fe(IV) center.

methoxy-3,5-dimethylpyridyl-2-methyl)amine) (**G**, Scheme I.8), the authors have synthesized and characterized a library of diiron(IV) intermediate species with open and closed cores related to those of sMMO,^{69, 90} with a special interest on **Q**.³⁵ One of the first binuclear intermediate species targeted was **7** (scheme I.10), a $\text{Fe}_2(\text{IV})(\mu\text{-oxo})_2$ diamond core, proposed as a synthetic model for the intermediate **Q** of the sMMO. In the natural enzyme both iron centers are found in a $S = 2$ spin state, but the $\text{Fe}_2(\text{IV})(\mu\text{-oxo})_2$ diamond core **7** possesses low spin $S = 1$ iron centers, which is

in disagreement with intermediate **Q** of sMMO. This encourage the authors to generate new intermediates with the same Fe(TPA*) platform to gain more insight about sMMO. Not only this, also other relevant intermediates were obtained with the same ligand platform, allowing to study the relative reactivity and spin state of open and closed core forms (scheme I.10).³⁹ Following the scheme I.10, intermediate **7** can be converted to **9**, a mixed-valent species with an Fe(III)Fe(IV) open core structure, where the Fe(IV)=O moiety changed its spin state from a low-spin $S = 1$ to a high-spin $S = 2$. The axial ligand of the iron(III) atom in **9** can be displaced by others, such as F or OMe, forming **9F** and **9OMe**, respectively. Similarly, **5** can be obtained from **4**, presenting a Fe₂(IV)(O)(OH) open core, where both iron atoms display a $S = 1$ spin state. This intermediate **5** can be converted in the diamond core **7** closed form by protonation, or in the opened form **6** by deprotonation with a base, where both iron centers display a $S = 2$ spin state (in one of the isomeric forms).⁹¹ Intermediate **6** the only complex of this family with a high-spin dioxodiiron(IV) that presents parameters related to sMMO-**Q**, similarly to intermediate **2** from Kodera. This big variety of high-valent diiron complexes stabilized by the same ligand **TPA*** gives the opportunity to study the impact of the structure in the reactivity, in particular toward C-H bond cleavage. L. Que and coworkers compared the oxidation rates for 9,10-dihydroanthracene (DHA) at -80 °C and the results are summarized in Figure I.8. All diiron complexes were compared with the most reactive mononuclear non-heme $S = 2$ Fe^{IV}=O

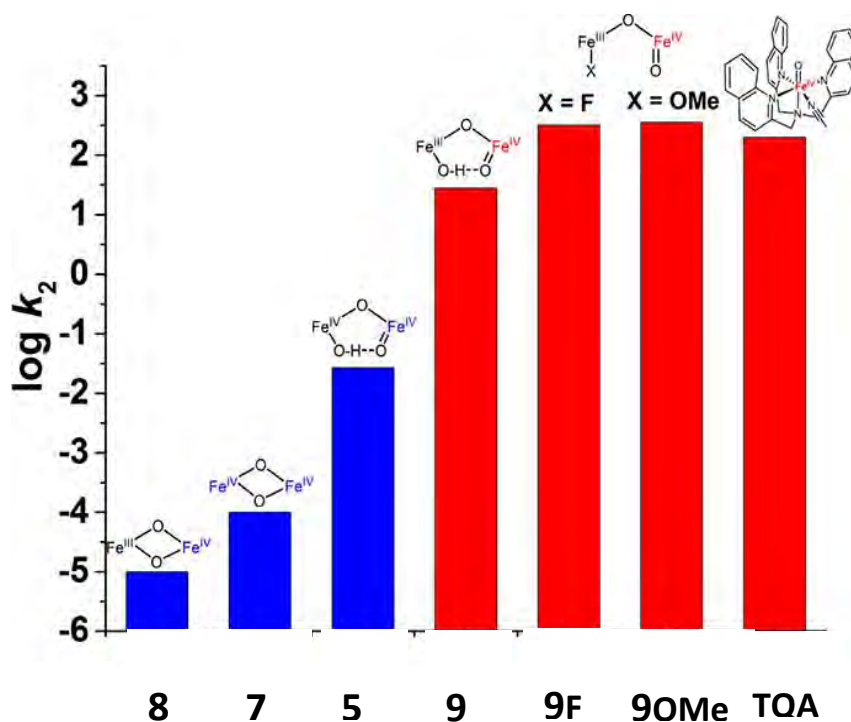


Figure I.8. DHA oxidation rates by high-valent diiron complexes supported by TPA* ligand at -80 °C. Blue bars indicate $S = 1$ Fe^{IV} center, red bars indicate $S = 2$ Fe^{IV} center. 9F and 9OMe are the same as 9 where an OH ligand is replaced for F or OMe respectively.

General introduction

complex. Generally, closed-core structures react with a much lower rate than open-core ones (**7** and **5** respectively). Also spin states seems to play a role, where low spin $S = 1$ complexes react with a much lower rate than those with $S = 2$, with a difference of 7-8 orders of magnitude between the less reactive complex (**8**) and the most reactive one (**9F** or **9OMe**). From these observations relevant information can be extracted regarding the factors affecting the cleavage rate of C-H bonds. Two main features control the reactivity of diiron complexes: First, a terminal Fe=O unit is around 100 times more reactive than a bridging oxo ligand when cleaving a C-H bond. The second is that an $S = 2$ Fe^{IV}=O is between 3-4 orders of magnitude more reactive than a $S = 1$ Fe^{IV}=O, based on this data.

I.4. Rising complexity in bioinspired model complexes.

The excellent reactivity displayed by enzymes is not just a fact of a reactive enough catalytic site. The active site of enzymes is composed by two main parts: first, the catalytic site, which is composed by the metal center that promotes the reaction with the substrate (described in previous sections) and second, the binding site, a pocket located close to the catalytic site that has a strong affinity for the substrate, thus, producing its preorganization in a confined space (figure I.9).⁹²⁻⁹³

The substrate locates in the binding site of the enzyme, experiencing a series of “confinement effects” imposed by the size and shape of the pocket that translates in limiting the substrate movement, and thus, accesibility to only certain conformations. This is translated to the reactivity, restricting the number of possible reaction pathways, but also lowering the activation energy of the

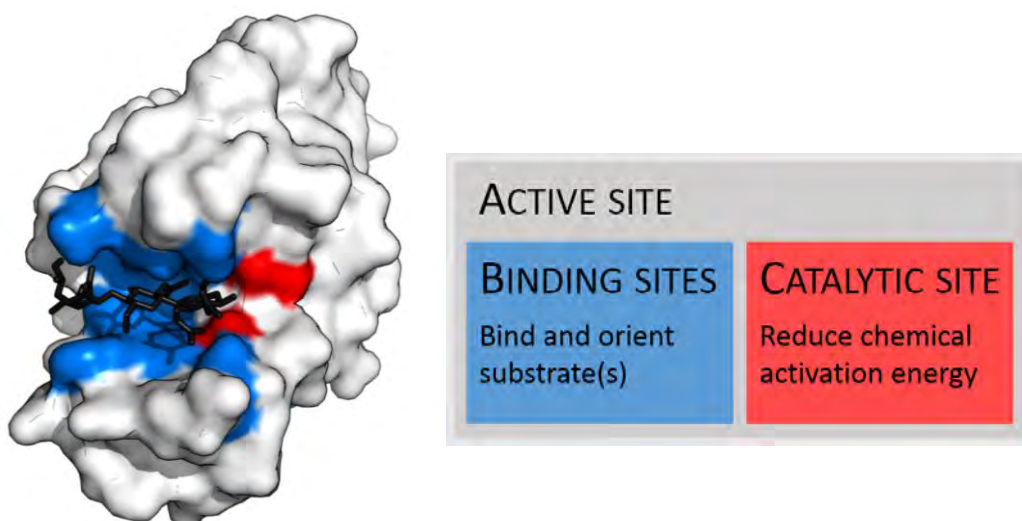


Figure I.9. 3D model representing the enzyme active site. Blue color represents the binding sites, red color the catalytic site and black the substrate. Image adapted from: Thomas Shafee, Enzyme structure, CC BY 4.0

process, enhancing the reaction rate.⁹⁴ The proximity of the reactive groups to the reactive center is also driven by the binding site, orientating the molecule, fact that determines the selectivity of the process. A wide variety of weak interactions cooperate to orient and recognize the substrate, exposing only specific positions to the oxidizing species and thus, overriding the intrinsic reactivity of the molecule bonds and preventing undesired reactivities,⁹⁵ producing highly chemoselective, stereoselective and enantioselective reactions, non-approachable from a conventional synthetic point of view. A key property of these interactions is their weak nature that ensures the reversibility of the process, factor that allows the turnover for a catalytic process. However, when more specific are these interactions, the substrate scope becomes narrower, which is a drawback from the synthetic point of view.

I.4.1. Supramolecular tool as approach for enzyme mimics.

In molecular synthetic catalysts, selectivity follows the intrinsic nature of the bonds which is in turn governed by electronic,⁹⁶⁻⁹⁷ steric⁹⁸ or stereoelectronic⁹⁹ factors. Another approach consists in the installation of directing groups in the substrate able to guide the oxidation of a nearby site of the molecule.¹⁰⁰⁻¹⁰¹ However, bonds that do not meet this requirement cannot be selectively attacked. Inspired by nature,¹⁰² the main idea pursued has been the use of lock-and-key principle of enzymes, where a substrate fits well in a host containing a catalytic function (figure I.10), thus, enhancing its reaction rate. Supramolecular host-guest chemistry can help to reproduce the binding site of an enzyme by recognizing specifically a certain molecule and/or by establishing delicate interactions that provoke substrate preorganization¹⁰³ in which the geometry of the substrate-receptor

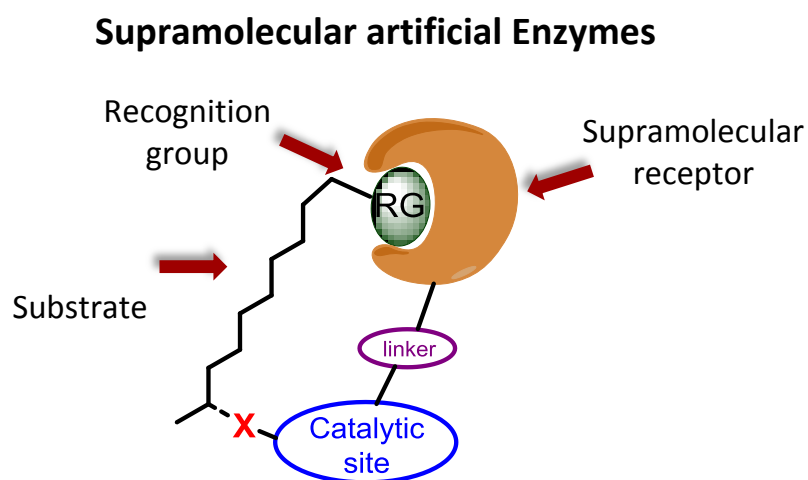


Figure I.10. Supramolecular approach to build artificial enzymes.

General introduction

determines which bond are exposed to the reactive species. One of the approaches to mimic the recognition properties of an enzyme is to use reaction vessels in order to create a cavity that imitates the isolated environment inside the protein pocket. Frequently, the positioning of the substrate is not only determined by the size and shape of the cavity, but also by interactions between functional groups of the substrate and those of the recognition site, such as hydrogen bonding, ionic interactions or reversible covalent bonding.¹⁰⁴ The fact of confining a molecule allows not only to speed up the reaction promoting the substrate to be in close proximity to the active site, but also could serve as a phase transfer, allowing the reaction to take place.¹⁰⁵

I.4.1.1. Artificial enzymes. From stoichiometric to catalysis.

Since 1980, supramolecular chemistry has created through the years a collection of cages and containers with host-guest properties in order to create a confined space with the aim of mimicking the pocket of enzymes. The goal is not only to achieve reactivity inside a molecular host, but also reach a catalytic behavior. The most targeted molecules as substrates are unactivated alkanes, due to their inert character that nature is able to solve impressively. In the so-called host-guest catalysis, non-covalent interactions help in the construction of the hosts and more importantly, direct and position the substrate to restrict its possible conformations. The strength of these interactions

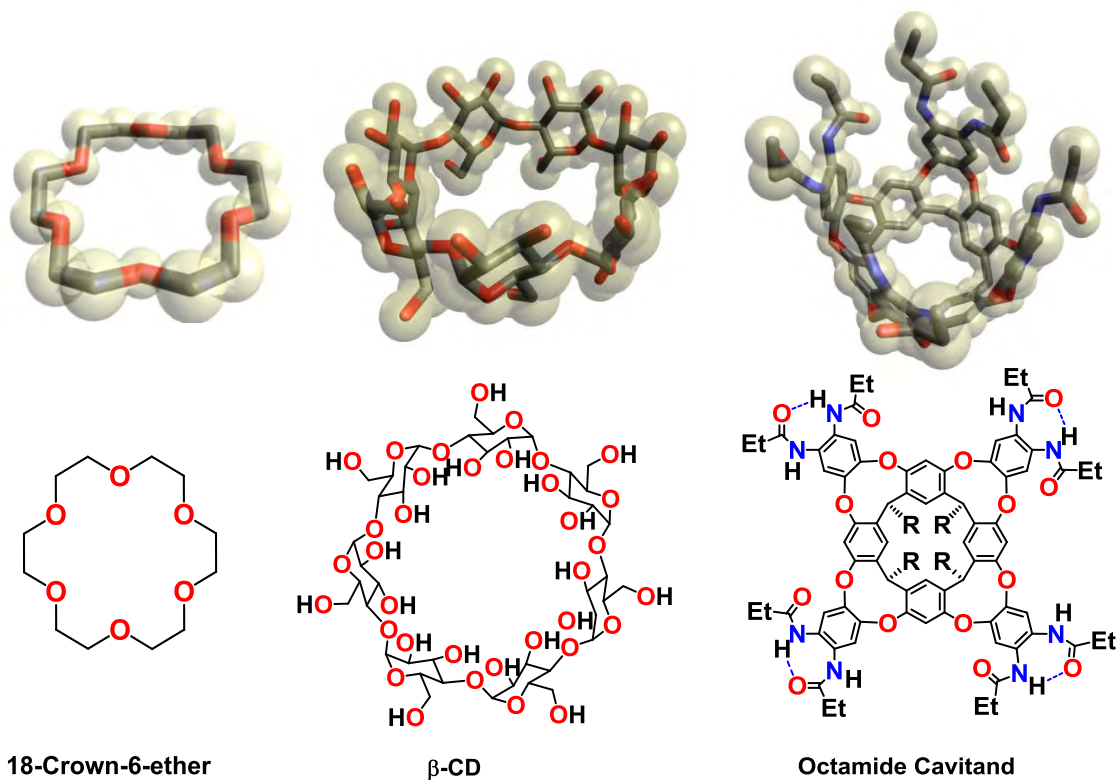


Figure I.11. Structures of supramolecular receptors used to mimic enzyme reactivity.

together with the reversibility of the host-guest adduct dictates the turnover. If the interactions are reversible, (host-guest adduct formation-dissociation rates are faster than the reaction rate) and there is no product inhibition (higher affinity of the host with the products rather than the substrate), then catalytic activity could be possible. But even fulfilling these requisites, turnover is not guaranteed. The first examples employed a metal-free supramolecular receptor and reactive site. However, there is a growing interest in the knowledge of how metalloenzymes work, and there is a lack of hybrid organic-inorganic supramolecular systems to put together both bioinspired and confined space chemistry that is rising in the last years. Some of the most remarkable supramolecular receptors used are cyclodextrins, cavitands, crown ethers and their derivatives (figure I.11). Initially, these structures were metal-free, that later on have been incorporating metals, with the aim to develop metal-catalyzed reactions. Some are discussed in the following lines.

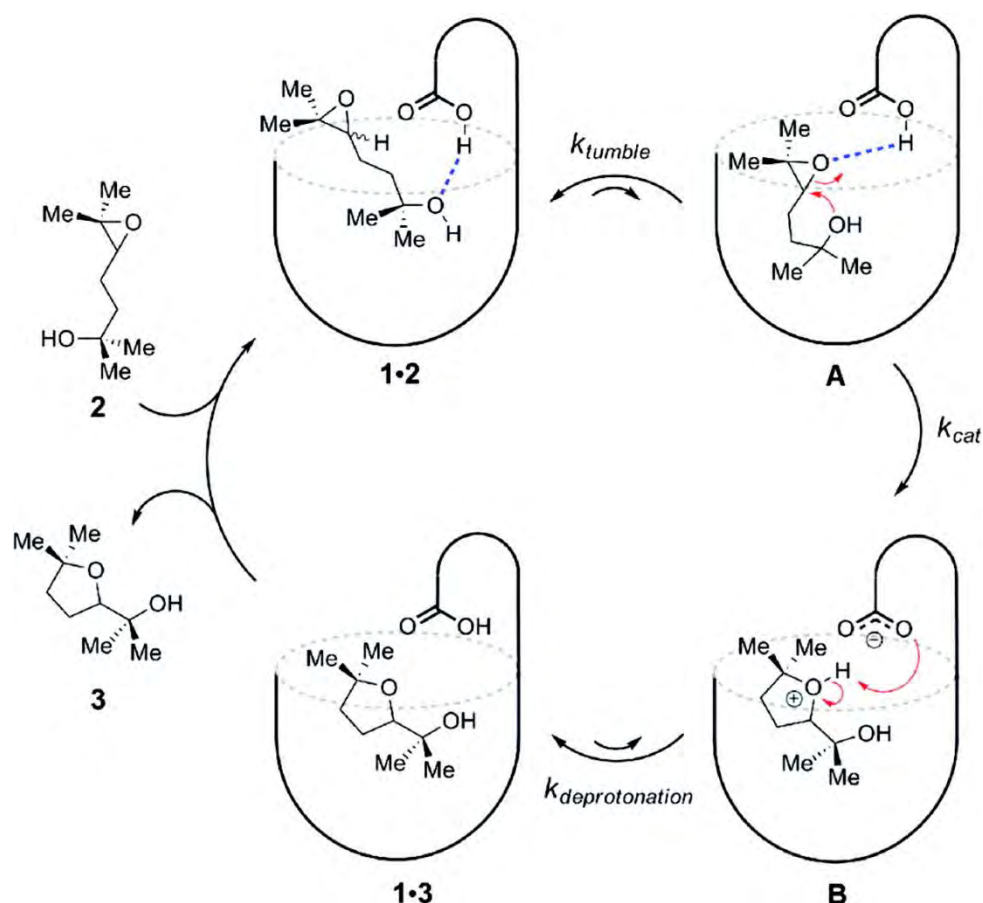
Crown ethers (figure I.11, left) are one of the simplest receptors used. In this regard, there are examples of these molecules used as catalysis and chiral recognition in transacylations of amino esters reported by Cram,¹⁰⁶ or rate enhancement of thiolysis of aminoesters by Jean-Marie Lehn¹⁰⁷ and more recently, the artificial aspartic proteinase system reported by Gao.¹⁰⁸ Cyclodextrins (figure I.11, center) have been one of the most investigated hosts in this regard because they are easily accessible, water soluble and possess a hydrophobic cavity that has strong affinity for apolar substrates, serving as “nanoreactors”,¹⁰⁹ targeting challenging molecules as unactivated C-H bonds. A very recent example by Wong employed stoichiometric amounts of cyclodextrins with dioxiranes to oxidize C-H bonds in water,¹¹⁰ where the inclusion complex formed avoids indiscriminate substrate oxidation, presenting a moderate selectivity. However, if catalytic amounts of cyclodextrins were used, the selectivity is lost. Hu *et al.* proved that a chiral organocatalytic unit covalently linked to the cyclodextrin was highly efficient for the aldol reaction of symmetric ketones with aromatic aldehydes.¹¹¹ Remarkably, the system was catalytic and they could observe induction of enantioselectivity, attributed to the restriction of conformations inside the cavity, together with secondary interactions.

Deep Cavitands (figure I.11, right) are organic macrocycles derived from calixarenes, organic macrocycle molecules that are able to include smaller molecules inside, developed by Cram in 1983.¹¹² Cavitands are the expanded wall version of calixarenes, being the most evolved and complex of these receptors. Cavitands were developed by Julius Rebek Jr., considered one of the pioneers in the field of enzyme mimics. This supramolecular receptors have been developed for very early examples of host-guest reactivity,¹¹³ self-replicators and allosteric catalysis.¹¹⁴ These molecules display two simultaneous properties that make them a especial good model to mimic enzymes: one

General introduction

is the ability of adopting a vase conformation, wrapping around the substrate, isolating it in a different environment than the bulk thanks to the hydrogen bonding established by functional groups installed in the upper rim. Second, the hydrogen bond ability of the upper rim allows also assists the setting of interactions between the substrate and the active site to promote the recognition, resembling the function of the residues in the active site. This upper rim can be functionalized possessing an inwardly directed group for reactivity, for instance the reported cavitand functionalized with an aldehyde function.¹¹⁵ When this cavitand was mixed stoichiometrically with a primary amine, the aldehyde function attached to the upper rim reacted with the amine while the cavitand acted as a reaction vessel. This lead not only to the formation of products, but also the observation of the elusive hemiaminal intermediate,¹¹⁶ a highly-reactive intermediate that evolves to form the imine bond, thanks to the stabilization of the intermediate inside the cavitand due to secondary interactions.

A remarkable example is the catalytic system created by functionalizing the upper rim of a



Scheme I.11. Enzyme-like mechanism for the intermolecular ring opening of epoxyalcohols. From ref 118.

cavitand with an inwardly directed carboxylic acid function.¹¹⁷ Intermolecular ring-opening of epoxy alcohols (scheme I.11) was accelerated employing this cavitand as catalyst, leading to the formation

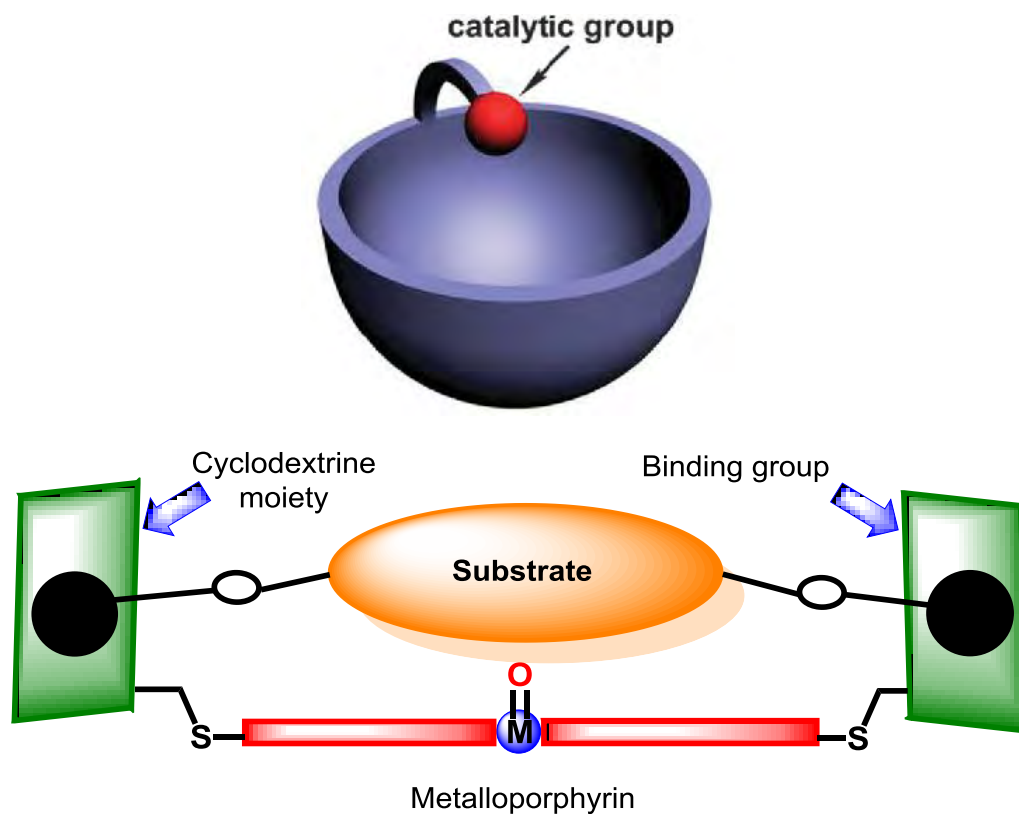


Figure I.12 Two strategies used to design supramolecular catalysts.

of THF derivatives as main product.¹¹⁸ This improved selectivity was attributed to the inclusion of the substrate inside the cavitand by the hydrophobic effect, but also hydrogen bond interactions between the substrate and the carboxylic acid function in the upper rim.

I.4.1.2. Supramolecular metal-complex catalysts

Pure organic supramolecular systems have been the first and most studied for enzyme-like reactivity, but there is a growing interest in develop systems where the reactivity is performed by a metal complex and not by a organocatalytic function. Two main challenges have to be overcome: first, the synthesis of a supramolecular structure with a specific functional group at a certain position is not trivial. Two, a chelating moiety able to bind a metal needs to be included. Third but most importantly, the ligand should form a well-defined coordination complex, robust enough to tolerate reaction conditions without degradation either of the receptor or the catalyst. An approach is depicted in figure I.12, where a traditional bioinspired complex is attached to a supramolecular receptor to accommodate the substrate in a specific geometry. Moreover, mimicking enzymes

General introduction

means performing the chemistry with non-noble metals as nature does, such as iron, manganese, etc., a step further in building an artificial enzyme. This section will focus on bioinspired systems, especially models for oxygenases with supramolecular systems using iron and manganese as metal ions in alkane-based oxidation reactions.

Two recognized pioneers in supramolecular oxidation chemistry have been John T. Groves and Ronald Breslow. They reported in the early 90's the first successful examples of enzyme-like oxidation catalysts using steroidal substrates. The idea was the same: place the substrate in a certain orientation assisted by the interactions created by the supramolecular structure to gain an enhancement in both activity and/or selectivity. The difference relies in the type of receptor that determines the interaction between host and guest, which in turn determines the properties of the final system as solubility, robustness or preferred substrate.¹¹⁹ The system of Groves and coworkers is guided by lipophilic interactions and consists in a Mn(III)-porphyrin complex decorated with pendant steroids,¹²⁰ forming an hydrophobic pocket ready to host an apolar substrate. The structure is enclosed in a phospholipid bilayer in water with the steroid alcohols prompting outside to the polar part of the bilayer. With this system, the authors were able to oxidize cholesterol as substrate reaching C-25 alcohol as the only product observed, attributed to the positioning of the substrate due to the interactions with the bilayer. The main drawback is the substrate-to-catalyst ratio of the reaction with only 0.8 TON. The analogous Fe(III) complex is totally inactive for C-H bonds, but presents a good activity in regioselective epoxidation of unsaturated fatty acids or diolefinic sterols.¹²¹ On the

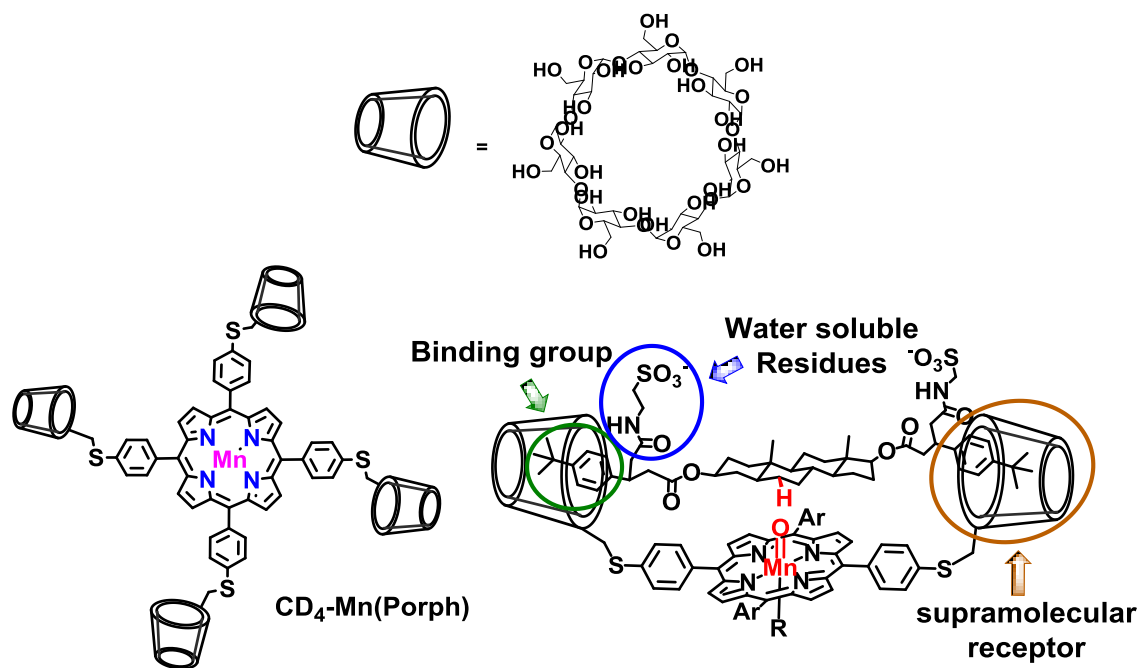
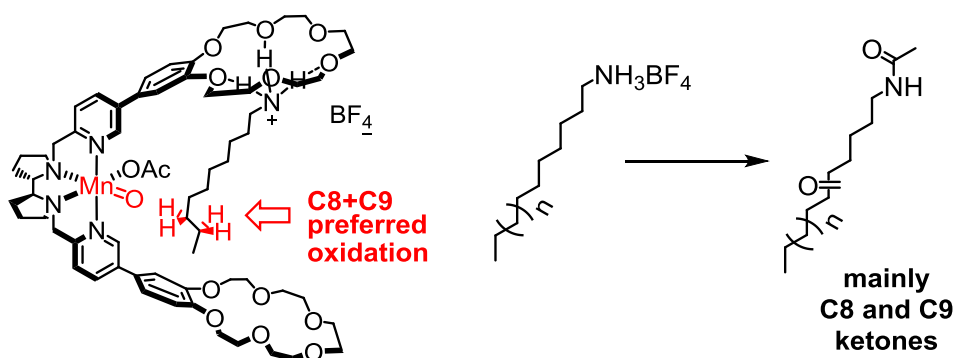


Figure I.13 Breslow's supramolecular Catalyst (left) and schematic model of catalyst-substrate binding.

other hand, Breslow and co-workers pioneered the use of cyclodextrins as supramolecular host, (based on hydrophobic interactions between the host and the guest) and attached them to a conventional bioinspired catalyst. The most relevant achievement has been the design of a Mn(III)-porphyrin complex functionalized with four cyclodextrins at the phenyl rings.¹²² The system was able to oxidize steroidal substrates functionalized with *t*-butyl-phenyl as binding groups in water as solvent with an impressive site-selectivity for position located at C-6 of the alkane skeleton (figure I.13), attributed to the tight binding of the substrate along the porphyrin to the cyclodextrins.¹²³ The regioselectivity was also controlled by pointing only the α face of the substrate to the porphyrin, using a coligand to block the other face, obtaining thus only one regioisomer as product. Once the substrate has been hydroxylated, the product is liberated from the receptor, driven by the higher affinity of the substrate, inducing control of the chemoselectivity, avoiding overoxidation of the alcohol product, thus, producing the α -C6 alcohol as mostly only product. The most remarkable achievement of this system is the catalytic behavior, with a value of 10 TON for the normal system, rising to 187 TON using a fluorinated porphyrin and 2900 TON replacing the fourth cyclodextrin by an *o*-nitro group. Turnover happens because the product has less affinity for the receptor than the substrate. The same authors made strong efforts to improve the system. The principal targets were the expansion of the substrate scope and rising up the yield without compromising the TON.¹²⁴ If the substrate's recognition motif is slightly modified, the receptor is changed to cyclophanes,¹²⁵ or employing metal to ligand coordination recognition motifs in catalyst and substrate,¹²⁶ the selectivity and efficiency of the system is compromised, seeming that the system is limited for this exclusive substrate and receptor.

A similar idea has been applied to other systems, but guided by hydrogen bonding interactions between catalyst and substrate. It's worth to mention the contribution of Crabtree and Brudvig,¹²⁷ able to perform selective oxidations using ibuprofen as model substrate, simpler substrate compared to steroidal ones. The selectivity and substrate scope are not the most impressive



Scheme I.12 Schematic representation of the Olivo, Di Stefano and Costas supramolecular catalyst and its selective catalytic C-H oxidation reaction.

General introduction

reported, but the advantage of the system relies in the non-necessity of installing binding groups on the substrate. The intrinsic nature of ibuprofen, that already possess a carboxylic acid moiety, is the responsible of host-guest interaction and consequently, the selectivity. Similar to this system there is the one reported by Bach and coworkers,¹²⁸ in which they install an hydrogen bond donor in the catalyst, able to bind spiroxindoles and 3,4-hydroquinolones. The authors observed that oxidation of these substrates produced highly stereoselection on the products, up to 99%, induced by the hydrogen bonding of the catalyst-substrate. It's worth to mention the recent report by Olivo, Costas et al.¹²⁹ also based in hydrogen bonding, due to the use of a non-porphyrinic platform as ligand and H₂O₂ as oxidant. In this case, they install 18-Crown-6-ether receptors in a non-heme bioinspired complex that are able to bind simple lineal protonated alkylamines (scheme I.12). The preorganization of the substrate in the receptor lead to enhance the selectivity, favoring the oxidation in the most accessible sites, the ones closest to the catalytic unit.

I.4.2. Cavittands as platform for enzyme-like reactions.

Cavittands have strong similarities with enzymes in two points: One is the ability of having catalytic centers inwardly directed towards the cavity. Two, the hydrophobic cavity is large, concave, gently curved and half-opened, so guests can readily enter and leave with a high level of freedom. However, hybrid organic-inorganic metallocavittands have been underdeveloped due to the difficulty to synthesize functionalized cavittands even in a laboratory-scale. Directly related is the preparation of metallocavittands where the inwardly directed functionality must serve as a well define ligand

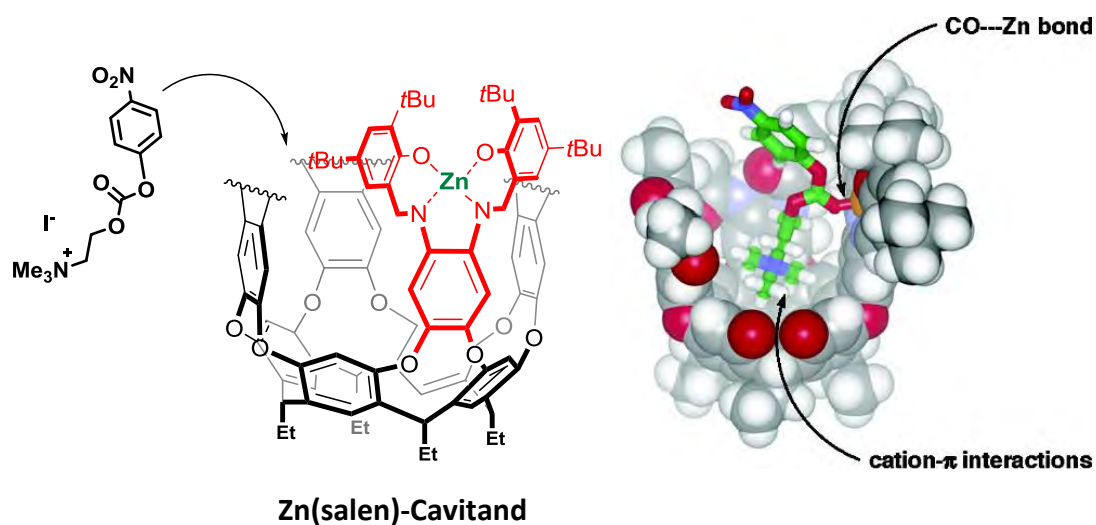


Figure I.14. Zn(Salen)-Cavittand developed by Richeter and Rebek. Ref 130.

good enough to support transition metal complexes.

A metallocavitand catalyst should perform a reaction with turnover, but importantly, the rate of the reaction inside the cavity and/or the selectivity should be enhanced respect to the one lacking the supramolecular receptor. The geometric control of the substrate due to specific interactions is the driving force to reach conformations energetically favorable inside the cavitand, which in a non-recognition situation are energetically unfavorable, being unstable. One of the earliest examples was reported by Rebek and Richeter¹³⁰ and consists in an hexaamide cavitand lacking one of the walls which is functionalized with a salen ligand. Its Zn(II) complex (figure I.14) is able to catalyze the hydrolysis of *p*-nitrophenyl choline carbonate (PNPCC), where the Zn(II) activates the carbonyl moiety. The reaction rate is significantly increased by the presence of the Zn(salen)-cavitand more than 50-fold when 1 equivalent of the cavitand is present. When the simple Zn(II) complex without cavitand is used, the reaction is accelerated but as much lower rate, meaning that the confinement and preorganization of the substrate makes the reaction more feasible.

A similar system is the functionalized cavitand recently reported by Pablo Ballester et al.,¹³¹ where they installed a terpyridine (tpy) ligand on the upper rim. They chose Ru(II) to coordinate the ligand and 2-(phenylazo)pyridine (azpy) as the ancillary ligand for epoxidation of styrene's (figure I.15), because the parent complex $trans\text{-}[Ru^{II}(tpy)(azpy)(OH_2)]^{2+}$ have been previously reported as an active catalyst for this oxidation reaction using a sacrificial oxidant.¹³² As seen in previous sections, oxidation reactions are not trivial in general terms, performed only by a relatively small group of metal complexes that meet special requirements.^{1, 133} This means that attachment of an active inorganic metal complex to a cavitand does not led automatically the reaction to proceed as the

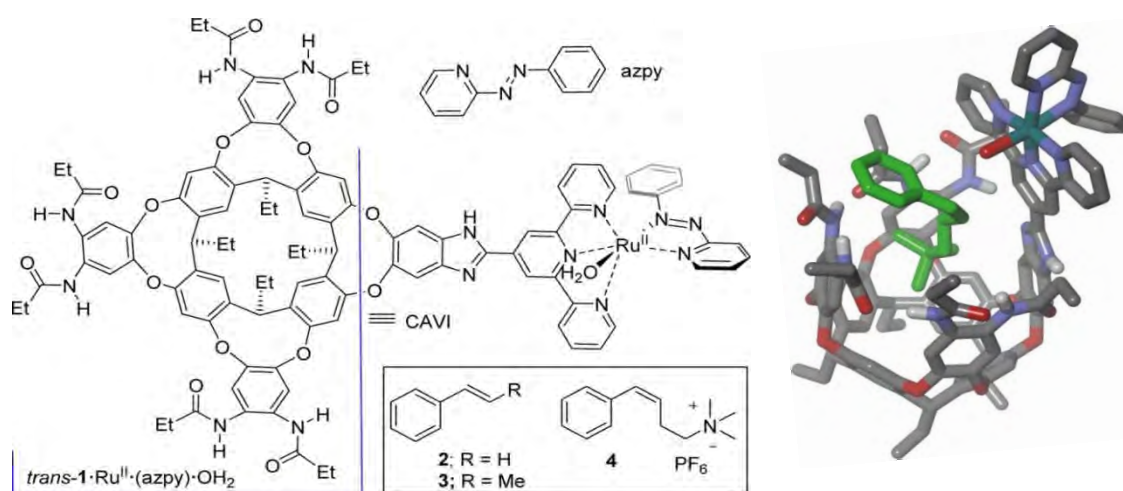


Figure I.15 Schematic structure of $trans\text{-}Ru^{II}(tpy)(azpy)(OH)_2$ metallocavitand (left) and 3D model of the host-guest adduct formed with alkylammonium styrene substrate **4** (right). Ref 131.

General introduction

simple complex does. Moreover, supramolecular receptors are organic molecules potentially susceptible to oxidation and decomposition due to harsh reaction conditions, and there is a lack of reports employing a metallocavitand for oxidation reactions, being the main achievement for this system. They modified styrene substrates by introducing an alkylammonium group as recognition motif (figure I.15), known to have strong affinity for this cavitand, with the aim of enhancing the epoxidation reaction in presence of the receptor. Unfortunately, the amount of the epoxide produced from *cis*- β -alkyl styrene olefin equipped with a terminal trimethylammonium function using the Ru-metallocavitand as catalyst was almost identical to that obtained using the neutral olefins, meaning that the supramolecular receptor does not have a positive influence in this substrate. Moreover, after 2-3 turnovers the reaction does not proceed significantly and the metallocavitand catalyst is partially destroyed.

There are almost no reports using iron in combination with cavitand-like structures for bioinspired chemistry, which represents a breakthrough in the construction of artificial enzymes. Only two examples have been reported bearing this metal: One is the calixarene functionalized with

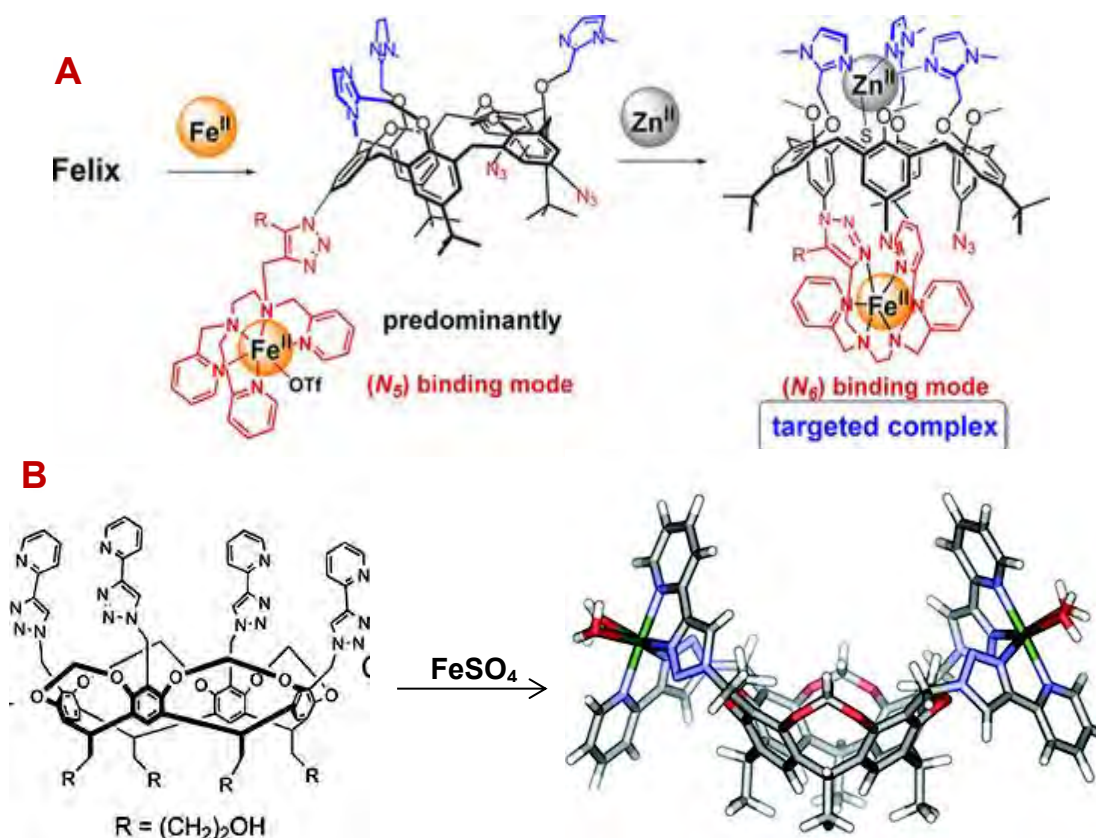


Figure I.16 Hybrid organic-inorganic iron supramolecular systems reported from Olivia Reinaud (A, ref 134) and Richard Hooley (B, ref 135).

two different coordination sites from Olivia Reinaud et al.,¹³⁴ where one site is occupied by iron(II) and the other by Zn(II) (figure 1.16, top). The authors reported the generation of Fe(IV)=O intermediate within the cavitand, albeit with low yield (15-20%). However, the intermediate is not reactive toward substrates and the cavitand structure decomposes.

One of the few examples of oxidation of unactivated C-H bonds with a cavitand bearing iron as metal is the reported by Hooley et al.¹³⁵ In this system is employed a slightly different cavitand, with a shallower cavity. The upper rim of the cavitand is functionalized with four bidentate ligands, constituting a pyridine bound covalently to a triazole, where two nitrogens (one of the former and one of the latter) chelate the metal. Coordination of iron follows a 2:1 ligand:metal stoichiometry, thus forming a bimetallic molecule bearing two iron atoms. However, this bidentate ligand does not give rise to a well-defined coordination complex due to the relatively lability of the iron-N bonds. Aminopyridine tetradentate ligands are usually employed to generate a well-defined iron coordination complex, and triazoles are not very extended for oxidation chemistry. Moreover, sulfate anions are known to strongly coordinate iron, preventing it for catalysis and rendering it inactive. However, in this report non-activated strong C-H bonds¹³⁶ such as *cis/trans*-decaline are oxidized forming alcohol and ketone as products with moderate to good yields. This in combination with the strong coordination of sulfate anion to iron could be indicative of some free radical oxidation pathway and not metal-based as is observed in enzymes.

CHAPTER II

MAIN OBJECTIVES

Non-heme iron oxygenases are a subclass of enzymes that perform challenging and selective reactions of potential relevance in organic synthesis. In this context, bioinspired model complexes are of relevant importance to mimic the catalytic site of the enzyme by reproducing aspects of the first coordination sphere of the metal center in the active site. The final goal of this approach is to develop either structural or functional models. Non-heme enzymes operate through high-valent iron(IV)-oxo species in many of the cases, being extremely reactive species responsible for the oxidation of strong and unactivated C-H bonds. Mononuclear iron model complexes have been the most explored, but binuclear iron model complexes are more scarce.

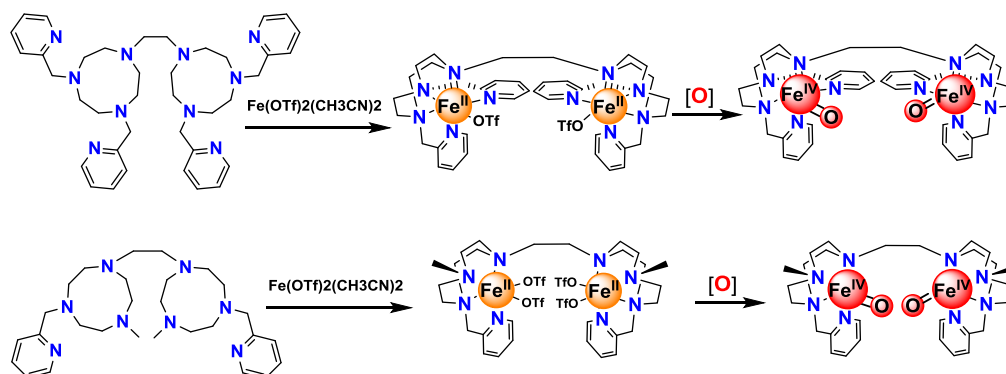
The unique reactivity of proteins, and most especially the selectivities of their reactions, cannot be explained only by considering the metal center, but also needs to consider weak interactions and structural constraints imposed by the enzyme active site. Enzymes often contain well defined binding sites, where the substrate is accommodated in close proximity to the catalytic site in a restricted conformation due to delicate and subtle interactions that direct it. So, to mimic both catalytic and binding site of an enzyme is of the same relevant importance and can lead to the preparation of more efficient and elaborated model systems.

In order to create models for binuclear iron enzymes, **chapter III** addresses the synthesis and characterization of two novel dinucleating ligands based on the triazacyclononane macrocycle and its related diiron complexes (scheme II.1). Our research group has previously reported the use of the mononucleating Pytacn ligand (define Pytacn) based on the triazacyclononane macrocycle as a model for non-heme iron oxygenases that is active for alkane and alkene oxidation and is able to support and stabilize iron(IV)-oxo species. Thus, with this two dinuclear iron complexes we target the generation of high-valent dioxodiiron(IV) species (scheme II.1) which are related to sMMO enzyme and study their reactivity towards oxygen atom transfer (OAT) and hydrogen atom abstraction (HAT) reactions, for which high-valent iron(IV)-oxo species constitute a key aspect. The ability to reform the O-O bond has been also considered.

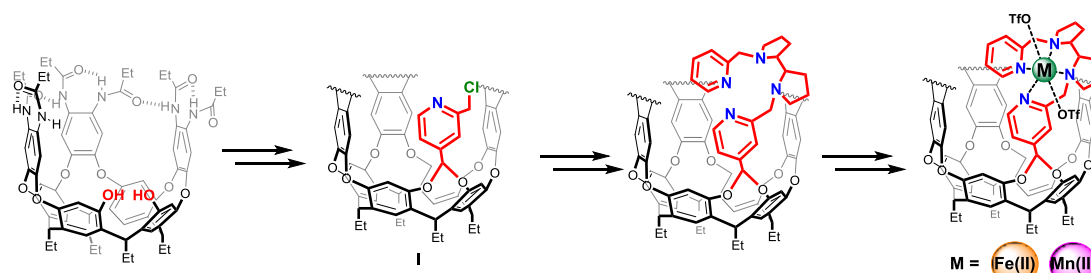
To mimic the binding site of a protein, in **chapter IV** we have taken advantage of supramolecular host-guest chemistry. Deep cavitands have been chosen as supramolecular binding platforms, and connected to standard ligands employed in biomimetic oxidation catalysis. Cavitands are derived from calixarenes, where the wall of the upper rim is extended; creating a relatively large cavity with a bowl structure that can harbor smaller molecules inside them thanks to hydrogen bond interactions, which overall resembles very much an enzyme. Our aim consists in; starting from a cavitand lacking one of the walls, functionalize it with a mononucleating ligand able to chelate first-

Main objectives

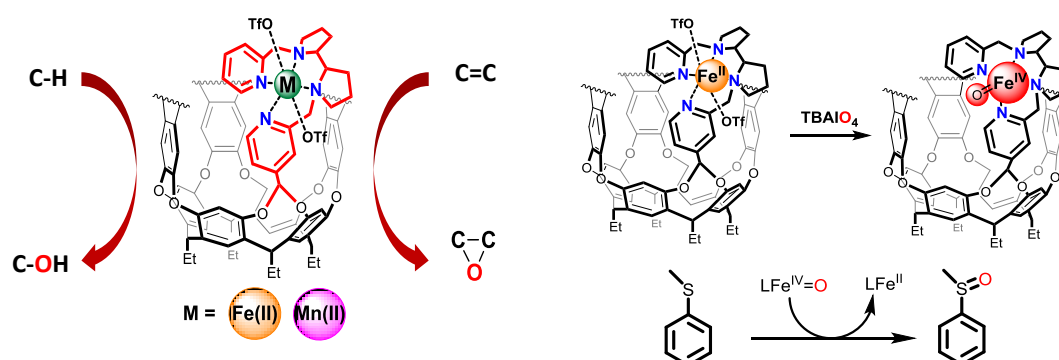
row transition metals such as iron or manganese and create well defined coordination complexes attached to the supramolecular receptor (scheme II.2). In **chapter V**, we ask ourselves if this metallocavitand can be useful as a functional model of iron oxygenases for bioinspired oxidation reactions (figure II.3, left), using it as a catalyst for selective oxidation of alkanes and alkenes. Parallel, we explore a clean generation and stabilization of intermediate species within a cavitand, as a model for the active species of the enzyme, and if this species is able to react with substrates (scheme II.3, right).



Scheme II.1. Tetradentate (bottom) and pentadentate (top) dinucleating ligands and their related iron(II) complexes as platform to generate dioxodiiron(IV) intermediate species.



Scheme II.2. Schematic representation of the preparation of hybrid inorganic/organic metallocavitands.



Scheme II.3. Reactivity of the metallocavitands as catalyst towards C-H and C=C (left). Iron(IV)=O generated in a cavitand and its reactivity towards sulfides (right).

CHAPTERS III, IV AND V

RESULTS AND
DISCUSSION

III.1. SYNTHESIS, CHARACTERIZATION AND REACTIVITY OF DIIRON COMPLEXES WITH DINUCLEATING bis-TACN-BASED LIGANDS.

III.1.1. Synthesis and characterization of two novel dinucleating ligands based on the tacn scaffold and their related iron complexes.

In the last two decades, many efforts have been devoted to develop models of non-heme iron enzymes by means of the so called “bioinspired model complexes”. In order to reproduce in a simple manner the first coordination sphere of iron in enzyme active sites, as well as its reactivity, different tetra and pentadentate aminopyridine chelating ligands have been employed (see section I.3.1. figure I.5).¹⁶

High-valent iron(IV)-oxo species have been proved to be key reactive intermediate species in enzymes, capable of performing a large array of transformations. The ligands aforementioned have been useful to synthesize, isolate and characterize iron(IV)-oxo complexes,^{51, 65, 137} and more than 70 mononuclear iron(IV)-oxo complexes have been characterized in the last years.^{42, 62, 86, 138-139} The employment of azamacrocyclic ligands have been useful for the stabilization iron(IV)-oxo species,¹⁴⁰ thus helping for its characterization and further reactivity studies. One remarkable example used as basis of this work was reported by Company, et. al., where the azamacrocyclic chelating triazacyclononane (tacn) scaffold was used to obtain the tetradentate ligand **Pytacn** (figure IV.1, bottom left).¹⁴¹⁻¹⁴² Its related iron(II) complex, $[\text{Fe}^{\text{II}}(\text{Pytacn})(\text{CF}_3\text{SO}_3)_2]$, was used as a platform to synthesize and stabilize high-valent iron(IV)-oxo species.^{42, 143} Also the pentadentate version of the ligand, **MePy₂tacn** (figure IV.1, top left) and its related iron(II) complex was able to generate and stabilize iron(IV)-oxo species.^{56, 60} However, in comparison with mononuclear iron systems there is a lack of well-defined examples of binuclear iron complexes that generate and stabilize high-valent iron species related to important binuclear iron enzymes, as is the case of soluble methane monooxygenase (sMMO).

In this chapter we present our approach towards modelling diiron enzymes, with the synthesis, characterization and reactivity studies of two novel diiron complexes employing a dinucleating version of the tacn scaffold: on one hand employing a novel tetradentate ligand, **EBPytacn**, the dinucleating version of the **Pytacn** ligand, and on the other hand a pentadentate one, **Py₄btacn**, the

Synthesis, characterization and reactivity of diiron complexes

dinucleating version of the **MePy₂tacn**. Both ligands were able to house two iron atoms, forming stable and well-defined diiron(II) complexes $[\text{Fe}^{\text{II}}_2(\text{EBPytacn})(\text{CH}_3\text{CN})_4](\text{CF}_3\text{SO}_3)_4$ **1** and $[\text{Fe}^{\text{II}}_2(\text{Py}_4\text{btacn})(\text{CH}_3\text{CN})_2](\text{CF}_3\text{SO}_3)_4$ **2**. Using the diiron(II) complexes **1** and **2** as platform, two novel diiron(IV)-oxo intermediates, **1^{IV}=O** and **2^{IV}=O** have been prepared. Reactivity studies have been carried out with **2^{IV}=O** in oxygen atom transfer (OAT) reactions to thioanisoles and hydrogen atom transfer (HAT) reactions with weak C-H bonds.

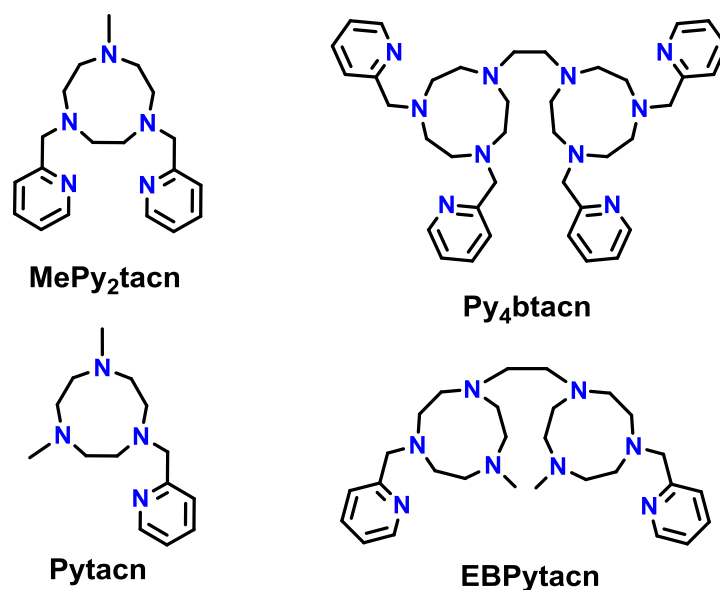


Figure III.1. Schematic structure of two reported mononucleating ligands: Pytacn and MePy₂tacn and their novel dinucleating versions studied in this thesis: EBPytacn and Py₄btacn.

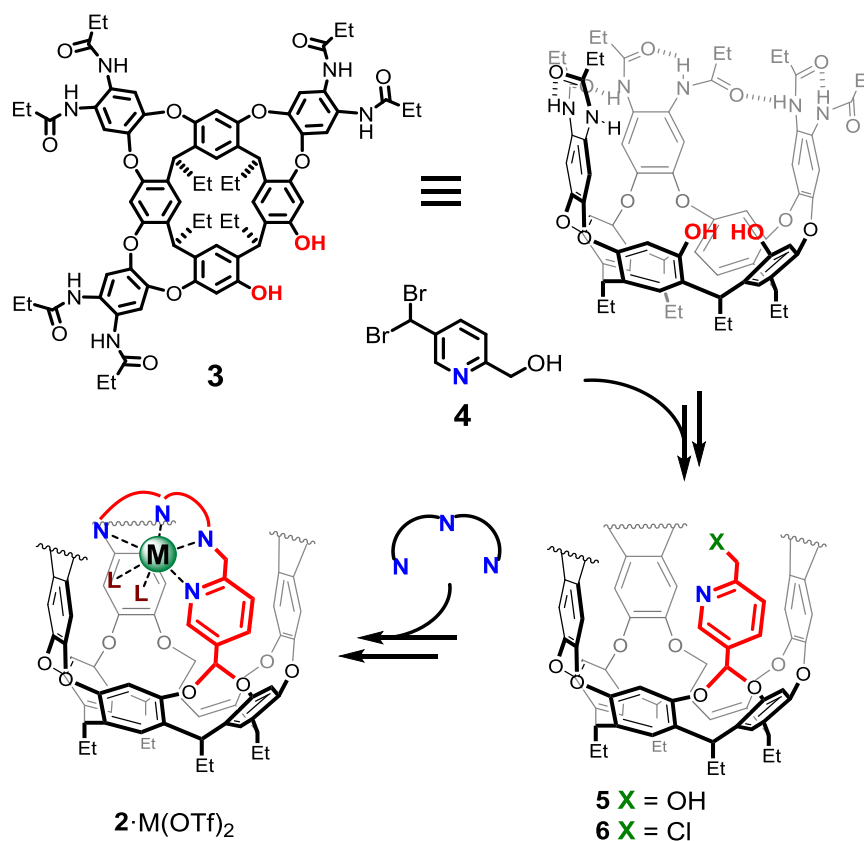
PAPER IN PREPARATION. EMBARGO UNTIL PUBLICATION DATE

IV.1. SYNTHESIS AND CHARACTERIZATION OF A NEW FUNCTIONALIZED METALLOCAVITAND.

IV.1.1. Synthesis of a novel cavita nd platform functionalized with a chelating ligand scaffold and their Fe(II), Mn(II) and Zn(II) complexes.

IV.1.1.1 Synthesis of a functionalized cavita nd with an aminopyridine ligand scaffold.

In this chapter we approach the preparation of a well-defined non-heme iron complex covalently attached to a cavita nd. It was initially planned to take advantage of a supramolecular cavity where the metal site will be isolated from the bulk and the substrate will be placed in a certain conformation in order to promote novel selectivity patterns in catalytic oxidations.

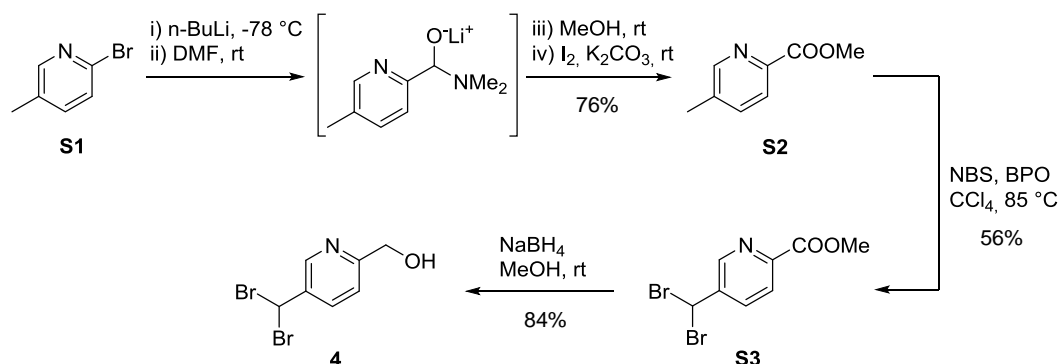


Scheme IV.1. General schematic synthesis of the new functionalized metallocavita nds.

For the synthesis of the functionalized metallocavita nd we took advantage of the method reported for preparing a cavita nd lacking a wall (hexaamide diol cavita nd **3**, scheme IV.1), described

Synthesis and characterization of a new functionalized metallocavitand

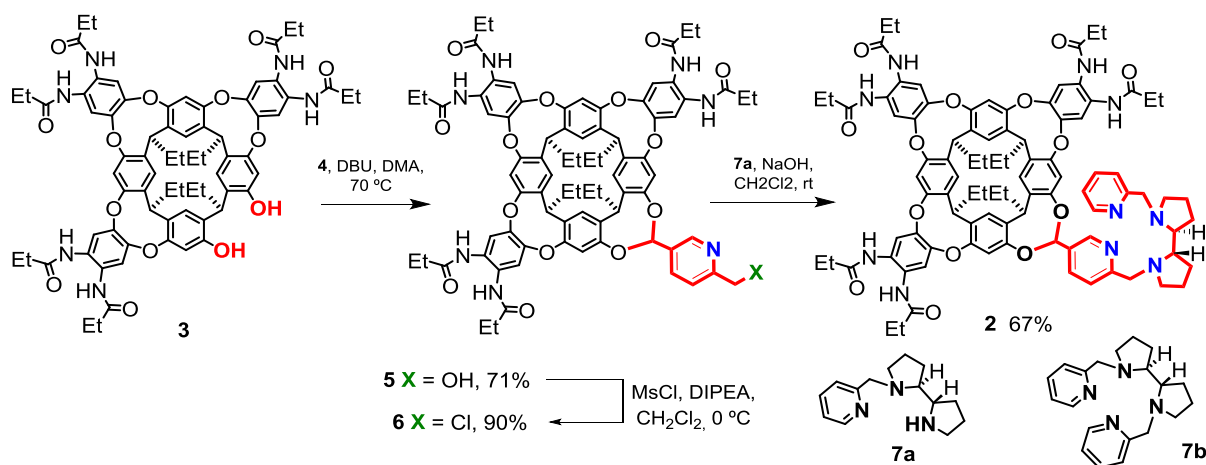
by Rebek.¹⁶⁶ With this structure, it has been possible to modify cavitands introducing different functional groups directed inwardly and outwardly and explore them for different host-guest studies and catalysis.¹⁶⁷⁻¹⁶⁹ Herein we report the synthesis and characterization of a new pyridine synthon moiety **4** that could be easily modified and attached directly to a hexaamide diol cavitand **3** bridged by an acetal group in order to place the metal center as close as possible to the deep part of the cavity. The first stage of the synthesis starts with the versatile hexaamido diol cavitand **3** previously mentioned, which was prepared following a reported procedure.^{113, 170} This structure represents the



Scheme IV.2. Schematic synthesis of **4**.

starting supramolecular scaffold.

In parallel, pyridine synthon **4** must be prepared. This synthon meets two special requirements: In one hand, it has a moiety that can be coupled to the cavitand and in the other, the resulting structure can be further elaborated to reach the final ligand. The commercially available pyridine **S1** is submitted to a 4 step synthesis. First, a methyl ester group is installed in the alpha position of the pyridine following a reported procedure¹⁷¹ to give **S2**. This molecule is subsequently brominated at the 5-methyl position of the pyridine with N-bromosuccinimide (NBS) as brominating agent and



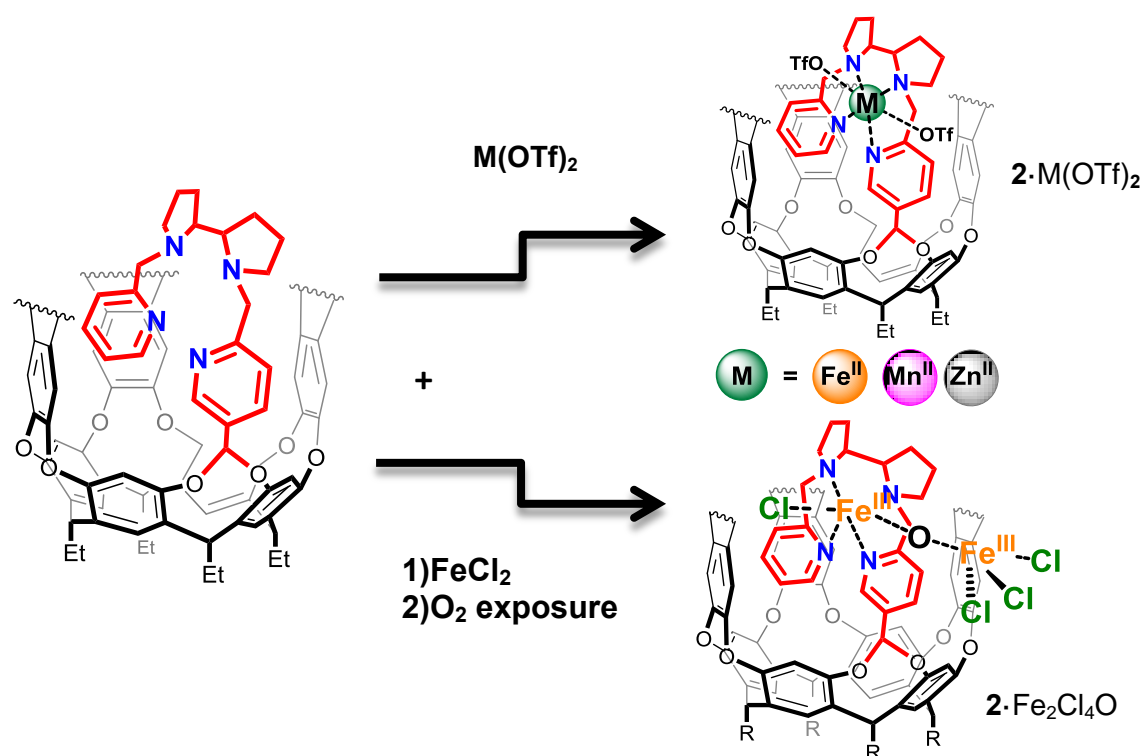
Scheme IV.3. Schematic synthesis of cavitand **2**.

benzoyl peroxide (BPO) as initiator, with a procedure similar to a reported one¹⁷² to obtain the dibromide derivative **53**. Then, the methyl ester is further reduced to the benzyl alcohol employing sodium borohydride obtaining **4**, which is the synthon employed to couple with cavitand **3**.

The next stage consists in the preparation of the bis(pyridyl)dipyrrolidine cavitand **2** depicted in scheme IV.3. The first step is the condensation of cavitand **3** with the versatile dibromide synthon **4**, following the reported procedure by Rebek,¹⁶⁷ to finally obtain 2-hydroxymethylpyridine-cavitand **5**. Mesylation of hydroxyl derivative **5** with mesyl chloride proceeded with concomitant substitution by chloride to deliver key intermediate **6**, which was univocally characterized by X-ray crystallography (figure IV.2, top). This supramolecular platform constitutes a key molecule to build diverse functionalized cavitands, since the methylene chloride group is very versatile and easy to modify with different moieties. The last step consists in the nucleophilic displacement of 2-chloromethylpyridine derivative **6** with secondary amines, which is an attractive entry into structurally diverse cavitand-ligand hybrids. For the work presented herein we chose to use known pyridyl bispyrrolidine (**S,S**)-**7a**,¹⁷³ which reacted smoothly with **6** in the presence of base to deliver cavitand **2** in good yield. Cavitand **2** was characterized by ¹H and ¹³C NMR, high resolution mass spectrometry (HRMS), and elemental analysis (EA).

IV.1.1.2. Synthesis of the Fe(II), Mn(II) and Zn(II) coordination complexes.

With cavitand **2** in hand, we then proceed to explore its coordination chemistry with different metal ions. When Fe(II), Mn(II) or Zn(II) triflate salts were reacted in THF with cavitand **2** (scheme IV.4, top) the corresponding metal complexes $2 \cdot M(\text{OTf})_2$ ($M = \text{Fe(II)}, \text{Mn(II)}, \text{Zn(II)}$) were obtained as crystalline materials in 78%, 67% and 82% yields respectively. The formation of the corresponding Fe and Mn complexes can be followed by UV-Vis spectroscopy and by ^1H NMR in the case of Zn (prepared as a surrogate devoid of paramagnetic interferences, in order to better study the properties of our system by $^1\text{HNMR}$) by titration experiments that will be explained in more detail in the next section, confirming the coordination of the metal in a 1:1 metal:cavitand stoichiometry. This conclusion was further supported by HRMS and EA. Interestingly, when **2** is treated with FeCl_2 as precursor and subsequent exposure to air let to the growing of single crystals suitable for X-ray diffraction, revealing that the structure corresponded to an oxidized iron(III) dimer, $2 \cdot \text{Fe}_2\text{Cl}_4\text{O}$ (scheme IV.4, bottom) with a simplified formula $\text{Cl-Fe}^{\text{III}}-(\mu\text{-O})\text{-Fe-Cl}_3$. This behavior has been observed previously and described for O_2 sensitive ferrous TPA (tris(2-pyridylmethyl)amine) complexes.¹⁷⁴



Scheme IV.4. Exploration of cavitand **2** coordination chemistry different metal ions. Amide groups of cavitand walls are omitted for clarity.

IV.1.2. Characterization studies of the new cavitant and its metal complexes.

IV.1.2.1. Structural characterization of **2** and its metal complexes.

Functionalized cavitant **2** and their metal complexes were characterized by diverse techniques:

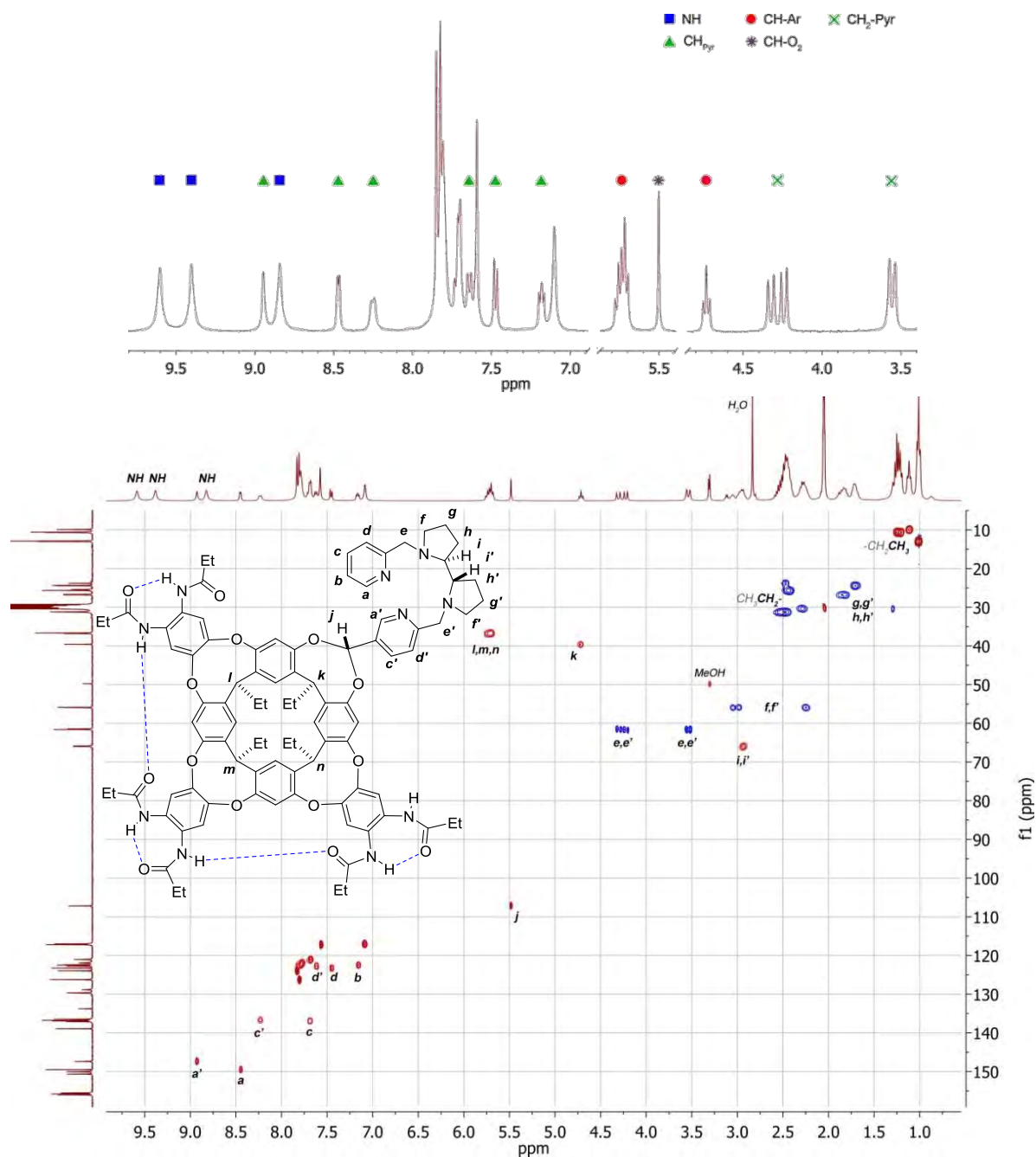


Figure IV.1. Selected regions and assignment of the ^1H NMR spectrum of **2** (400 MHz, acetone- d_6). Multiplicity edited ^1H - ^{13}C HSQC spectrum of **2** (400 MHz, acetone- d_6 , 298K). Assignment made with the help of the corresponding COSY spectrum.

Synthesis and characterization of a new functionalized metallocavitand

X-ray crystallography (XRD), elemental analysis (EA) and high resolution mass spectrometry (HRMS). The EA revealed the presence of some solvents within the molecules, a fact that can be explained by their entrapment inside the cavitand, as observed in the solid state structures (See chapter VII section VII.2.2.2), where solvent molecules are included inside the cavitand. In the case of the Fe(II) complex, solvent molecules can also be observed in the ^1H NMR spectrum (figure IV.6). The directionality established on the hydrogen bond seam formed by the amide groups renders Rebek's octaamido cavitand¹⁶⁸ chiral. In the absence of hydrogen-bond-disrupting molecules, the former exists as an even mixture of two cycloenantiomers which interconvert slowly relative to the NMR time scale.¹⁷⁵ Accordingly, **2** must exist (by virtue of the added homochiral ligand fraction) as an undetermined mixture of cyclodiastereomers. These may appear as different sets of signals in the ^1H NMR spectrum, complicating further analysis. However, in the presence of acetone- d_6 amide rotation is fast in the NMR time scale, notably simplifying the ^1H NMR spectrum (Figure IV.1, top) and the assignment by means of 2D HSQC NMR experiments (figure IV.1, bottom). Because of its distance to the chiral backbone of the ligand, the amide NHs experience little magnetic asymmetry and therefore appear as three separate resonances only.

Cavitands can adopt two conformations depending on the environment and interactions, features that are the basis of the host-guest chemistry. These are: Vase (closed) conformation, when the cavitand is folded acquiring a bowl shape due to the establishment of hydrogen bonds among the amide groups of the upper rim. The other possible conformation is the Kite (open), which consists in the loss of interactions among the upper rim of the cavitand, giving place to a planar structure preventing its bowl shape. This is an important feature since host-guest chemistry can only take place when the cavitand is in the vase conformation.

Examination of the solid state structures obtained for the cavitands **6** (figure IV.2, top) and **2**·Fe₂Cl₄O (figure IV.2, bottom) reveal some interesting features. The first regards the cavitand structure itself, where in both cases is observed that in the solid state the vase conformation is maintained, stabilized by the formation of an array of six intramolecular hydrogen bonds between six amides of the upper rim. The presence of a non-hydrogen bonding wall and the metal complexes does not interfere with the vase conformation as observed for **6** and **2**·Fe₂Cl₄O and importantly, the structure adopted does not interfere with the binding of smaller molecules, since in the X-ray structures are occupied by solvent molecules (See experimental section VII.2.2.2). Another important structural observation is the coordination of the metal to cavitand **2**, where the former is ligated by the aminopyridine group in the same fashion as in the parent complexes **7b**·Fe(CH₃CN)₂(SbF₆)₂⁹⁶ and **7b**·Fe(OTf)₂,¹⁷⁶ demonstrating that the functionalized cavitand **2** has the

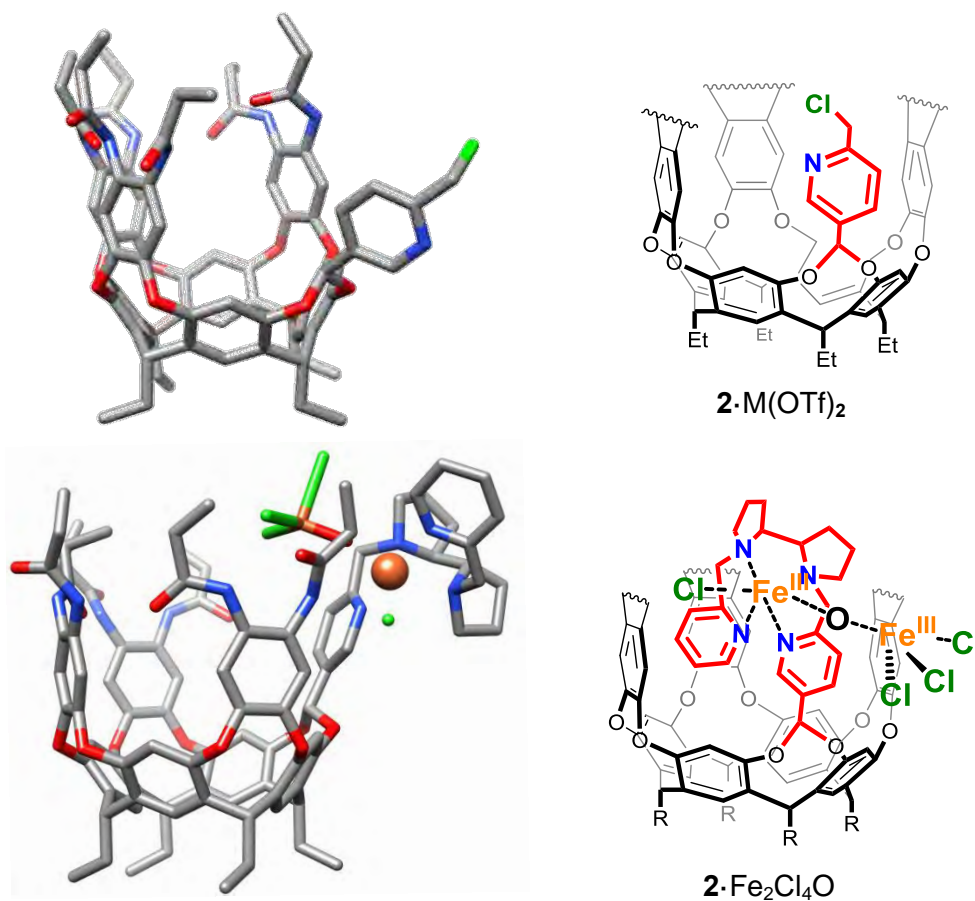


Figure IV.2. Solid state structure (left) and schematic drawing (right) of the 2-Chloromethylpyridine cavitant derivative **6** and metallocavitant $2 \cdot Fe_2Cl_4O$. Hydrogen atoms and amide groups of cavitant walls are omitted for clarity.

same coordination properties than the simple (*S,S*)-pdp (**7b**, scheme IV.3) ligand. Iron coordination complexes $7b \cdot Fe(OTf)_2$, $7b \cdot Fe(CH_3CN)_2(SbF_6)_2$ and $2 \cdot Fe_2Cl_4O$ display an iron center in a pseudo-octahedral geometry where the ligand wrapped around the metal in a *cis-α* topology, with four coordination sites occupied by the N atoms of the ligand, the two pyridine rings *trans* to each other and the two aliphatic nitrogen atoms in *cis*-relative position. The octahedral first coordination sphere of the metal is center is fulfilled with two extra ligands, *cis* to each other and *trans* with respect to the two aliphatic nitrogens.

To gain insight into the coordination properties of **2** and the metal to ligand stoichiometry cavitant **2** was titrated with increasing amounts of the corresponding metal triflates ($M(OTf)_2$, Fe, Mn and Zn). For Fe and Mn, UV-Vis spectroscopy was used to monitor the titration following the characteristic metal to ligand transfer band (MLCT) that appears upon complex formation. Incremental additions of the metal salt give rise to a proportional increase in the absorbance of the MLCT band. When 1 equivalent of metal is reached the absorbance reaches its maximum for both Fe

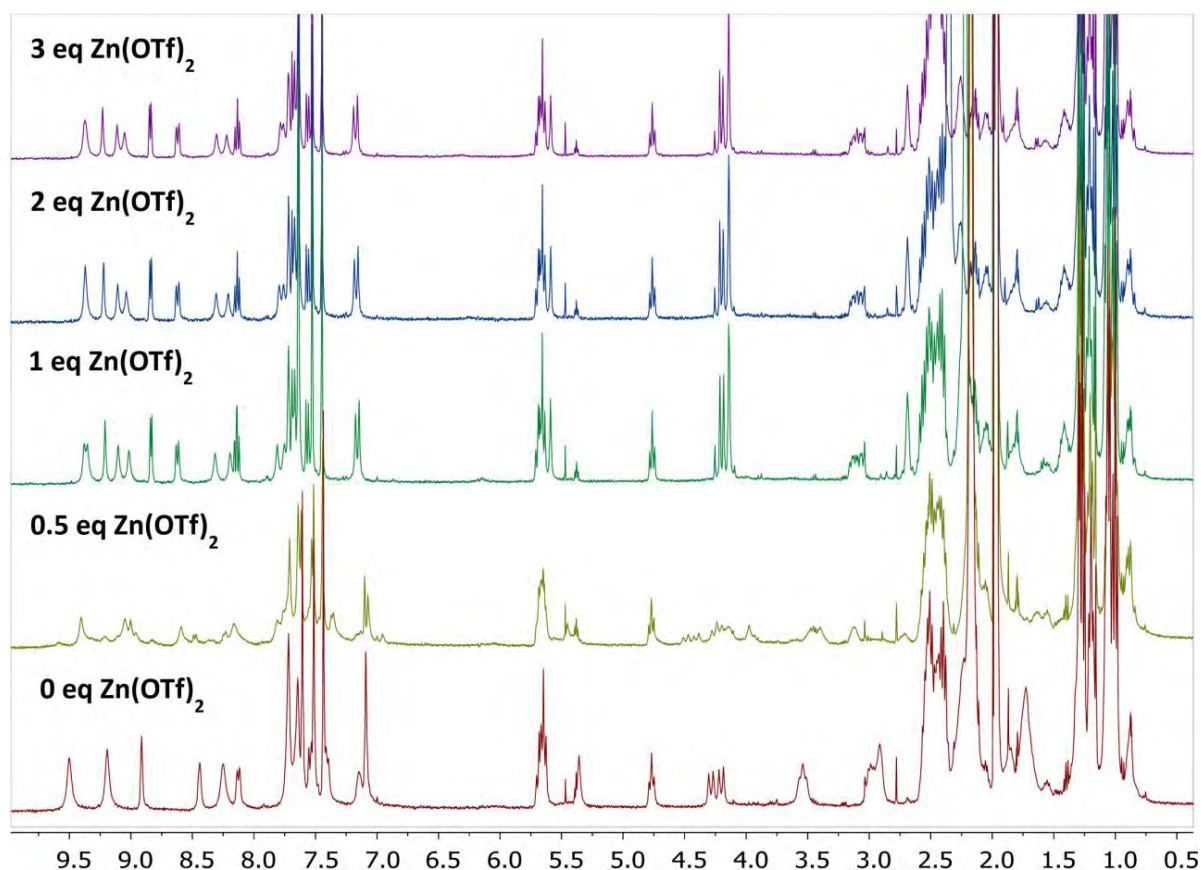


Figure IV.4 ^1H -NMR spectra of **2** in acetone- d_6 at 298 K upon titration with $\text{Zn}(\text{OTf})_2$.

and Mn. The stoichiometry is therefore 1:1. In the case of $\mathbf{2}\cdot\text{Zn}(\text{OTf})_2$, the MLCT band is absent. In this case, because of its diamagnetic nature, the coordination to Zn(II) was followed by ^1H -NMR spectroscopy (figure IV.4). After addition of 0.5 eq. of $\text{Zn}(\text{OTf})_2$ to **2** an unresolved NMR spectrum with ill-defined resonances is obtained, suggesting the presence of multiple species in equilibrium. When 1 equivalent of $\text{Zn}(\text{OTf})_2$ is reached, a clear spectrum with sharp resonances, identical to that of isolated $\mathbf{2}\cdot\text{Zn}(\text{OTf})_2$ is observed. After successive additions of $\text{Zn}(\text{OTf})_2$ (2, 3 eq.) no further changes are observed in the NMR spectrum, indicating that only a monometallic species with 1:1 stoichiometry are formed.

Detailed examination of the ^1H NMR spectrum of **2** and their metal complexes reveal more information about the behavior of these complexes in solution. First, regarding the conformational properties, the chemical shift of methine protons in resorcinarene-based deep cavitands is diagnostic for the conformation adopted in solution.¹⁷⁷⁻¹⁷⁸ In the vase (closed) conformation, the upper panels exert anisotropic deshielding on these protons, which appear between 5 and 6 ppm. On the contrary, when kite (open) conformations are populated, this effect is diminished and the methine resonances appear around 4 ppm. Polar solvents such as methanol or acetonitrile, force the adoption of a *kite* conformation that dimerizes through π - π stacking interactions. In contrast, in the

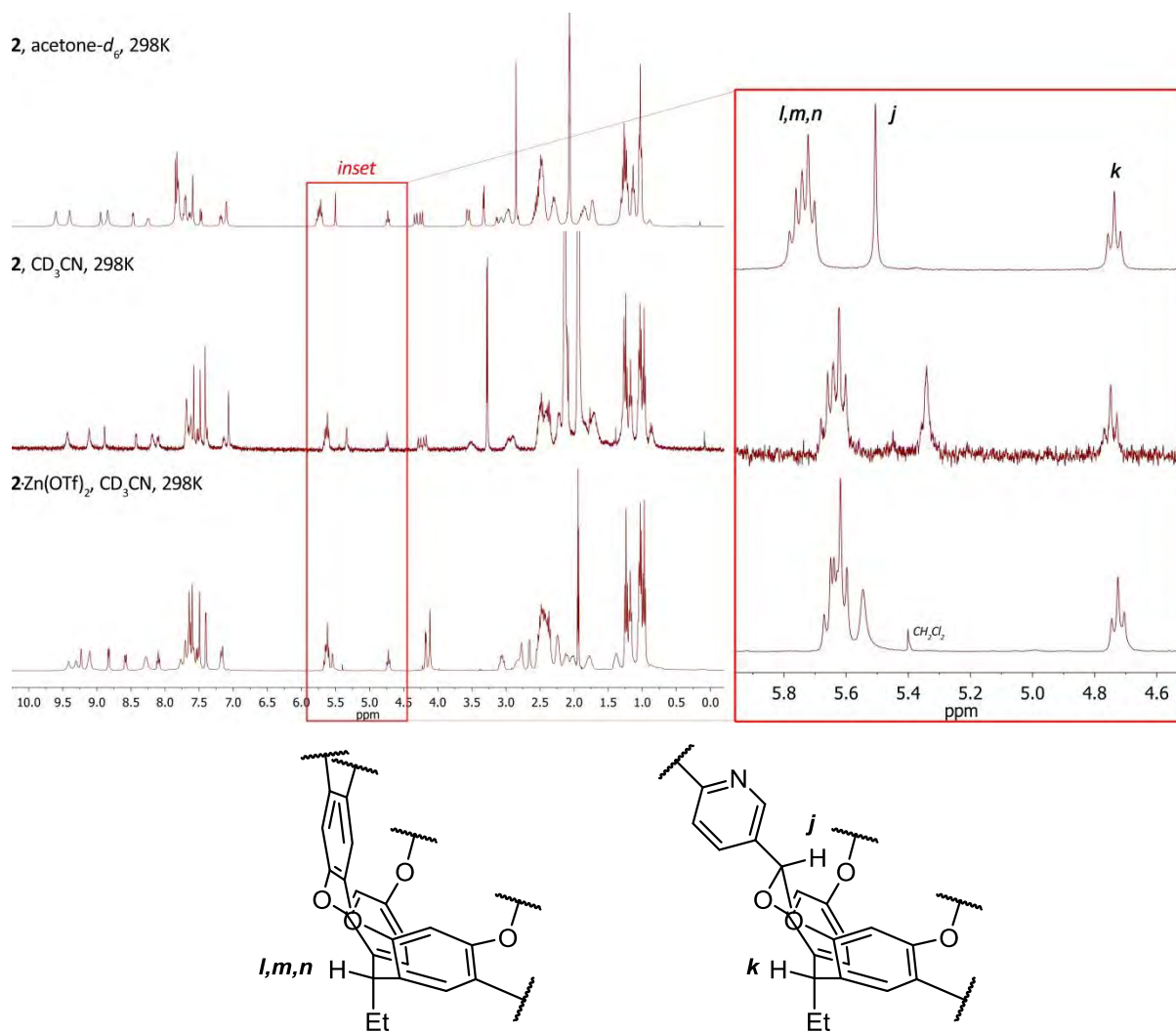


Figure IV.5 ^1H NMR spectra of **2** and **2**· $\text{Zn}(\text{OTf})_2$ in different solvents; inset of the methine region.

case of cavitand **2**, only 3 methine protons (**l,m,n**; figure IV.5) experience the anisotropic effect of the upper aromatic panels, with the fourth resonance (**k**) being adjacent to an acetal moiety, indicative of a folded vase conformation both in acetone- d_6 and CD_3CN as seen in the spectra below. Likewise, for the Zn(II) complex of **2** the diagnostic chemical shifts in CD_3CN indicate a vase conformation.

Similar features are observed in the ^1H NMR spectra of the Fe(II) complex (figure IV.6). By analogy, and owing to the similar coordination behavior of Fe(II) and Mn(II) complexes, we can conclude that **2**· $\text{Mn}(\text{OTf})_2$ also adopts a vase conformation (paramagnetic effects in this complex preclude further analysis by ^1H NMR).

Synthesis and characterization of a new functionalized metallocavitand

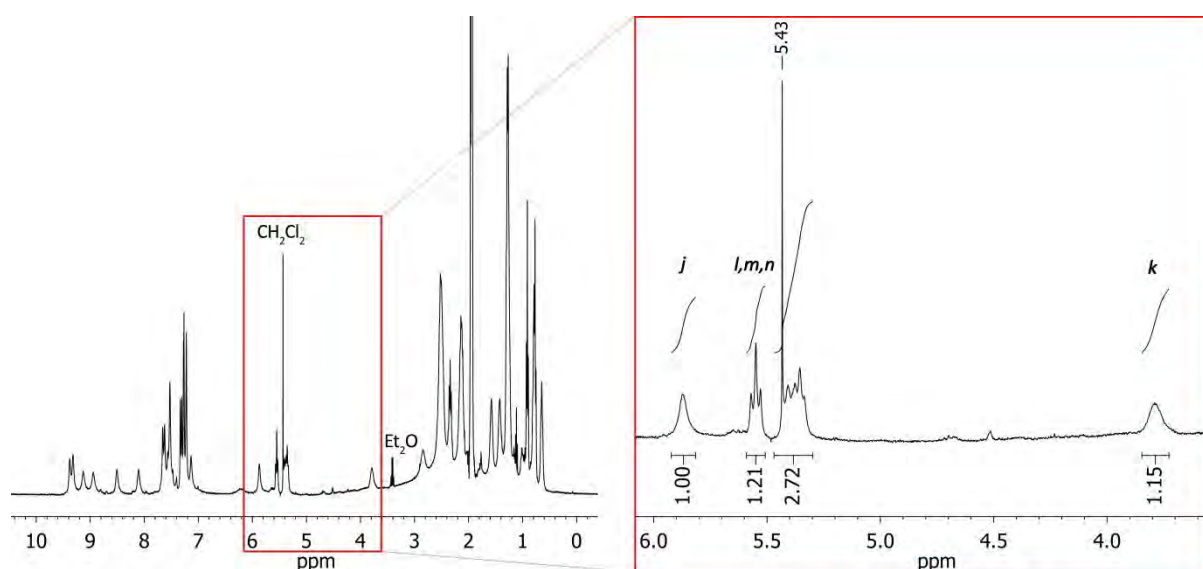


Figure IV.6 ^1H NMR spectrum of $2\cdot\text{Fe}(\text{OTf})_2$ in CD_3CN (400 MHz, 298 K); inset of the methine region.

From the ^1H NMR spectra of the $2\cdot\text{Fe}(\text{OTf})_2$ complex (figure IV.6) some information about the spin state can be extract. The ferrous complex displays only subtle paramagnetic effects on the ^1H NMR spectra at 300 K in CD_3CN , indicating that the iron center is in the diamagnetic low spin state. This is in strong contrast with the ^1H NMR of the parent complex $7\text{b}\cdot\text{Fe}(\text{OTf})_2$ in the same conditions, that possess high spin iron(II) center, observing signals up to 50 ppm (figure IV.7). These features suggest a subtle influence of the cavitant in modulating the electronic properties of the iron(II) center.

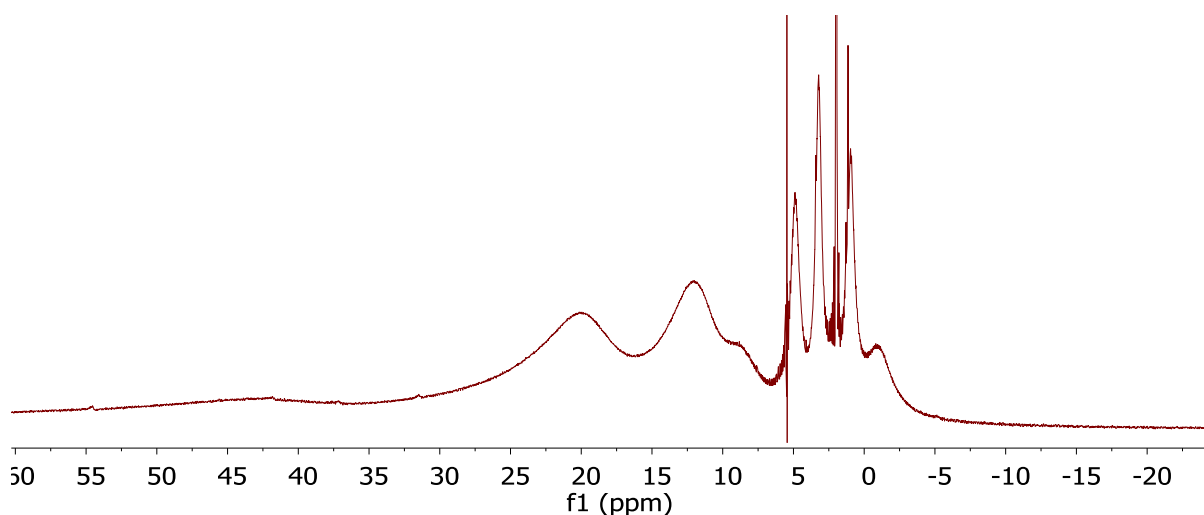
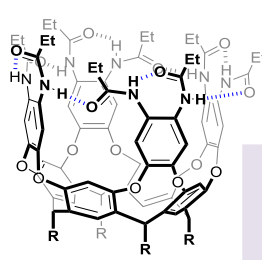
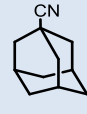
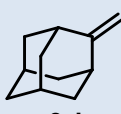
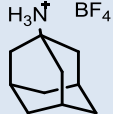
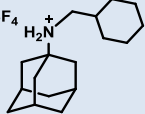
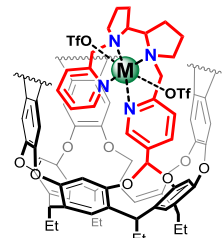
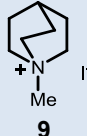
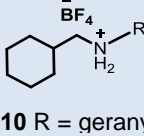
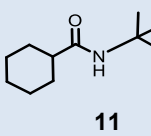
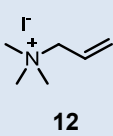


Figure IV.7 ^1H NMR spectrum of $7\text{b}\cdot\text{Fe}(\text{OTf})_2$ in CD_3CN with paramagnetic parameters (400 MHz, 298 K).

IV.1.3. Host-Guest studies.

One of the most special features that makes cavitands to resemble enzymes is the possibility of include smaller molecules inside them, thanks to the cavity created through the seam of hydrogen bonds of the upper rim that maintain the macrocycle in the aforementioned vase conformation, forming an hydrophobic pocket in the inside due to the walls environment.¹⁷⁵ As well as enzymes,

Table IV.1 Comparison of guest-binding in octaamide cavitand **1** and metallocavitands **2**·M(OTf)₂. Amide groups of cavitand walls are omitted for clarity.

 <p>1</p>	<p>1</p>	 <p>8a</p>	 <p>8a'</p>	 <p>8b</p>	 <p>8c</p>
		<p>2·M(OTf)₂</p>	<p>✓</p>	<p>✓</p>	<p>✓</p>
 <p>2·M(OTf)₂</p> <p>M = Fe^{II}, Mn^{II}, Zn^{II}</p>	<p>1</p>	 <p>9</p>	 <p>10 R = geranyl</p>	 <p>11</p>	 <p>12</p>
		<p>2·M(OTf)₂</p>	<p>✓</p>	<p>✓</p>	<p>✓</p>

cavitands can display a catalytic center inwardly directed towards the hydrophobic pocket¹⁷⁹ which is not tightly sealed, so substrates can readily fill the space of the cavity, enter and leave again to the bulk medium, and another guest molecule will approach again to the cavitand and follow the same process, being a dynamic process.¹¹⁸ The driving forces of the host-guest process in a cavitand remains in the weak and crucial interactions established with the guest: In a polar solvent (environment), the hydrophobic cavity created inside the cavitand forces non-polar substrates to enter inside the guest due to the hydrophobic effect. In the other hand, secondary interactions drive the inclusion of some guests, since the latter can owe functional groups able to settle hydrogen bond interactions with the amides of the upper rim, assisting the inclusion of the substrate inside the cavity.¹⁸⁰

Synthesis and characterization of a new functionalized metallocavitand

The most convenient way to identify molecules included inside a cavitand relies in the observation of the ^1H NMR, since the protons of external molecules buried inside the cavity experience a strong shielding, which is diagnosed by the appearance of resonances in the far upfield region of the spectrum (δ 0 to -4 ppm), corresponding to the shielded aliphatic protons of the guest.¹⁷⁵ Taking as reference the octaamido cavitand **1** reported by Rebek,¹⁸⁰ it can be observed from the literature that neutral adamantane guests as **8a** or **8a'** (table IV.1) are well accommodated inside the cavity due to the right size and shape of the adamantane to fill the cavity. Other good guests for **1** are those bearing functional groups able to establish hydrogen bonds with the upper rim of the cavity that assist the formation of kinetically stable host-guest adducts, especially those with positively charged amine groups (**8c-10**, **12** table IV.1) or amides (**11**, table IV.1). With these data in hand, it was performed a screening of proper guests for our metallocavitands $2\cdot\text{M}(\text{OTf})_2$ and compared in parallel with **1**, summarized in table IV.1. In contrast with octaamido cavitand **1**, neutral guests **8a** or **8a'** do not displace solvent molecules to form kinetically stable host-guest adducts with

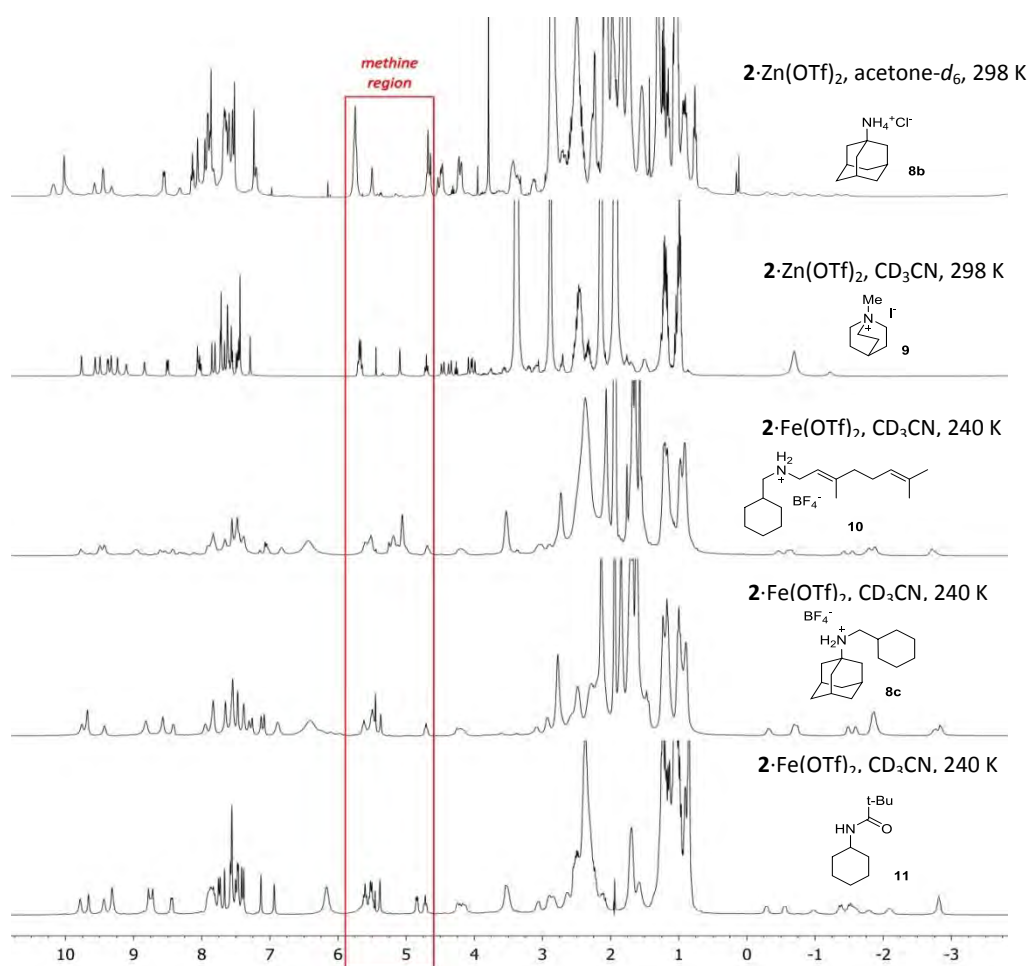


Figure IV.8 Top: ^1H NMR spectra (full sweep width) of various host-guest complexes with $2\cdot\text{M}(\text{OTf})_2$ with the methine region highlighted (in some cases overlapped with resonances of the unbound guest).

our metallocavitands $2\cdot\text{M}(\text{OTf})_2$. The same trend is observed when a positively charged guest lacking a good shape that fills the cavity is used, as lineal alkylammonium **12**, which also prevented the formation of any host-guest adduct with the metallocavitand. Only when a positively charged or a strong hydrogen bond donor is present in the guest as is the case of protonated amines or amides, used as anchor, in combination with a moiety that possess the right size and shape to fill the cavity, the formation of a host-guest adduct is observed. So, both criteria must to be met in order to observe the recognition of external molecules by our metallocavitands $2\cdot\text{M}(\text{OTf})_2$.

The identification of a guest inside the metallocavitand is diagnosed, as mentioned previously, by the appearance of resonances in the far upfield as observed in figures IV.8 and IV. 9 corresponding to buried aliphatic protons. The large upfield shifts observed up to -3 ppm are consistent with the receptor retaining the vase conformation,¹⁸¹ and the chemical shifts of the methine protons in the resulting ^1H NMR spectrum of the host-guest adducts (figure IV.8) corroborate this hypothesis. Guests **8b**, **c**, **9** and **10** bind with their bulky aliphatic moieties occupying the deep aromatic cavity through CH- π interactions, leaving the ammonium group in a suitable range to establish additional interactions with the amide groups of the upper rim. For primary and secondary ammonium moieties hydrogen bonding to the amide's carbonyl is settled, meanwhile quaternary ammonium groups set up cation-dipole interactions when the charged part is positioned close to the rim, as is the case of **9**.¹⁶⁸ In the absence of these secondary interactions, guests cannot compete with the solvent which is present in large excess. Also neutral strong hydrogen bond donor molecules as cyclohexylamides (**11**) have been found to be good guests that displace solvent molecules. Due to

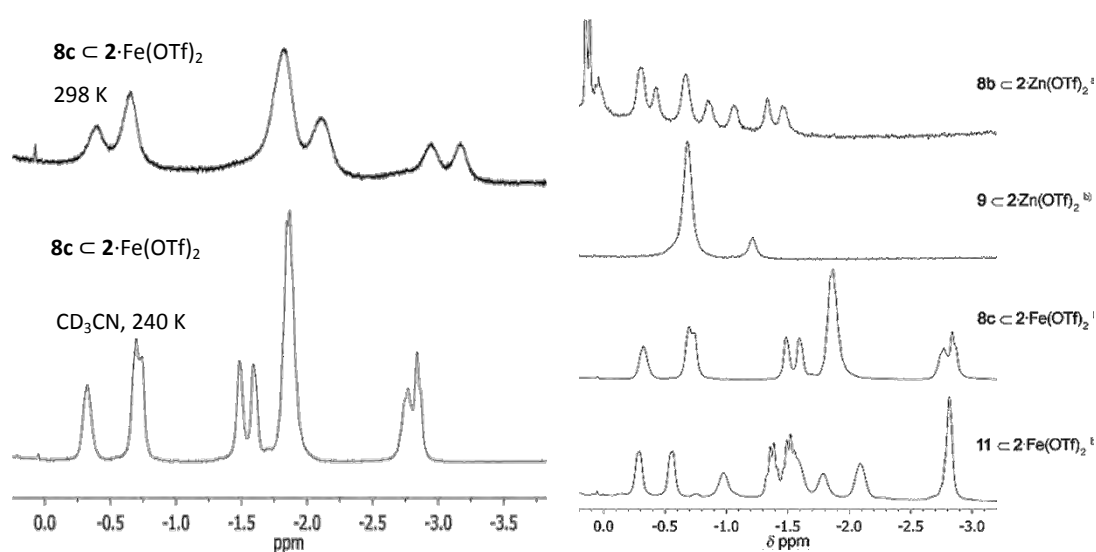


Figure IV.9. Right: Upfield regions taken from the full ^1H NMR spectra of figure IV.8. Left: Upfield region of the ^1H NMR spectra of $8\text{c} \cdot 2\cdot\text{Fe}(\text{OTf})_2$ at 298 K (top) and 240 K (bottom).

Synthesis and characterization of a new functionalized metallocavitand

the dynamic behavior of the host-guest process within the metallocavitand, the signals in the upfield of the ^1H NMR spectrum at room temperature (298 K, figure IV.9, top left) are broad. In contrast, when the NMR spectrum is registered at low temperature (240K, figure IV.9, bottom left) the dynamic process slows down and as a consequence of it, the resonances become sharp signals facilitating its identification. Indeed, this feature helped to elucidate the buried part in an ambidextrous guest, which is able to bind the cavitand by two different anchors, as is the case of guest **8c**, either by the adamantane or the cyclohexyl moiety. The first hypothesis was that **8c** would bind by its adamantane moiety as happens with **1**. Surprisingly, careful analysis of the 2D NMR spectra of **8c** \subset **2**·Fe(OTf) $_2$ at low temperature (figure IV.10) revealed that **8c** binds by the cyclohexyl moiety, suggesting that the space is slightly reduced in metallocavitands **2**·M(OTf) $_2$ with respect to **1**. To further support this hypothesis, the upfield region of the ^1H NMR spectra of host-guest adducts

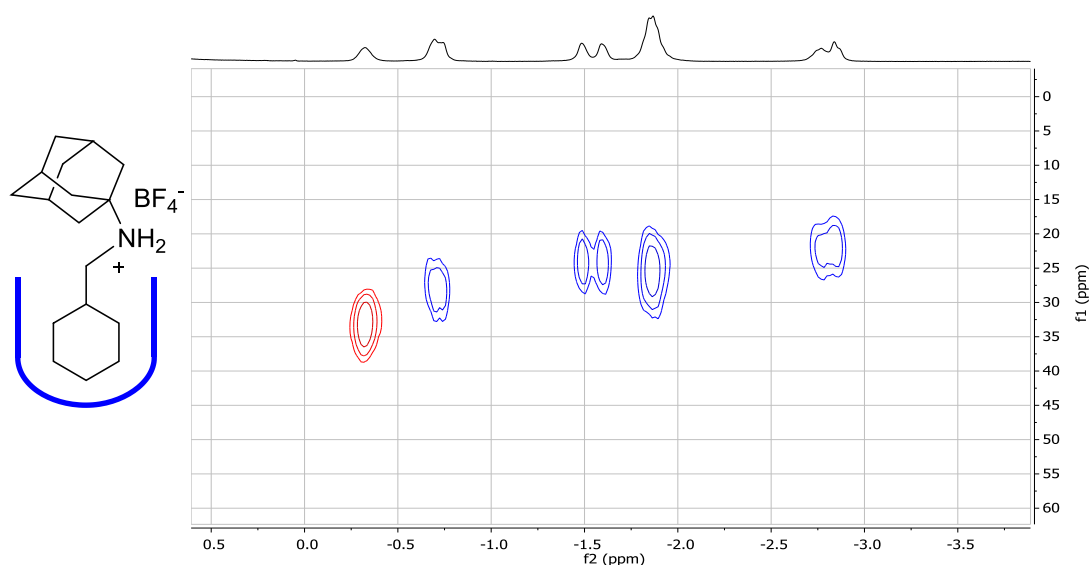


Figure IV.10. Multiplicity edited ^1H - ^{13}C HSQC (400 MHz, CD_3CN , 240 K) of **8c** \subset **2**·Fe(OTf) $_2$. Red CH/ CH_3 , blue CH_2 .

8c \subset **2**·Fe(OTf) $_2$ and **10** \subset **2**·Fe(OTf) $_2$ (see figure VII.1 experimental section VII.2.2.3) was compared, observing that resonances of both adducts are almost identical, and guest **10** can only bind the cavity by the cyclohexyl moiety. In addition, the integration of the prominent signals observed in the upfield of the ^1H NMR spectrum is in accordance with a cyclohexane molecule. With this data and those of the 2D NMR analysis we can conclude that guest **8c** binds the metallocavitands **2**·M(OTf) $_2$ by the cyclohexyl moiety.

IV.2. Concluding remarks.

In this chapter, a novel hybrid organic-inorganic metallocavitand **2** has been developed. It has been found that synthon cavitand **6** can be used as useful platform for the easy introduction of different functional groups in a cavitand platform. In our case, synthon cavitand **6** has been used to functionalize the lacking fourth wall with a bioinspired aminopyridine ligand, in order to chelate Fe(II), Mn(II) and Zn(II) metal ions. Remarkably, good quality x-ray diffraction crystals of the metallocavitand **2**·Fe₂Cl₄O were obtained, revealing the desired coordination arrangement of the ligand around the metal, in spite of the presence of the supramolecular cavity. From the characterization techniques of metallocavitands **2**·M(OTf)₂ (M = Fe(II), Mn(II), Zn(II)) it is observed that well defined coordination complexes are formed. Interestingly, the host-guest properties of **2**·M(OTf)₂ are not compromised due to the lack of a fourth hydrogen bonding wall or the presence of metal complexes. The recognition properties of the metallocavitands **2**·M(OTf)₂ make them potentially suitable for inducing selectivity in bioinspired oxidation reactions, where the recognition of the substrate is a key feature for this purpose.

V.1. REACTIVITY STUDIES OF METALLOCAVITANDS.

The use of cavitands as catalysts has been seldom investigated. In the first examples, pure organic cavitands were developed, usually modified to own a functional groups that enables catalytic reactivity.¹⁸² In the field of homogeneous transition metal catalysis, there is a growing interest in the last years to mimic metalloenzymes to design more efficient and more selective metal catalysts.^{1, 26, 133, 141, 183-184} Hybrid organic-inorganic metallocavitands can potentially meet these requirements since they strongly resemble natural enzymes. However, the reports regarding reactivity with this kind of systems¹⁸⁵ are scarcer than purely organic cavitands. Some successful reports in terms of catalytic activity have been reported in the last decade employing second or third row transition metals, such as Pd, Pt, Rh or Au.¹⁸⁶ These cavitands have been developed for reactions such as allylic alkylation,¹⁸⁷ hydroformylation¹⁸⁸ or hydrogenation¹⁸⁹. However, metallocavitands owing iron or manganese bioinspired metal complexes for C-H and C=C bioinspired oxidations are at a very early stage of development and only few reports can be found.^{134, 136, 190} Indeed, these supramolecular structures usually decompose under the high-oxidative environment of the oxidation reactions, due to the high reactivity nature of the metal, where the iron (and manganese)

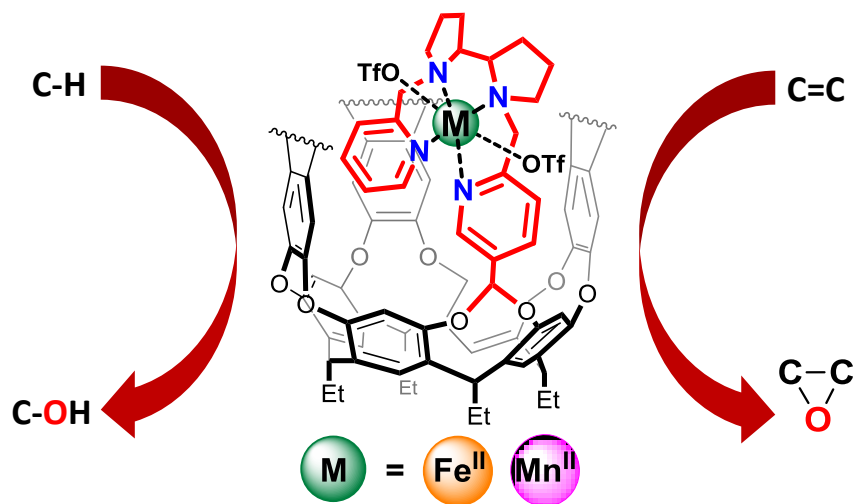


Figure V.1. Bioinspired alkane and alkene oxidations with Fe and Mn metallocavitands. can reach high oxidation states.

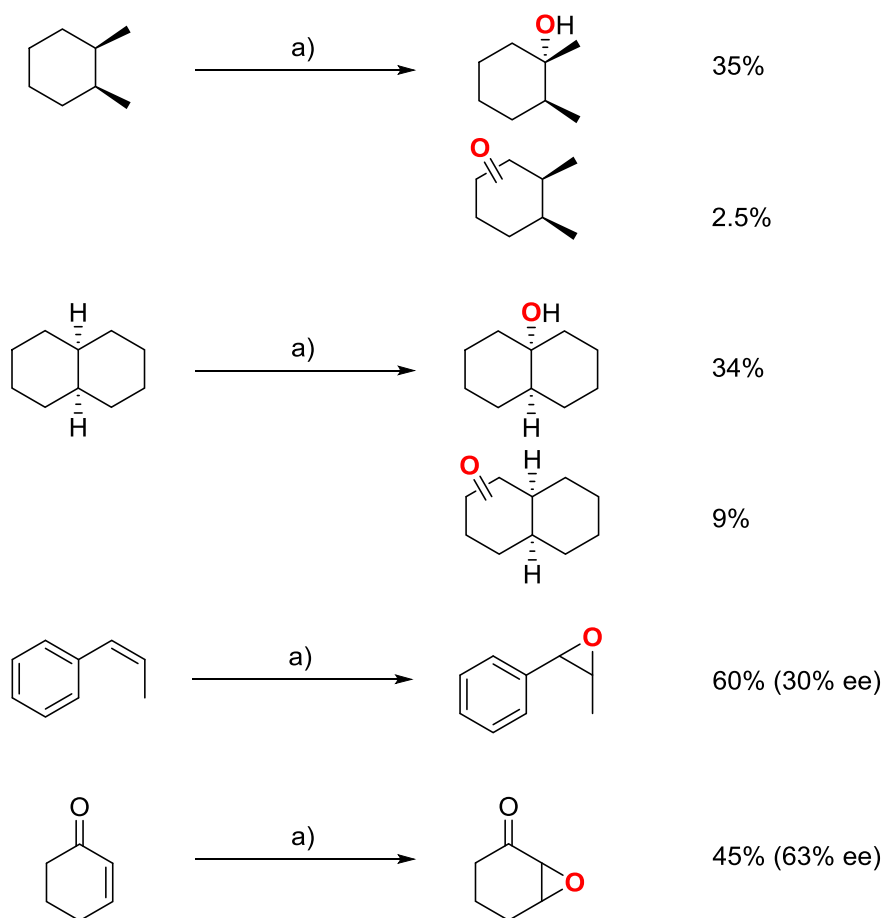
In this chapter we explore the reactivity of the iron(II) and manganese(II) metallocavitands described in the previous chapter, $2 \cdot M(OTf)_2$ ($M = Fe(II), Mn(II)$) for the catalytic oxidation of C-H and C=C bonds. Additionally, we studied the trapping, characterization and reactivity of high-valent

Reactivity of metallocavitands

unstable intermediate species within the metallocavitand **2**.Fe(OTf)₂. These species are known to be highly reactive, and isolation from the bulk within a cavitand is not trivial, since supramolecular structures tend to degrade in the presence of highly-reactive species.

V.1.1. Catalytic studies employing **2**.Fe(OTf)₂ and **2**.Mn(OTf)₂ metallocavitands.

Bioinspired C-H and C=C oxidation reactions are an interesting target for supramolecular chemistry.¹²⁹ These reactions are not trivial since current state of the art catalysts have emerged from an extensive exploration of numerous complexes, studied as potential catalysts, and small changes in their structure have profound impact in their catalytic activity.^{133, 191-192} Our design is based in the use of a previously described bioinspired catalyst^{96, 193}, which is covalently installed in the cavitand to yield the metallocavitands **2**.Fe(OTf)₂ and **2**.Mn(OTf)₂. We evaluated metallocavitands **2**.Fe(OTf)₂ and **2**.Mn(OTf)₂ in representative alkane and alkene catalytic oxidation



Scheme V.1. Catalytic oxidations with Fe catalyst. a) **2**.Fe(OTf)₂ (3 mol %), H₂O₂ (2.5 eq), AcOH (1.5 eq.), MeCN, 0 °C, 30 min.

reactions using H_2O_2 as terminal oxidant under standard catalytic conditions (scheme V.1). The catalytic performance of our metallocavitand catalysts was compared with the already reported complex $[\text{Fe}(\text{pdp})(\text{OTf})_2]^{176}$ (**7b**· $\text{Fe}(\text{OTf})_2$). In the first place, the stability of the metallocavitand **2**· $\text{Fe}(\text{OTf})_2$ as catalyst was tested in oxidation reactions for prototypical alkane (*cis*-decalin, *cis*-1,2-dimethylcyclohexane) and alkene (*cis*- β -methylstyrene, 2-cyclohexenone) substrates (scheme V.1). Comparing its activity with the one of the simple complex (**7b**· $\text{Fe}(\text{OTf})_2$) (scheme VII.5 and VII.6 in annex chapter V), it is noted that **2**· $\text{Fe}(\text{OTf})_2$ maintains mainly the same activity in C-H oxidation and asymmetric olefin epoxidation. Moreover, monitoring the evolution of the iron metallocavitand species during catalysis by HRMS reveals that the catalyst has not decomposed during the course of

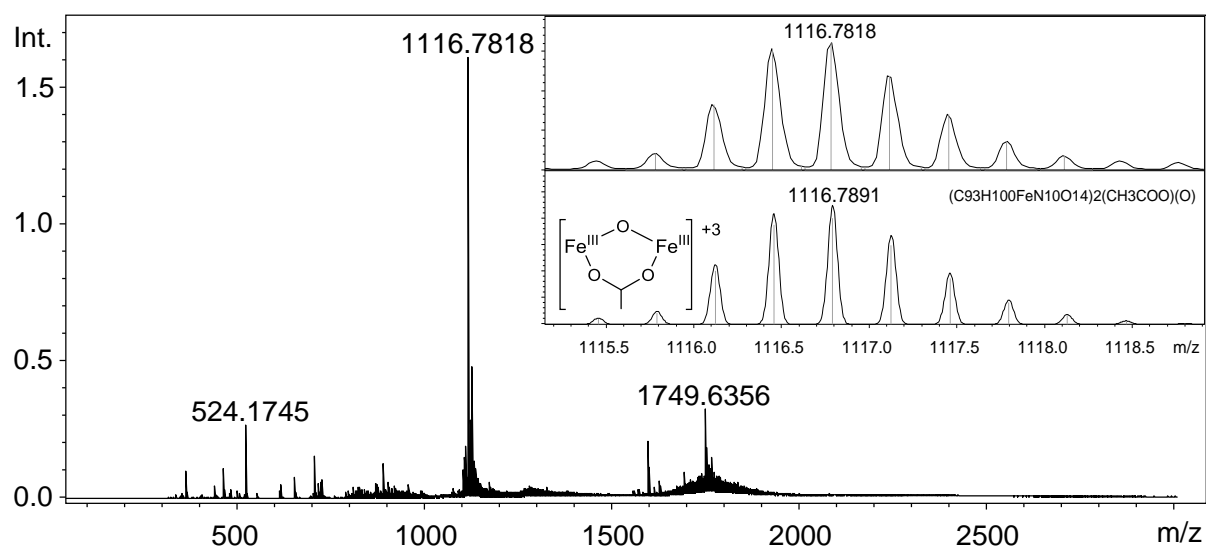


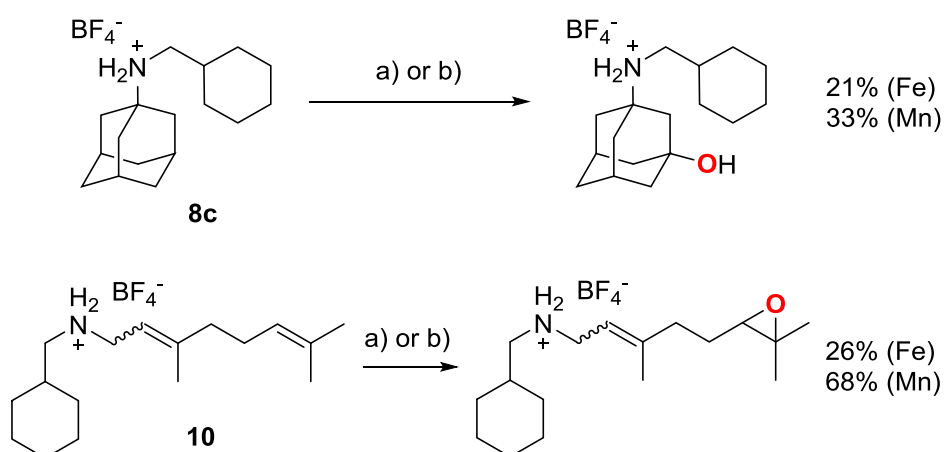
Figure V.2. HRMS of the reaction mixture just after finishing the reaction. Inset corresponding to the experimental and simulated peak of the detected species. CH_3CN as solvent

the reaction and maintains its integrity. This has been performed by analyzing an aliquot of the catalytic reaction mixture in the mass spectrometer after the reaction is finished. The dominant peak observed in the spectrum (figure V.2) at $m/z = 1116.7818$ is assigned to an oxo-carboxylate bridged iron(III) dimer by simulation, species usually found for bioinspired iron catalysts after the oxidation reaction.¹⁹⁴ The peak is in agreement with the formula $[(2\text{Fe}^{\text{III}})_2(\text{O})(\text{CH}_3\text{COO})]^{3+}$, meaning that the cavitand structure is intact and two metallocavitands are forming a dimer with a carboxylate and an oxo bridge. These kinds of species are observed in bioinspired iron complexes in oxidation reactions. The peak at $m/z = 1749.6356$ (annex chapter V) corresponds to the latter species with one triflate as counter ion, $[(2\text{Fe}^{\text{III}})_2(\text{O})(\text{CH}_3\text{COO})(\text{OTf})]^{2+}$ with a net charge of +2. The only species detected in the mass spectrum related with the degradation of the metallocavitand structure is the one at $m/z =$

Reactivity of metallocavitands

524.1745, that should correspond with the iron complex coordinated to the ligand, but detached of the cavitand. However, this peak is observed with low intensity, thus, in spite of we didn't perform quantitative ESI-MS, a priori this species should be present in small amount.

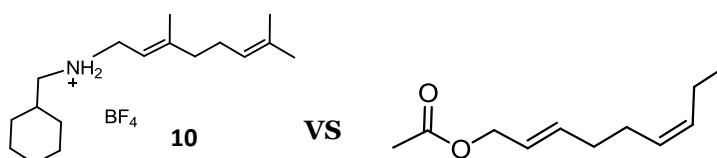
Under the reaction conditions described in scheme V.1, the catalytic hydroxylation of *cis*-decalin and *cis*-1,2-dimethylcyclohexane is selective for the tertiary C-H bond, observed as major product in 34-35% yield. More remarkably, retention of configuration was observed in the resulting tertiary alcohol product, suggesting the absence of free radical processes and the presence of a metal-based mechanism, similar to that of bioinspired iron complexes. The oxidation of the methylenic C-H bond is observed as a minor product in 3-9% yield. The catalytic asymmetric epoxidation of *cis*- β -methylstyrene and 2-cyclohexenone was also carried out successfully (scheme V.1). The epoxides were obtained as major product in 60% and 45% yields respectively, again with absolute retention of configuration. Remarkably in the last reactions, are the notable levels of enantioselectivity retained (30% and 63%, respectively). The high levels of retention of configuration and enantioselectivity in these reactions strongly suggest the involvement of a selective metal-based oxidant. In this regard, the most evoked species has been the highly-electrophilic metal-oxo ($M^V=O$, $M = Fe$ or Mn).^{26, 133, 195} For the substrates so far mentioned, we have not found evidences for the formation of *kinetically stable* host-guest adducts with the metallocavitand $2 \cdot M(OTf)_2$, despite these substrates have the appropriate size to enter the cavitand. On the other hand, the cyclohexane moiety can only bind in the cavity in the case of carrying a strongly hydrogen bonding group, such as cyclohexyl amide (**11**, chapter IV) or positively-charged protonated amines (**8c**, **10**, chapter IV).



Scheme V.2. Catalytic oxidations with Fe and Mn catalysts for substrates that bind inside the cavitand. a) $2 \cdot Fe(OTf)_2$ (3 mol %), H_2O_2 (2.5 eq), AcOH (1.5 eq.), MeCN, 0 °C, 30 min. b) $2 \cdot Mn(OTf)_2$ (1 mol %), H_2O_2 (2.0 eq), AcOH (17 eq.), MeCN, 0 °C, 30 min.

Oxidation of substrates that do form *kinetically stable* host-guest adducts with the metallocavitand $2 \cdot M(\text{OTf})_2$, as **8c** and **10** (scheme V.2), was also accomplished. Oxidation of **8c** is selective for the tertiary C-H of the adamantane moiety, this bond being the most prone to oxidation on the basis of its relatively weak nature (BDE values). Epoxidation of substrate **10** occurs in the most remote olefinic bond from the ammonium unit, due to the strongest deactivation exerted by the protonated amine group. For both substrates, the manganese catalyst $2 \cdot \text{Mn}(\text{OTf})_2$ shows better activity than its iron analog, which is translated in higher conversions and yields (scheme V.2). However, taking a look at the selectivity pattern for the oxidation of **8c** and **10** with metallocavitands $2 \cdot M(\text{OTf})_2$, it is observed that is the same exhibited by the simple parent complexes $[M(\text{pdp})(\text{OTf})_2]$ (**7b**· $M(\text{OTf})_2$, $M = \text{Fe}(\text{II}), \text{Mn}(\text{II})$) (scheme VII.7, annex chapter V). This observation suggests that in our metallocavitands the oxidation occurs at substrate molecules when they are not bound to the cavity.¹⁹⁶ This suggests that the selectivity is governed by the intrinsic nature of the substrate, and the substrate recognition does not have an impact on the selectivity. A supramolecular effect could potentially favor, for instance, the oxidation of a methylenic CH_2 bond over a tertiary CH one in the same molecule, or override electronic effects as deactivation of an alkyl chain. This is driven by preorganization of the substrate inside the supramolecular capsule, exposing just certain bonds in close proximity to the active site. We evaluated the impact of the recognition of the substrate, by setting a competition experiment where two similar substrates are combined in one pot with the metallocavitand and submitted to catalytic epoxidation: one substrate that binds to the cavity, as is **10**, and another with similar bonds (in terms of BDE) that does not bind to the cavity (table 1). If there was an impact of the reactivity of the bound substrate, **10** should be preferentially oxidized against the not bounded one. In the case of using the parent complex as catalyst, **7b**· $\text{Mn}(\text{OTf})_2$, binding of substrate **10** is not possible and thus, the oxidation would occur equally on both

Table V.1. Catalytic epoxidation reaction with Mn catalysts $2 \cdot \text{Mn}(\text{OTf})_2$ and **7b**· $\text{Mn}(\text{OTf})_2$ for a 1:1 mixture of substrates. Conditions: catalyst (1 mol %), H_2O_2 (2.0 eq), AcOH (17 eq.), MeCN, 0 °C, 30 min.



Catalyst	Conversion	Epox	Conversion	Epox
$2 \cdot \text{Mn}(\text{OTf})_2$	46%	35%	51%	47%
7b · $\text{Mn}(\text{OTf})_2$	66%	53%	68%	62%

Reactivity of metallocavitands

substrates. Comparing the data in table 1, it is observed for both catalysts $2\cdot\text{Mn}(\text{OTf})_2$ and $7\text{b}\cdot\text{Mn}(\text{OTf})_2$ that both substrates are oxidized in a 1:1 ratio, meaning that both catalysts oxidize both substrates equally, and there is no preference for any of them. This situation could be expected for $7\text{b}\cdot\text{Mn}(\text{OTf})_2$. However, as $2\cdot\text{Mn}(\text{OTf})_2$ shows the same pattern, it could be concluded that preferential oxidation of the bound substrate does not occur.

With all these results in hand, the powerful catalytic activity of supramolecular catalysts is demonstrated, however with limitations in our design. One of the main drawbacks is the low barrier for the rotation of the pyridyl-acetal linkage, which is presumably able to orient the metal complex outside when a substrate is bound into the cavity, probably due to steric effects. However, if this pyridyl moiety would be anchored anyhow to the walls of the rest of the cavitand and oriented inwardly, the incoming guest would be forced to be in close proximity to the active metal center, overriding repulsions or steric effects that pull the metal towards outside of the cavity.

V.1.2. Intermediate species and reactivity.

V.1.2.1. Generation and characterization of high-valent iron(IV)-oxo species in a metallocavitand platform.

Finally, we wonder if our metallocavitand platform $2\cdot\text{Fe}(\text{OTf})_2$ has the ability to support the

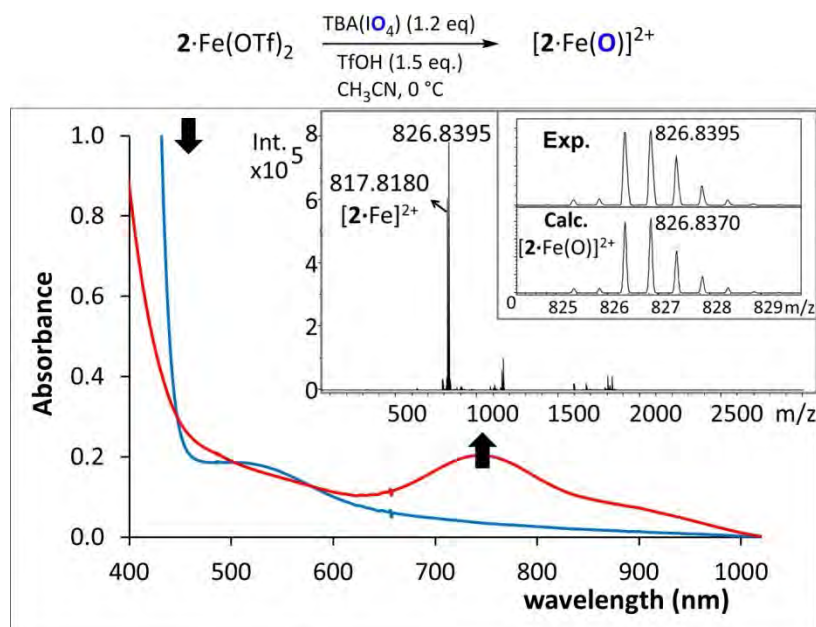


Figure V.3. Formation of an Fe(IV) oxo species $[\text{2}\cdot\text{Fe}(\text{O})]^{2+}$. Evolution of the UV-vis spectra upon treatment of $2\cdot\text{Fe}(\text{OTf})_2$ with TBAIO_4 at 0°C in CH_3CN . Inset: ESI-MS spectrum of the same reaction mixture.

formation of high valent iron-oxo species. As explained in previous chapters, iron(IV)-oxo species are of relevant importance in non-heme iron oxygenases.¹⁹⁷ Non-heme iron(IV)-oxo complexes are appropriate models of these enzymes, which are highly reactive species that readily engage in C–H oxidation and oxygen transfer reactions.¹⁹⁸⁻¹⁹⁹ They are more stable than iron(V)-oxo species, which are involved in the catalytic oxidation of C–H and C=C bonds with $\text{H}_2\text{O}_2/\text{AcOH}$ ^{67, 133} and because of that they have been prepared and studied extensively with bioinspired iron complexes.^{62, 164} Nevertheless, the high reactivity nature of iron(IV)-oxo complexes is usually non compatible with elaborated supramolecular scaffolds,¹³⁴ which would provide a chemically richer and closer model to enzymatic active sites. Reaction of $\mathbf{2}\cdot\text{Fe}(\text{OTf})_2$ with tetra(n-butyl)ammonium periodate (TBAIO_4 , 1.2 equiv, TfOH 1.5 equiv) was monitored by UV-vis, revealing that the ferrous complex is smoothly converted to a new species $[\mathbf{2}\cdot\text{Fe}(\text{O})]^{2+}$ that exhibits a characteristic low energy band ($\lambda = 747 \text{ nm}$, $\epsilon = 210 \text{ M}^{-1} \text{ cm}^{-1}$) of a low spin ($S = 1$) iron(IV) oxo species (Figure V.3), assigned by comparison with related species reported in literature.¹⁹⁹ Indeed, High resolution ESI-MS analysis of the complex (inset figure V.3) shows cluster ions at m/z 826.8238 and 1828.5134, consistent with $[\mathbf{2}\cdot\text{Fe}^{\text{IV}}(\text{O})]^{2+}$ and $[\mathbf{2}\cdot\text{Fe}^{\text{IV}}(\text{O})(\text{IO}_3)]^+$ cations, respectively. The spectrum also shows a peak at $m/z = 817.8180$ corresponding to an oxidative degradation entailing a formal desaturation reaction ($[\mathbf{2}\cdot\text{Fe}^{\text{II}}-2\text{H}]^{2+}$). Remarkably, the new compound $[\mathbf{2}\cdot\text{Fe}(\text{O})]^{2+}$ remains relatively stable at $0 \text{ }^\circ\text{C}$ ($t_{1/2} \sim 20 \text{ min}$). Peaks corresponding to analogous species are observed when $\mathbf{7b}\cdot\text{Fe}(\text{OTf})_2$ is reacted with TBAIO_4 under analogous reaction conditions, suggesting that formation of these species does not occur via oxidation of the cavitand. Interestingly, when the species is generated with the simple complex, the intensity of the characteristic low energy UV-Vis feature of $[\mathbf{7b}\cdot\text{Fe}^{\text{IV}}(\text{O})]^{2+}$ is lower than the one observed for $[\mathbf{2}\cdot\text{Fe}^{\text{IV}}(\text{O})]^{2+}$, meaning that the iron(IV)-oxo species $[\mathbf{7b}\cdot\text{Fe}^{\text{IV}}(\text{O})]^{2+}$ is being formed in lower yield compared to $[\mathbf{2}\cdot\text{Fe}^{\text{IV}}(\text{O})]^{2+}$ (figure V.4). Moreover, $[\mathbf{7b}\cdot\text{Fe}^{\text{IV}}(\text{O})]^{2+}$ has a shorter half-life time than $[\mathbf{2}\cdot\text{Fe}^{\text{IV}}(\text{O})]^{2+}$, being $t_{1/2} \sim 8 \text{ min}$.

V.1.2.2. Reactivity of high-valent iron(IV)-oxo species in oxygen atom transfer to sulfides in a cavitand platform.

To prove the reaction ability of ($[\mathbf{2}\cdot\text{Fe}^{\text{IV}}(\text{O})]^{2+}$), it was studied the reaction towards a prototypical substrate such as thioanisole in oxygen atom transfer reaction. The reactivity of iron(IV)-oxo intermediates in simple model complexes has been well studied, but in complex supramolecular structures the reaction of such iron(IV)-oxo with an external substrate may not be compatible, competing for instance with the degradation of the cavitand.

Reactivity of metallocavitands

However in this case, meanwhile the intermediate species $[2\cdot\text{Fe}^{\text{IV}}(\text{O})]^{2+}$ is relatively stable at 0 °C, it reacts with excess of thioanisole within seconds (figure V.5). Just after the total generation of $[2\cdot\text{Fe}^{\text{IV}}(\text{O})]^{2+}$ with $\text{TBAIO}_4/\text{TfOH}$ following the reaction by UV-Vis, 100 equivalents of the substrate are added to the reaction mixture, resulting in a rapid decay of the band at 747 nm corresponding to the

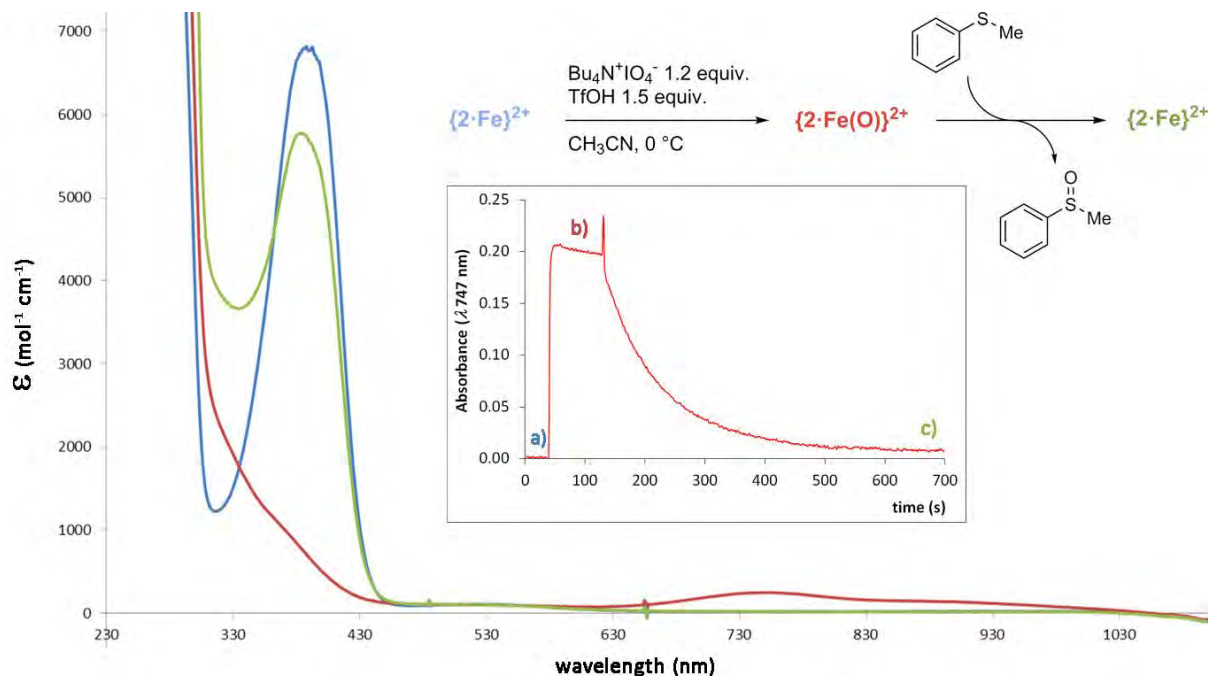


Figure V.4. Evolution of the UV-Vis spectra of $2\cdot\text{Fe}(\text{OTf})_2$ (1 mM, CH_3CN): a) blue, start; b) red, after addition of TBAIO_4 ; c) green: after addition of thioanisole. Inset: evolution of the Fe(IV) oxo band at $\lambda=747$ nm.

iron(IV)-oxo species following an exponential decay. The disappearing of the band corresponds to the recovery of the initial iron(II) complex and analysis of the products from the reaction media revealed the presence of 0.9 equivalent of sulfoxide as product. All these features together, imply the clean reaction of an iron(IV)-oxo species with a sulfide, where an oxygen atom is transferred from the metal to the substrate to form the sulfoxide as product. Overall, this data indicates that the embedment of the complex in the cavitand stands the formation of high valent iron-oxo species without apparent degradation of the supramolecular vessel,¹³⁴ while not compromising its reactivity in oxygen atom transfer reactions against external substrates. Reactivity studies were also carried out with C-C and C=C substrates such as *cis*-1,2-dimethylcyclohexane, *cis*- β -methylstyrene respectively, and also substrates that bind to the cavity such as 8c and 10. However, following the reaction by UV-vis no acceleration of the decay of the band corresponding to the high-valent Fe(IV)=O intermediate was observed upon the addition of a high amount of substrate (100 eq). Moreover, analysis of the reaction mixture revealed no presence of products. These results a priori

would indicate that the Fe(IV)=O intermediate does not react with these kind of substrates, at least the ones tried

V.2. Concluding remarks.

In this chapter, the oxidizing ability of Fe(II) and Mn(II) metallocavitands described in chapter IV have been evaluated, using them for bioinspired C-H and C=C oxidation reactions. Remarkably, low catalytic loadings (1-3%) of the complexes $2\cdot\text{Fe}(\text{OTf})_2$ and $2\cdot\text{Mn}(\text{OTf})_2$ could be used to perform the catalytic hydroxylation of challenging substrates.

The activity of the metallocavitands $2\cdot\text{Fe}(\text{OTf})_2$ and $2\cdot\text{Mn}(\text{OTf})_2$ complexes as catalysts is maintained along the reaction in the same manner than the simple parent complex, thus, the supramolecular complex is not deactivated. In the same way, the cavitand structure is maintained, so the active species react exclusively with the substrate and does not degrade the supramolecular scaffold.

The metallocavitand $2\cdot\text{Fe}(\text{OTf})_2$ is able to support high-valent iron(IV)-oxo species and the formation of these species does not occur via oxidation of the cavitand. Moreover, the intermediate is able to react with thioanisole as substrate, producing the stoichiometric amount of sulfoxide as product.

However, the selectivities obtained in the oxidation reactions so far tested with substrates that form kinetically stable complexes with the receptor do not significantly differ from those obtained with a model compound, suggesting that the oxidation steps are occurring outside the cavity. Future developments in this area will address the limitations of the system presented, including the development of conformationally restricted analogues, which prevented free rotation of the ligand scaffold.

CHAPTER VI

GENERAL CONCLUSIONS

In **chapter III** two new binuclear ferrous complexes (**1**, **2**) bearing aminopyridine triazacyclonane-based ligands have been synthesized and characterized. **2** is based in a previously described bis-pentadentate ligand, while **1** was prepared with a new bis-tetradentate dinucleating ligand (**EBPytacn**). Using diferrous complexes **1** and **2**, two novel diiron(IV)-oxo species(**1^{IV}=O**, **2^{IV}=O**) have been generated and characterized by means of UV-vis and HRMS. **1^{IV}=O**, **2^{IV}=O** oxidize thioanisoles (OAT reactivity) and abstract weak C-H bonds, such as the ones of cyclohexadiene (CHD), dihydroanthracene (DHA) triphenylmethane or cumene, given the corresponding desaturated or oxygenated products.

In **chapter IV**, an organic-inorganic hybrid supramolecular platform, specifically a cavitand having a bioinspired iron or manganese complex anchored in the upper rim (**2·M(OTf)₂** (M = Fe(II), Mn(II)) have been prepared. In these complexes, a reactive unit has been combined with a supramolecular recognition one in order to have a proper metalloenzyme model. The dynamic behavior regarding the structure of the cavitand (for instance vase/kite conformations) as well as the recognition properties of the prepared metallocavitand complexes have been studied through NMR spectroscopy. Moreover, the crystal structure of one of these metallocavitand complexes (**2·Fe₂Cl₄O**) has been obtained, providing information about its structure in the solid state, confirming the vase conformation suggested by NMR spectroscopy.

Host-guest studies show that these metallocavitands, as well as the simple cavitand are capable to recognize guest molecules. However, the number of possible guest molecules are reduced in our metallocavitands **2·M(OTf)₂** with respect to the simple cavitand, probably because of steric hindrance or repulsion effects provoked by the charged metal, located close to the entrance of the guest molecule inside of the cavitand.

In **chapter V**, the reactivity of the metallocavitands **2·M(OTf)₂** has been studied. On one side, catalytic studies were performed using these supramolecular metal complexes as catalysts in alkane and alkene oxidation reactions. In one hand, prototypic substrates such as simple alkanes and alkenes have been used. On the other hand, molecules that have host-guest properties with the cavitand have been used as substrates. The results obtained indicate that the metallocavitand complexes **2·M(OTf)₂** are active for C-H and C=C bond oxidation, maintaining the same activity as the simple complex without cavitand. This indicates that the metallocavitands are robust enough to stand the reaction conditions and the cavitand structure is not degraded during the reaction, with has been also observed by following the catalytic reaction by HRMS. However, the selectivity pattern for these oxidations using **2·M(OTf)₂** are found to be essentially the same as the one observed for

General conclusions

the simpler complexes **7b**·M(OTf)₂ that do not contain the cavitand, which could suggest that the catalytic oxidation reactions are occurring with substrate molecules placed outside of the cavitand, so intramolecular reactions cannot take place due to a large bending of the attached complex outside the cavity due to free rotation of the linkage to the cavitand.

Moreover, it has been possible to generate and characterize an iron(IV)-oxo species using the metallocavitand **2**·Fe(OTf)₂ as platform. The reaction of the iron(II) complex with a strong oxidant such as tetra(n-butyl)ammonium periodate (TBAIO₄) leads to the formation of a metastable intermediate characterized as an iron(IV)-oxo species. Remarkably, the cavitand scaffold remains intact in all the course of the reaction and does not decompose due to secondary reactions with the strong oxidant, or with the high-valent iron(IV)-oxo species itself intramolecularly. Interestingly, the metastable iron(IV)-oxo species generated with the cavitand have been observed by means of UV-Vis spectroscopy techniques to be approximately two times more stable than the one generated with the simple complex under the same conditions, maybe due to protection of the oxo group by the cavitand structure. Maybe the oxo group is placed inside of the cavitand, or could be interacting with the upper rim of the cavitand, slowing down its decay rate. In addition, the iron(IV)-oxo species react with external sulfides via a OAT reaction, following it by UV-Vis spectroscopy, generating sulfoxide as products in a high yield confirmed by GC analysis. To the best of our knowledge, this is one of the first examples of an iron(IV)-oxo group generated in high yield in a cavitand, and which remains able to react with external substrates without being degraded during this process.

CHAPTER VII

EXPERIMENTAL SECTION

VII.1. Experimental section chapter III.

VII.1.1. Materials and methods.

All reagents were purchased from Sigma-Aldrich, TCI Europe or Fluorochem and were used as received. Solvents were purchased from SDS and Scharlab and were purified and dried by passing through an activated alumina purification system (M-Braun SPS-800). Anhydrous Acetonitrile was purchased from Sigma-Aldrich and used without further purification and stored strictly under N₂. Substrates were filtered in basic alumina before doing oxidation reactions. Solvents were purchased from SDS and Scharlab, purified and dried by passing through an activated alumina purification system (MBraun SPS – 800) and stored in an anaerobic glovebox under N₂. Tri-Ts-diethylenetriamine and tetrabutylammonium periodate (N₄BuIO₄) were purchased from Sigma-Aldrich and used without further purification. Fe^{II}(CF₃SO₃)₂(CH₃CN)₂ and Zn^{II}(CF₃SO₃)₂(CH₃CN)₂ were prepared according to a literature procedure from FeCl₂ and ZnCl₂ respectively.²⁰⁰ Iodosylbenzene (PhIO) was synthesized according to reported procedures.²⁰¹ Compounds **Ts₃tacn**,²⁰² **Tstacn**,¹⁴⁴ **Pytacn**,^{141, 143} **MePy₂tacn**,^{56, 203} **Py₄btacn**,¹⁴⁶ [Fe^{II}(**MePy₂tacn**)(CF₃SO₃)],⁵⁶ [Fe^{II}(**Pytacn**)(CF₃SO₃)₂]^{42, 141, 143} were prepared as previously described. High-valent iron(IV)-oxo compounds [Fe^{IV}(O)(**MePy₂tacn**)],^{56, 58} [Fe^{IV}(O)(**Pytacn**)(S)]^{42, 58, 141} were generated accordingly to reported procedures.

High resolution mass spectra (HRMS) were recorded on a Bruker MicroTOF-Q IITM instrument using ESI or Cryospray ionization sources at Serveis Tècnics of the University of Girona. Samples were introduced into the mass spectrometer ion source by direct infusion using a syringe pump and were externally calibrated using sodium formate. A cryospray attachment was used for CSI-MS (cryospray mass spectrometry). The temperature of the nebulizing and drying gases was set at -40 °C. The instrument was operated in positive ion mode. UV-vis spectroscopy was performed with an Agilent 50 Scan (Varian) UV-vis spectrophotometer with 1 cm quartz cells. Low temperature control was achieved with a cryostat from Unisoku Scientific Instruments, Japan. GC product analyses were performed on an Agilent 7820A gas chromatograph equipped with an HP-5 capillary column 30m × 0.32 mm × 0.25 μm and a flame ionization detector. Oxidation products were identified by comparison of their GC retention times and GC/MS with those of authentic compounds and/or by 1H NMR analyses. GC analyses were carried out on a gas chromatograph equipped with a capillary methylsilicone column (30 m x 0.25 mm x 25 μm) Chrompack CP-Sil 5 CB. GC-MS analyses were performed with a mass detector (EI at 70 eV) coupled with a gas chromatograph equipped with a melted silica capillary column (30 m x 0.2 mm x 25 μm) covered with a methylsilicone film (5% phenylsilicone, OV5). NMR spectra were recorded on a Bruker DPX400 spectrometer, and were

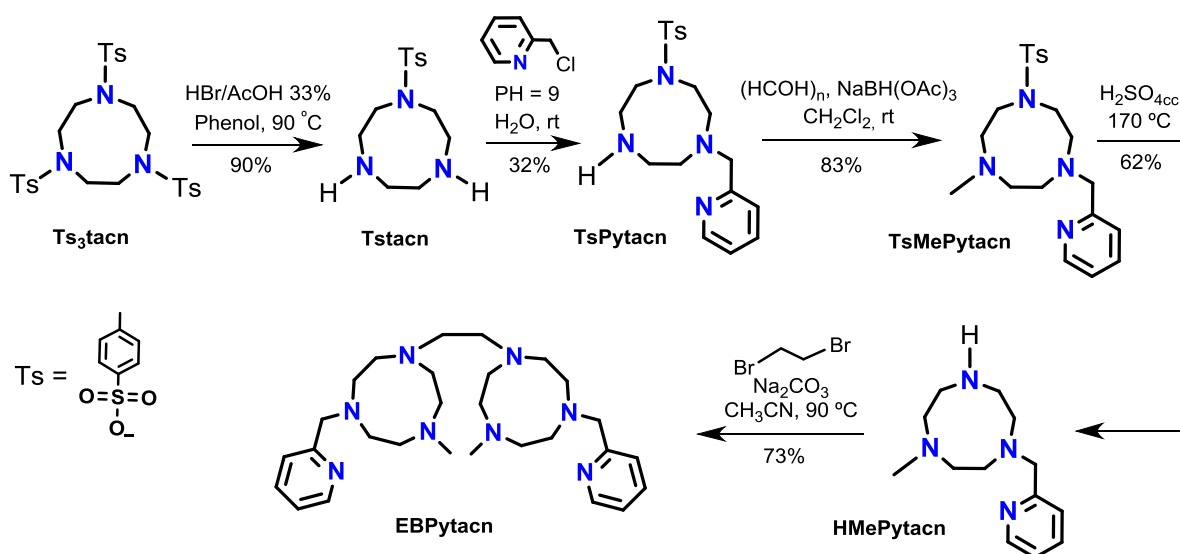
Experimental section

internally referenced to tetramethylsilane or, alternatively, to the residual proton solvent signal. X-Ray structure determination was carried out on a *BRUKER SMART APEX CCD* diffractometer using graphite-monochromated Mo $K\alpha$ radiation ($\alpha = 0.71073 \text{ \AA}$) from an x-Ray Tube. Elemental analyses were performed using a CHNS-O EA-1108 elemental analyzer from Fisons. Electrospray ionization mass spectrometry (ESI-MS) experiments were performed on a Bruker Daltonics Esquire 3000 Spectrometer using solutions $>1 \text{ mM}$ of the analyzed compound. High resolution mass spectra (HRMS) were recorded on a Bruker MicroTOF-Q IITM instrument with an ESI source. Samples were introduced into the mass spectrometer ion source by direct infusion through a syringe pump and were externally calibrated using sodium formate.

VII.1.2. Experimental protocols.

VII.1.2.1. Synthesis of ligands.

Tstacn¹⁴⁴ and ligand **Py₄btacn**¹⁴⁶ was synthesized according to the reported procedure. Ligand **EBPytacn** was synthesized following scheme VII.1:



Scheme VII.1. Schematic synthesis of the EBPytacn ligand.

TsPytacn. **Tstacn** (10g, 22.5 mmol) was mixed with 1.1 equivalents of 2-Picolyl chloride hydrochloride. 300 mL of water are added until complete dissolution. Then, the pH is adjusted to 9 with NaOH 2M. The resulting red solution was stirred for 3 days at room temperature. After this time, NaOH is added to pH 13 to quench the reaction, and the solution is extracted with CH_2Cl_2 several times. The combined organic layers were dried over anhydrous Na_2SO_4 , filtered, and the solvent was removed under reduced pressure. The crude was purified with silica gel column

chromatography (CH₂Cl₂:MeOH:NH₄⁺ 90:10:3). The product **TsPytacn** is obtained (2.6g, 32%) as a slightly orange oil. ¹H NMR (400 MHz, CDCl₃): δ 8.78 (m, 1H, pyH_α), 7.77 – 7.62 (m, 3H, 2ArH + pyH_γ), 7.40 – 7.31 (m, 2H, ArH), 7.28 – 7.27 (m, 1H, pyH_β), 7.16 (m, 1H, pyH_β), 4.08 (s, 2H, py-CH₂), 3.65 (m, 8H, N-CH₂-CH₂), 3.15 (t, *J* = 4.4 Hz, 2H, N-CH₂-CH₂), 2.95 (t, *J* = 5.8 Hz, 2H, N-CH₂-CH₂), 2.45 (s, 3H, Ar-CH₃). ¹³C NMR (101 MHz, CDCl₃): δ 157.49 (pyC_q), 149.29 (pyC_α), 144.27 (arC-CH₃), 137.79 (pyC_v), 134.44 (arC-SO₂), 130.02 (2H, arC-H), 127.29 (2H, arC-H), 123.13, 122.27 (pyC_β), 58.70 (py-CH₂-N), 58.27, 52.86, 51.67, 50.99, 49.77, 47.28 (N-CH₂-CH₂), 21.54 (Ar-CH₃). HRMS (ESI-TOF) *m/z* calcd. for C₁₉H₂₆N₄O₂S ([M+H]⁺): 375.1849; found: 375.1847.

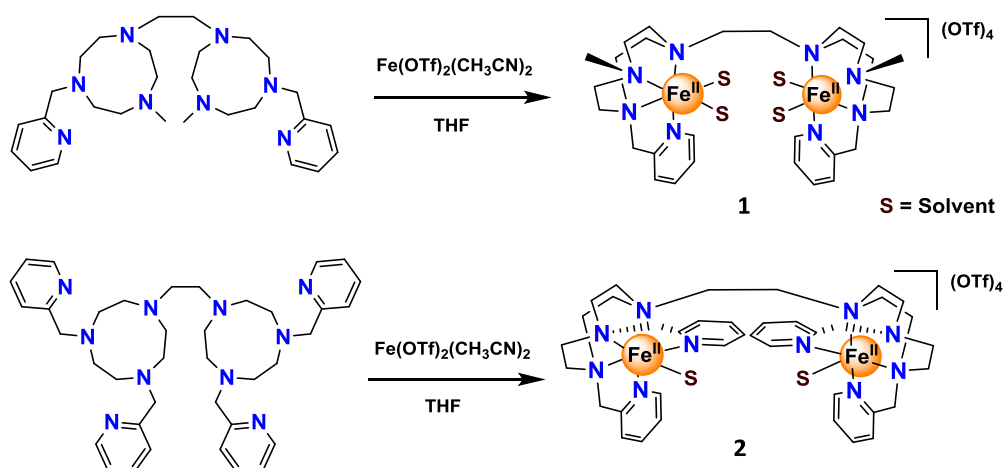
TsMePytacn. **TsPytacn** (2.5g, 6.7 mmol) and a high excess of paraformaldehyde (40 eq) were dissolved in CH₂Cl₂ (150 mL). Then, the solution was cooled at 0 °C and NaBH(OAc)₃ (8 eq) were added slowly. The solution was stirred overnight at room temperature under N₂ atmosphere. After this time, the reaction was quenched with NaOH 2M to pH 14 and extracted with CH₂Cl₂. The crude was purified with silica gel column chromatography (CH₂Cl₂:MeOH:NH₄⁺ 95:5:2). The product is obtained (2.16g, 83%) as slightly yellow oil. ¹H NMR (400 MHz, CDCl₃): δ 8.53 – 8.43 (m, 1H, pyH_α), 7.74 – 7.53 (m, 3H, 2ArH + pyH_γ), 7.45 (d, *J* = 7.8 Hz, 1H, pyH_β), 7.28 – 7.23 (m, 2H, ArH), 7.11 (m, 1H, pyH_β), 3.86 (s, 2H, py-CH₂), 3.25 (dt, *J* = 6.8, 2.0 Hz, 2H, N-CH₂-CH₂), 3.17 (dt, *J* = 6.7, 1.9 Hz, 2H, N-CH₂-CH₂), 3.03 (dt, *J* = 6.7, 1.9 Hz, 2H, N-CH₂-CH₂), 2.99 (dt, *J* = 6.8, 2.0 Hz, 2H, N-CH₂-CH₂), 2.79 (dt, *J* = 7.0, 2.0 Hz, 2H, N-CH₂-CH₂), 2.71 – 2.66 (m, 2H, N-CH₂-CH₂), 2.37 (m, 6H, Ar-CH₃ + N-CH₃). ¹³C NMR (101 MHz, CDCl₃): δ 159.92 (pyC_q), 148.97 (pyC_α), 142.99 (arC-CH₃), 136.39 (pyC_v), 135.96 (arC-SO₂), 129.60 (2H, arC-H), 127.09 (2H, arC-H), 123.30, 121.92 (pyC_β), 64.03 (py-CH₂-N), 57.09, 57.02, 55.83, 55.50, 50.92, 50.25 (N-CH₂-CH₂), 45.63 (N-CH₃), 21.46 (Ar-CH₃). HRMS (ESI-TOF) *m/z* calcd. for C₂₀H₂₈N₄O₂S ([M+H]⁺): 389.2006; found: 389.2020.

HMePytacn. In a 100 mL round bottom flask **HMePytacn** (2g, 5.14 mmol) were added 24.4 mL of H₂SO₄. A sand bath is pre-heated at 175 °C and when is exactly at 175 °C the mixture is refluxed exactly with 160-170 °C for exactly 40mins. After this time, the reaction mixture was allowed to cool down to room temperature and cooled afterwards at 0 °C. Then, 40 mL of cold EtOH were added carefully to quench the reaction. When the mixture is totally quenched, 150 mL of cold Et₂O was added dropwise with stirring to precipitate the product as a grey/brown pasty oil and the solution was left overnight in the freezer. Next day, the precipitate is filtered. Then, the solid is basified at pH 14 with NaOH 2M and extracted with CH₂Cl₂. The organic layers were combined and dried over Na₂SO₄ anhydrous. Then, the solvent is removed under vacuum to obtain **HMePytacn** (746 mg, 67%) as transparent colorless oil. ¹H NMR (400 MHz, CDCl₃): δ 8.59 – 8.48 (m, 1H, pyH_α), 7.69 – 7.62 (m, 1H, pyH_γ), 7.54 – 7.42 (m, 1H, pyH_β), 7.21 – 7.11 (m, 1H, pyH_β), 3.98 – 3.89 (m, 2H, py-CH₂), 2.92 –

Experimental section

2.61 (m, 10H, N-CH₂-CH₂), 2.50 – 2.42 (m, 2H, N-CH₂-CH₂), 2.38 (s, 3H, N-CH₃). ¹³C NMR (101 MHz, CDCl₃): δ 159.71 (pyC_q), 149.07 (pyC_α), 136.61 (pyC_γ), 122.90, 122.17 (pyC_β), 62.29 (py-CH₂-N), 53.97, 52.71, 52.53, 50.45, 45.95, 45.73 (N-CH₂-CH₂), 44.64 (N-CH₃). HRMS (ESI-TOF) m/z calcd. for C₁₃H₂₂N₄ ([M+H]⁺): 235.1917; found: 235.1927.

EBPyTacn. Under a N₂ atmosphere, 2 equivalents of **HMePytacn** (1g, 4.3 mmol) were placed in a 100 mL round bottom flask and 50 mL of anhydrous CH₃CN were added. In parallel, a solution of 1,2-dibromoethane (1.2 eq) in anhydrous CH₃CN was prepared and added to the reaction mixture. The reaction is refluxed overnight. After that time, solvent was evaporated under vacuum and the product was basified with NaOH 2M until pH 14, extracted with CH₂Cl₂ and the combined organic phases dried over anhydrous Na₂SO₄. Solvents were removed under reduced pressure and the crude is purified by silica gel column (80:15:5 CH₂Cl₂:MeOH:NH₄⁺) to obtain the final ligand **EBPytacn** (771 mg, 73%). ¹H NMR (400 MHz, CDCl₃): δ 8.51 (m, 2H, pyH_α), 7.65 (td, *J* = 7.6, 1.8 Hz, 2H, pyH_γ), 7.50 (d, *J* = 7.9 Hz, 2H, pyH_β), 7.14 (m, 2H, pyH_β), 3.83 (s, 4H, py-CH₂), 2.90 – 2.70 (m, 20H, N-CH₂-CH₂), 2.65 (m, 4H, N-CH₂-CH₂), 2.61 (s, 4H, N-CH₂), 2.36 (s, 6H, N-CH₃). ¹³C NMR (101 MHz, CDCl₃): δ 160.45 (pyC_q), 148.82 (pyC_α), 136.20 (pyC_γ), 123.23, 121.75 (pyC_β), 64.90 (py-CH₂-N), 57.64, 56.91, 56.56, 56.45, 56.36, 55.81 (N-CH₂-CH₂), 46.33 (N-CH₃), 29.66 (Ar-CH₃). HRMS (ESI-TOF) m/z calcd. for C₂₈H₄₆N₈ ([M/2+H]⁺): 248.1995; found: 248.2001.



Scheme VII.2. Schematic synthesis of diiron(II) **1** and **2** complexes.

VII.1.2.2. Synthesis of complexes.

[Fe^{II}₂(Py₄bPytacn)(CH₃CN)₂](CF₃SO₃)₄, **2.** Synthesis of this complex was carried under anaerobic atmosphere. 100 mg of **Py₄bPytacn** (0.15 mmol) were dissolved in the minimum quantity of anhydrous THF and put under stirring. Then, 131 mg of Fe(CF₃SO₃)₂(CH₃CN)₂ (0.30 mmol, 2 eq.) were solved in minimum quantity of THF and added dropwise to the vial containing the stirring ligand solution. After 3h stirring, a precipitate corresponding to the iron complex was formed. At this point, stirring was stopped and the solid filtrated and dried under vacuum. Once dried, solid was solved in CH₃CN, filtered over celite and recrystallized from CH₃CN/Et₂O by slow diffusion to obtain the pure compound as dark red crystals suitable for x-ray diffraction in 73% yield (0.11 mmol, 157 mg). ¹H NMR (400 MHz, CD₃CN) δ, ppm: 9.00 (d, 1H PyH), 8.79 (d, 1H PyH), 7.98 (t, 1H PyH), 7.88 (t, 1H PyH), 7.80 – 7.71 (m, 2H PyH), 7.66 – 7.57 (m, 1H PyH), 7.59 – 7.51 (m, 2H PyH), 7.44 (d, 2H PyH), 7.38 (t, 1H PyH), 7.13 – 7.04 (m, 3H PyH), 6.94 (d, 1H PyH), 4.67 – 4.45 (m, 5H CH₂ – Py), 4.15 – 4.08 (m, 1H CH₂ – Py), 4.05 – 3.92 (m, 2H CH₂ – Py), 3.30 – 3.04 (m, 10 H N – CH₂), 3.02 – 2.78 (m, 4 H N – CH₂), 2.76 – 2.22 (m, 14 H N – CH₂). HRMS (ESI-TOF) m/z calcd. for C₄₁H₅₂F₉Fe₂N₁₀O₉S₃ ([M-OTf]⁺): 1207.1632; found: 1207.1614. EA calc. for C₄₆H₅₈F₁₂Fe₂N₁₂O₁₂S₄·(2 CH₃CN): C 39.48; H 4.24; N 12.89; found: C 39.51; H 3.95; N 12.98.

[Fe^{II}₂(EBPytacn)(CH₃CN)₄](CF₃SO₃)₄, **1.** Synthesis of this complex was carried with the same procedure as **2**. It was recrystallized from CH₂Cl₂:CH₃CN/Et₂O by slow diffusion to obtain the pure compound as yellow crystals suitable for x-ray diffraction in 67% yield (0.10 mmol, 157 mg). ¹H NMR (CD₂Cl₂, 400 MHz, 298 K) δ, ppm: 142.39, 121.91, 96.94, 51.13, 50.79, 36.29, 29.55, 13.38. HRMS (ESI-TOF) m/z calcd. for C₃₁H₄₆F₉Fe₂N₈O₉S₃ ([M-OTf]⁺): 1053.1101; found: 1053.1101. EA calc. for C₃₂H₄₆F₁₂Fe₂N₈O₁₂S₄·(CH₂Cl₂): C 30.78; H 3.76; N 8.70; found: C 30.57; H 3.84; N 8.45.

[Zn^{II}₂(Py₄bPytacn)(CF₃SO₃)₂](CF₃SO₃)₂, **2-Zn.** Synthesis of this complex was carried with the same procedure as **2** but using Zn(CF₃SO₃)₂ as salt. It was recrystallized from CH₃CN/Et₂O by slow diffusion to obtain the pure compound as white crystals corresponding to the bis-triflate complex suitable for x-ray diffraction in 82% yield (0.12 mmol, 179 mg). HRMS (ESI-TOF) m/z calcd. for C₄₁H₅₂F₉Zn₂N₁₀O₉S₃ ([M-OTf]⁺): 1227.1472; found: 1227.1456.

[Fe^{II}₂(Py₄bPytacn)(CH₃CN)₂](SbF₆)₄, **2-SbF₆.** Synthesis of this complex was carried under anaerobic atmosphere. 100 mg of **Py₄bPytacn** (0.15 mmol) were dissolved in the minimum quantity of CH₃CN and put under stirring. Then, 38 mg of FeCl₂ (0.30 mmol, 2 eq.) were solved in 0.2 mL of CH₃CN and added dropwise to the vial containing the stirring ligand solution. After 3h stirring, the

Experimental section

corresponding chloride complex has been formed. At this point, 206 mg AgSbF_6 (0.6 mmol, 4 eq) were added in the minimum quantity of CH_3CN to the stirring chloride complex solution and the vial covered with aluminum foil to protect from light. After stirring overnight, a white solid corresponding to AgCl was formed. The solution was then filtered over celite and dried under vacuum. The resulting solid was recrystallized from $\text{CH}_3\text{CN}/\text{Et}_2\text{O}$ by slow diffusion to obtain the pure compound as dark red crystals suitable for x-ray diffraction in 65% yield (0.09 mmol, 174 mg). HRMS (ESI-TOF) m/z calcd. for $\text{C}_{38}\text{H}_{52}\text{F}_{12}\text{Fe}_2\text{N}_{12}\text{Sb}_2$ ($[\text{M}/2\text{-2OTf}]^+$): 630.0511; found: 630.0482.

NMR (CD_3CN , 400 MHz, 273 K) δ , ppm: 8.90 (d, 1H, PyH), 7.94 - 7.18 (m, 7H, PyH), 4.72 (d, 1H, CH2 - Py), 4.56 (m, 2H, CH2 - Py), 4.06 (d, 1H, CH2 - Py), 3.38 - 2.94 (m, 9H, N - CH2), 2.59 - 2.56 (m, 4H, N - CH2 and N - CH3), 1.60 (m, 1H, N - CH2).

VII.1.2.3. General procedure for the generation and reactivity of the Fe(IV)-oxo species.

VII.1.2.3.1. Generation of the Fe(IV)-oxo intermediates.

In a glovebox under anaerobic atmosphere, 1 or 0.5 mM solution of the diiron(II) complex **1** or **2** in anhydrous acetonitrile (2 mL) were placed in a UV-vis quartz cuvette and sealed with a septum. Then, the cuvette was taken out from the glovebox and introduced in a UV-vis spectrometer thermostated to the desired temperature, and all the spectra were recorded with a cycle time of 1 s. When the solution in the cuvette reaches the desired temperature, the oxidant (2.2 eq, 1.1 eq for each iron atom) is added directly to the cuvette in anhydrous acetonitrile solution using a Hamilton syringe, and the formation of the characteristic band at approx. 750 nm was followed until it reached its maximum absorbance.

VII.1.2.3.2. Reactivity studies of the Fe(IV)-oxo intermediates towards OAT/HAT.

The oxidation capacity of complex $\mathbf{2}^{\text{IV}}=\text{O}$ has been studied with typically substrates that gives OAT (Oxygen Atom Transfer) and HAT (Hydrogen Atom Transfer) reactions. In all reactions done with complex $\mathbf{2}^{\text{IV}}=\text{O}$, the intermediate species were prepared as described above. The OAT and HAT reactions had been studied by following the decay of the Fe(IV)-oxo species band at approx. $\lambda = 750$ nm, assuming that the disappearing of complex and $\mathbf{2}^{\text{IV}}=\text{O}$ is due to the oxidation of the substrate. Then, an internal standard was added and the solution was rapidly filtered through a silica and alumina plug to remove the catalyst. The solution was then analyzed by GC. Substrate and product

were identified by comparison of the retention time with commercially available samples and quantified by internal standardization. The points obtained by UV-vis spectroscopy were adjusted to a first order exponential decay regression to obtain the k_{obs} values. The plot of k_{obs} vs. substrate concentration gives k_2 values as the slope of the linear regression fits, which is the rate constant of oxidation. On HAT reactivity k_2 values were divided by the number of equivalent hydrogen atoms that can react, to obtain the k_2' .

VII.1.3. X-ray diffraction data.

The measurements were carried out on a BRUKER SMART APEX CCD diffractometer using graphite-monochromated Mo K α radiation ($\lambda = 0.71073 \text{ \AA}$) from an X-ray tube. Programs used: data

Table III.3. Crystal data for **2** and **2**-Zn binuclear complexes.

	$[\text{Fe}^{\text{II}}_2(\text{Py}_4\text{bPytacn})(\text{CH}_3\text{CN})_2](\text{CF}_3\text{SO}_3)_4$	$[\text{Zn}^{\text{II}}_2(\text{Py}_4\text{bPytacn})(\text{CF}_3\text{SO}_3)_2](\text{CF}_3\text{SO}_3)_2$
Empirical formula	$\text{C}_{46}\text{H}_{58}\text{F}_{12}\text{Fe}_2\text{N}_{12}\text{O}_{12}\text{S}_4$	$\text{C}_{42}\text{H}_{52}\text{F}_{12}\text{Zn}_2\text{N}_{12}\text{O}_{12}\text{S}_4$
Molar weight	1438.95 g/mol	1375.92 g/mol
Temperature	130(2) K	130(2) K
Wavelength	0.71073 \AA	0.71073 \AA
Crystal system	Triclinic	Triclinic
space group	$P\bar{1}$	$P\bar{1}$
Unit cell dimensions	$a = 14.197(6) \text{ \AA}$ $\alpha = 70.219(8)^\circ$. $b = 15.286(7) \text{ \AA}$ $\beta = 66.764(7)^\circ$. $c = 17.716(8) \text{ \AA}$ $\gamma = 64.003(8)^\circ$.	$a = 8.8491(16) \text{ \AA}$ $\alpha = 110.207(3)^\circ$. $b = 13.054(2) \text{ \AA}$ $\beta = 100.157(3)^\circ$. $c = 14.218(3) \text{ \AA}$ $\gamma = 93.208(4)^\circ$.
Volume	$3111(2) \text{ \AA}^3$	$1505.0(5) \text{ \AA}^3$
Z	2	1
Calculated density	1.580 Mg/m^3	1.609 Mg/m^3
Absorption coefficient	0.705 mm^{-1}	1.040 mm^{-1}
F(000)	1520	746
Reflections collected	19132	23980
Independent reflections	13624 [R(int) = 0.0773]	7333 [R(int) = 0.0608]
Final R indices	$R1 = 0.1052$, $wR2 = 0.2514$	$R1 = 0.0417$, $wR2 = 0.1032$
[I > 2σ(I)]		
R indices (all data)	$R1 = 0.1939$, $wR2 = 0.3114$	$R1 = 0.0503$, $wR2 = 0.1087$

Experimental section

Table III.4. Crystal data for **2**-SbF₆ and **1** binuclear complexes.

	[Fe^{II}₂(Py₄bPytacn)(CH₃CN)₂](SbF₆)₄	[Fe^{II}₂(EBPytacn)(CH₃CN)₄](CF₃SO₃)₄
Empirical formula	C ₄₂ H ₅₈ F ₂₄ Fe ₂ N ₁₂ Sb ₄	C ₄₀ H ₅₈ F ₁₂ Fe ₂ N ₁₂ O ₁₂ S ₄
Molar weight	1785.70 g/mol	1366.89 g/mol
Temperature	130(2) K	100(2) K
Wavelength	0.71073 Å	0.71073 Å
Crystal system	Monoclinic	Monoclinic
space group	C2/c	C2/c
Unit cell dimensions	a = 26.434(8) Å α = 90°. b = 12.296(4) Å β = 117.329(6)°. c = 22.938(7) Å γ = 90°.	a = 27.433(4) Å α = 90°. b = 16.642(2) Å β = 105.274(2)°. c = 15.084(2) Å γ = 90°.
Volume	6624(3) Å ³	6643.3(16) Å ³
Z	4	4
Calculated density	1.791 Mg/m ³	1.449 Mg/m ³
Absorption coefficient	2.141 mm ⁻¹	0.658 mm ⁻¹
F(000)	3464	2984
Reflections collected	50411	51056
Independent reflections	8255 [R(int) = 0.0657]	8170 [R(int) = 0.0882]
Final R indices [I > 2σ(I)]	R1 = 0.0477, wR2 = 0.1092	R1 = 0.0864, wR2 = 0.2072
R indices (all data)	R1 = 0.0660, wR2 = 0.1162	R1 = 0.1235, wR2 = 0.2285

collection, Smart version 5.631 (Bruker AXS 1997–02); data reduction, Saint + version 6.36A (Bruker AXS 2001); absorption correction, SADABS version 2.10 (Bruker AXS 2001). Structure solution and refinement were done using SHELXTL version 6.14 (Bruker AXS 2000–2003) and SHELXT version

2013_3. The structures were solved by direct methods and refined by full-matrix least-squares methods on F². The non-hydrogen atoms were refined anisotropically. The H atoms were placed in geometrically optimized positions and forced to ride on the atom to which they are attached.

VII.2. Experimental section chapter IV.

VII.2.1. Materials and methods.

All reagents were purchased from Sigma-Aldrich and TCI Europe, and were used as received. Solvents used for crystallizations were purchased from SDS and Scharlab and were purified and dried by passing through an activated alumina purification system (M-Braun SPS-800). Anhydrous DMF and DMA were purchased from Sigma-Aldrich. HPLC-grade acetonitrile (Sigma-Aldrich) was employed for oxidation reactions. Iron (II) bis(trifluoromethanesulfonate) bis(acetonitrile), manganese (II) bis(trifluoromethanesulfonate), and zinc (II) bis(trifluoromethanesulfonate) were prepared according to a literature procedure from Fe(II) chloride.²⁰⁰ Compounds **3**,¹¹³ **7a**,¹⁷³ **7b**·Fe(CH₃CN)₂(SbF₆)₂,⁹⁶ **7b**·Fe(OTf)₂,^{176, 194, 204} **d** and **7b**·Mn(OTf)₂,²⁰⁵ were prepared according to previously reported procedures.

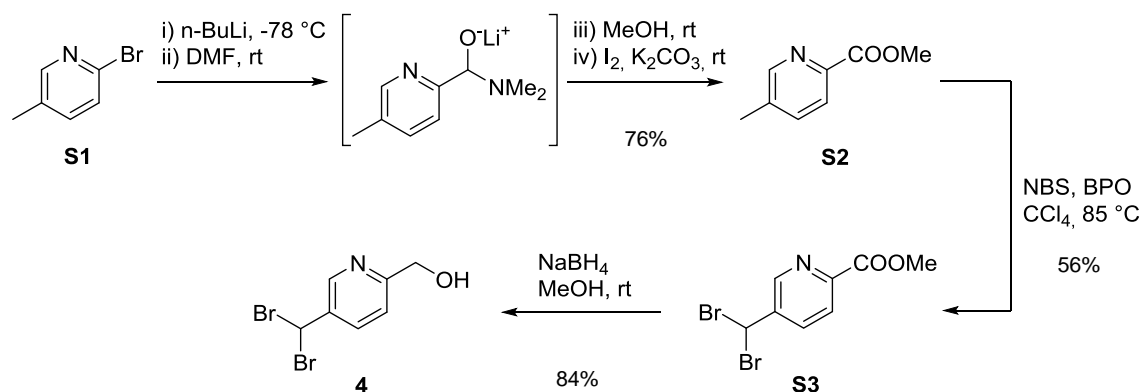
GC analyses were carried out on a gas chromatograph equipped with a capillary methylsilicone column (30 m x 0.25 mm x 25 μm) Chrompack CP-Sil 5 CB. GC-MS analyses were performed with a mass detector (EI at 70 eV) coupled with a gas chromatograph equipped with a melted silica capillary column (30 m x 0.2 mm x 25 μm) covered with a methylsilicone film (5% phenylsilicone, OV5). NMR spectra were recorded on a Bruker DPX400 spectrometer, and were internally referenced to tetramethylsilane or, alternatively, to the residual proton solvent signal. UV-vis spectroscopy was performed on a Cary 50 Scan (Varian) UV-vis spectrophotometer or on an Agilent 8453 diode array spectrophotometer with 1 cm quartz cells. A cryostat from Unisoku Scientific Instruments was used for the temperature control. X-Ray structure determination was carried out on a *BRUKER SMART APEX CCD* diffractometer using graphite-monochromated Mo K α radiation ($\alpha = 0.71073 \text{ \AA}$) from an x-Ray Tube. Elemental analyses were performed using a CHNS-O EA-1108 elemental analyzer from Fisons. Electrospray ionization mass spectrometry (ESI-MS) experiments were performed on a Bruker Daltonics Esquire 3000 Spectrometer using solutions >1 mM of the analyzed compound. High resolution mass spectra (HRMS) were recorded on a Bruker MicroTOF-Q IITM instrument with an ESI source. Samples were introduced into the mass spectrometer ion source by direct infusion through a syringe pump and were externally calibrated using sodium formate.

VII.2.2. Experimental protocols.

VII.2.2.1. Synthetic procedures.

Pyridine building block **4** was synthesized according to the following reaction scheme:

Experimental section

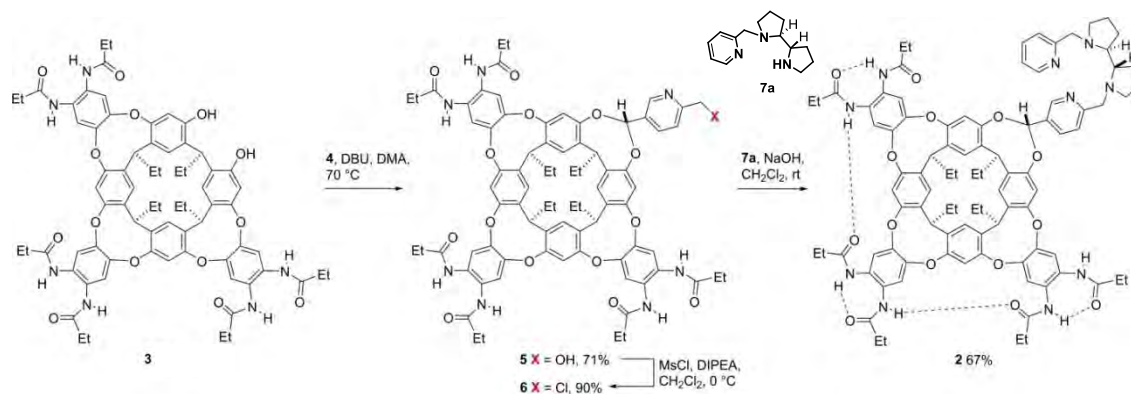


Scheme VII.3. Schematic synthesis for the obtention of synthon 4.

Methyl 5-methylpicolinate (S2). This compound was synthesized from 5-methyl-2-bromopyridine following a reported protocol¹⁷¹ in 76% isolated yield. The spectral data matches the previously described.²⁰⁶ ^1H NMR (400 MHz, CDCl_3): δ 8.48 (s, 1H, CH), 7.95 (dd, $J = 8.0, 1.8$ Hz, 1H), 7.56 (dd, $J = 8.0, 2.0$ Hz, 1H), 3.91 (s, 3H, CH_3), 2.34 (s, 3H, CH_3) ppm. ^{13}C NMR (101 MHz, CDCl_3): δ 165.7, 150.3, 145.26, 137.4, 137.3, 124.7, 52.6, 18.6 ppm.

Methyl 5-dibromomethylpicolinate (S3). This compound was synthesized from S2 following a reported procedure.¹⁷² Spectral data is in agreement with the previously reported.²⁰⁷ ^1H NMR (400 MHz, CDCl_3): δ 8.86 (dd, $J = 2.3, 0.9$ Hz, 1H), 8.27 – 8.14 (m, 2H), 6.72 (s, 1H), 4.05 (s, 3H) ppm.

5-Dibromomethyl-2-hydroxymethylpyridine (4). S3 (940 mg, 3.04 mmol) was dissolved in anhydrous MeOH (150 mL). NaBH_4 (690 mg, 18.25 mmol) was then added at $0\text{ }^\circ\text{C}$ in small portions, and the solution was stirred at room temperature for 12 h. After this time, the solvent was removed under reduced pressure and the solid residue was treated with aq. NaHCO_3 and extracted with CH_2Cl_2 . The combined organic layers were dried over Na_2SO_4 , concentrated on a rotatory evaporator and purified by silica gel column chromatography, eluting with hexanes/ethyl acetate (1:1) to yield 802 mg of a beige solid (2.86 mmol, 84%). ^1H NMR (400 MHz, CDCl_3): δ 8.56 (d, $J = 2.5$ Hz, 1H, CH), 7.95 (dd, $J = 8.2, 2.5$ Hz, 1H, CH), 7.37 (d, $J = 8.2$ Hz, 1H, CH), 6.64 (s, 1H, CH), 4.75 (s, 2H, CH_2), 4.44 (s, 1H, CHBr_2). ^{13}C NMR (101 MHz, CDCl_3): δ 161.5 (Cq), 145.3 (CH), 136.7 (Cq), 136.1 (CH), 120.9 (CH), 64.2 (CH_2), 37.0 (CH) ppm. HRMS (ESI-TOF) m/z calcd. for $\text{C}_7\text{H}_7\text{NOBr}_2^+$ ($[\text{M}+\text{H}]^+$): 281.8947; found: 281.8934.



Scheme VII.4. Schematic synthesis for the obtention of cavitand **2**.

2-Hydroxymethylpyridine cavitand 5. Following a reported protocol,¹⁶⁷ hexaamido-diol cavitand (500 mg, 0.400 mmol), (5-(dibromomethyl)pyridin-2-yl)methanol **4** (560 mg, 1.99 mmol), and DBU (303 μ L, 2.03 mmol) were mixed in a vial equipped with a screw cap and dissolved in dry DMA (30 mL). The vial was flushed with nitrogen, sealed and heated in an oil bath at 70 °C for 4 days. The mixture was then evaporated to dryness *in vacuo*. The residue was diluted in AcOEt and washed with saturated aqueous NaHCO₃ solution. After separation, the aqueous layer was extracted with AcOEt (x3). The organic layers were combined, dried over Na₂SO₄ and concentrated. The crude was purified by flash chromatography on silica gel (CH₂Cl₂/MeOH 98:2), and then triturated with MeOH to afford the desired acetal cavitand **5** (388 mg, 71%) as an off-white solid. ¹H NMR (400 MHz, acetone-*d*₆): δ 9.58 (s, 2H, NH), 9.38 (s, 2H, NH), 8.97 (s, 1H, CH), 8.82 (s, 2H, NH), 8.29 (d, *J* = 8.2 Hz, 1H, CH), 7.83 (s, 2H, CH), 7.81 (s, 2H, CH), 7.79 (s, 2H, CH), 7.76 (s, 2H, CH), 7.68 (s, 2H, CH), 7.64 (d, *J* = 8.1 Hz, 1H, CH), 7.58 (s, 2H, CH), 7.08 (s, 2H, CH), 5.77 (t, *J* = 8.5 Hz, 1H, CH), 5.72 (t, *J* = 8.3 Hz, 2H, CH), 4.76 (m, 2H, CH₂), 4.72 (t, *J* = 8.6 Hz, 1H, CH), 5.51 (s, 1H, CH), 4.50 (s, 1H, OH), 2.62 – 2.36 (m, 16H, CH₂), 2.36 – 2.22 (m, 4H, CH₂), 1.38 – 1.17 (m, 12H, CH₃), 1.10 (t, *J* = 7.5 Hz, 6H, CH₃), 1.01 (t, *J* = 7.2 Hz, 12H, CH₃) ppm. ¹³C NMR (101 MHz, acetone-*d*₆): δ 174.5 (CO), 174.3 (CO), 173.2 (CO), 162.5 (Cq), 156.1 (Cq), 155.8 (Cq), 155.54 (Cq), 155.51 (Cq), 150.7 (Cq), 150.1 (Cq), 145.0 (Cq), 147.5 (CH), 139.0 (Cq), 137.1 (Cq), 136.8 (CH), 136.7 (Cq), 136.5 (Cq), 134.2 (Cq), 129.7 (Cq), 128.9 (Cq), 126.3 (CH), 123.9 (CH), 122.5 (CH), 122.0 (CH), 121.0 (CH), 120.7 (CH), 117.2 (CH), 117.07 (CH), 107.09 (CH), 65.4 (CH₂), 39.6 (CH), 36.8 (CH), 36.6 (CH), 31.22 (CH₂), 31.17 (CH₂), 30.4 (CH₂, overlap with CD₃COCD₃), 25.7 (CH₂), 25.4 (CH₂), 23.7 (CH₂), 13.0 (CH₃), 12.90 (CH₃), 12.85 (CH₃), 10.7 (CH₃), 10.6 (CH₃), 9.9 (CH₃) ppm. HRMS (ESI-TOF) *m/z* calcd. for C₇₉H₈₁N₇O₁₅Na⁺ ([M+Na]⁺): 1390.5683; found: 1390.5686.

2-Chloromethylpyridine cavitand 6. In a round bottom flask, cavitand **5** (388 mg, 0.284 mmol) was dissolved in anhydrous CH₂Cl₂ (50 mL) under an inert atmosphere, and cooled at 0 °C. Then,

Experimental section

mesyl chloride (110 μ L, 1.42 mmol) was added dropwise followed by the addition of DIPEA (494 μ L, 2.83 mmol), and then slowly warmed up to room temperature. The reaction was monitored by TLC until completion. The volatiles were then removed under reduced pressure and the crude was purified by flash chromatography on silica gel ($\text{CH}_2\text{Cl}_2/\text{MeOH}$ 99:1) to afford cavitand **6** (330 mg, 84%) as an off-white solid. Crystals suitable for X-ray diffraction were obtained by slow evaporation of a MeOH solution of **6**. ^1H NMR (400 MHz, acetone- d_6): δ 9.58 (s, 2H, NH), 9.38 (s, 2H, NH), 9.02 (s, 1H, CH), 8.81 (s, 2H, CH), 8.35 (d, J = 8.1 Hz, 1H, CH), 7.84 (s, 2H, CH), 7.81 (s, 2H, CH), 7.79 (s, 2H, CH), 7.76 (s, 2H, CH), 7.71 (d, J = 8.1 Hz, 1H, CH), 7.68 (s, 2H, CH), 7.58 (s, 2H, CH), 7.09 (s, 2H, CH), 5.74 (t, J = 8.2 Hz, 1H, CH), 5.70 (t, J = 8.2 Hz, 2H, CH), 5.53 (s, 1H, CH), 4.82 (s, 2H, CH_2), 4.71 (t, J = 8.2 Hz, 1H, CH), 2.67 – 2.37 (m, 16H, CH_2), 2.30 (m, 4H, CH_2), 1.33 – 1.17 (m, 12H, CH_3), 1.11 (t, J = 7.5 Hz, 6H, CH_3), 1.01 (t, J = 7.2 Hz, 12H, CH_3) ppm. ^{13}C NMR (101 MHz, acetone- d_6): δ 174.5 (CO), 174.4 (CO), 173.1 (CO), 157.9 (Cq), 156.0 (Cq), 155.8 (Cq), 155.55 (Cq), 155.46 (Cq), 150.7 (Cq), 150.1 (Cq), 150.0 (Cq), 148.3 (CH), 138.9 (Cq), 137.4 (CH), 137.1 (Cq), 136.8 (Cq), 136.6 (Cq), 135.3 (Cq), 129.7 (Cq), 128.9 (Cq), 126.3 (CH), 124.0 (CH), 123.6 (CH), 122.4 (CH), 122.0 (CH), 121.0 (CH), 117.2 (CH), 117.0 (CH), 106.8 (CH), 47.5 (CH_2), 39.6 (CH), 36.8 (CH), 36.6 (CH), 31.2 (CH_2), 30. (CH_2 , overlap with CD_3COCD_3), 25.7 (CH_2), 25.4 (CH_2), 23.8 (CH_2), 13.0 (CH_3), 12.9 (CH_3), 12.8 (CH_3), 10.7 (CH_3), 10.6 (CH_3), 9.9 (CH_3) ppm. HRMS (ESI-TOF) m/z calcd. for $\text{C}_{79}\text{H}_{80}\text{ClN}_7\text{O}_{14}\text{Na}^+$ ($[\text{M}+\text{Na}]^+$): 1408.5344; found: 1408.5361.

Bis(pyridyl)dipyrrolidine cavitand 2. In a round bottom flask, cavitand **6** (330 mg, 0.238 mmol) was dissolved in 50 mL of CH_2Cl_2 and a solution of **7a** (165 mg, 0.71 mmol) in CH_2Cl_2 (3 mL) was added. Then, a solution of NaOH (57 mg, 1.42 mmol) in water (10 mL) was added, and the resulting biphasic solution was vigorously stirred for 24 h at room temperature. After this time, the organic layer was separated and the aqueous phase was further extracted with CH_2Cl_2 (3x 20 mL). The organic layers were combined, dried over Na_2SO_4 and concentrated. The crude was purified by flash chromatography on silica gel ($\text{CH}_2\text{Cl}_2/\text{MeOH}/\text{NH}_4^+\text{OH}^-_{(\text{aq.})}$ 97.5:2:0.5) and then triturated from MeOH, to afford the desired cavitand **2** (245 mg, 65%) as a white solid. ^1H NMR (400 MHz, acetone- d_6): δ 9.59 (s, 2H, NH), 9.38 (s, 2H, NH), 8.93 (s, 1H, CH), 8.82 (s, 2H, NH), 8.45 (d, J = 4.8 Hz, 1H, CH), 8.23 (d, J = 8.1 Hz, 1H, CH), 7.92 – 7.74 (m, 8H, CH), 7.74 – 7.65 (m, 3H, CH), 7.62 (d, J = 8.0 Hz, 2H, CH), 7.58 (s, 2H, CH), 7.46 (d, J = 7.8 Hz, 1H, CH), 7.16 (dd, J = 7.5, 5.0 Hz, 1H, CH), 7.08 (s, 2H, CH), 5.74 (t, J = 8.2 Hz, 1H), 5.70 (t, J = 8.1 Hz, 2H, CH), 5.48 (s, 1H, CH), 4.71 (t, J = 8.1 Hz, 1H, CH), 4.31 (d, J = 14.7 Hz, 1H, CH_2), 4.22 (d, J = 14.3 Hz, 1H, CH, CH_2), 3.54 (d, J = 14.6 Hz, 2H, CH_2), 3.08 – 2.89 (m, 4H, CH_2+CH), 2.66 – 2.36 (m, 16H, CH_2), 2.28 (m, 6H, CH_2), 1.84 (m, 4H, CH_2), 1.71 (m, 4H, CH_2), 1.40 – 1.16 (m, 12H, CH_3), 1.12 (t, J = 7.5 Hz, 6H, CH_3), 1.01 (t, J = 7.1 Hz, 12H, CH_3) ppm. ^{13}C NMR (101 MHz, acetone- d_6): δ 174.45 (CO), 174.35 (CO), 173.1 (CO), 161.8 (Cq), 161.4 (Cq), 156.0 (Cq), 155.8 (Cq),

155.6 (Cq), 155.5 (Cq), 150.7 (Cq), 150.1 (Cq), 149.5 (CH), 147.4 (CH), 138.9 (Cq), 137.1 (Cq), 136.9 (CH), 136.8 (CH), 136.5 (Cq), 133.8 (Cq), 129.6 (Cq), 128.9 (Cq), 126.3 (CH), 124.0 (CH), 123.3 (CH), 122.8 (CH), 122.5 (CH), 122.4 (CH), 121.9 (CH), 121.0 (CH), 117.2 (CH), 117.0 (CH), 107.2 (CH), 66.0 (CH), 65.9 (CH), 61.6 (CH₂), 61.4 (CH₂), 55.93 (CH₂), 55.87 (CH₂), 39.6 (CH), 36.8 (CH), 36.6 (CH), 31.2 (CH₂), 30.4 (CH₂), 26.8 (CH₂), 26.7 (CH₂), 25.7 (CH₂), 25.4 (CH₂), 24.4 (CH₂), 24.3 (CH₂), 23.8 (CH₂), 13.0 (CH₃), 12.9 (CH₃), 12.9 (CH₃), 10.7 (CH₃), 10.6 (CH₃), 9.9 (CH₃) ppm. HRMS (ESI-TOF) m/z calcd. for C₉₃H₁₀₁N₁₀O₁₄⁺ ([M+H]⁺): 1582.7525; found: 1582.7526. EA calc. for C₉₆H₁₁₂N₁₀O₁₇ (**2**·(3·CH₃OH)₃): C 68.72; H 6.73; N 8.35; found: C 68.49; H 6.47; N 8.49.

Synthesis of cavitand triflate complexes, general procedure: In a glovebox, cavitand **2** (80 mg, 0.05 mmol) was dissolved in 1 mL of THF. The corresponding metal triflate salt-Zn(OTf)₂, Fe(OTf)₂(CH₃CN)₂ or Mn(OTf)₂, (1.1 eq.)- was dissolved in 0.5 mL THF and slowly added to the solution of the ligand. The solution turned yellow and was stirred overnight at room temperature. After this time, the solvent was removed under vacuum and the solid was redissolved in CH₂Cl₂ and recrystallized by slow diffusion of Et₂O to obtain the desired complex.

[Zn(2)(CH₃CN)₂](CF₃SO₃)₂·2·Zn(OTf)₂, a microcrystalline white solid, obtained in 82% yield. ¹H NMR (400 MHz, CD₃CN): δ 9.42 (bs, 1H), 9.31 (bs, 1H), 9.23 (s, 1H), 9.11 (bs, 2H), 8.83 (d, *J* = 5.1 Hz, 1H), 8.58 (d, *J* = 7.9 Hz, 1H), 8.29 (s, 2H), 8.10 (t, *J* = 7.6 Hz, 1H), 7.87 – 7.44 (m, 12H), 7.40 (d, *J* = 2.7 Hz, 2H), 7.28 – 7.09 (m, 2H), 5.68 – 5.60 (m, 3H), 5.55 (s, 1H), 4.73 (t, *J* = 8.1 Hz, 1H), 4.18 (d, *J* = 4.6 Hz, 2H), 4.12 (s, 2H), 3.11 – 3.02 (m, 2H), 2.89 – 2.73 (m, 3H), 2.66 (s, 2H), 2.58 – 2.32 (m, 17H), 2.24 (s, 4H), 2.17 – 1.98 (m, 4H), 1.86 – 1.71 (m, 2H), 1.43 – 1.31 (m, 2H), 1.31 – 0.61 (m, 31H) ppm. ¹³C NMR (101 MHz, CD₃CN): δ 174.2, 174.1, 173.3, 172.7, 155.9, 155.4, 155.3, 155.1, 154.8, 154.0, 153.9, 149.7, 149.6, 149.2, 148.9, 147.4, 145.2, 140.8, 140.3, 138.4, 136.1, 135.9, 135.6, 128.9, 128.7, 128.3, 128.1, 127.8, 125.04, 125.00, 124.9, 124.7, 123.1, 123.0, 122.3, 121.6, 120.8, 119.8, 119.1, 116.8, 116.3, 116.2, 104.7, 66.8, 66.6, 57.7, 57.6, 52.9, 52.8, 38.8, 35.95, 35.8, 30.4, 30.2, 29.8, 29.6, 24.9, 24.2, 24.0, 22.47, 22.53, 22.4, 11.9, 11.8, 9.7, 9.63, 9.57, 9.0 ppm. ¹⁹F NMR (377 MHz, CD₃CN): δ -79.1 ppm. HRMS (ESI-TOF) m/z calcd. for ([C₉₃H₁₀₀ZnN₁₀O₁₄]²⁺): 818.3411; found: 818.3413.

[Fe(2)(CH₃CN)₂](CF₃SO₃)₂·2·Fe(OTf)₂, a microcrystalline yellow solid, obtained in 78% yield. ¹H NMR (400 MHz, CD₃CN): δ 9.40 (bs, sH), 9.34 (bs, 2H), 9.13 (s, 1H), 8.92 (bs, 2H), 8.45 (bs, 1H), 8.07 (d, *J* = 5.8 Hz, 1H), 7.78 – 7.61 (m), 7.56 (d, *J* = 8.7 Hz), 7.41 – 7.24 (m), 7.19 (bs), 6.53 (bs), 5.99 (s), 5.59 (t, *J* = 8.2 Hz), 5.52 – 5.48 (m), 5.45 – 5.35 (m), 3.96 (bs), 3.79 (bs), 3.63 (bs), 2.91 – 2.31 (m), 2.21 (bs), 1.83 – 1.73 (m), 1.53 (bs), 1.45 – 1.21 (m), 0.96 (t, *J* = 7.1 Hz), 0.91 – 0.78 (m), 0.74 (bs). ¹⁹F NMR (377 MHz, CD₃CN): δ -77.5 ppm. HRMS (ESI-TOF) m/z calcd. for ([C₉₃H₁₀₀FeN₁₀O₁₄]²⁺): 818.8302;

Experimental section

found: 818.8396. EA calc. for $C_{95}H_{100}F_6FeN_{10}O_{20}S_2 \cdot (H_2O; 2CH_2Cl_2; 2Et_2O)$: C 55.51; H 5.59; N 6.17; found: C 55.30; H 5.78; N 6.50.

$[Mn(2)(CH_3CN)_2](CF_3SO_3)_2 \cdot 2 \cdot Mn(OTf)_2$, a microcrystalline white solid, obtained in 67% yield. HRMS (ESI-TOF) m/z calcd. for $([C_{93}H_{100}MnN_{10}O_{14}]^{2+})$: 823.3339; found: 823.3358.

$[Fe_2(\mu-O)(Cl)_4(2)(CH_3CN)_2] \cdot 2 \cdot Fe_2Cl_3O$. Cavitand **2** (80 mg, 0.05 mmol) was dissolved in 1 mL of THF. $FeCl_2$ (1 eq.) was dissolved in 0.5 mL THF and added slowly to the solution of the ligand. The solution turned bright yellow and was stirred overnight at room temperature under air. After this time, solvent was removed under vacuum. Crystals suitable for X-ray diffraction were obtained by slow diffusion of Et_2O in a CH_3CN solution of $2 \cdot Fe_2Cl_3O$, to obtain the product as brown crystals in a 78% yield.

VII.2.2.1.1. Synthesis of guests 8-11.

Guests **8a**, **8b** were purchased from Sigma-Aldrich. Guest **9**²⁰⁸ and **11**²⁰⁹ were prepared according to reported procedures.

8c: 1-Adamantylamine (500 mg, 3.31 mmol) was dissolved in 20 mL of anhydrous MeOH. Cyclohexanecarboxaldehyde (407 mg, 3.63 mmol) was added solved in the minimum amount of anhydrous MeOH. The mixture was stirred at room temperature for 30 min. After this time, $NaBH_4$ (657 mg, 16.5 mmol) was added at 0 °C. The flask was let to warm up and stirred at room temperature overnight. The solvent was then removed under reduced pressure and the residue was redissolved in CH_2Cl_2 (20 mL) and quenched with sat. $NaHCO_3$ (20 mL). The layers were separated the aqueous fraction was further extracted with CH_2Cl_2 (2 x 20 mL). The combined organic layers were dried over Na_2SO_4 and concentrated under reduced pressure. The crude was purified by flash chromatography on silica gel ($CH_2Cl_2/MeOH/NH_4^+OH^-_{(aq.)}$ 93:5:2) to obtain the pure amine as a yellowish oil. The amine was then dissolved in 10 mL of CH_2Cl_2 and $HBF_4 \cdot OEt_2$ (429 mg, 2.67 mmol) added at 0 °C. The mixture was stirred for 30 min. and then the solvent was removed under vacuum. To the resulting white solid Et_2O was added and stirred for 15 min. at room temperature. The solvent was then decanted to obtain a white crystalline solid which was dried under high vacuum (59% yield). 1H NMR (400 MHz, CD_3CN): δ 6.23 (bs, 2H), 2.85 – 2.79 (m, 2H), 2.19 (s, 4H), 1.90 (d, $J = 2.7$ Hz, 6H), 1.80 – 1.71 (m, 7H), 1.70 – 1.58 (m, 5H), 1.34 – 1.14 (m, 3H), 1.06 – 0.94 (m, 2H). ^{13}C NMR (75 MHz, CD_3CN): δ 60.2, 46.9, 38.7, 36.1, 36.0, 31.0, 30.1, 26.6, 26.1 ppm. HRMS (ESI-TOF) m/z calcd. for $C_{17}H_{30}N$ ($[M+H]^+$): 248.2382; found: 248.2373.

10: This compound was prepared from cyclohexylmethylamine (500 mg, 4.42 mmol) and 3,7-Dimethyl-2,6-octadienal (706 mg, 4.64 mmol) following the procedure described for **8c**. Compound **10** (*E/Z* mixture) was obtained as a white crystalline solid in a 42% yield. ^1H NMR (300 MHz, CDCl_3): δ 6.60 (s, 2H), 5.30 (t, $J = 7.5$ Hz, 1H), 5.09 – 5.00 (m, 1H), 3.80 – 3.70 (m, 2H), 2.85 – 2.78 (m, 2H), 2.13 – 2.09 (m, 4H), 1.82 – 1.65 (m, 13H), 1.61 (s, 3H), 1.37 – 1.09 (m, 4H), 1.07 – 0.91 (m, 2H). ^{13}C NMR (101 MHz, CD_3CN): δ 147.5/147.2, 133.3/132.8, 124.5/124.3, 114.8/114.1, 54.0/53.8, 46.9, 40.2, 35.7, 32.8, 30.9, 27.0, 26.8, 26.6, 26.1, 25.8, 23.7, 17.8, 16.8 ppm. HRMS (ESI-TOF) m/z calcd. for $\text{C}_{17}\text{H}_{32}\text{N}$ ($[\text{M}+\text{H}]^+$): 250.2530; found: 250.2529.

VII.2.3 X-ray diffraction data.

2-Chloromethylpyridine cavitand **6**.

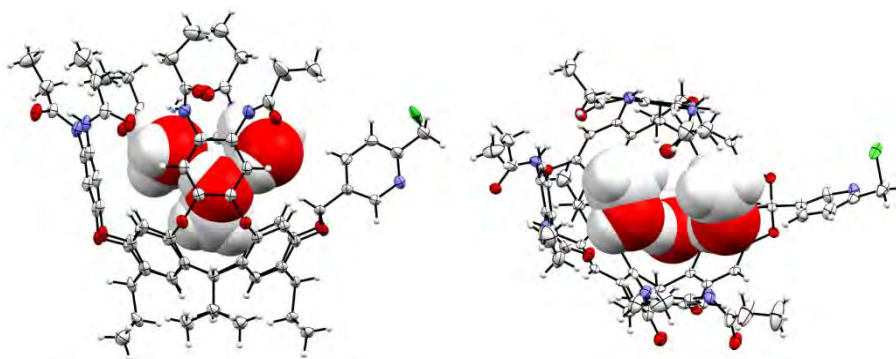


Figure VII.1. Side and top views of the X-ray diffraction structure of **6**. Ellipsoids are shown at 50% probability (gray: C, blue: N, red: O, green: Cl). Solvent molecules (MeOH) occupying the cavity are shown in space filling representation.

Crystal-Structure Determination. – Colorless crystals of **6** were grown from MeOH, and used for low temperature (100(2) K) X-ray structure determination. The measurement was carried out on a BRUKER SMART APEX CCD diffractometer using graphite-monochromated Mo $K\alpha$ radiation ($\lambda = 0.71073$ Å) from an x-Ray Tube. The measurements were made in the range 2.223 to 27.600° for θ . Full-sphere data collection was carried out with ω and ϕ scans. A total of 61384 reflections were collected of which 18851 [$R(\text{int}) = 0.0660$] were unique. Programs used: data collection, Smart¹⁵; data reduction, Saint¹⁶; absorption correction, SADABS¹⁷. Structure solution and refinement was done using SHELXTL¹⁸.

Experimental section

The structure was solved by direct methods and refined by full-matrix least-squares methods on F₂. The non-hydrogen atoms were refined anisotropically. The H-atoms were placed in geometrically optimized positions and forced to ride on the atom to which they are attached.

Table VII.1. Crystal data and structure refinement for **6**.

2-Chloromethylpyridine cavitand (6)	
Empirical formula	C ₁₆ H ₂₀ Cl ₂ N ₁₄ O ₃
Molar weight	3110.31 g/mol
Temperature	100(2) K
Wavelength	0.71073 Å
Crystal system	Triclinic
space group	P 1
Unit cell dimensions	a = 12.016(3) Å alpha = 94.269(4) deg. b = 13.709(3) Å beta = 95.583(4) deg. c = 25.728(5) Å gamma = 101.129(4) deg.
Volume	4119.8(16) Å ³
Z	1
Calculated density	1.252 Mg/m ³
Absorption coefficient	0.120 mm ⁻¹
F(000)	1652
Reflections collected	61384
Independent reflections	18851 [R(int) = 0.0660]
Final R indices [I > 2σ(I)]	R1 = 0.0995, wR2 = 0.2721
R indices (all data)	R1 = 0.1443, wR2 = 0.3057

Complex 2·Fe₂Cl₄O.

Crystal-Structure Determination. – Orange crystals of 2(C₉₃H₁₀₀Cl₄Fe₂N₁₀O₁₅), 4(C₄H₁₀O), 3(C₂H₃N), were grown from slow diffusion of ethyl ether in a CH₃CN solution of the compound, and used for low temperature (100(2) K) X-ray structure determination. The measurement was carried out on a BRUKER SMART APEX CCD diffractometer using graphite-monochromated Mo K α radiation ($\lambda = 0.71073$ Å) from an x-Ray Tube. The measurements were made in the range 2.008 to 28.398° for θ . Full-sphere data collection was carried out with ω and ϕ scans. A total of 345735 reflections were collected of which 53987 [R(int) = 0.1189] were unique. Programs used: data collection, Smart; data reduction, Saint+; absorption correction, SADABS. Structure solution and refinement was done using SHELXTL.

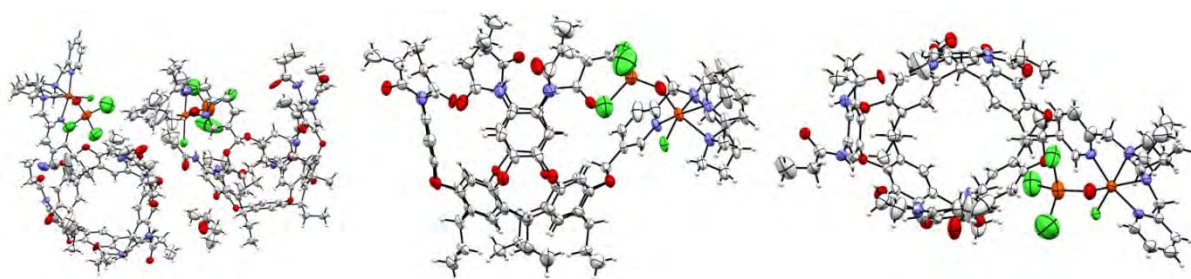


Figure VII.2. X-ray diffraction structure of 2·Fe₂Cl₄O: unit cell (left), side view (center) and top view (right). Ellipsoids are shown at 50% probability (gray: C, blue: N, red: O, green: Cl, orange: Fe). Disordered solvent molecules in the cavity not shown.

The structure was solved by dual-space algorithm and refined by full-matrix least-squares methods on F₂. The non-hydrogen atoms were refined anisotropically. The H-atoms were placed in geometrically optimized positions and forced to ride on the atom to which they are attached. A considerable amount of electron density attributable to a two disordered ethyl ether molecules (located inside the basket-like cavities formed by the ligand) and two disordered CH₃CN solvent molecules per asymmetric unit was removed with the SQUEEZE option of PLATON. Those solvent molecules are, however, included in the reported chemical formula and derived values (e.g. formula weight, F(000), etc.).

Table VII.2. Crystal data and structure refinement for 2·Fe₂Cl₃O.

Complex 2·Fe₂Cl₄O.	
Empirical formula	C208 H249 Cl8 Fe4 N23 O34
Molar weight	4122.29 g/mol
Temperature	100(2) K
Wavelength	0.71073 Å
Crystal system	Orthorhombic
space group	P 21 21 21
Unit cell dimensions	a = 16.153(2) Å alpha = 90 deg. b = 36.453(4) Å beta = 90 deg. c = 36.835(5) Å gamma = 90 deg.
Volume	21689(5) Å ³
Z	4
Calculated density	1.262 Mg/m ³
Absorption coefficient	0.433 mm ⁻¹
F(000)	8680
Reflections collected	345735
Independent reflections	53987 [R(int) = 0.1189]
Final R indices [I>2sigma(I)]	R1 = 0.1123, wR2 = 0.2990
R indices (all data)	R1 = 0.1985, wR2 = 0.3538

VI.2.2.3. Host-Guest studies.

VI.2.2.3.1. Standard protocol for ^1H NMR Host-Guest studies.

^1H NMR binding experiments of the cavitand **1** and metallocavitands $2\cdot\text{M}(\text{OTf})_2$ with external guests were performed at 300 or 240 ± 5 K on a Bruker DPX400 spectrometer, internally referenced to tetramethylsilane or, alternatively, to the residual proton solvent signal. 0.4 mL of a 8.5 mM solution of **1** in acetone- d_6 or 6.5 mM solution of $2\cdot\text{M}(\text{OTf})_2$ in CD_3CN were placed in an NMR tube. Then, 100 μL (5 eq.) of a 170 mM solution of the guest in acetone- d_6 were added to **1** and 100 μL (5 eq.) of a 130 mM solution of the guest in CD_3CN were added to $2\cdot\text{M}(\text{OTf})_2$ and mixed. Afterwards, the ^1H NMR spectra was recorded.

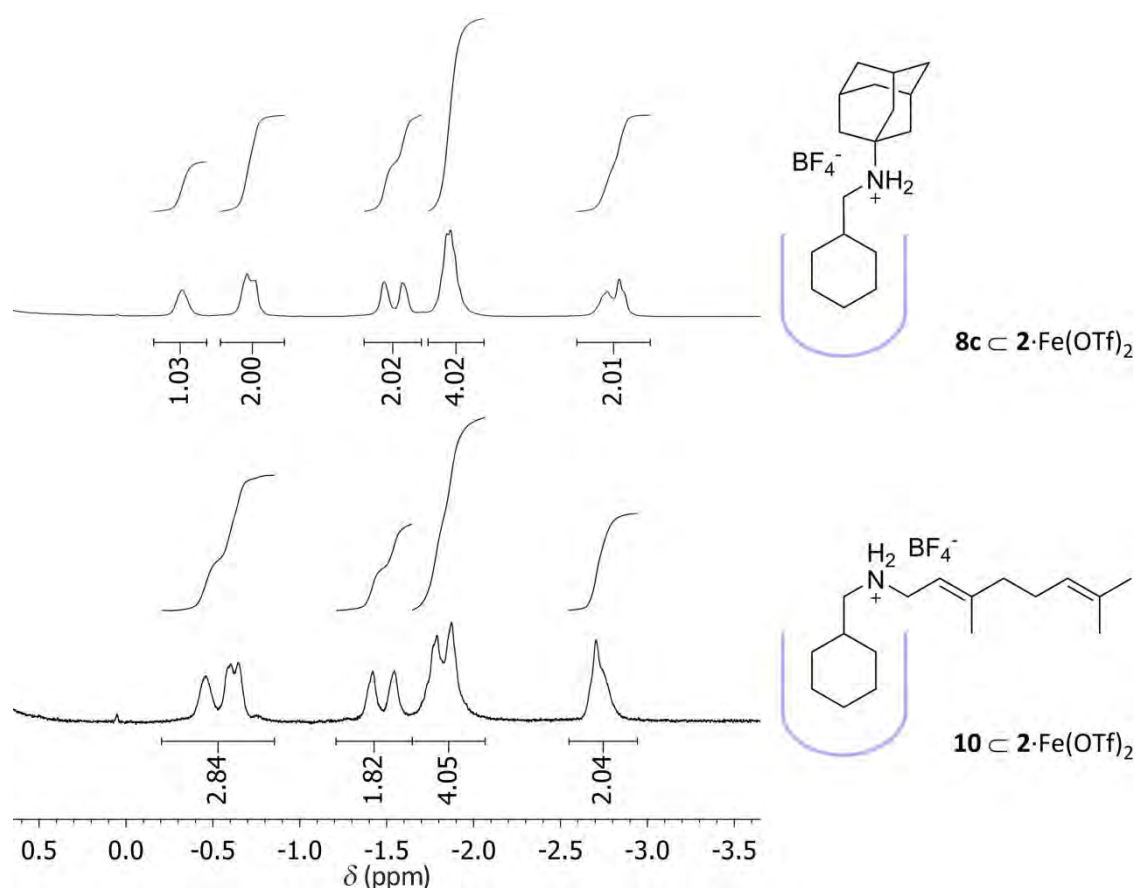


Figure VII.3. Upfield regions in the ^1H NMR spectra in CD_3CN of **8c** \cdot $2\cdot\text{Fe}(\text{OTf})_2$ (top) and **10** \cdot $2\cdot\text{Fe}(\text{OTf})_2$ (bottom), showing the resonances of the cyclohexyl moiety buried in the aromatic pocket of the cavitand (blue).

VII.3. Experimental section chapter V.

VII.3.1. Materials and methods.

All reagents were purchased from Sigma-Aldrich and TCI Europe, and were used as received. Solvents used for crystallizations were purchased from SDS and Scharlab and were purified and dried by passing through an activated alumina purification system (M-Braun SPS-800). Anhydrous DMF and DMA were purchased from Sigma-Aldrich. HPLC-grade acetonitrile (Sigma-Aldrich) was employed for oxidation reactions. Iron (II) bis(trifluoromethanesulfonate) bis(acetonitrile), manganese (II) bis(trifluoromethanesulfonate), and zinc (II) bis(trifluoromethanesulfonate) were prepared according to a literature procedure from Fe(II) chloride.²⁰⁰ Compounds **3**,¹¹³ **7a**,¹⁷³ **7b**,¹⁹⁴ **7b**·Fe(OTf)₂,²⁰⁴ and **7b**·Mn(OTf)₂,²⁰⁵ were prepared according to previously reported procedures.

Oxidation products were identified by comparison of their GC retention times and GC/MS with those of authentic compounds and/or by ¹H NMR analyses. GC analyses were carried out on a gas chromatograph equipped with a capillary methylsilicone column (30 m x 0.25 mm x 25 μm) Chrompack CP-Sil 5 CB. GC-MS analyses were performed with a mass detector (EI at 70 eV) coupled with a gas chromatograph equipped with a melted silica capillary column (30 m x 0.2 mm x 25 μm) covered with a methylsilicone film (5% phenylsilicone, OV5). NMR spectra were recorded on a Bruker DPX400 spectrometer, and were internally referenced to tetramethylsilane or, alternatively, to the residual proton solvent signal. UV – vis spectroscopy was performed on a Cary 50 Scan (Varian) UV-vis spectrophotometer or on an Agilent 8453 diode array spectrophotometer with 1 cm quartz cells. A cryostat from Unisoku Scientific Instruments was used for the temperature control. X-Ray structure determination was carried out on a *BRUKER SMART APEX CCD* diffractometer using graphite-monochromated Mo K α radiation ($\lambda = 0.71073 \text{ \AA}$) from an x-Ray Tube. Elemental analyses were performed using a CHNS-O EA-1108 elemental analyzer from Fisons. Electrospray ionization mass spectrometry (ESI-MS) experiments were performed on a Bruker Daltonics Esquire 3000 Spectrometer using solutions >1 mM of the analyzed compound. High resolution mass spectra (HRMS) were recorded on a Bruker MicroTOF-Q IITM instrument with an ESI source. Samples were introduced into the mass spectrometer ion source by direct infusion through a syringe pump and were externally calibrated using sodium formate.

VII.3.2. Experimental protocols.

VII.3.2.1. Catalytic oxidation reactions.

VII.3.2.1.1. General procedure for catalytic oxidations.

An acetonitrile solution (400 μL) of the substrate (0.25 M) and the corresponding metal complex (7.5 mM for Fe; 2.5 mM for Mn) was prepared in a 10 mL vial equipped with a stir bar, and cooled to 0 °C. Acetic acid was added directly to the solution. Then, a 1.5 M hydrogen peroxide solution in CH_3CN (165 μL , 2.5 equiv. for Fe; 135 μL , 2 equiv. for Mn) was added by syringe pump over a period of 30 min. At this point, an internal standard (biphenyl) was added and the solution was quickly filtered through a basic alumina plug, which was subsequently rinsed with 2 x 1 mL portions of AcOEt. GC analysis of the solution provided substrate conversions and product yields relative to the internal standard integration. Commercially unavailable products were identified by a combination of GC and GC-MS. Chromatographic resolution of enantiomers was performed on an Agilent 7820A gas chromatograph using a CYCLOSIL-B column, using the method specified in Annex Chapter V.

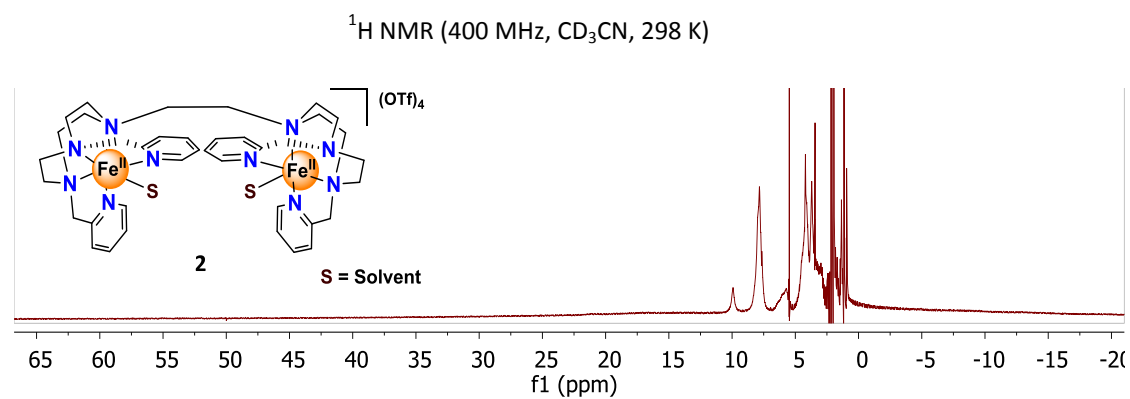
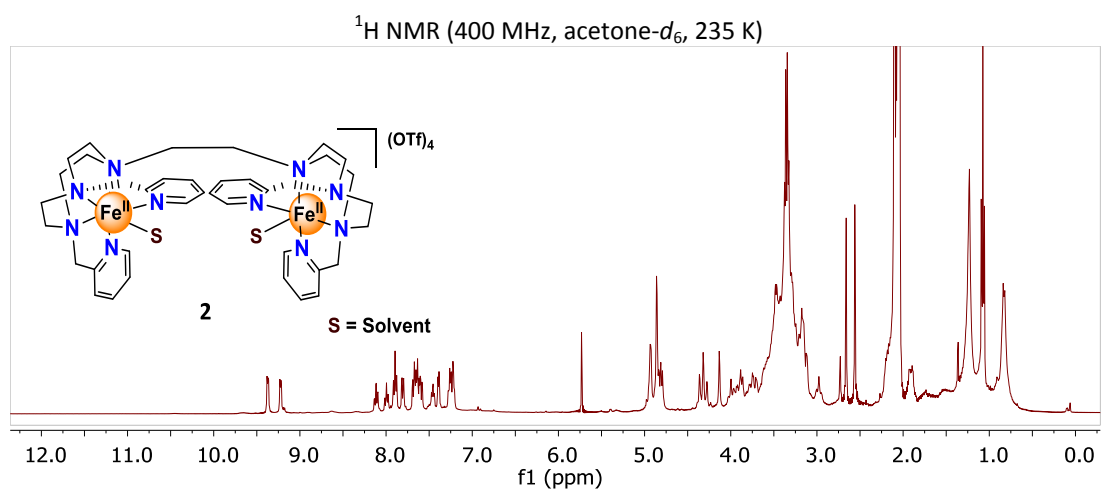
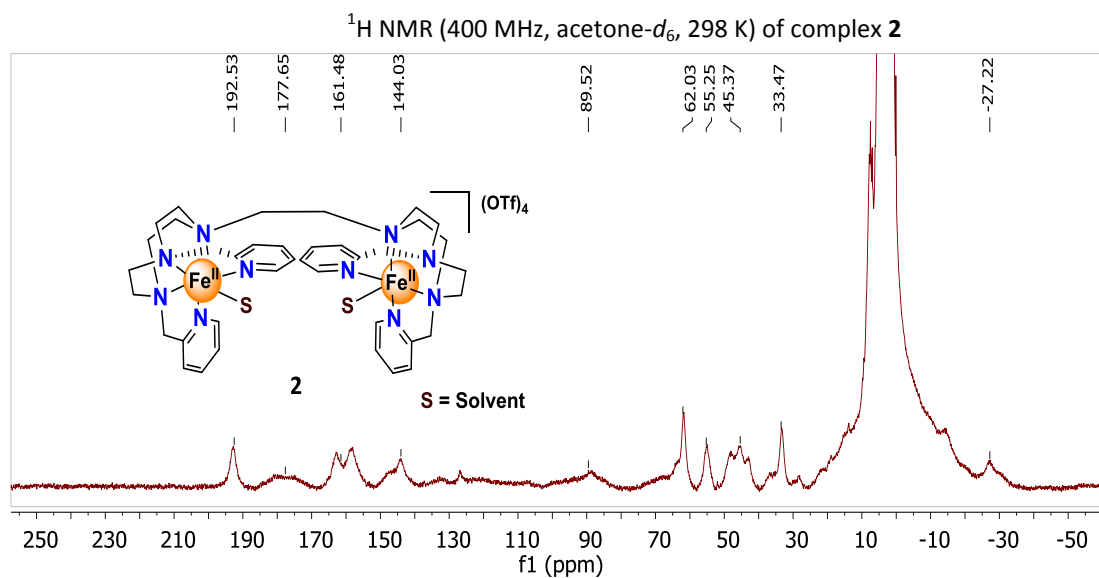
VII.3.2.1.2. Generation and reactivity of the cavitand-Fe(IV) oxo species $[\mathbf{2}\cdot\text{FeIV}(\text{O})]^{2+}$.

A 1 mM solution of the $\mathbf{2}\cdot\text{Fe}(\text{OTf})_2$ complex in anhydrous acetonitrile (2 mL) were placed in a UV-vis quartz cuvette, under inert atmosphere. Then, the cuvette was introduced in a UV-vis spectrometer precooled at 0 °C, and all the spectra were recorded with a cycle time of 1 s. The oxidant ($\text{Bu}_4\text{N}^+\text{IO}_4^-$, 1.2 eq.) and triflic acid (TfOH, 1.5 eq.) were added together directly to the cuvette in anhydrous acetonitrile solution using a Hamilton syringe, and the formation of the characteristic band at 747 nm was followed until it reached its maximum absorbance. At this point, 10 equivalents of thioanisole were added in anhydrous acetonitrile solution via Hamilton syringe. The decay of the band was followed until it reached a plateau. Then, 1 equivalent of internal standard (trimethoxybenzene) was added and the solution was rapidly filtered through a silica and alumina plug to remove the catalyst. The solution was then analyzed by GC. Substrate and product were identified by comparison of the retention time with commercially available samples and quantified by internal standardization. 0.9 equiv. of methyl phenyl sulfoxide are obtained (GC), and 0.85 equiv. of $(\mathbf{2}\cdot\text{Fe})^{2+}$ are regenerated (UV, λ 387 nm).

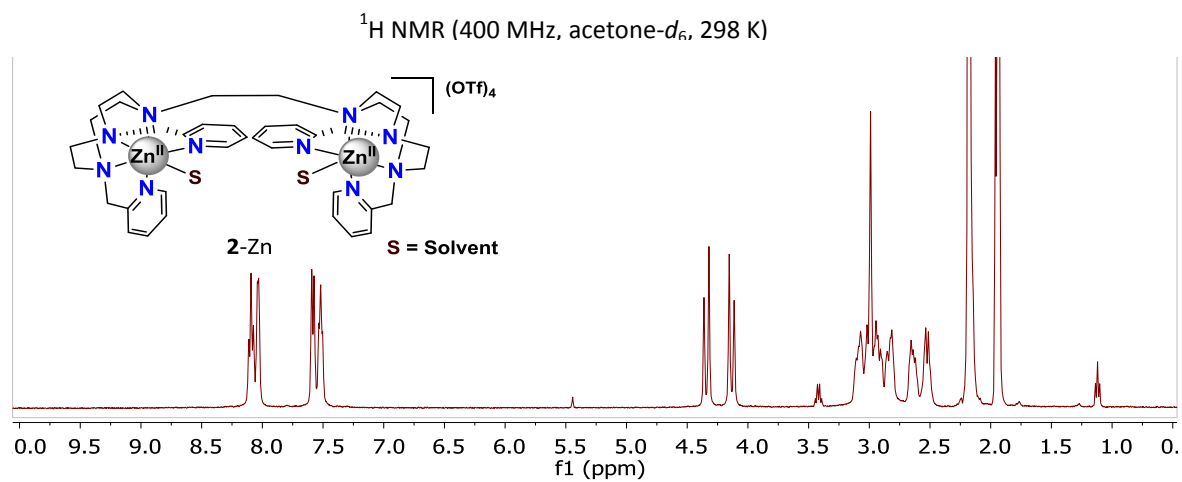
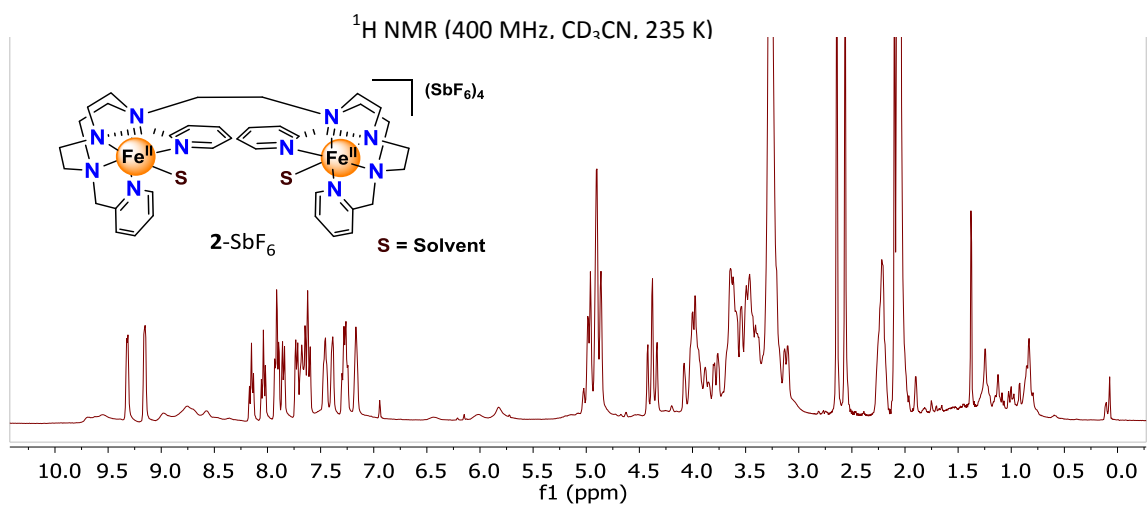
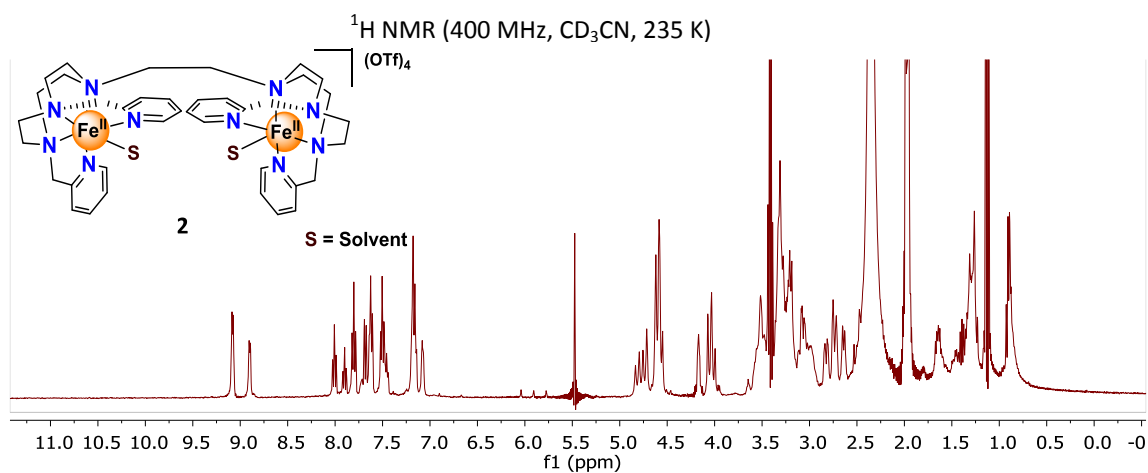


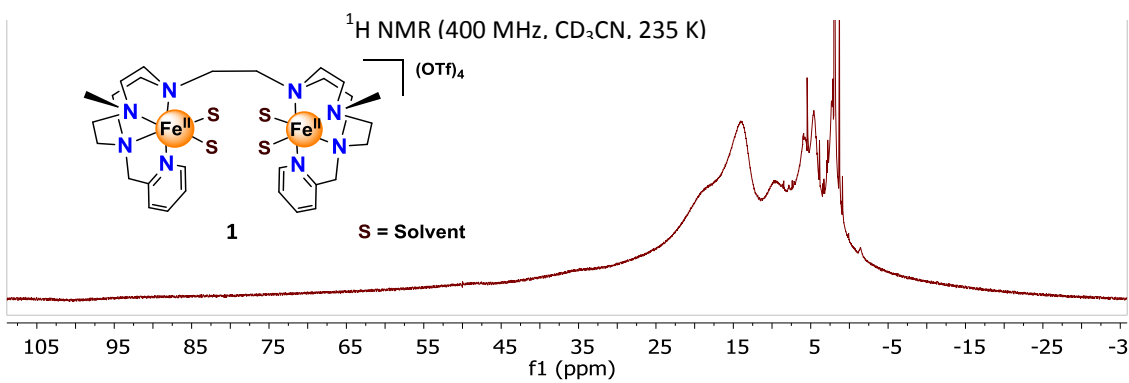
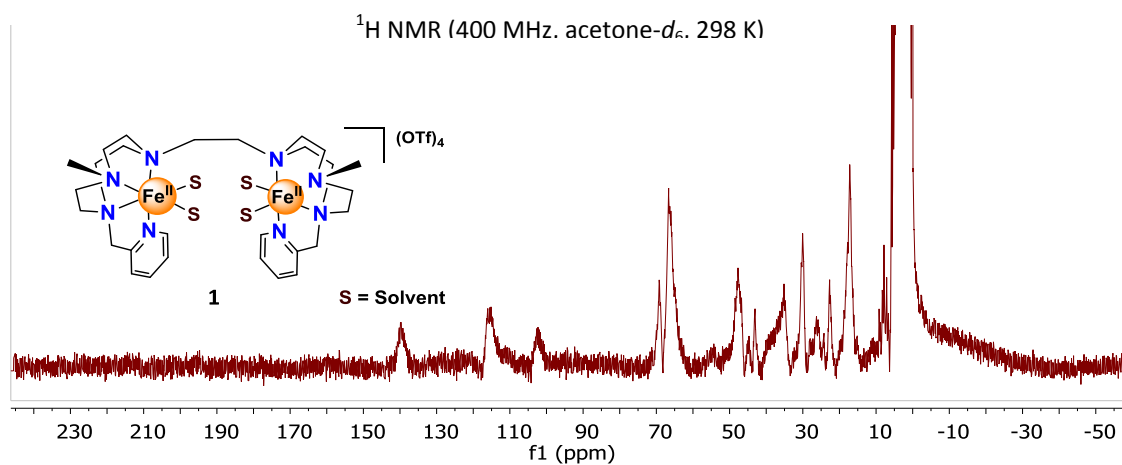
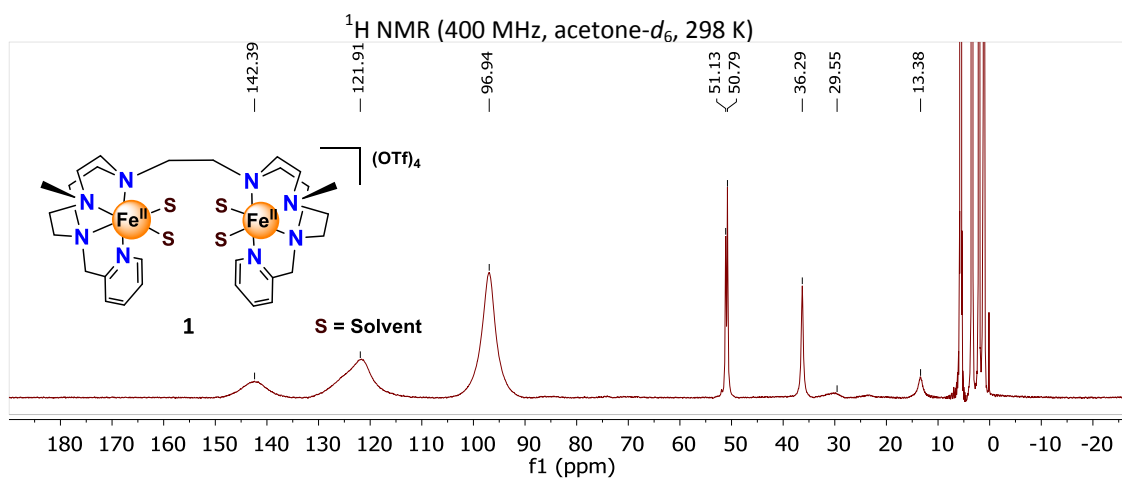
ANNEX

Annex chapter III.

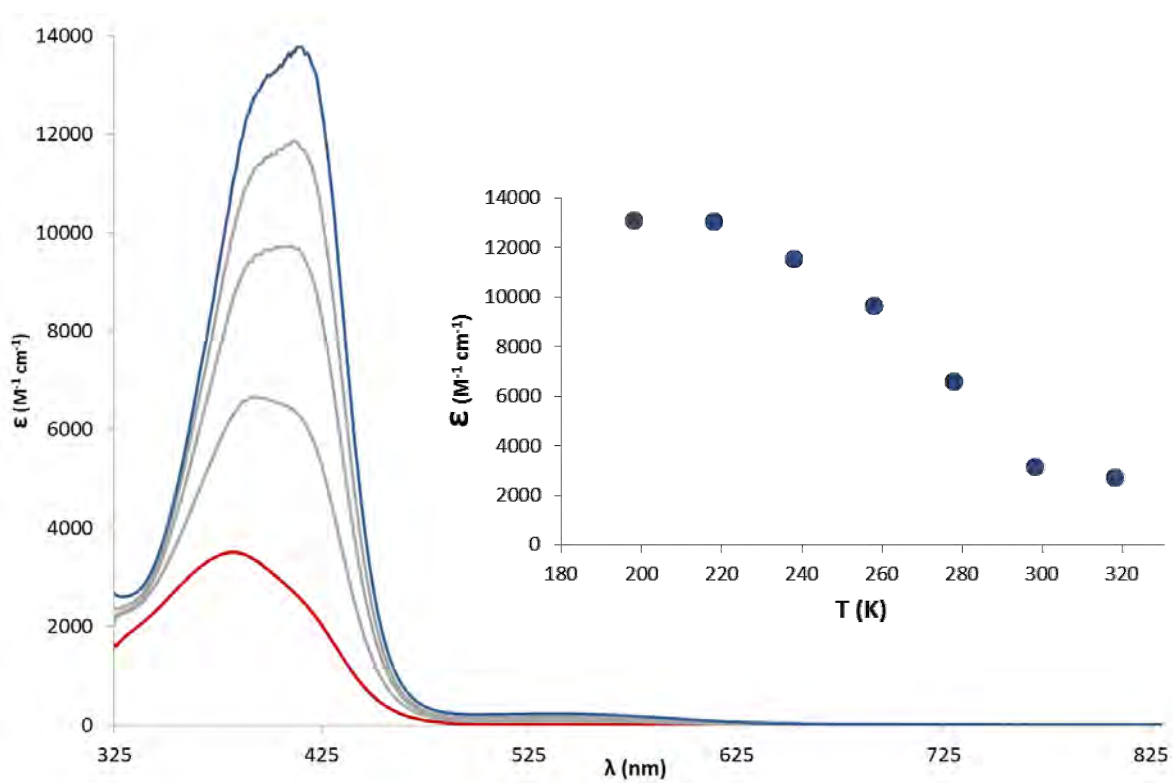
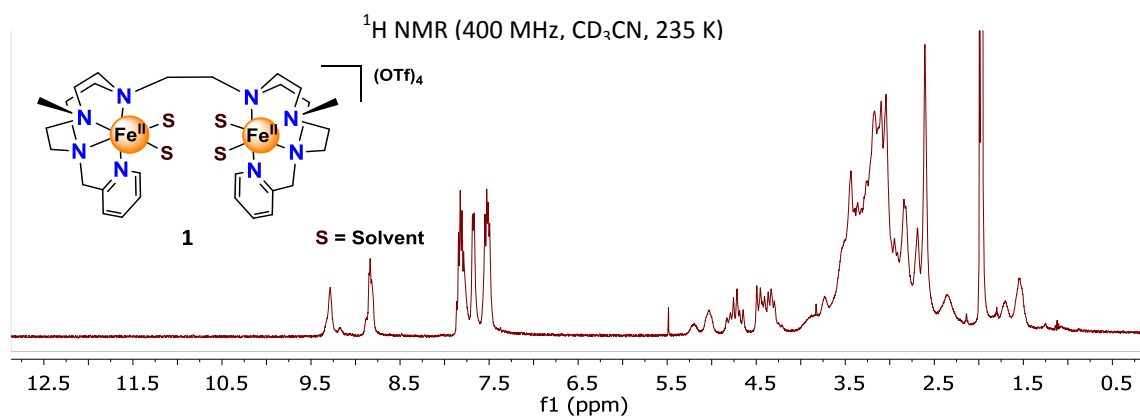


Annex

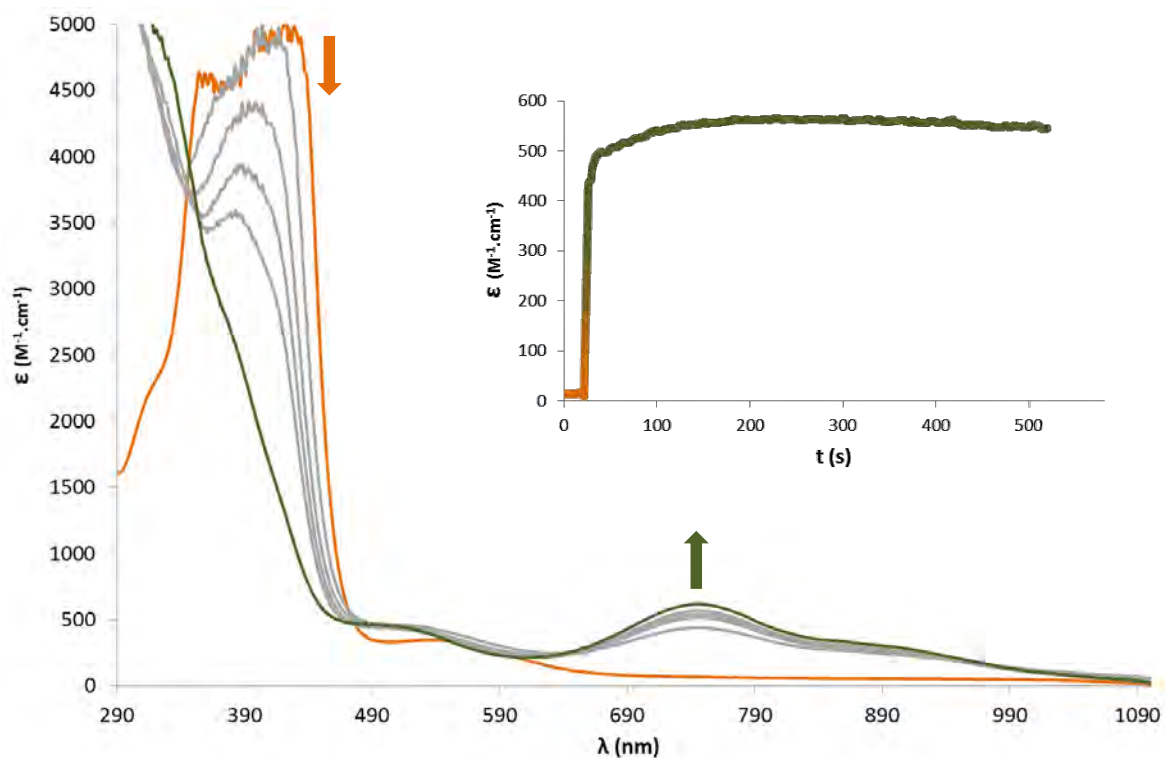




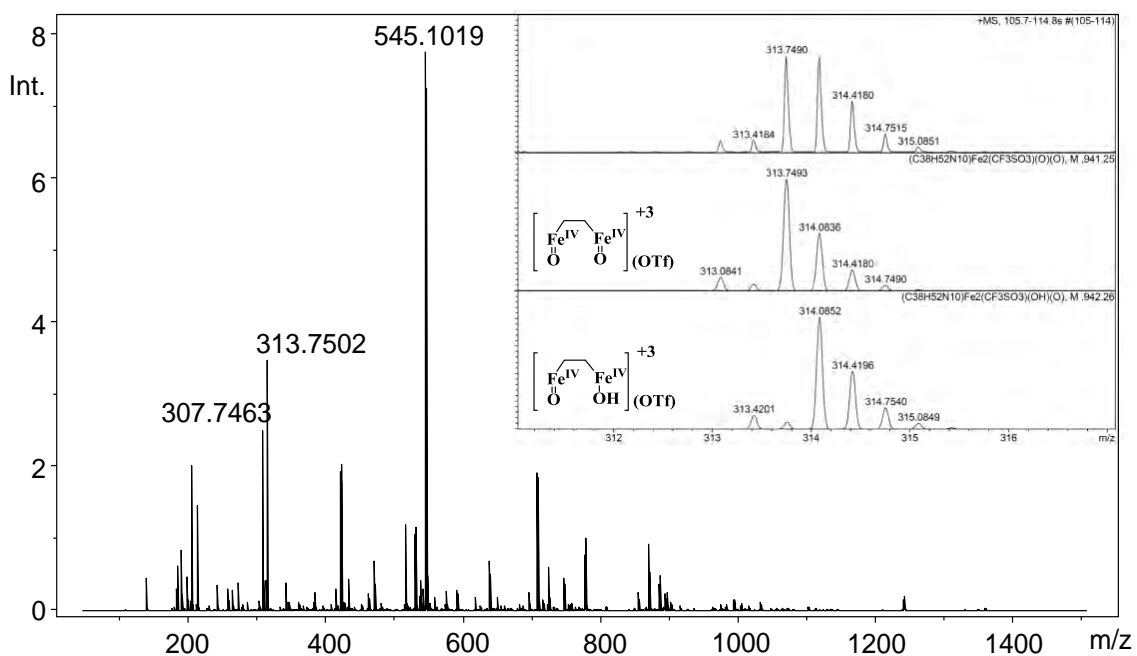
Annex



UV-vis spectra of **2-SbF₆** in acetone at different temperatures: from 320 K (red spectra) to 198 K (blue spectra). Top right: inset of the plot ϵ Vs T, corresponding to changes of MLCT band upon cooling.

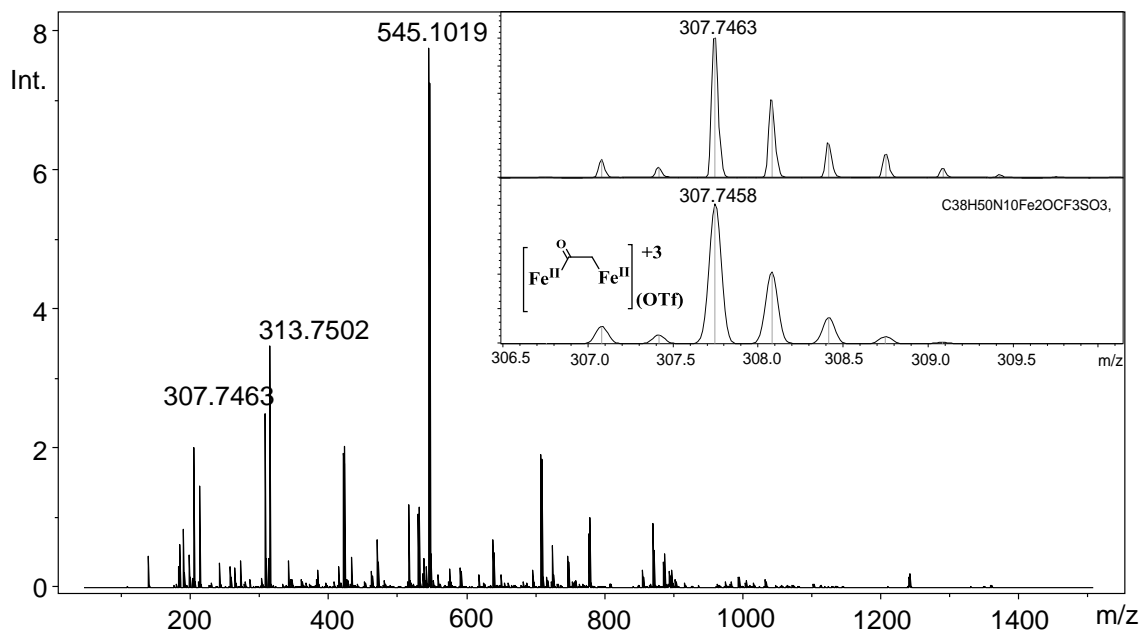


UV-vis spectra of changes of **2** (orange line) and **2^{IV}=O** (red line). Grey lines show the progressive formation of **2^{IV}=O** upon addition of 2 equiv oxidant to **2** in CH₃CN at 273 K. The inset show the kinetic traces for the formation of **2^{IV}=O** on its maximum of absorbance band at 748 nm.

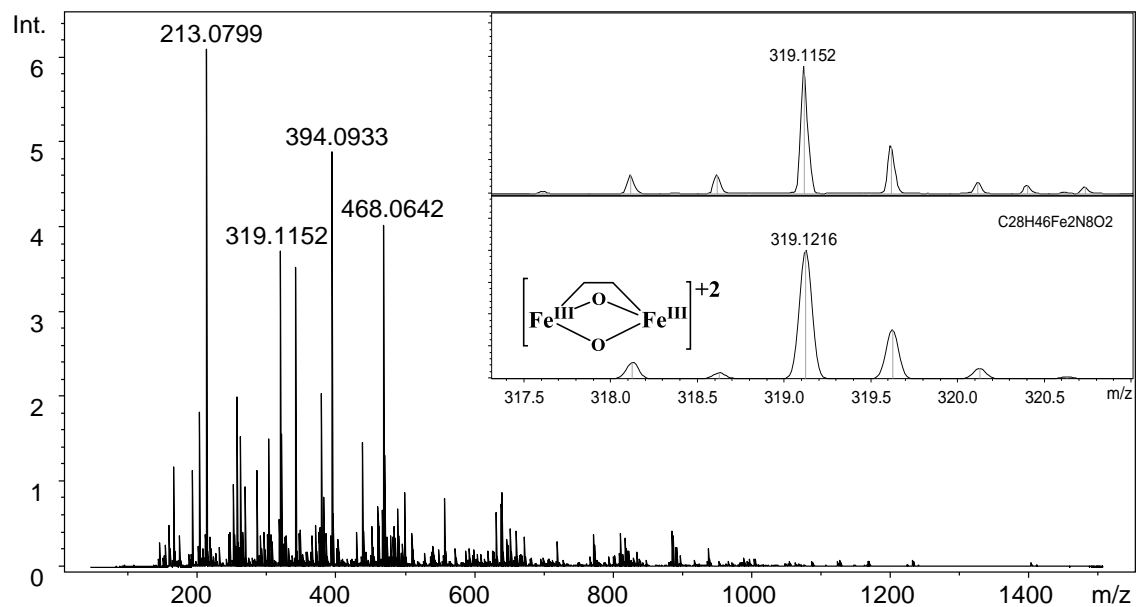


High resolution ESI-MS spectra of complex **2^{IV}=O** in acetonitrile with sPhIO. Top right: inset of the simulations of the peak at 313.7502 and 314.0852 m/z .

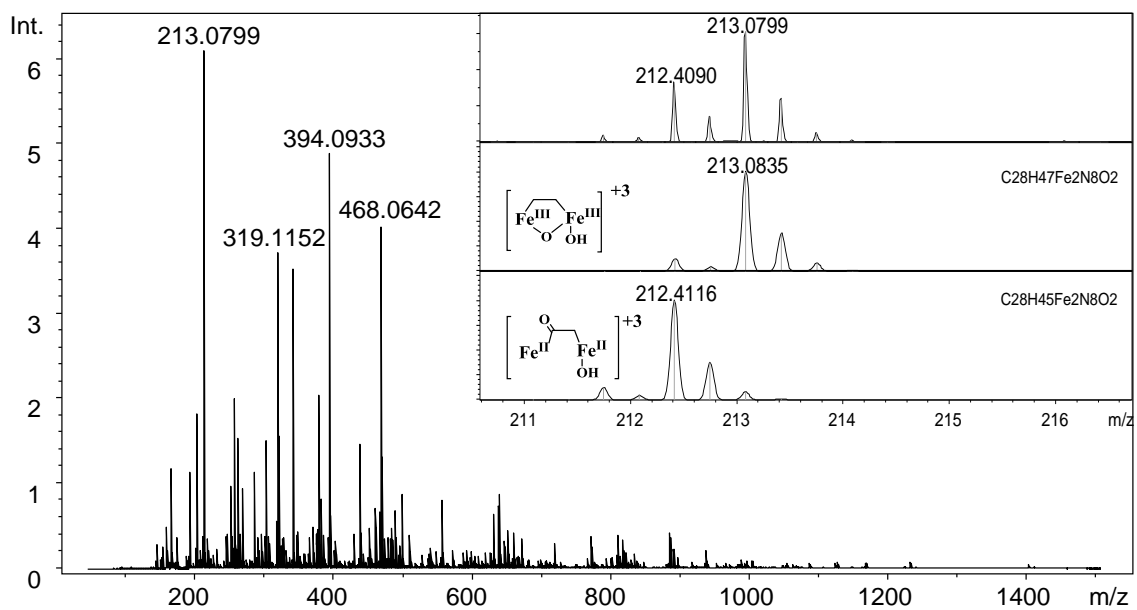
Annex



High resolution ESI-MS spectra of complex $2^{IV}=\text{O}$ in acetonitrile with sPhIO. Top right: inset of the simulation of the peak at 307.7463 m/z .



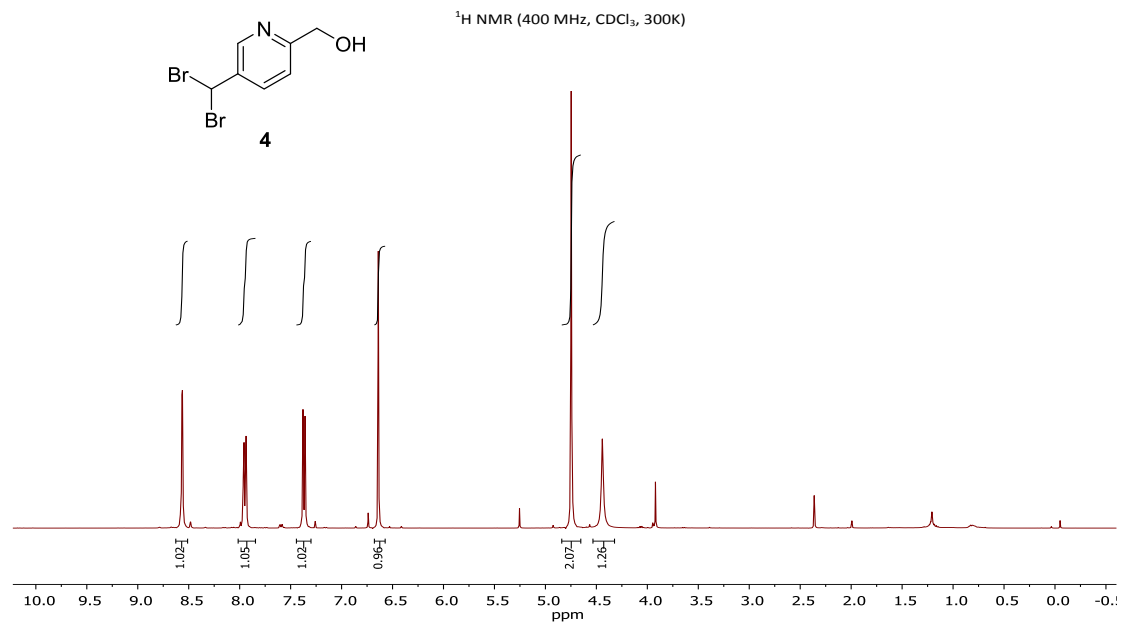
High resolution ESI-MS spectra of complex $1^{IV}=\text{O}$ in acetonitrile with TBAIO₄. Top right: inset of the simulation of the peak at 319.1152 m/z .



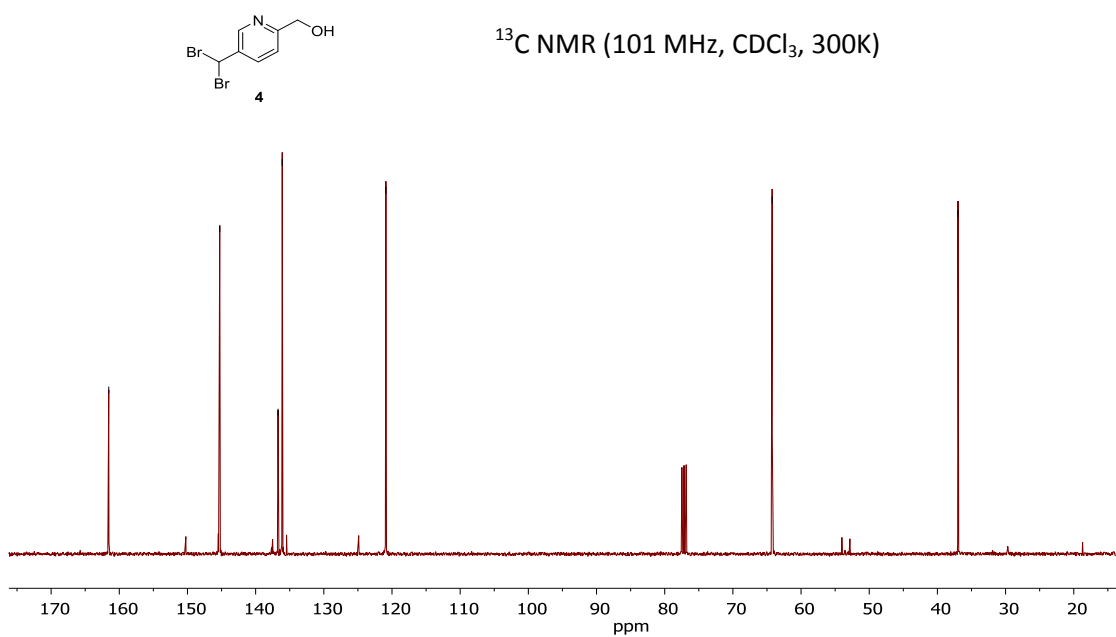
High resolution ESI-MS spectra of complex **1^{IV}=O** in acetonitrile with TBAIO₄. Top right: inset of the simulations at 213.0799 and 212.4090 m/z.

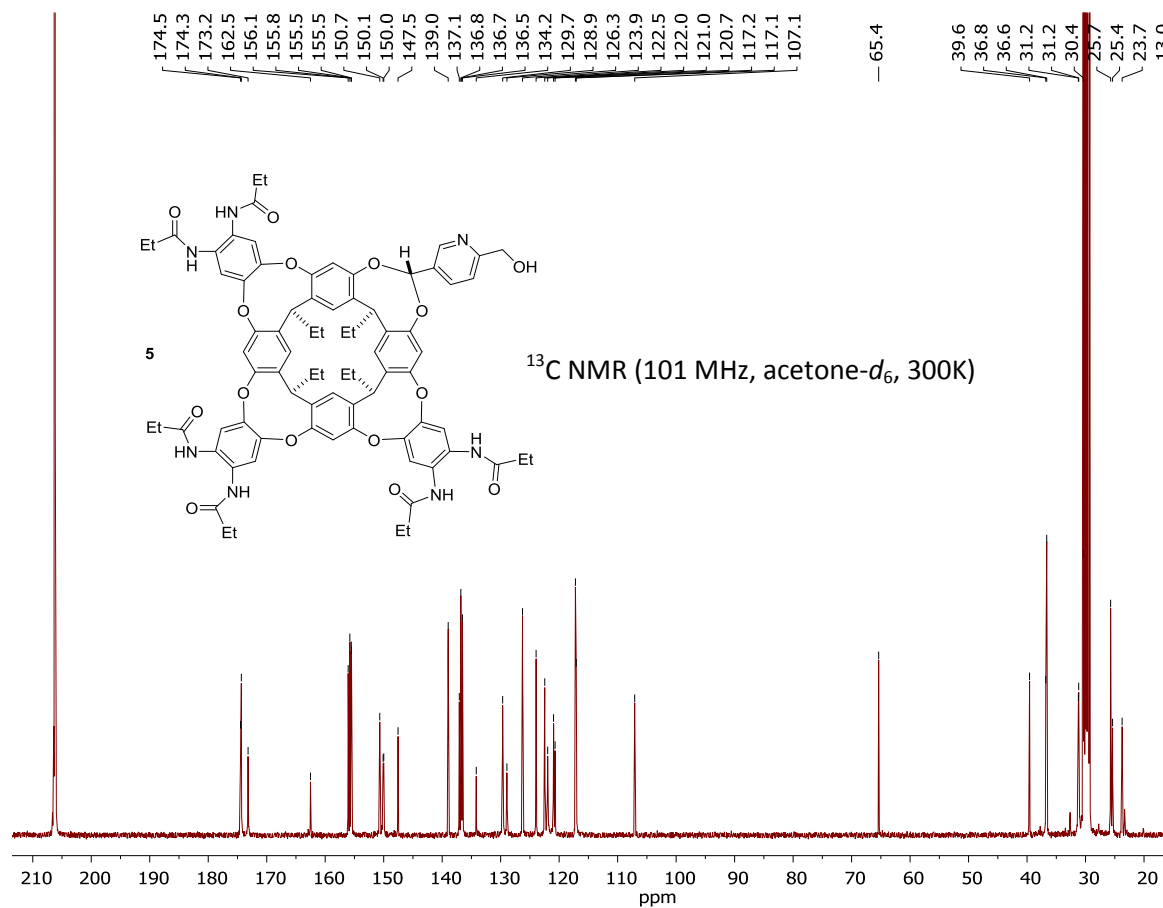
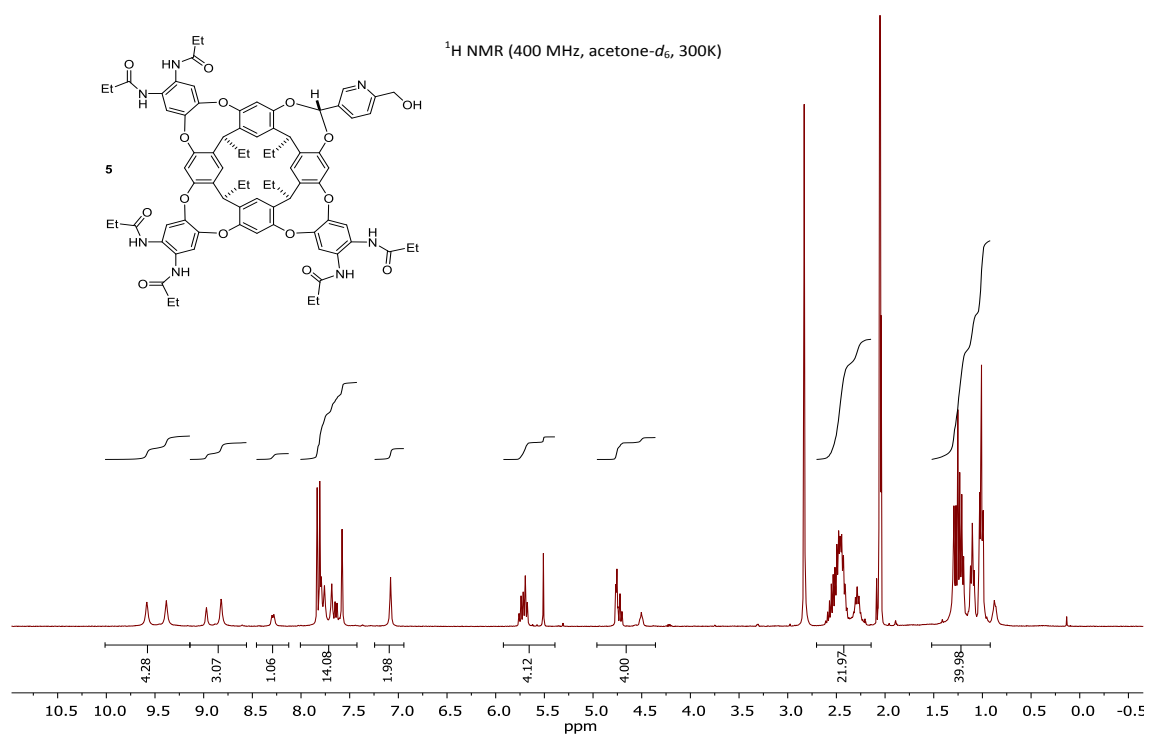
Annex chapter IV.

8. NMR and HMRS spectra

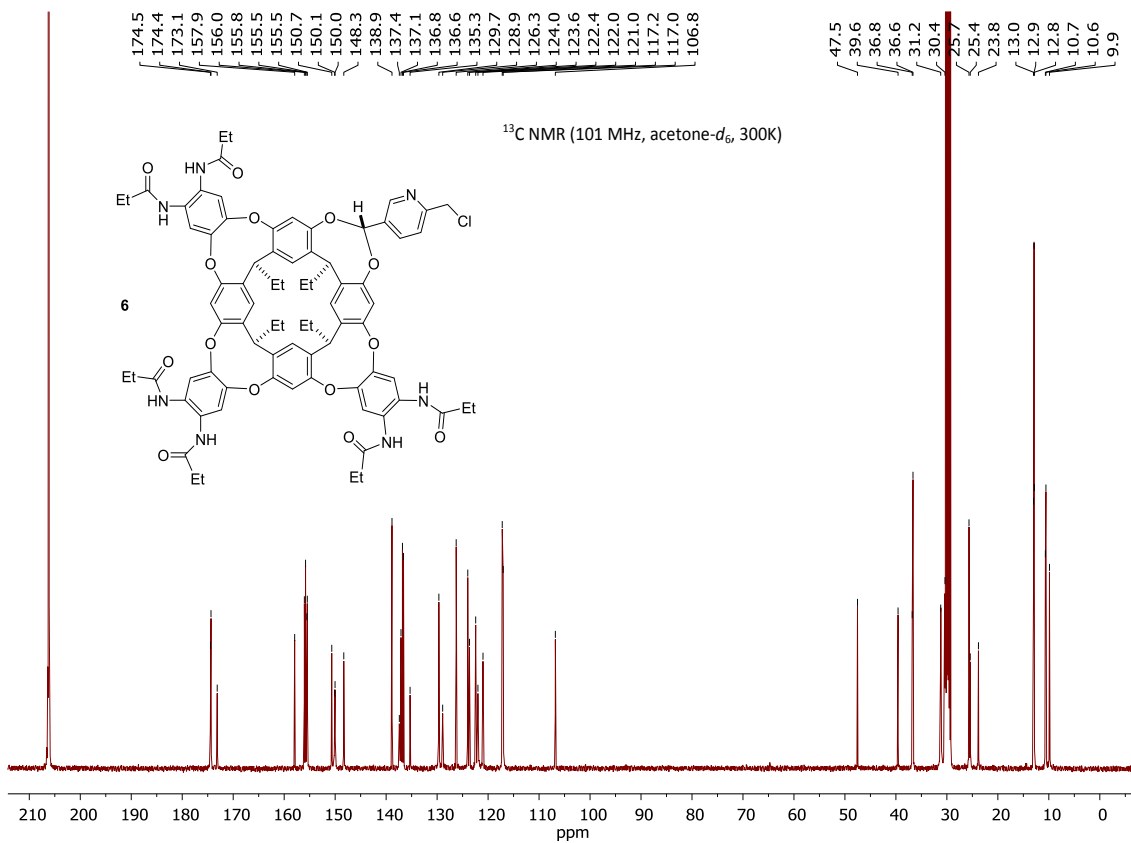
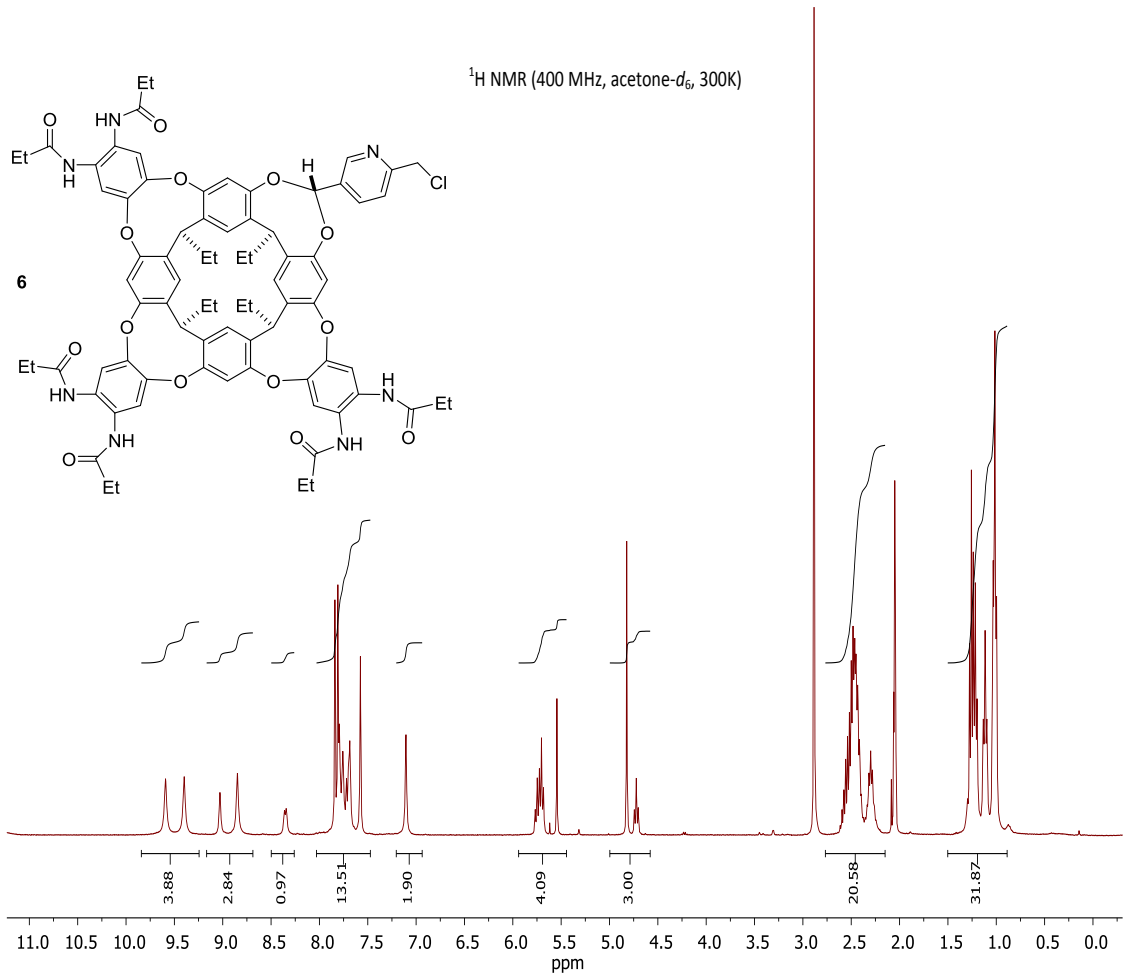


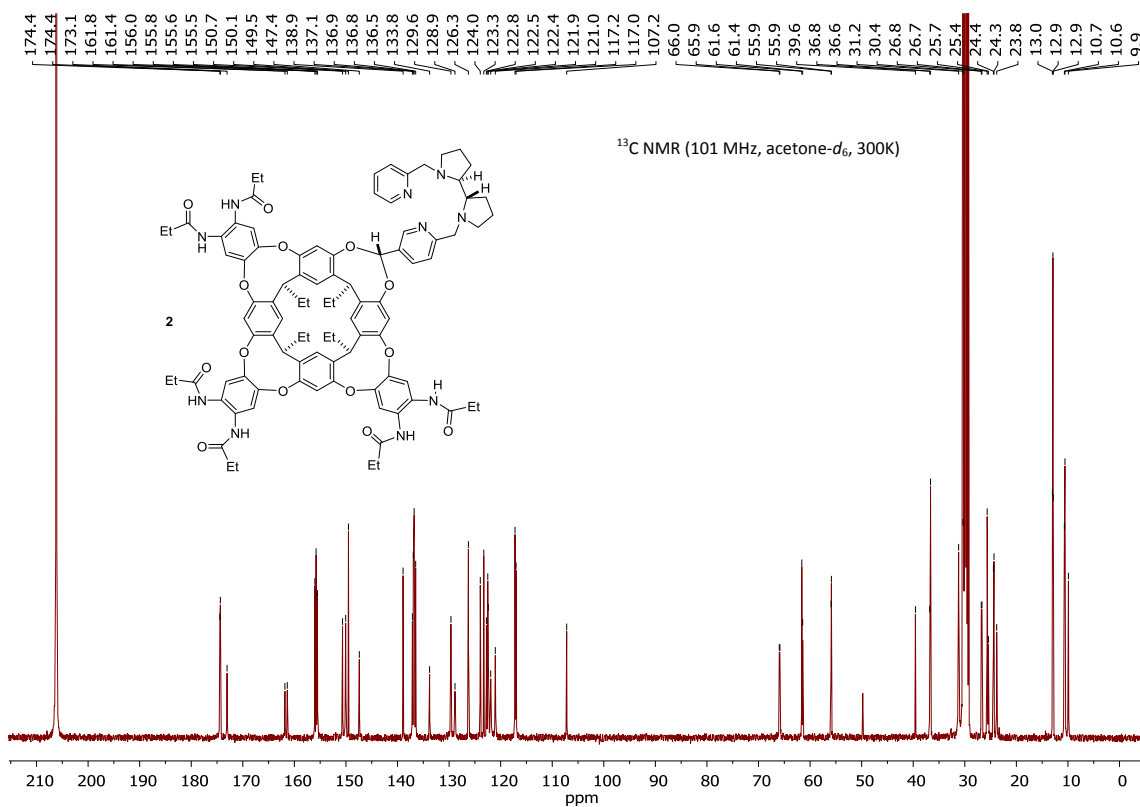
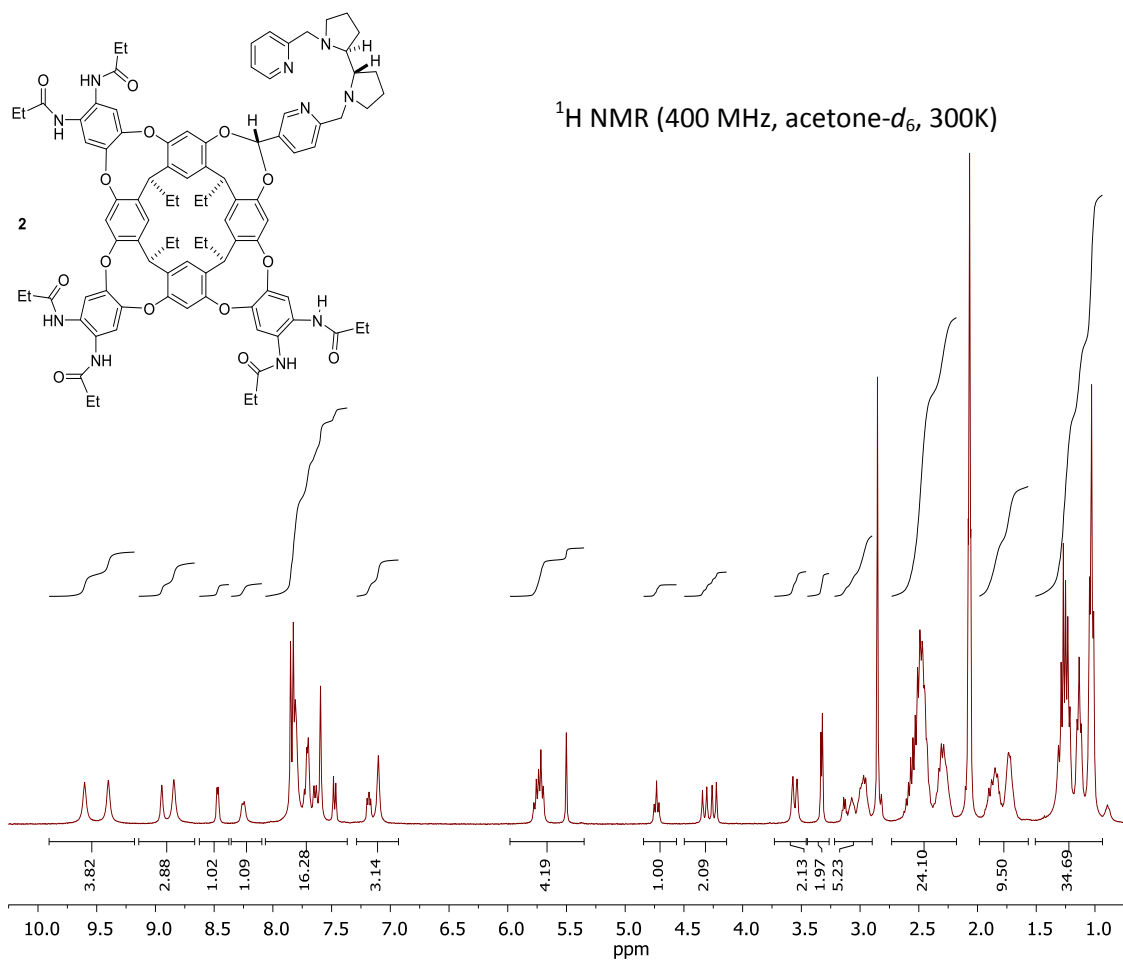
— 161.5 — 145.3 — 136.7 — 136.1 — 120.9 — 64.2 — 37.0

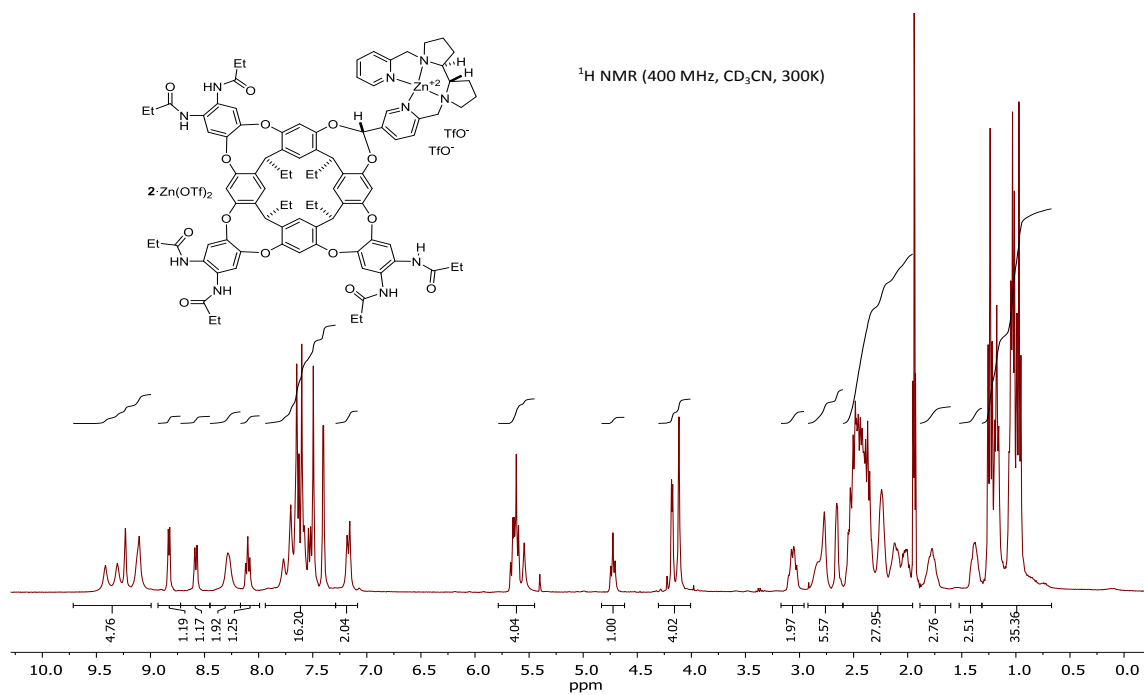
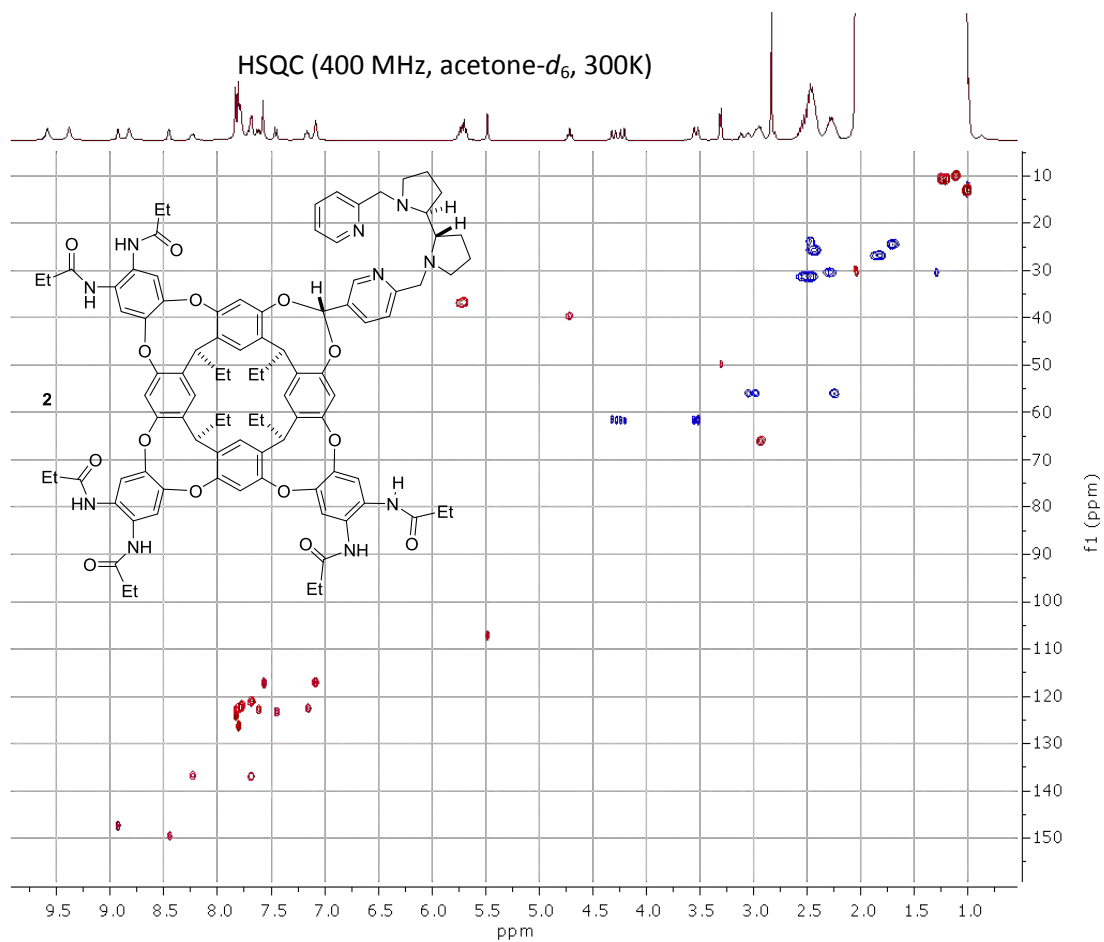


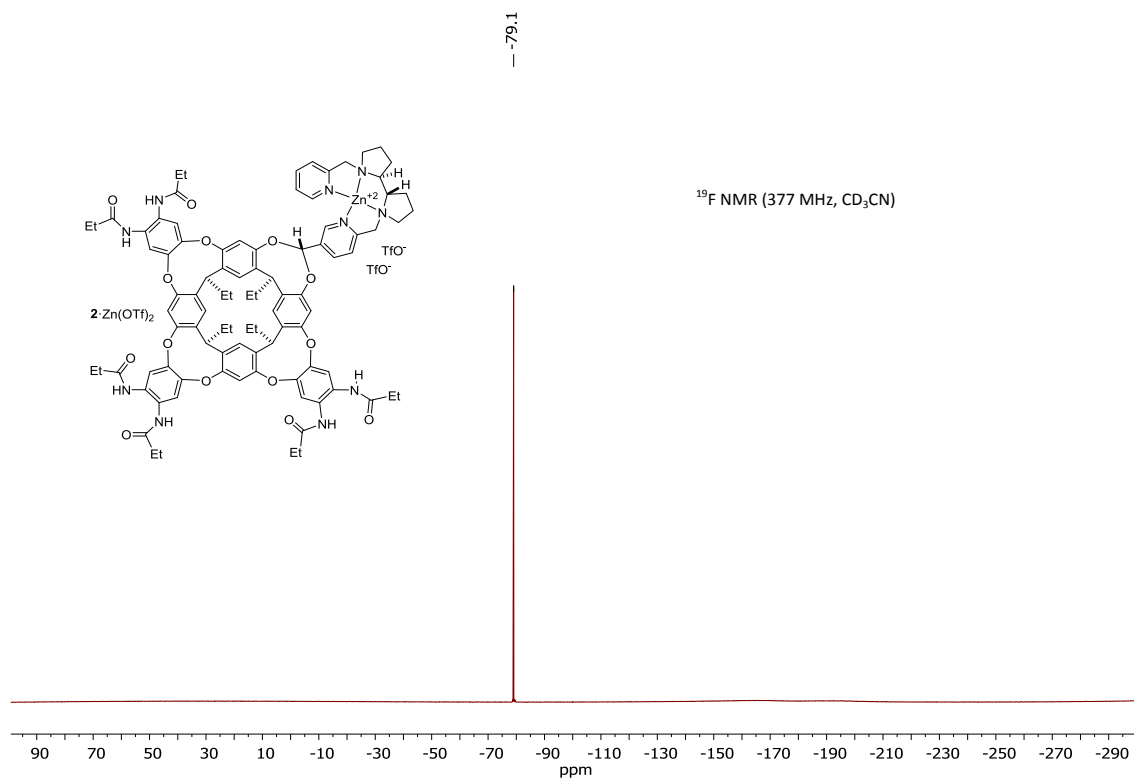
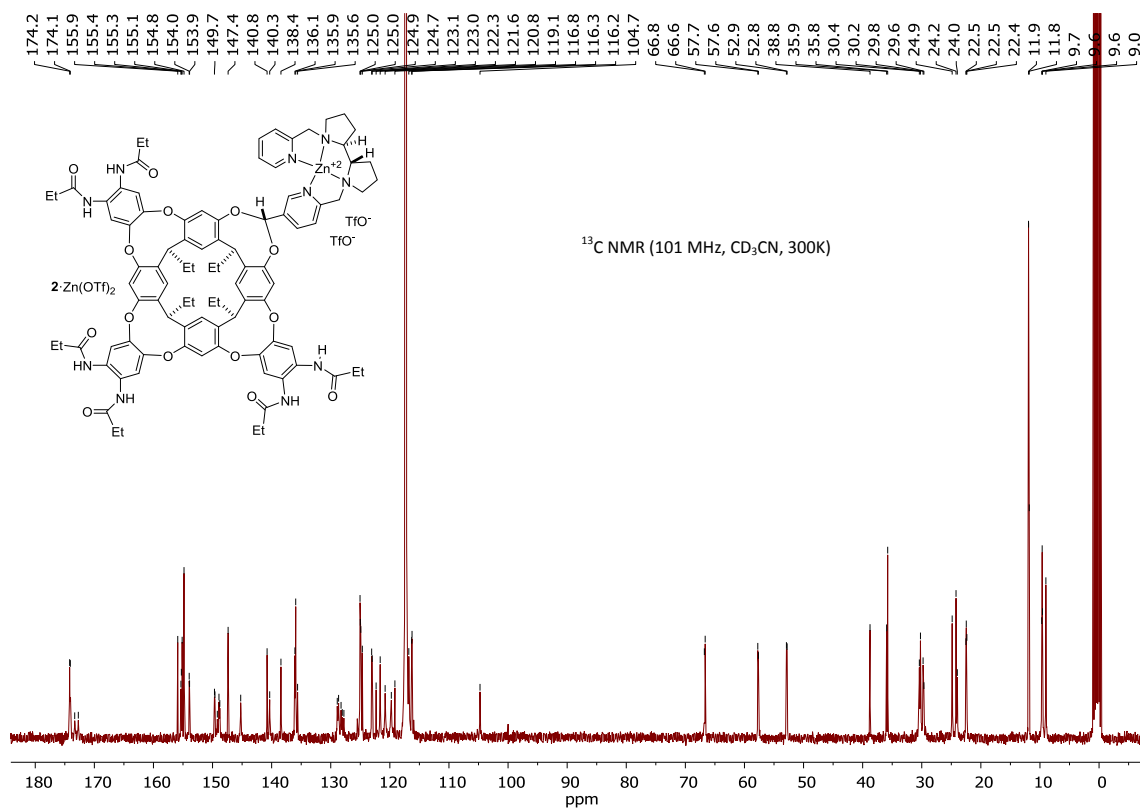


Annex

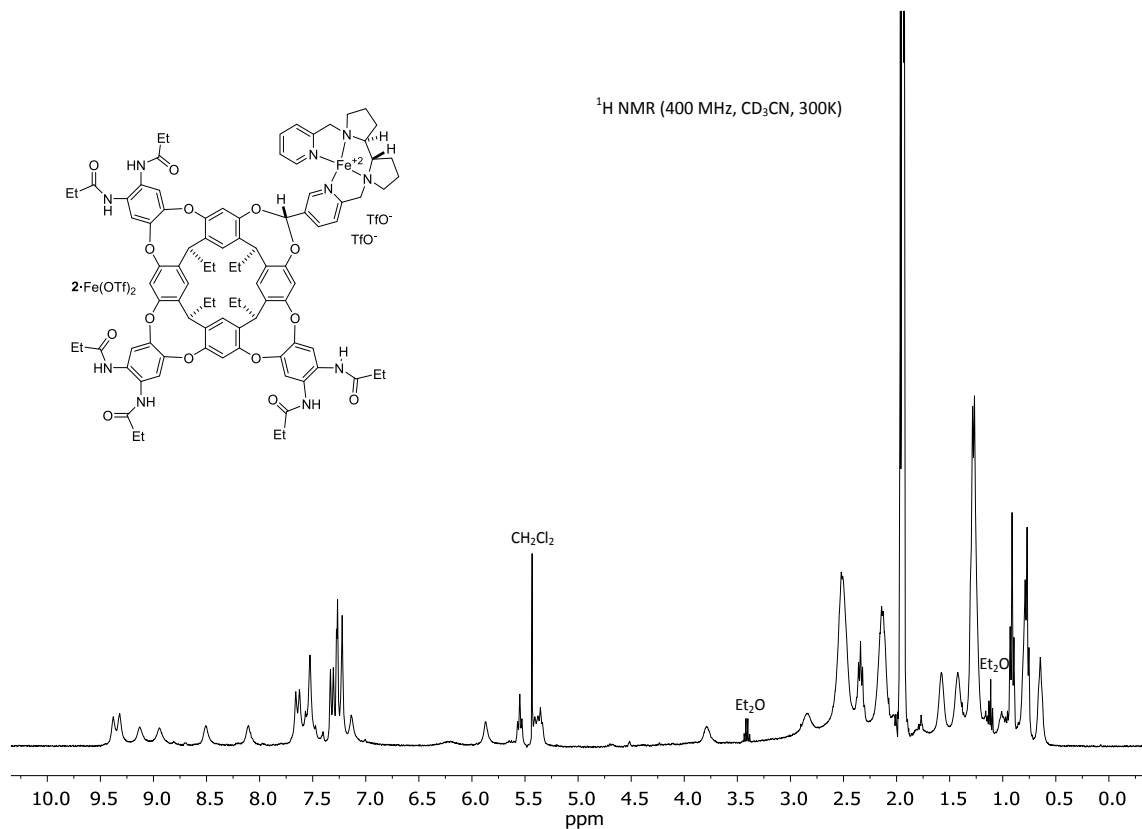




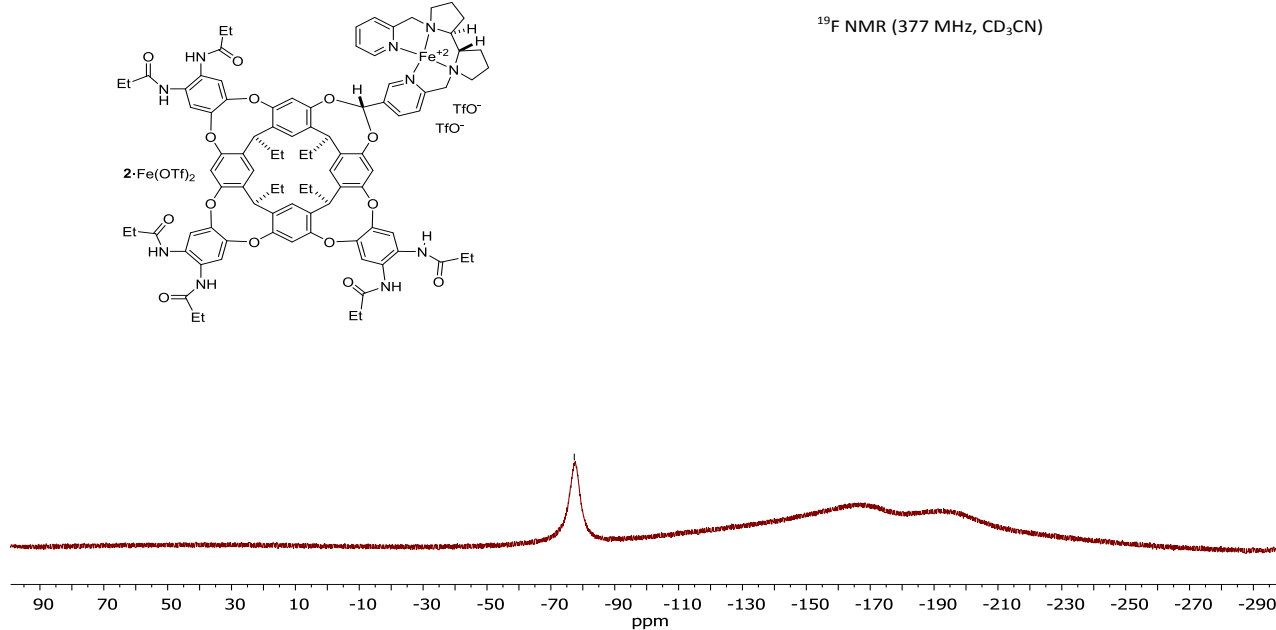


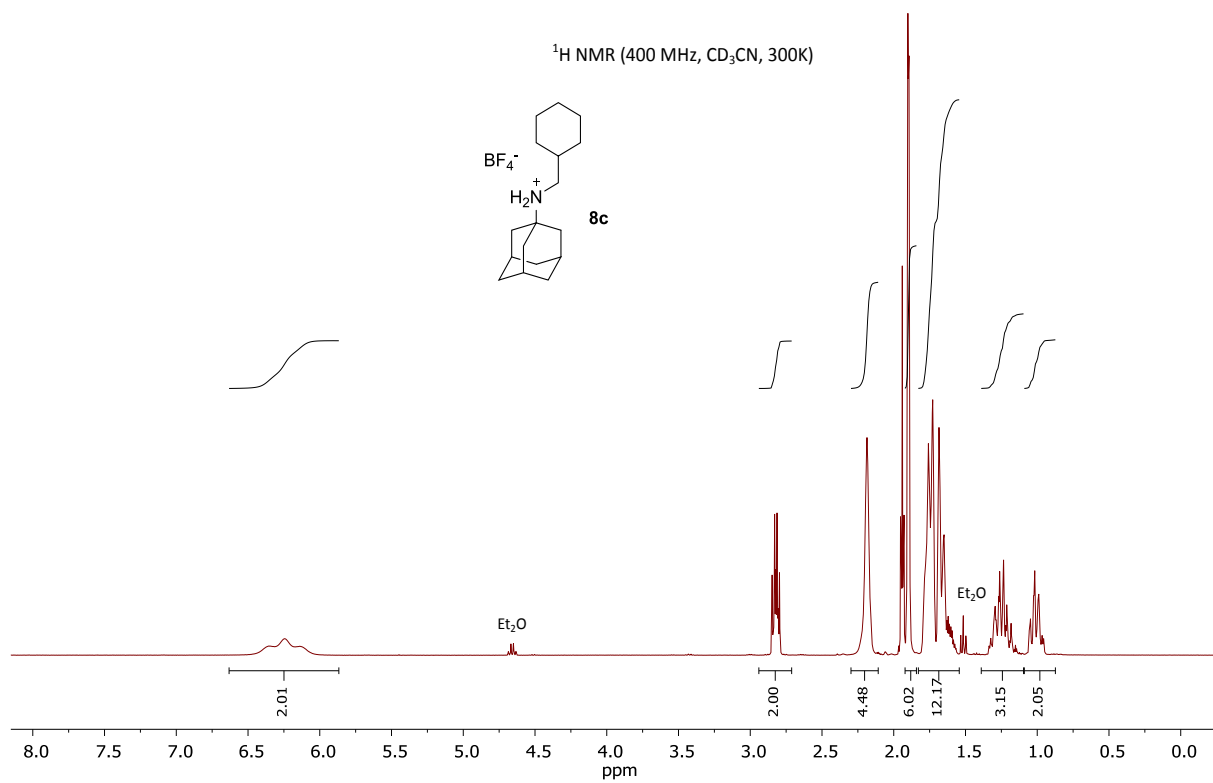
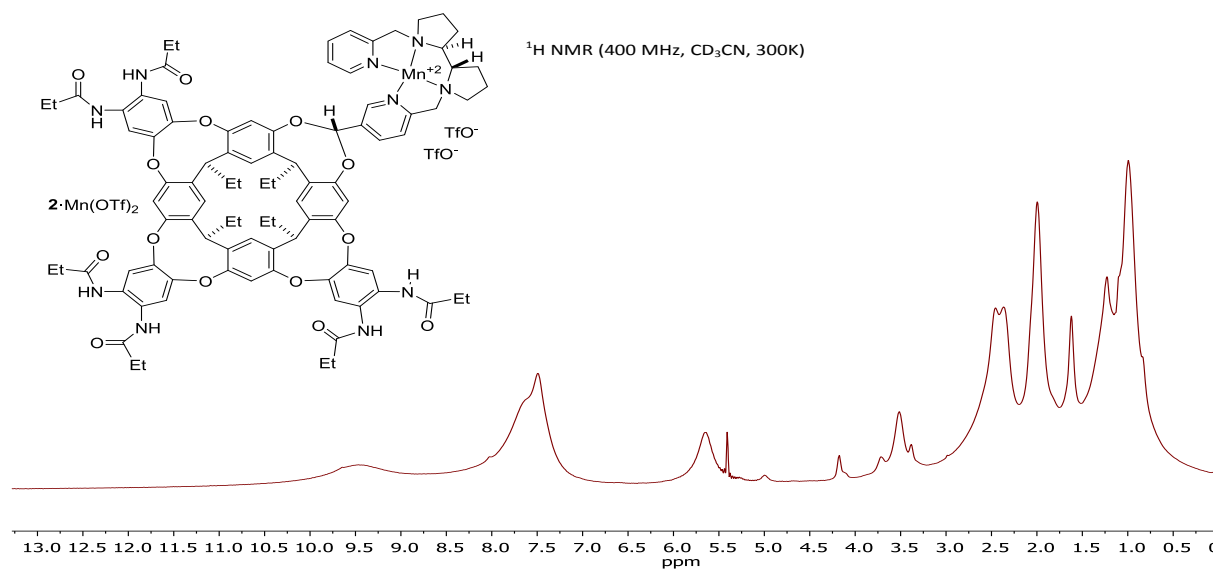


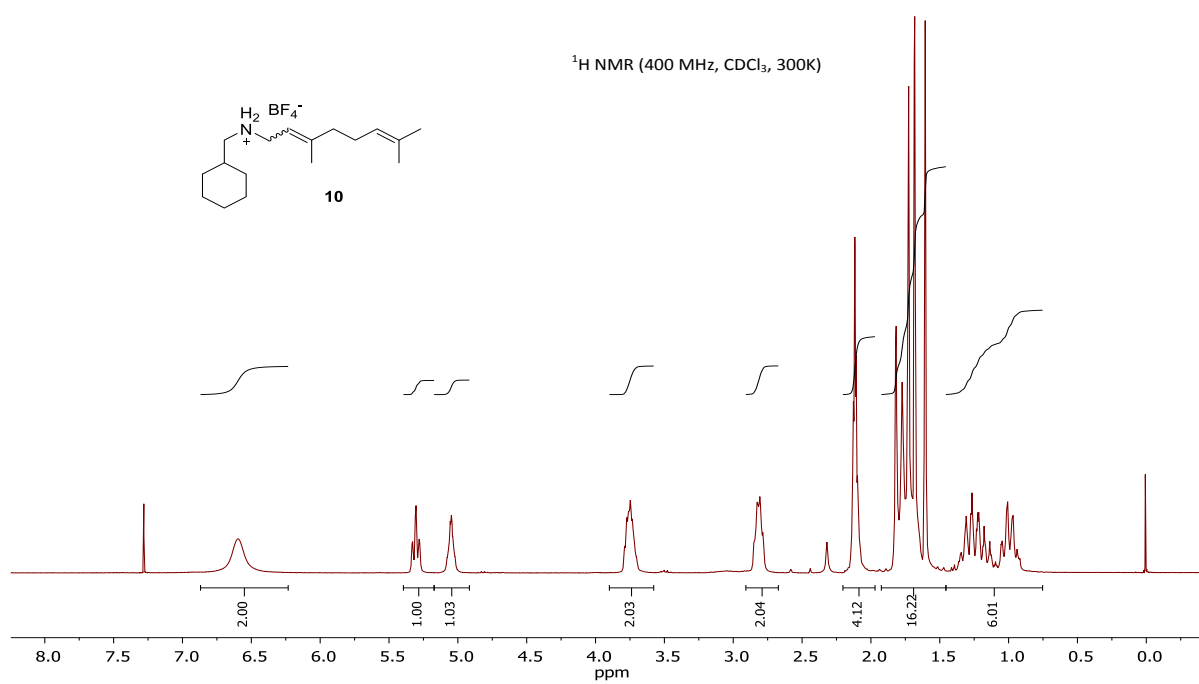
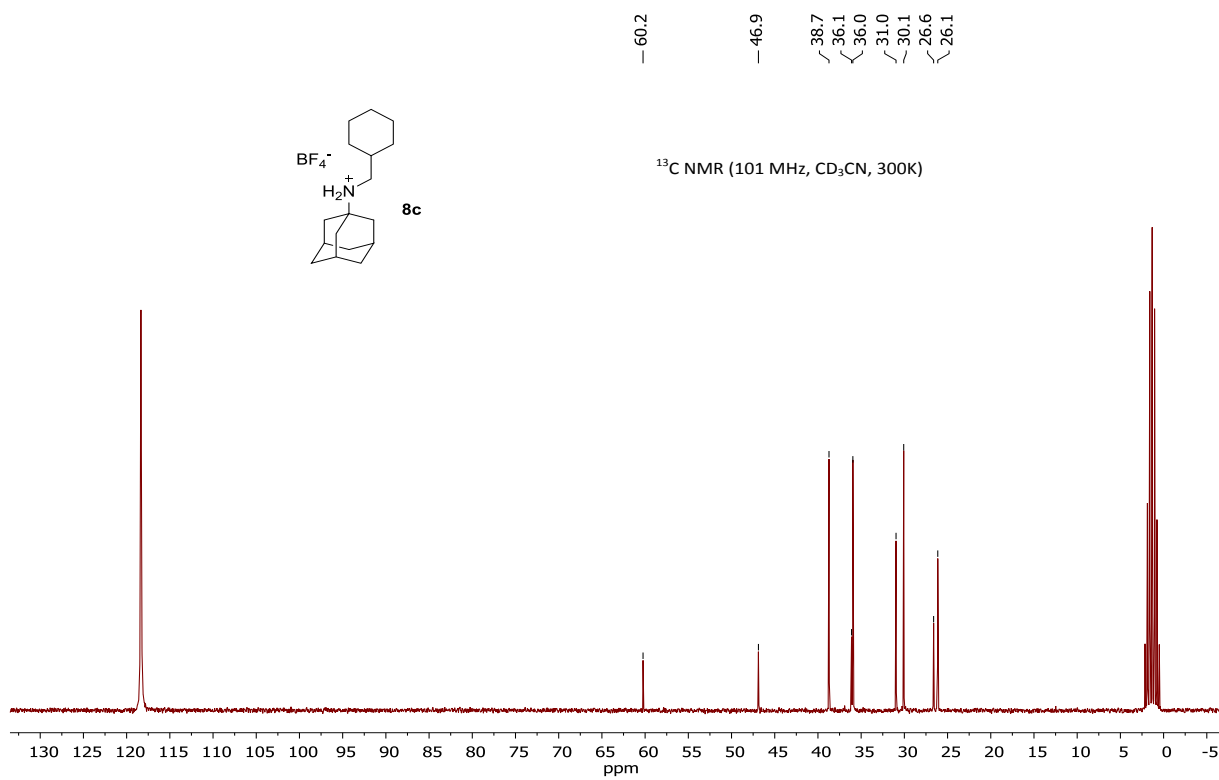
Annex

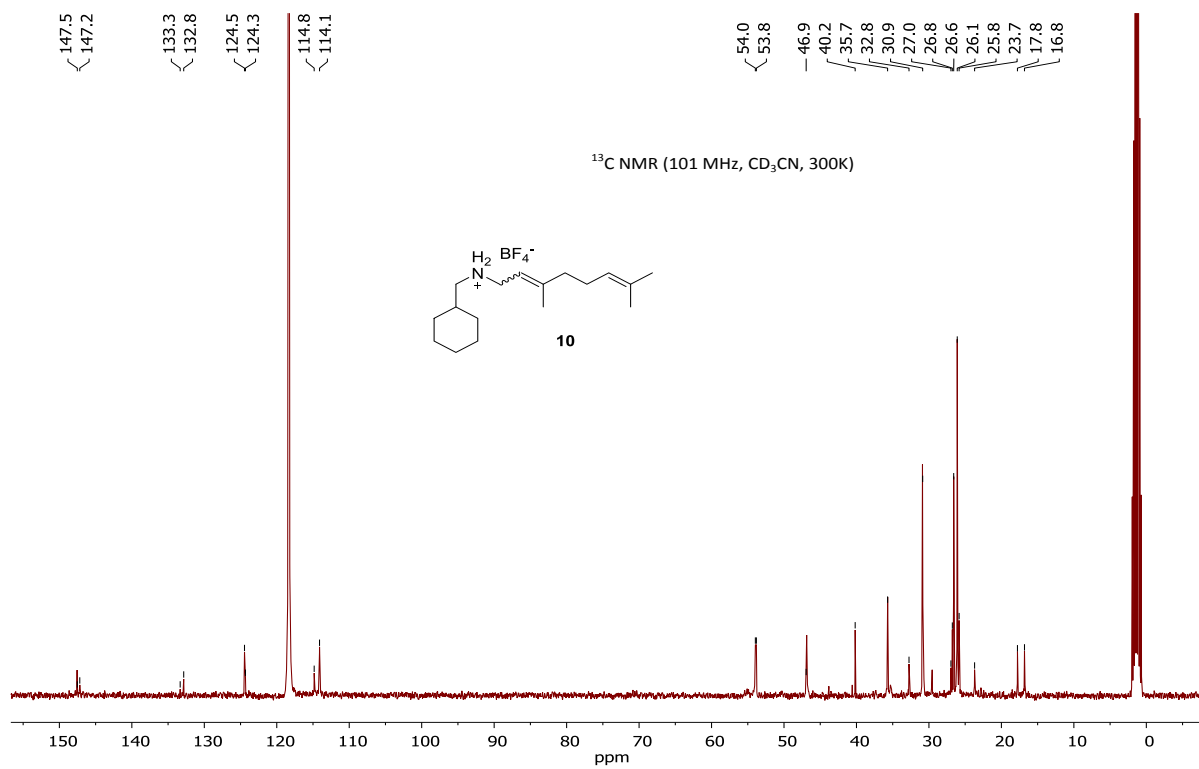


-77.3









4 HRMS (ESI-QTOF)

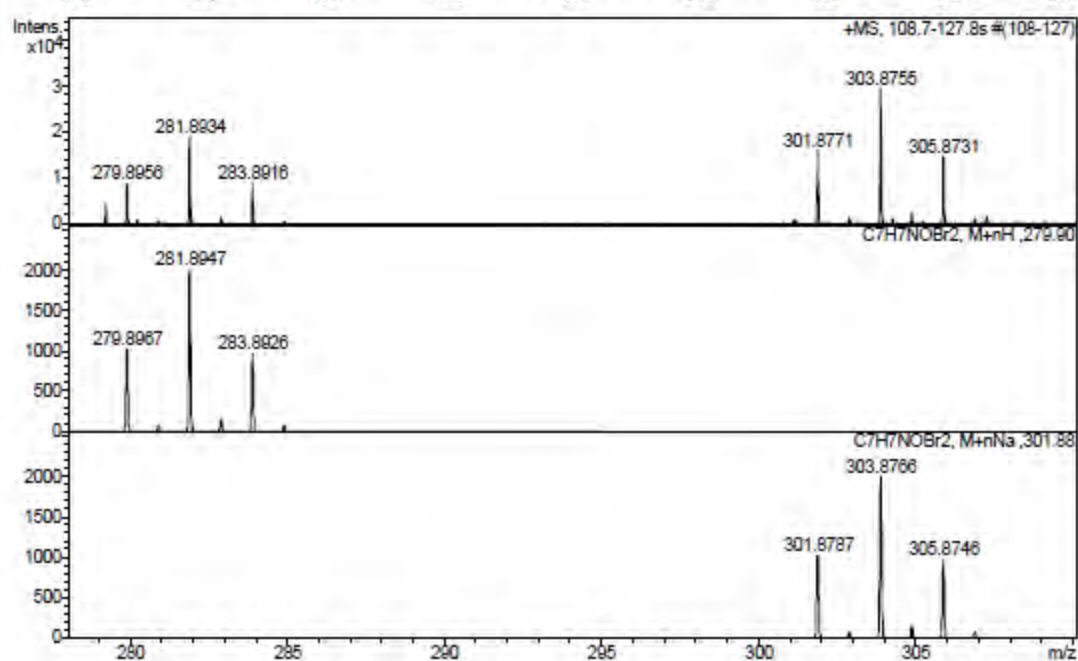
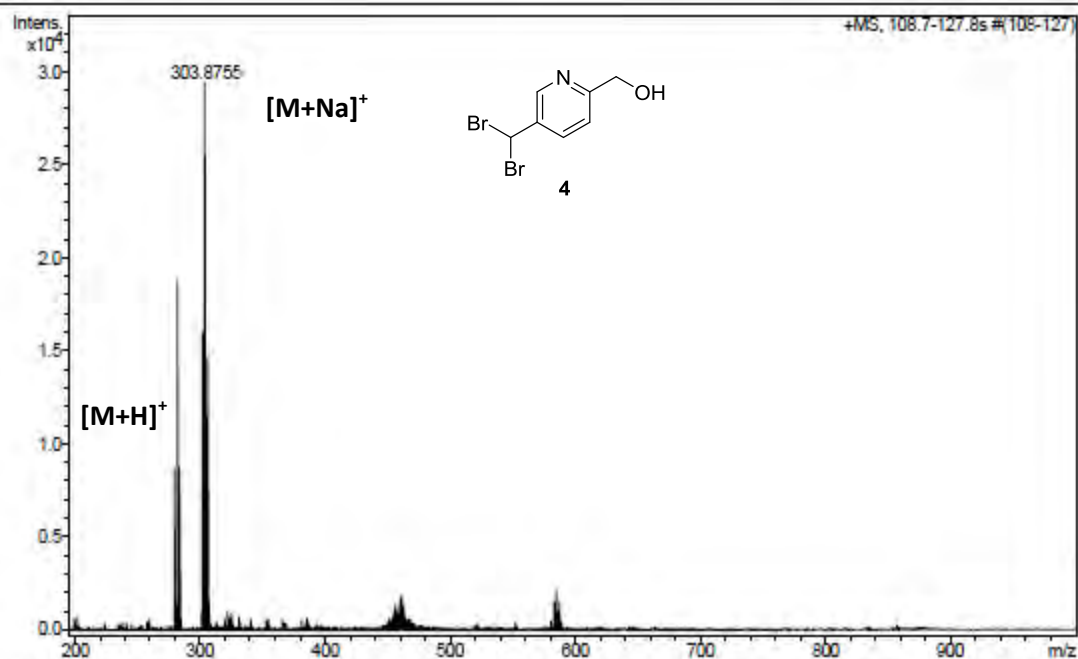
Generic Display Report

Analysis Info

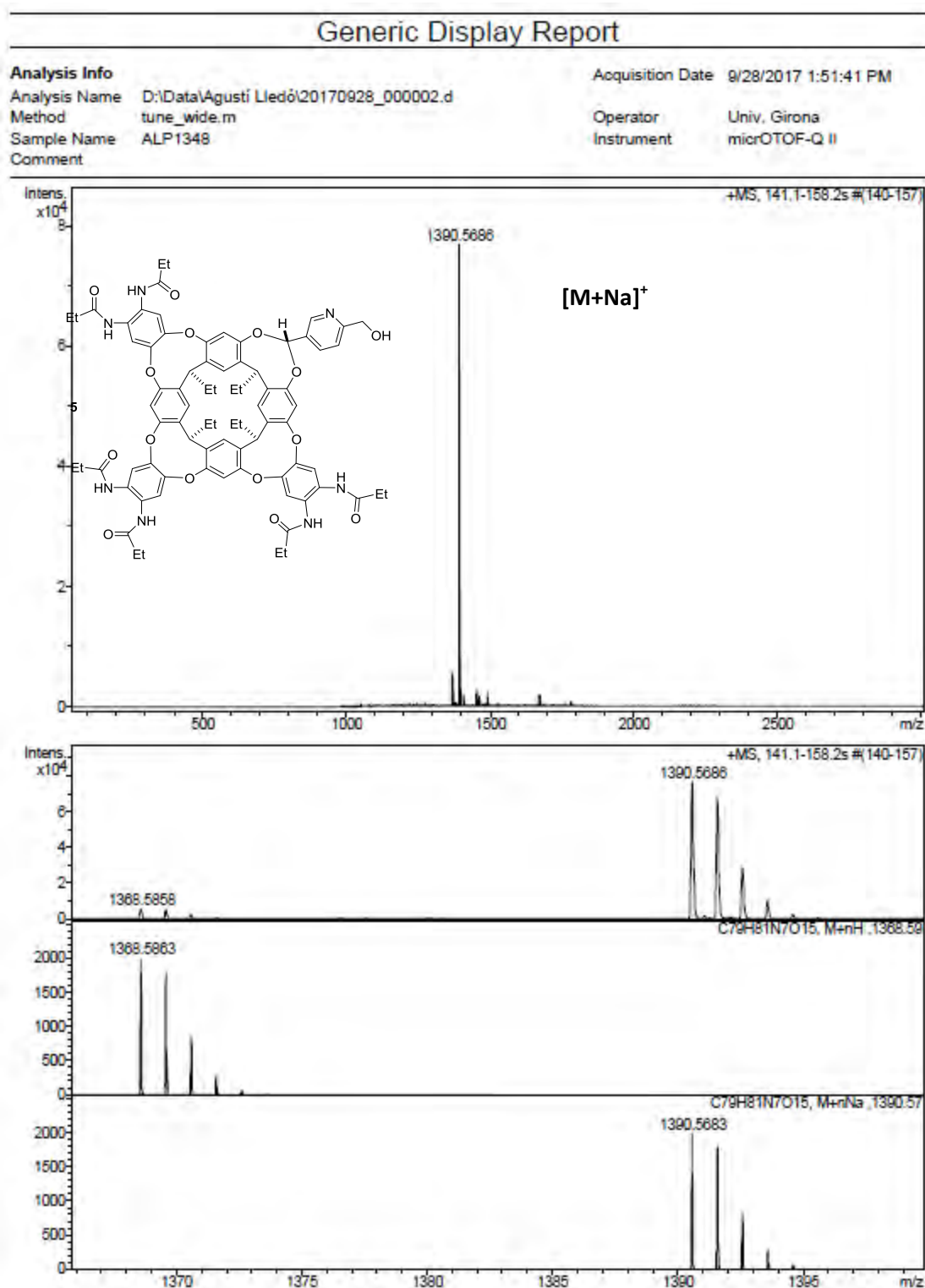
Analysis Name D:\Data\Diego Vidal\20170529_000001.d
Method tune_low.m
Sample Name DV306 (Br2-pyr-OH)
Comment

Acquisition Date 5/29/2017 11:51:39 AM

Operator Univ. Girona
Instrument micrOTOF-Q II



5 HRMS (ESI-QTOF)



6 HRMS (ESI-QTOF)

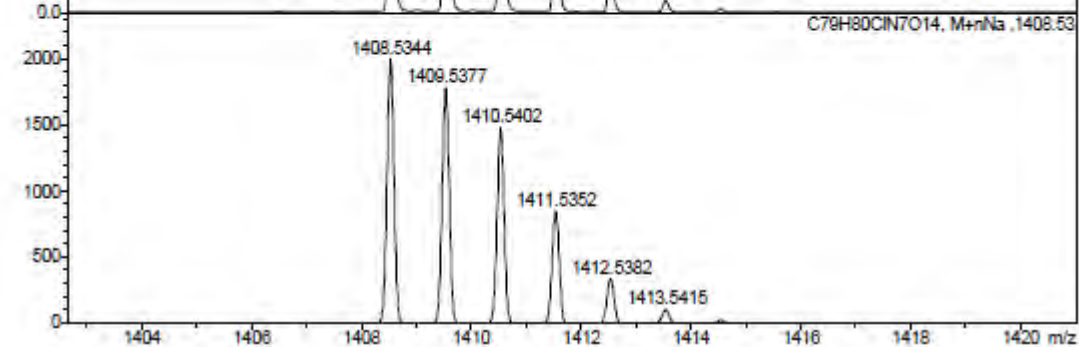
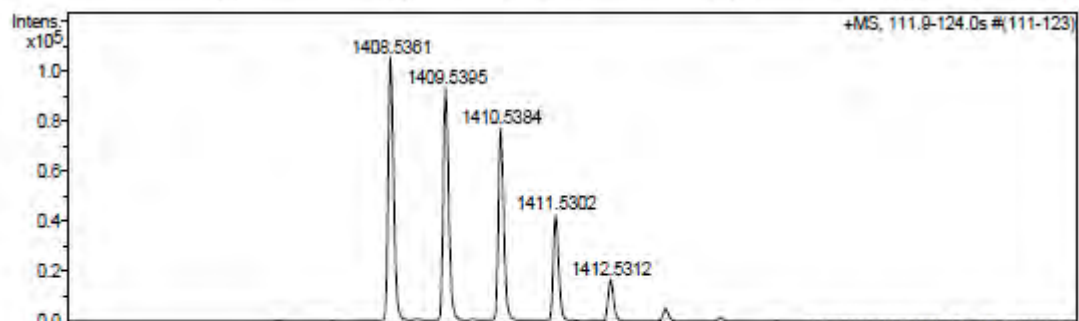
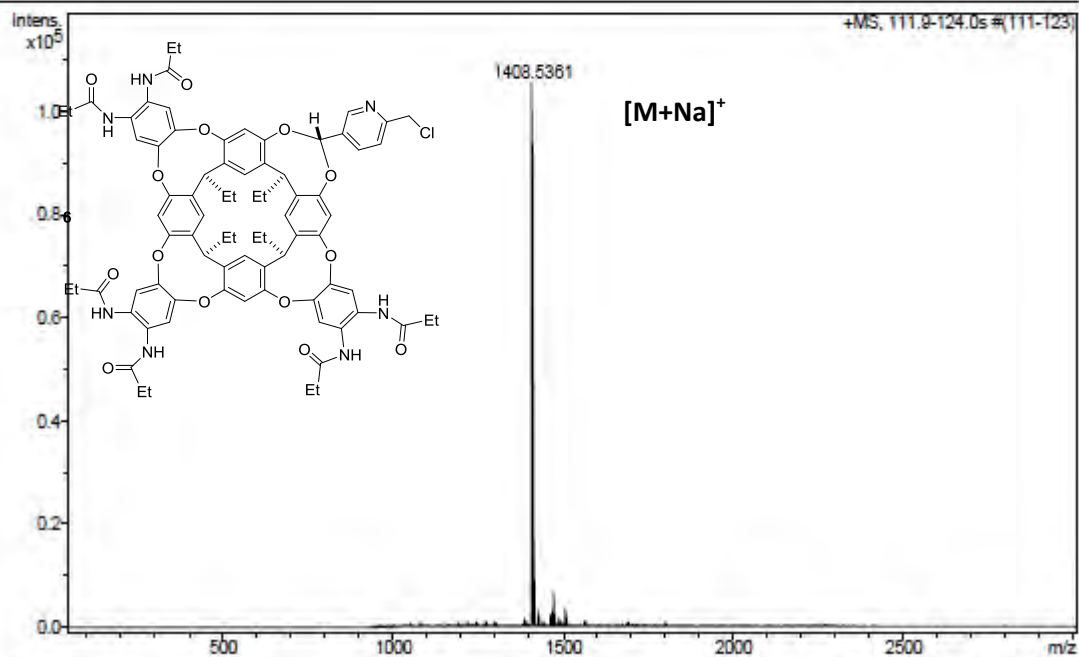
Generic Display Report

Analysis Info

Analysis Name D:\Data\Agusti Lledó\20170928_000003.d
Method tune_wide.m
Sample Name ALP1351
Comment

Acquisition Date 9/28/2017 2:00:11 PM

Operator Univ. Girona
Instrument micrOTOF-Q II



2 HRMS (ESI-QTOF)

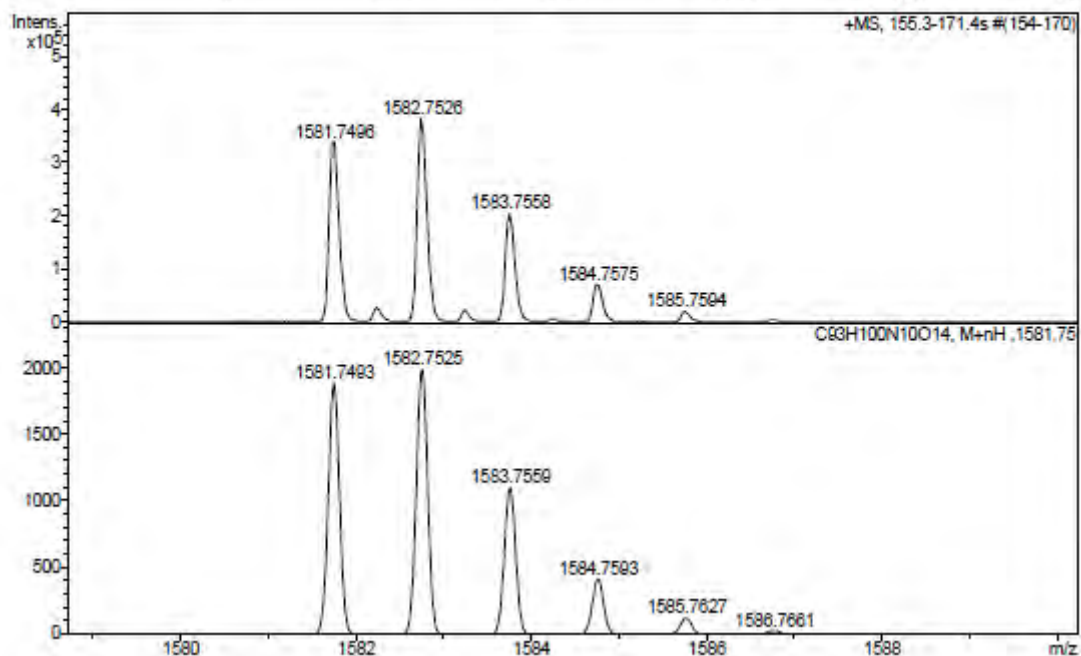
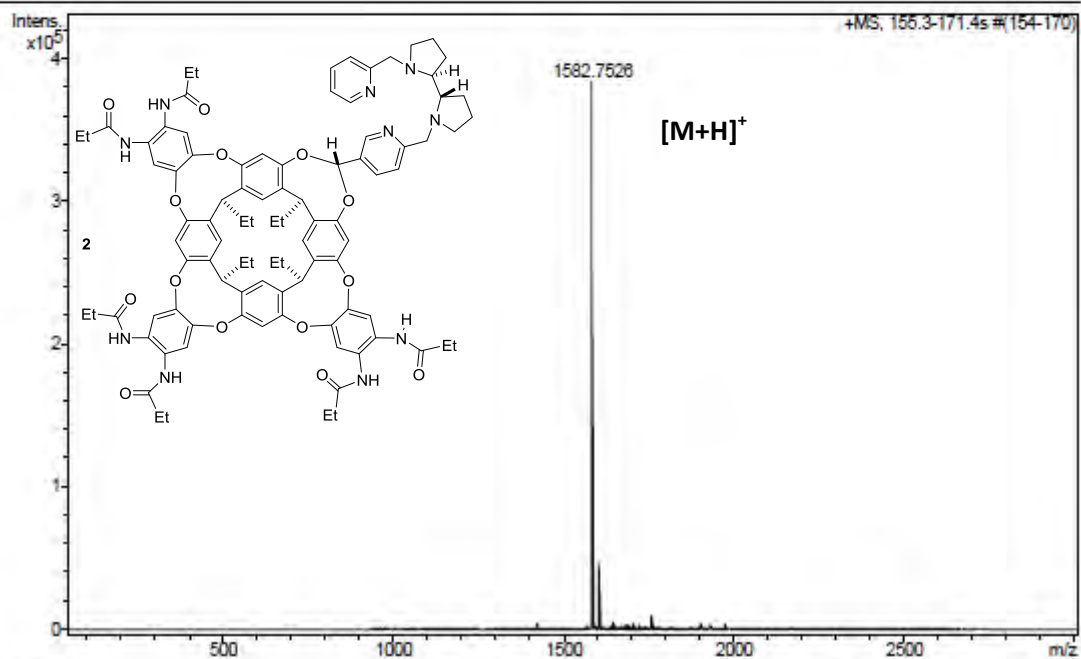
Generic Display Report

Analysis Info

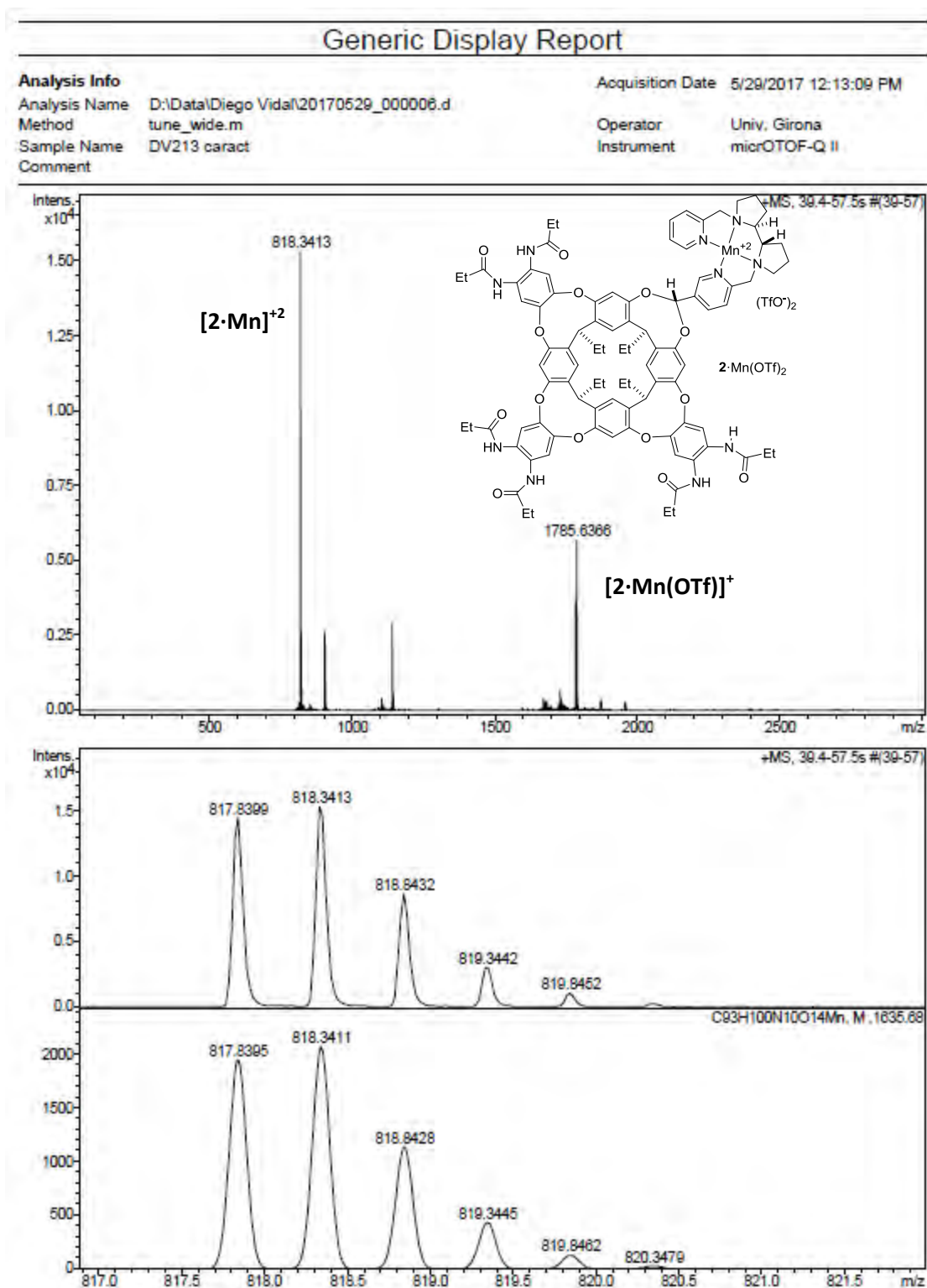
Analysis Name D:\Data\Agusti Lledó\20170828_000004.d
Method tune_wide.m
Sample Name CAL
Comment

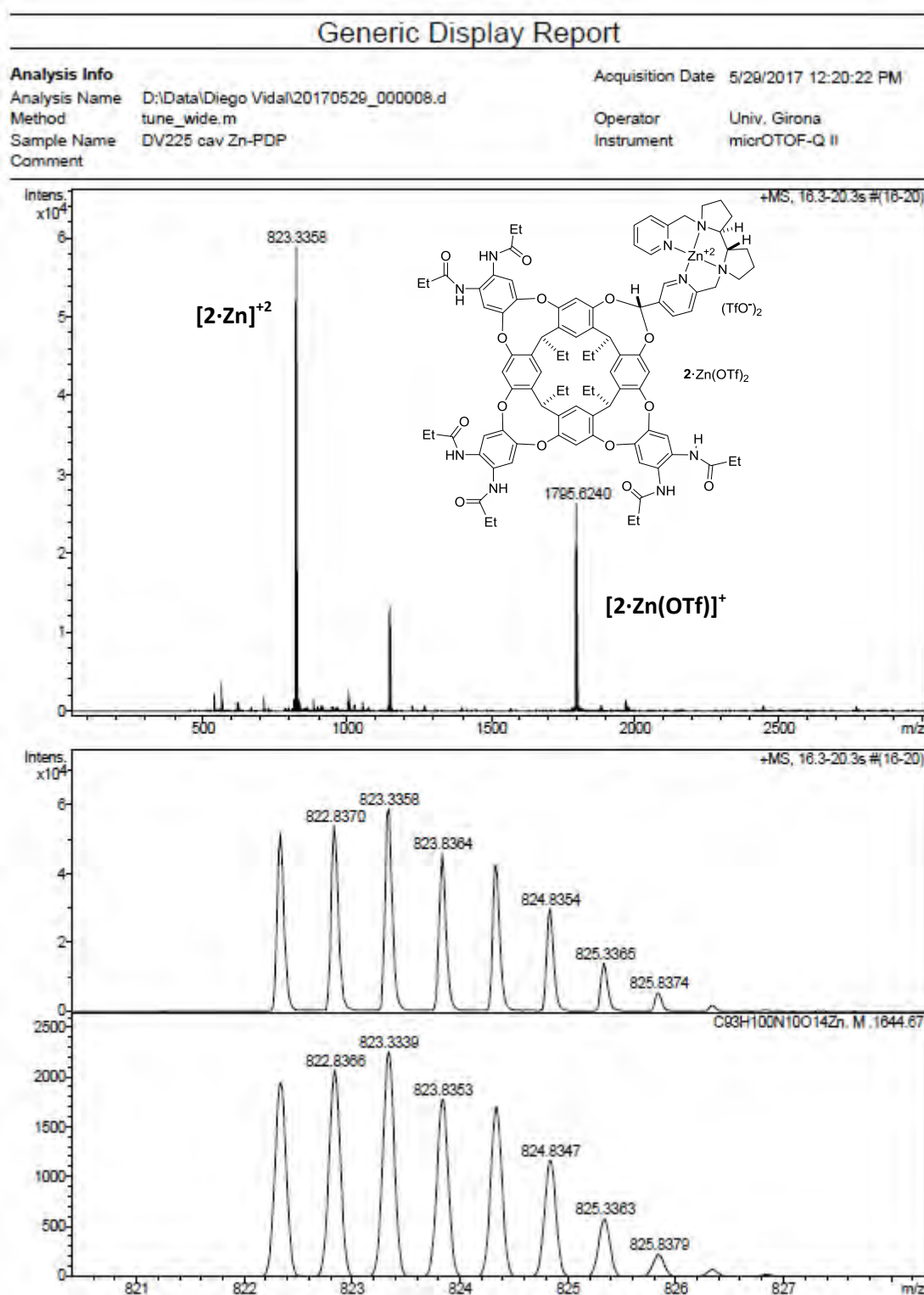
Acquisition Date 9/28/2017 3:44:03 PM

Operator Univ. Girona
Instrument micrOTOF-Q II



2-Mn(OTf)₂ HRMS (ESI-QTOF)



2-Zn(OTf)₂ HRMS (ESI-QTOF)

8c HRMS (ESI-QTOF)

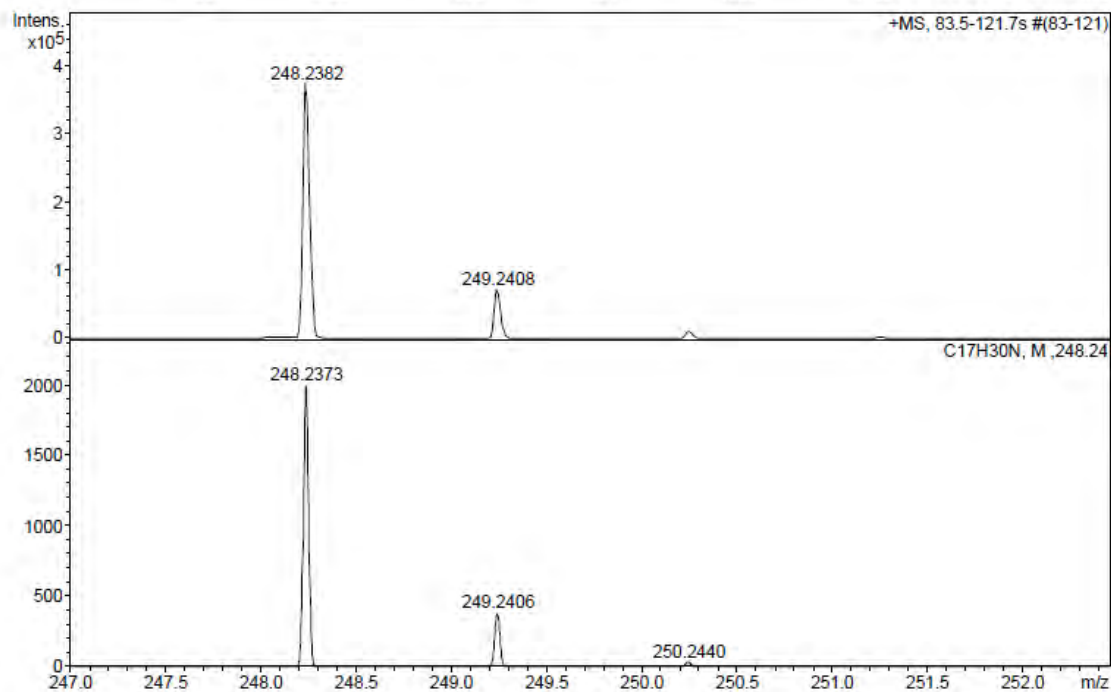
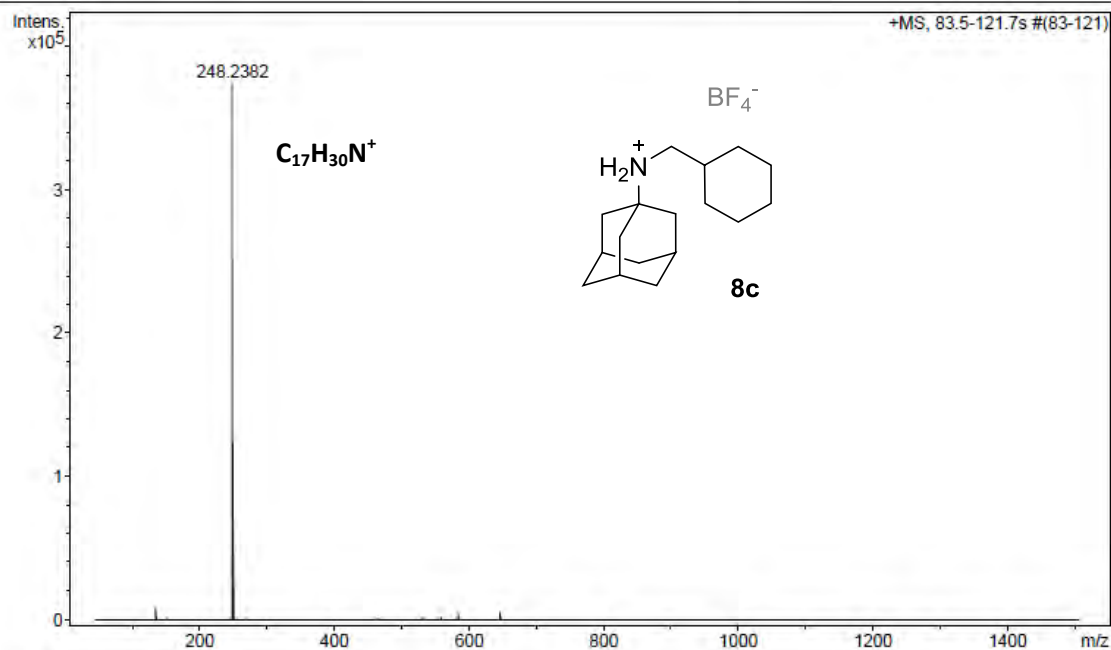
Generic Display Report

Analysis Info

Analysis Name D:\Data\Diego Vidal\20171006_000005.d
Method tune_low.m
Sample Name cyH-Ad
Comment

Acquisition Date 10/6/2017 10:12:28 AM

Operator Univ. Girona
Instrument micrOTOF-Q II



10 HRMS (ESI-QTOF)

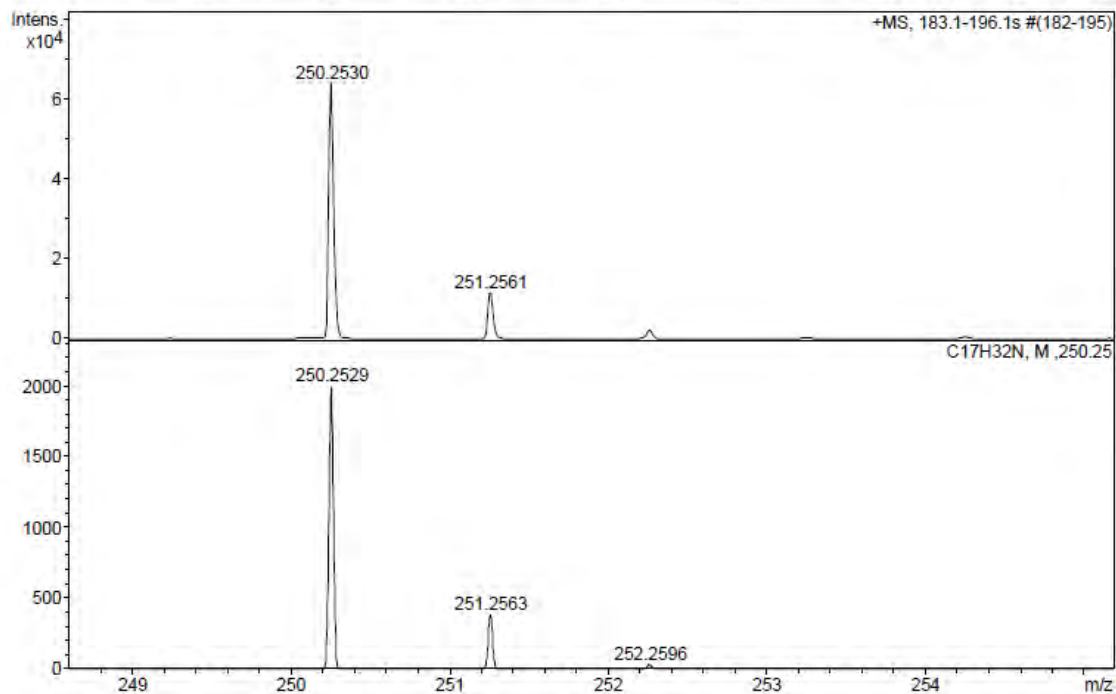
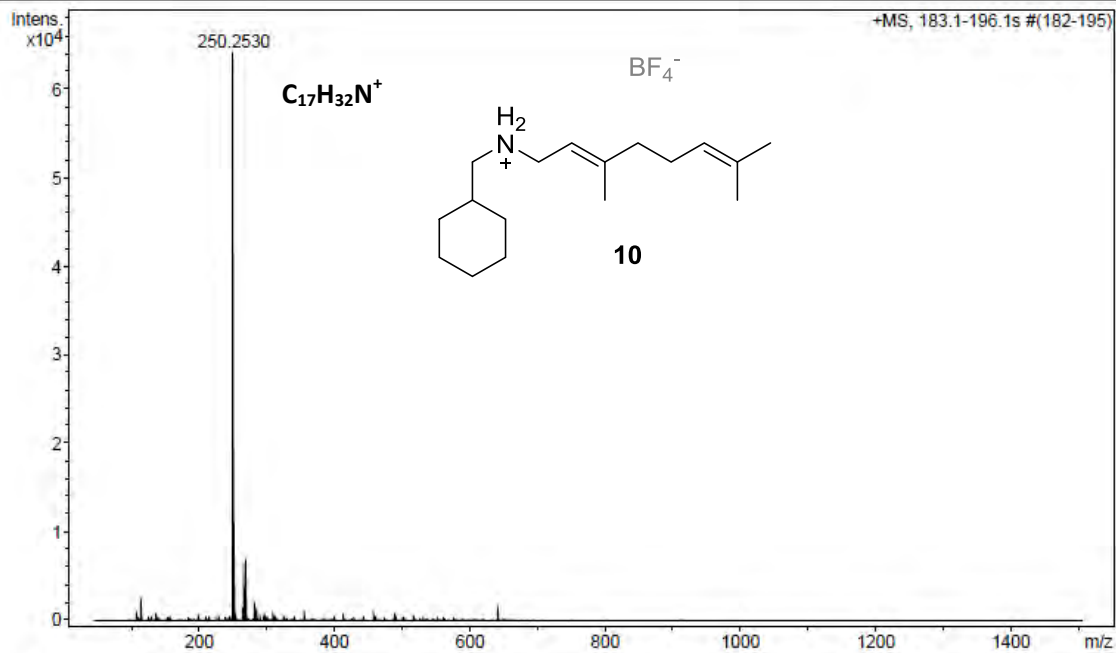
Generic Display Report

Analysis Info

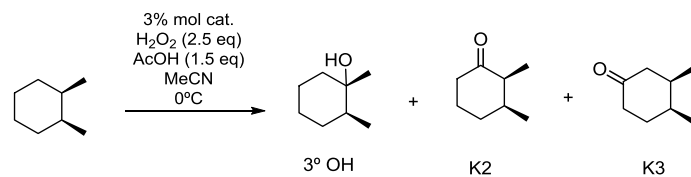
Analysis Name D:\Data\Diego Vidal\20171006_000002.d
Method tune_low.m
Sample Name cyH-geraniol
Comment

Acquisition Date 10/6/2017 9:56:50 AM

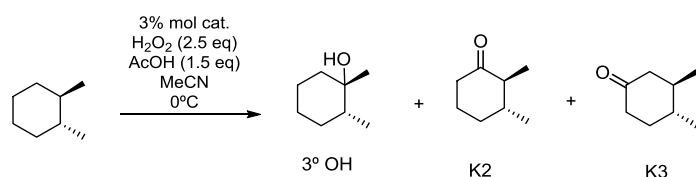
Operator Univ. Girona
Instrument microTOF-Q II



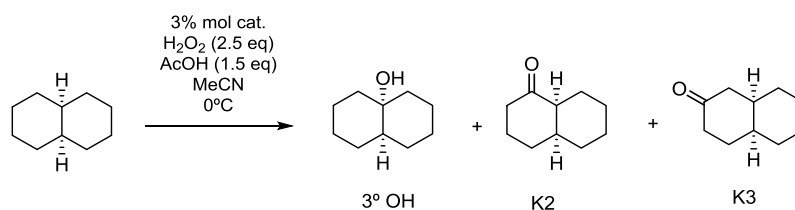
Annex chapter V.



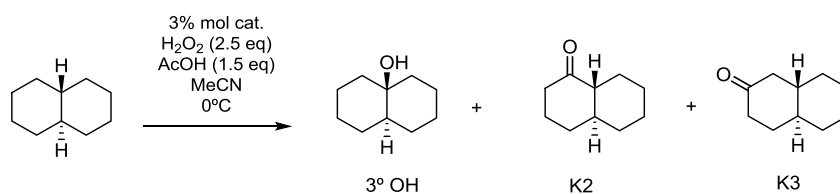
Catalyst	Conversion	Yield 3° OH	Yield K1 + K2
2·Fe(OTf)₂	69%	35%	2,5%
7b·Fe(OTf)₂	92%	46%	8%



Catalyst	Conversion	Yield 3° OH	Yield K1	Yield K2
2·Fe(OTf)₂	52%	10%	4%	4%
7b·Fe(OTf)₂	70%	20	8%	8%

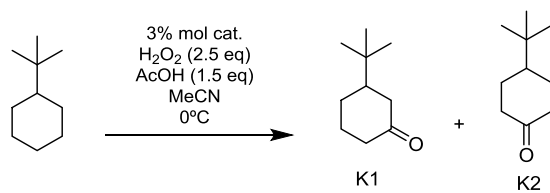


Catalyst	Conversion	Yield 3° OH	Yield K1	Yield K2
2·Fe(OTf)₂	83%	34%	5%	4%
7b·Fe(OTf)₂	99%	22%	6%	5%



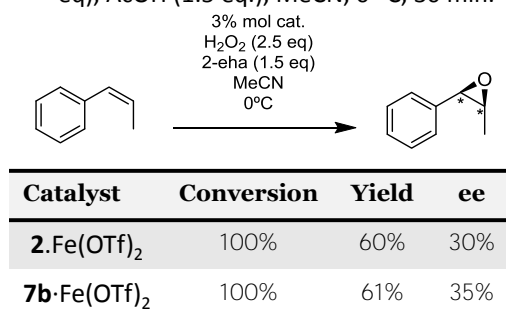
Catalyst	Conversion	Yield 3° OH	Yield K1	Yield K2
2·Fe(OTf)₂	57%	7%	12%	12%
7b·Fe(OTf)₂	80%	8%	19%	22%

Scheme VII.5. Catalytic oxidations with Fe catalysts. a) **2·Fe(OTf)₂** (3 mol %), H₂O₂ (2.5 eq), AcOH (1.5 eq.), MeCN, 0 °C, 30 min.

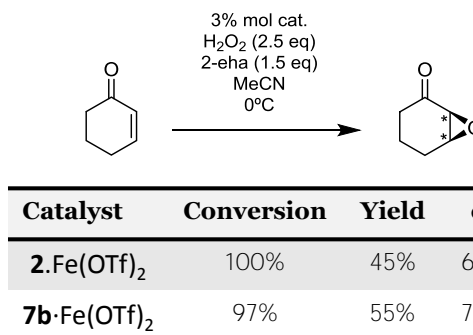


Catalyst	Conversion	Yield K1	Yield K2
2 ·Fe(OTf) ₂	29%	14%	4%
7b ·Fe(OTf) ₂	73%	44%	13%

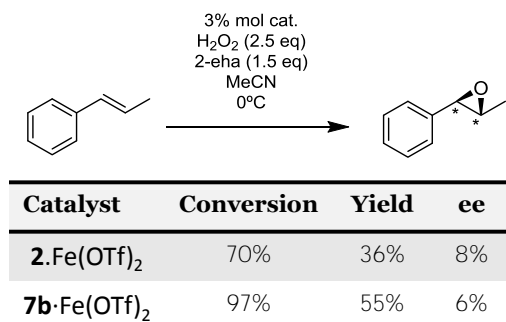
Scheme VII.5. Catalytic C-H oxidations with Fe catalysts. a) **2**·Fe(OTf)₂ (3 mol %), H₂O₂ (2.5 eq), AcOH (1.5 eq.), MeCN, 0 °C, 30 min.



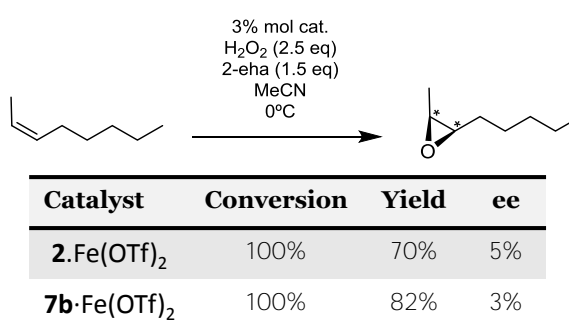
Catalyst	Conversion	Yield	ee
2 ·Fe(OTf) ₂	100%	60%	30%
7b ·Fe(OTf) ₂	100%	61%	35%



Catalyst	Conversion	Yield	ee
2 ·Fe(OTf) ₂	100%	45%	63%
7b ·Fe(OTf) ₂	97%	55%	70%

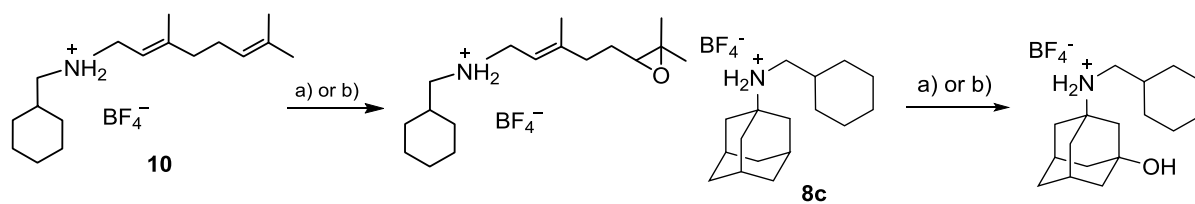


Catalyst	Conversion	Yield	ee
2 ·Fe(OTf) ₂	70%	36%	8%
7b ·Fe(OTf) ₂	97%	55%	6%



Catalyst	Conversion	Yield	ee
2 ·Fe(OTf) ₂	100%	70%	5%
7b ·Fe(OTf) ₂	100%	82%	3%

Scheme VII.6. Catalytic olefin epoxidations with Fe catalysts. a) **2**·Fe(OTf)₂ (3 mol %), H₂O₂ (2.5 eq), AcOH (1.5 eq.), MeCN, 0 °C, 30 min.



Catalyst	Conversion	Epox
2 ·Fe(OTf) ₂	38%	26%
7b ·Fe(OTf) ₂	85%	65%
Catalyst	Conversion	Epox
2 ·Mn(OTf) ₂	86%	68%
7b ·Mn(OTf) ₂	88%	63%

Catalyst	Conversion	Epox
2 ·Fe(OTf) ₂	25%	21%
7b ·Fe(OTf) ₂	37%	26%
Catalyst	Conversion	Epox
2 ·Mn(OTf) ₂	77%	33%
7b ·Mn(OTf) ₂	75%	32%

Scheme VII.7. Catalytic oxidations with Fe and Mn catalysts for substrates that bind inside the cavitand. a) **2**·Fe(OTf)₂ (3 mol %), H₂O₂ (2.5 eq), AcOH (1.5 eq.), MeCN, 0 °C, 30 min. b) **2**·Mn(OTf)₂ (1 mol %), H₂O₂ (2.0 eq), AcOH (17 eq.), MeCN, 0 °C, 30 min.

The following GC method were used to separate the enantiomers:

Table VII.3. Analytical method for ee measurement of epoxide products in C=C oxidation.

	Rate °C/min	Value °C	Hold time (min)	Run time (min)
Initial		75	0.5	0.5
Ramp 1	10	180	1	12
Ramp 2	13	75	0	20.077



REFERENCES

1. Que Jr, L.; Tolman, W. B., *Nature* **2008**, *455*, 333.
2. Newhouse, T.; Baran, P. S., *Angew. Chem. Int. Ed.* **2011**, *50*, 3362.
3. Brückl, T.; Baxter, R. D.; Ishihara, Y.; Baran, P. S., *Acc. Chem. Res.* **2012**, *45*, 826.
4. Curci, R.; D'Accolti, L.; Fusco, C., *Acc. Chem. Res.* **2006**, *39*, 1.
5. Neufeldt, S. R.; Sanford, M. S., *Acc. Chem. Res.* **2012**, *45*, 936.
6. Hartwig, J. F.; Larsen, M. A., *ACS Cent. Sci.* **2016**, *2*, 281.
7. Kovaleva, E. G.; Lipscomb, J. D., *Nat. Chem. Biol.* **2008**, *4*, 186.
8. Costas, M.; Mehn, M. P.; Jensen, M. P.; Que, L., *Chem. Rev.* **2004**, *104*, 939.
9. Sahu, S.; Goldberg, D. P., *J. Am. Chem. Soc.* **2016**, *138*, 11410.
10. Oloo, W. N.; Que Jr, L., 6.26 - Hydrocarbon Oxidations Catalyzed by Bio-Inspired Nonheme Iron and Copper Catalysts A2 - Reedijk, Jan. In *Comprehensive Inorganic Chemistry II (Second Edition)*, Poeppelmeier, K., Ed. Elsevier: Amsterdam, 2013; pp 763.
11. Oloo, W. N.; Banerjee, R.; Lipscomb, J. D.; Que, L., *J. Am. Chem. Soc.* **2017**, *139*, 17313.
12. Krebs, C.; Galonić Fujimori, D.; Walsh, C. T.; Bollinger, J. M., *Acc. Chem. Res.* **2007**, *40*, 484.
13. Hedstrom, L., Enzyme Specificity and Selectivity. In *eLS*, John Wiley & Sons, Ltd: 2001.
14. McLean, K. J.; Girvan, H. M.; Mason, A. E.; Dunford, A. J.; Munro*, A. W., Chapter 8 Structure, Mechanism and Function of Cytochrome P450 Enzymes. In *Iron-Containing Enzymes: Versatile Catalysts of Hydroxylation Reactions in Nature*, The Royal Society of Chemistry: 2011; pp 255.
15. Poulos, T. L., *Chem. Rev.* **2014**, *114*, 3919.
16. Bruijninx, P. C. A.; van Koten, G.; Klein Gebbink, R. J. M., *Chem. Soc. Rev.* **2008**, *37*, 2716.
17. Bugg, T. D. H., Chapter 2 Non-heme Iron-Dependent Dioxygenases: Mechanism and Structure. In *Iron-Containing Enzymes: Versatile Catalysts of Hydroxylation Reactions in Nature*, The Royal Society of Chemistry: 2011; pp 42.
18. Solomon, E. I.; Goudarzi, S.; Sutherlin, K. D., *Biochemistry* **2016**, *55*, 6363.
19. Feig, A. L.; Lippard, S. J., *Chem. Rev.* **1994**, *94*, 759.
20. Que, L.; Ho, R. Y. N., *Chem. Rev.* **1996**, *96*, 2607.
21. Ray, K.; Pfaff, F. F.; Wang, B.; Nam, W., *J. Am. Chem. Soc.* **2014**, *136*, 13942.

References

22. Groves, J. T., *PNAS* **2003**, *100*, 3569.
23. Groves, J. T.; McClusky, G. A., *J. Am. Chem. Soc.* **1976**, *98*, 859.
24. Groves, J. T.; Van der Puy, M., *J. Am. Chem. Soc.* **1976**, *98*, 5290.
25. Rittle, J.; Green, M. T., *Science* **2010**, *330*, 933.
26. Oloo, W. N.; Que, L., Jr., *Acc. Chem. Res.* **2015**, *48*, 2612.
27. Kovaleva, E. G.; Neibergall, M. B.; Chakrabarty, S.; Lipscomb, J. D., *Acc. Chem. Res.* **2007**, *40*, 475.
28. Price, J. C.; Barr, E. W.; Tirupati, B.; Bollinger, J. M.; Krebs, C., *Biochemistry* **2003**, *42*, 7497.
29. Wolfe, M. D.; Parales, J. V.; Gibson, D. T.; Lipscomb, J. D., *J. Biol. Chem.* **2001**, *276*, 1945.
30. Galonić, D. P.; Barr, E. W.; Walsh, C. T.; Bollinger Jr, J. M.; Krebs, C., *Nat. Chem. Biol.* **2007**, *3*, 113.
31. Kovaleva, E. G.; Lipscomb, J. D., *Science* **2007**, *316*, 453.
32. Eser, B. E.; Barr, E. W.; Frantom, P. A.; Saleh, L.; Bollinger, J. M.; Krebs, C.; Fitzpatrick, P. F., *J. Am. Chem. Soc.* **2007**, *129*, 11334.
33. Roach, P. L.; Clifton, I. J.; Hensgens, C. M. H.; Shibata, N.; Schofield, C. J.; Hajdu, J.; Baldwin, J. E., *Nature* **1997**, *387*, 827.
34. Jasniewski, A. J.; Que, L., *Chem. Rev.* **2018**, *118*, 2554.
35. Banerjee, R.; Proshlyakov, Y.; Lipscomb, J. D.; Proshlyakov, D. A., *Nature* **2015**, *518*, 431.
36. Lee, S.-K.; Lipscomb, J. D., *Biochemistry* **1999**, *38*, 4423.
37. Tinberg, C. E.; Lippard, S. J., *Biochemistry* **2009**, *48*, 12145.
38. Shu, L.; Nesheim, J. C.; Kauffmann, K.; Münck, E.; Lipscomb, J. D.; Que, L., *Science* **1997**, *275*, 515.
39. Xue, G.; De Hont, R.; Münck, E.; Que Jr, L., *Nat. Chem.* **2010**, *2*, 400.
40. Kim, C.; Chen, K.; Kim, J.; Que, L., *J. Am. Chem. Soc.* **1997**, *119*, 5964.
41. Company, A.; Gómez, L.; Güell, M.; Ribas, X.; Luis, J. M.; Que, L.; Costas, M., *J. Am. Chem. Soc.* **2007**, *129*, 15766.
42. Company, A.; Prat, I.; Frisch, J. R.; Mas-Ballesté, D. R.; Güell, M.; Juhász, G.; Ribas, X.; Münck, D. E.; Luis, J. M.; Que, L.; Costas, M., *Chem. Eur. J.* **2011**, *17*, 1622.
43. Costas, M.; Lawrence Que, J., *Angew. Chem. Int. Ed.* **2002**, *41*, 2179.
44. Costas, M.; Tipton, A. K.; Chen, K.; Jo, D.-H.; Que, L., *J. Am. Chem. Soc.* **2001**, *123*, 6722.

45. Serrano-Plana, J.; Oloo, W. N.; Acosta-Rueda, L.; Meier, K. K.; Verdejo, B.; García-España, E.; Basallote, M. G.; Münck, E.; Que, L.; Company, A.; Costas, M., *J. Am. Chem. Soc.* **2015**, *137*, 15833.
46. Jensen, M. P.; Costas, M.; Ho, R. Y. N.; Kaizer, J.; Mairata i Payeras, A.; Münck, E.; Que, L.; Rohde, J.-U.; Stubna, A., *J. Am. Chem. Soc.* **2005**, *127*, 10512.
47. Bruijninx, P. C. A.; Buurmans, I. L. C.; Gosiewska, S.; Moelands, M. A. H.; Lutz, M.; Spek, A. L.; van Koten, G.; Klein Gebbink, R. J. M., *Chem. Eur. J.* **2008**, *14*, 1228.
48. Beck, A.; Barth, A.; Hübner, E.; Burzclaff, N., *Inorg. Chem.* **2003**, *42*, 7182.
49. Chow, T. W.-S.; Wong, E. L.-M.; Guo, Z.; Liu, Y.; Huang, J.-S.; Che, C.-M., *J. Am. Chem. Soc.* **2010**, *132*, 13229.
50. Grapperhaus, C. A.; Mienert, B.; Bill, E.; Weyhermüller, T.; Wieghardt, K., *Inorg. Chem.* **2000**, *39*, 5306.
51. Rohde, J.-U.; In, J.-H.; Lim, M. H.; Brennessel, W. W.; Bukowski, M. R.; Stubna, A.; Münck, E.; Nam, W.; Que, L., *Science* **2003**, *299*, 1037.
52. Lim, M. H.; Rohde, J.-U.; Stubna, A.; Bukowski, M. R.; Costas, M.; Ho, R. Y. N.; Münck, E.; Nam, W.; Que, L., *PNAS* **2003**, *100*, 3665.
53. Balland, V.; Charlot, M. F.; Banse, F.; Girerd, J. J.; Mattioli, Tony A.; Bill, E.; Bartoli, J. F.; Battioni, P.; Mansuy, D., *Eur. J. Inorg. Chem.* **2004**, *2004*, 301.
54. Bukowski, M. R.; Koehntop, K. D.; Stubna, A.; Bominaar, E. L.; Halfen, J. A.; Münck, E.; Nam, W.; Que, L., *Science* **2005**, *310*, 1000.
55. Kaizer, J.; Klinker, E. J.; Oh, N. Y.; Rohde, J.-U.; Song, W. J.; Stubna, A.; Kim, J.; Münck, E.; Nam, W.; Que, L., *J. Am. Chem. Soc.* **2004**, *126*, 472.
56. Company, A.; Sabenya, G.; González-Béjar, M.; Gómez, L.; Clémancey, M.; Blondin, G.; Jasniewski, A. J.; Puri, M.; Browne, W. R.; Latour, J.-M.; Que, L.; Costas, M.; Pérez-Prieto, J.; Lloret-Fillol, J., *J. Am. Chem. Soc.* **2014**, *136*, 4624.
57. Mitra, M.; Nimir, H.; Demeshko, S.; Bhat, S. S.; Malinkin, S. O.; Haukka, M.; Lloret-Fillol, J.; Lisensky, G. C.; Meyer, F.; Shteinman, A. A.; Browne, W. R.; Hrovat, D. A.; Richmond, M. G.; Costas, M.; Nordlander, E., *Inorg. Chem.* **2015**, *54*, 7152.
58. Puri, M.; Company, A.; Sabenya, G.; Costas, M.; Que, L., *Inorg. Chem.* **2016**, *55*, 5818.
59. Thibon, A.; England, J.; Martinho, M.; Young, V. G.; Frisch, J. R.; Guillot, R.; Girerd, J. J.; Münck, E.; Que, L.; Banse, F., *Angew. Chem. Int. Ed.* **2008**, *47*, 7064.
60. Wang, D.; Ray, K.; Collins, M. J.; Farquhar, E. R.; Frisch, J. R.; Gomez, L.; Jackson, T. A.; Kerscher, M.; Waleska, A.; Comba, P.; Costas, M.; Que, L., *Chem. Sci.* **2013**, *4*, 282.
61. Klinker, E. J.; Kaizer, J.; Brennessel, W. W.; Woodrum, N. L.; Cramer, C. J.; Que, L., *Angew. Chem. Int. Ed.* **2005**, *44*, 3690.

References

62. Que, J. L.; Puri, M., *Bull. Jpn. Soc. Coord. Chem.* **2016**, *67*, 10.
63. Kal, S.; Que, L., *J. Biol. Inorg. Chem* **2017**, *22*, 339.
64. Kleespies, S. T.; Oloo, W. N.; Mukherjee, A.; Que, L., *Inorg. Chem.* **2015**, *54*, 5053.
65. Puri, M.; Que, L., *Acc. Chem. Res.* **2015**, *48*, 2443.
66. Biswas, A. N.; Puri, M.; Meier, K. K.; Oloo, W. N.; Rohde, G. T.; Bominaar, E. L.; Münck, E.; Que, L., *J. Am. Chem. Soc.* **2015**, *137*, 2428.
67. Serrano-Plana, J.; Oloo, W. N.; Acosta-Rueda, L.; Meier, K. K.; Verdejo, B.; Garcia-Espana, E.; Basallote, M. G.; Münck, E.; Que, L., Jr.; Company, A.; Costas, M., *J. Am. Chem. Soc.* **2015**, *137*, 15833.
68. Que, J. L., *J. Chem. Soc., Dalton Trans.* **1997**, 3933.
69. Xue, G.; Wang, D.; De Hont, R.; Fiedler, A. T.; Shan, X.; Münck, E.; Que, L., *PNAS* **2007**, *104*, 20713.
70. Zhang, X.; Furutachi, H.; Fujinami, S.; Nagatomo, S.; Maeda, Y.; Watanabe, Y.; Kitagawa, T.; Suzuki, M., *J. Am. Chem. Soc.* **2005**, *127*, 826.
71. Brunold, T. C.; Tamura, N.; Kitajima, N.; Moro-oka, Y.; Solomon, E. I., *J. Am. Chem. Soc.* **1998**, *120*, 5674.
72. Kim, K.; Lippard, S. J., *J. Am. Chem. Soc.* **1996**, *118*, 4914.
73. Kryatov, S. V.; Taktak, S.; Korendovych, I. V.; Rybak-Akimova, E. V.; Kaizer, J.; Torelli, S.; Shan, X.; Mandal, S.; MacMurdo, V. L.; Mairata i Payeras, A.; Que, L., *Inorg. Chem.* **2005**, *44*, 85.
74. Ookubo, T.; Sugimoto, H.; Nagayama, T.; Masuda, H.; Sato, T.; Tanaka, K.; Maeda, Y.; Ōkawa, H.; Hayashi, Y.; Uehara, A.; Suzuki, M., *J. Am. Chem. Soc.* **1996**, *118*, 701.
75. LeCloux, D. D.; Barrios, A. M.; Mizoguchi, T. J.; Lippard, S. J., *J. Am. Chem. Soc.* **1998**, *120*, 9001.
76. Shan, X.; Que, L., *Proceedings of the National Academy of Sciences of the United States of America* **2005**, *102*, 5340.
77. Kitajima, N.; Tamura, N.; Amagai, H.; Fukui, H.; Moro-oka, Y.; Mizutani, Y.; Kitagawa, T.; Mathur, R.; Heerwegh, K., *J. Am. Chem. Soc.* **1994**, *116*, 9071.
78. Kodera, M.; Itoh, M.; Kano, K.; Funabiki, T.; Reglier, M., *Angew. Chem. Int. Ed.* **2005**, *44*, 7104.
79. Friedle, S.; Kodanko, J. J.; Morys, A. J.; Hayashi, T.; Moënne-Loccoz, P.; Lippard, S. J., *J. Am. Chem. Soc.* **2009**, *131*, 14508.
80. Baldwin, J.; Krebs, C.; Saleh, L.; Stelling, M.; Huynh, B. H.; Bollinger, J. M.; Riggs-Gelasco, P., *Biochemistry* **2003**, *42*, 13269.

- 81.Fiedler, A. T.; Shan, X.; Mehn, M. P.; Kaizer, J.; Torelli, S.; Frisch, J. R.; Kodera, M.; Que, J. L., *The Journal of Physical Chemistry A* **2008**, *112*, 13037.
- 82.Kodera, M.; Tsuji, T.; Yasunaga, T.; Kawahara, Y.; Hirano, T.; Hitomi, Y.; Nomura, T.; Ogura, T.; Kobayashi, Y.; Sajith, P. K.; Shiota, Y.; Yoshizawa, K., *Chem. Sci.* **2014**, *5*, 2282.
- 83.Tinberg, C. E.; Lippard, S. J., *Biochemistry* **2010**, *49*, 7902.
- 84.Tinberg, C. E.; Lippard, S. J., *Acc. Chem. Res.* **2011**, *44*, 280.
- 85.Ghosh, A.; Tiago de Oliveira, F.; Yano, T.; Nishioka, T.; Beach, E. S.; Kinoshita, I.; Münck, E.; Ryabov, A. D.; Horwitz, C. P.; Collins, T. J., *J. Am. Chem. Soc.* **2005**, *127*, 2505.
- 86.Wang, D.; Farquhar, E. R.; Stubna, A.; Münck, E.; Que Jr, L., *Nat. Chem.* **2009**, *1*, 145.
- 87.Kodera, M.; Kawahara, Y.; Hitomi, Y.; Nomura, T.; Ogura, T.; Kobayashi, Y., *J. Am. Chem. Soc.* **2012**, *134*, 13236.
- 88.Dong, Y.; Zang, Y.; Shu, L.; Wilkinson, E. C.; Que, L.; Kauffmann, K.; Münck, E., *J. Am. Chem. Soc.* **1997**, *119*, 12683.
- 89.Masahito, K.; Shin, I.; Tomokazu, T.; Katsutoshi, S.; Yutaka, H.; Yoshihito, S.; K., S. P.; Kazunari, Y.; Kaoru, M.; Takashi, O., *Chem. Eur. J.* **2016**, *22*, 5924.
- 90.Xue, G.; Fiedler, A. T.; Martinho, M.; Münck, E.; Que, L., *PNAS* **2008**, *105*, 20615.
- 91.Stoian, S. A.; Xue, G.; Bominaar, E. L.; Que, L.; Münck, E., *J. Am. Chem. Soc.* **2014**, *136*, 1545.
- 92.Ortiz De Montellano, P. R., *Chem. Rev.* **2010**, *110*, 932.
- 93.Larsen, A. T.; May, E. M.; Auclair, K., *J. Am. Chem. Soc.* **2011**, *133*, 7853.
- 94.Fasan, R., *ACS cat.* **2012**, *2*, 647.
- 95.Lewis, J. C.; Coelho, P. S.; Arnold, F. H., *Chem. Soc. Rev.* **2011**, *40*, 2003.
- 96.Chen, M. S.; White, M. C., *Science* **2007**, *318*, 783.
- 97.Canta, M.; Font, D.; Gómez, L.; Ribas, X.; Costas, M., *Adv. Synth. & Cat.* **2014**, *356*, 818.
- 98.Font, D.; Canta, M.; Milan, M.; Cussò, O.; Ribas, X.; Klein Gebbink, R. J. M.; Costas, M., *Angew. Chem. Int. Ed.* **2016**, *55*, 5776.
- 99.Ke, C.; Albert, E.; S., B. P., *Angew. Chem. Int. Ed.* **2009**, *48*, 9705.
- 100.Biggi, M. A.; Reed, S. A.; White, M. C., *J. Am. Chem. Soc.* **2012**, *134*, 9721.
- 101.Simmons, E. M.; Hartwig, J. F., *Nature* **2012**, *483*, 70.

References

102. Raynal, M.; Ballester, P.; Vidal-Ferran, A.; van Leeuwen, P. W. N. M., *Chem. Soc. Rev.* **2014**, *43*, 1734.
103. Dydio, P.; Reek, J. N. H., *Chem. Sci.* **2014**, *5*, 2135.
104. Ringe, D.; Petsko, G. A., *Science* **2008**, *320*, 1428.
105. Hooley, R. J.; Biroš, S. M.; Rebek, J., *Angew. Chem. Int. Ed.* **2006**, *45*, 3517.
106. Chao, Y.; Cram, D. J., *J. Am. Chem. Soc.* **1976**, *98*, 1015.
107. Lehn, J.-M.; Sirlin, C., *Journal of the Chemical Society, Chemical Communications* **1978**, 949.
108. Jiang, L.; Liu, Z.; Liang, Z.; Gao, Y., *Bioorganic & Medicinal Chemistry* **2005**, *13*, 3673.
109. Tabushi, I., *Acc. Chem. Res.* **1982**, *15*, 66.
110. Yang, B.; Cui, J.-F.; Wong, M. K., *RSC Advances* **2017**, *7*, 30886.
111. Hu, S.; Li, J.; Xiang, J.; Pan, J.; Luo, S.; Cheng, J.-P., *J. Am. Chem. Soc.* **2010**, *132*, 7216.
112. Cram, D. J., *Science* **1983**, *219*, 1177.
113. Purse, B. W.; Ballester, P.; Rebek, J., *J. Am. Chem. Soc.* **2003**, *125*, 14682.
114. Gissot, A.; Rebek, J., *J. Am. Chem. Soc.* **2004**, *126*, 7424.
115. Hooley, R. J.; Iwasawa, T.; Rebek, J., *J. Am. Chem. Soc.* **2007**, *129*, 15330.
116. Iwasawa, T.; Hooley, R. J.; Rebek, J., *Science* **2007**, *317*, 493.
117. Shenoy, S. R.; Pinacho Crisóstomo, F. R.; Iwasawa, T.; Rebek, J., *J. Am. Chem. Soc.* **2008**, *130*, 5658.
118. Pinacho Crisóstomo, F. R.; Lledó, A.; Shenoy, S. R.; Iwasawa, T.; Rebek, J., *J. Am. Chem. Soc.* **2009**, *131*, 7402.
119. Breslow, R., *Acc. Chem. Res.* **1995**, *28*, 146.
120. Groves, J. T.; Neumann, R., *J. Org. Chem.* **1988**, *53*, 3891.
121. Groves, J. T.; Neumann, R., *J. Am. Chem. Soc.* **1989**, *111*, 2900.
122. Breslow, R.; Huang, Y.; Zhang, X.; Yang, J., *PNAS* **1997**, *94*, 11156.
123. Breslow, R.; Zhang, X.; Huang, Y., *J. Am. Chem. Soc.* **1997**, *119*, 4535.
124. Yang, J.; Gabriele, B.; Belvedere, S.; Huang, Y.; Breslow, R., *J. Org. Chem.* **2002**, *67*, 5057.

125. Breslow, R.; Fang, Z., *Tetrahedron Lett.* **2002**, *43*, 5197.
126. Belvedere, S.; Breslow, R., *Bioorganic Chemistry* **2001**, *29*, 321.
127. Das, S.; Incarvito, C. D.; Crabtree, R. H.; Brudvig, G. W., *Science* **2006**, *312*, 1941.
128. Finn, B.; Maxime, G.; Stefan, B.; Alexander, P.; Thorsten, B., *Angew. Chem. Int. Ed.* **2018**, *57*, 2953.
129. Giorgio, O.; Giulio, F.; Alessia, B.; Osvaldo, L.; Stefano, D. S.; Miquel, C., *Angew. Chem. Int. Ed.* **2017**, *56*, 16347.
130. Richeter, S.; Rebek, J. *Am. Chem. Soc.* **2004**, *126*, 16280.
131. Korom, S.; Ballester, P., *J. Am. Chem. Soc.* **2017**, *139*, 12109.
132. Vaquer, L.; Riente, P.; Sala, X.; Jansat, S.; Benet-Buchholz, J.; Llobet, A.; Pericas, M. A., *Cat. Sci. & Tech.* **2013**, *3*, 706.
133. Olivo, G.; Cussó, O.; Costas, M., *Chem. Asian J.* **2016**, *11*, 3148.
134. Nathalie, S.; Constance, D. T.; Caroline, D.; Katell, S. D.; Amandine, D. S.; Vincent, S.; Philippe, M.; Jean-Noël, R.; Frédéric, B.; Olivia, R., *Chem. Eur. J.* **2017**, *23*, 2894.
135. Djernes, K. E.; Moshe, O.; Mettry, M.; Richards, D. D.; Hooley, R. J., *Org. Lett.* **2012**, *14*, 788.
136. Djernes, K. E.; Padilla, M.; Mettry, M.; Young, M. C.; Hooley, R. J., *Chem. Commun.* **2012**, *48*, 11576.
137. Klinker, E. J.; Kaizer, J.; Brennessel, W. W.; Woodrum, N. L.; Cramer, C. J.; Que, L., *Angew. Chem. Int. Ed.* **2005**, *44*, 3690.
138. Lee, Y.-M.; Hong, S.; Morimoto, Y.; Shin, W.; Fukuzumi, S.; Nam, W., *J. Am. Chem. Soc.* **2010**, *132*, 10668.
139. Seo, M. S.; Kim, N. H.; Cho, K.-B.; So, J. E.; Park, S. K.; Clemancey, M.; Garcia-Serres, R.; Latour, J.-M.; Shaik, S.; Nam, W., *Chem. Sci.* **2011**, *2*, 1039.
140. Suh, Y.; Seo, M. S.; Kim, K. M.; Kim, Y. S.; Jang, H. G.; Tosha, T.; Kitagawa, T.; Kim, J.; Nam, W., *J. Inorg. Biochem.* **2006**, *100*, 627.
141. Company, A.; Gómez, L.; Güell, M.; Ribas, X.; Luis, J. M.; Que Jr., L.; Costas, M., *J. Am. Chem. Soc.* **2007**, *129*, 15766.
142. Company, A.; Feng, Y.; Güell, M.; Ribas, X.; Luis, J. M.; Que, L.; Costas, M., *Chem. Eur. J.* **2009**, *15*, 3359.
143. Company, A.; Gomez, L.; Fontrodona, X.; Ribas, X.; Costas, M., *Chem. Eur. J.* **2008**, *14*, 5727.

References

144. Cao, R.; Müller, P.; Lippard, S. J., *J. Am. Chem. Soc.* **2010**, *132*, 17366.
145. Wiegardt, K.; Tolksdorf, I.; Herrmann, W., *Inorg. Chem.* **1985**, *24*, 1230.
146. Brudenell, S. J.; Spiccia, L.; Tiekink, E. R. T., *Inorg. Chem.* **1996**, *35*, 1974.
147. Spiccia, L.; Fallon, G. D.; Grannas, M. J.; Nichols, P. J.; Tiekink, E. R. T., *Inorg. Chim. Acta* **1998**, *279*, 192.
148. Prat, I.; Company, A.; Corona, T.; Parella, T.; Ribas, X.; Costas, M., *Inorg. Chem.* **2013**, *52*, 9229.
149. Diebold, A.; Hagen, K. S., *Inorg. Chem.* **1998**, *37*, 215.
150. Britovsek, G. J. P.; England, J.; White, A. J. P., *Inorg. Chem.* **2005**, *44*, 8125.
151. Simaan, A. J.; Döpner, S.; Banse, F.; Bourcier, S.; Bouchoux, G.; Boussac, A.; Hildebrandt, P.; Girerd, J.-J., *Eur. J. Inorg. Chem.* **2000**, *2000*, 1627.
152. Zang, Y.; Kim, J.; Dong, Y.; Wilkinson, E. C.; Appelman, E. H.; Que, L., *J. Am. Chem. Soc.* **1997**, *119*, 4197.
153. Constable, E. C.; Baum, G.; Bill, E.; Dyson, R.; van Eldik, R.; Fenske, D.; Kaderli, S.; Morris, D.; Neubrand, A.; Neuburger, M.; Smith, D. R.; Wiegardt, K.; Zehnder, M.; Zuberbühler, A. D., *Chem. Eur. J.* **1999**, *5*, 498.
154. Holzacker, C.; Calhorda, M. J.; Gil, A.; Carvalho, M. D.; Ferreira, L. P.; Stöger, B.; Mereiter, K.; Weil, M.; Müller, D.; Weinberger, P.; Pittenauer, E.; Allmaier, G.; Kirchner, K., *Dalton Trans.* **2014**, *43*, 11152.
155. England, J.; Gondhia, R.; Bigorra-Lopez, L.; Petersen, A. R.; White, A. J. P.; Britovsek, G. J. P., *Dalton Trans.* **2009**, 5319.
156. England, J.; Davies, C. R.; Banaru, M.; White, A. J. P.; Britovsek, G. J. P., *Adv. Synth. & Cat.* **2008**, *350*, 883.
157. Balland, V.; Banse, F.; Anxolabéhère-Mallart, E.; Nierlich, M.; Girerd, J.-J., *Eur. J. Inorg. Chem.* **2003**, *2003*, 2529.
158. Toftlund, H., *Coord. Chem. Rev.* **1989**, *94*, 67.
159. Mialane, P.; Nivorojkine, A.; Pratviel, G.; Azéma, L.; Slany, M.; Godde, F.; Simaan, A.; Banse, F.; Kargar-Grisel, T.; Bouchoux, G.; Sainton, J.; Horner, O.; Guilhem, J.; Tchertanova, L.; Meunier, B.; Girerd, J.-J., *Inorg. Chem.* **1999**, *38*, 1085.
160. Börzel, H.; Comba, P.; Hagen, K. S.; Lampeka, Y. D.; Lienke, A.; Linti, G.; Merz, M.; Pritzkow, H.; Tsybmal, L. V., *Inorg. Chim. Acta* **2002**, *337*, 407.
161. Britovsek, G. J. P.; England, J.; White, A. J. P., *Inorg. Chem.* **2005**, *44*, 8125.

162. Decker, A.; Clay, M. D.; Solomon, E. I., *J. Inorg. Biochem.* **2006**, *100*, 697.
163. Engelmann, X.; Monte-Pérez, I.; Ray, K., *Angew. Chem. Int. Ed.* **2016**, *55*, 7632.
164. Nam, W., *Acc. Chem. Res.* **2007**, *40*, 522.
165. Cho, K.-B.; Hirao, H.; Shaik, S.; Nam, W., *Chem. Soc. Rev.* **2016**, *45*, 1197.
166. Iwasawa, T.; Wash, P.; Gibson, C.; Rebek, J., *Tetrahedron* **2007**, *63*, 6506.
167. Degardin, M.; Busseron, E.; Kim, D.-A.; Ajami, D.; Rebek, J., *Chem. Commun.* **2012**, *48*, 11850.
168. Lledo, A.; Rebek Jr, J., *Chem. Commun.* **2010**, *46*, 1637.
169. Kanaura, M.; Ito, K.; Schramm, M. P.; Ajami, D.; Iwasawa, T., *Tetrahedron Lett.* **2015**, *56*, 4824.
170. Amrhein, P.; Shivanyuk, A.; Johnson, D. W.; Rebek, J., *J. Am. Chem. Soc.* **2002**, *124*, 10349.
171. Ushijima, S.; Moriyama, K.; Togo, H., *Tetrahedron* **2012**, *68*, 4701.
172. Yaremenko, A. G.; Volochnyuk, D. M.; Shelyakin, V. V.; Grygorenko, O. O., *Tetrahedron* **2013**, *69*, 6799.
173. Soler, M.; Figueras, E.; Serrano-Plana, J.; González-Bártulos, M.; Massaguer, A.; Company, A.; Martínez, M. Á.; Malina, J.; Brabec, V.; Feliu, L.; Planas, M.; Ribas, X.; Costas, M., *Inorg. Chem.* **2015**, *54*, 10542.
174. Machkour, A.; Mandon, D.; Lachkar, M.; Welter, R., *Inorg. Chem.* **2004**, *43*, 1545.
175. Rudkevich, D. M.; Hilmersson, G.; Rebek, J., *J. Am. Chem. Soc.* **1998**, *120*, 12216.
176. Suzuki, K.; Oldenburg, P. D.; Que, L., *Angew. Chem. Int. Ed.* **2008**, *47*, 1887.
177. Moran, J. R.; Ericson, J. L.; Dalcanale, E.; Bryant, J. A.; Knobler, C. B.; Cram, D. J., *J. Am. Chem. Soc.* **1991**, *113*, 5707.
178. Lledo, A.; Rebek Jr, J., *Chem. Commun.* **2010**, *46*, 8630.
179. Purse, B. W.; Butterfield, S. M.; Ballester, P.; Shivanyuk, A.; Rebek, J., *J. Org. Chem.* **2008**, *73*, 6480.
180. Rudkevich, D. M.; Hilmersson, G.; Rebek, J., *J. Am. Chem. Soc.* **1997**, *119*, 9911.
181. Ajami, D.; Iwasawa, T.; Rebek, J., *PNAS* **2006**, *103*, 8934.
182. Hooley, R. J.; Rebek, J., Jr., *Chemistry & Biology* **2009**, *16*, 255.
183. Costas, M.; Que Jr., L., *Angew. Chem. Int. Ed.* **2002**, *41*, 2179.

References

184. Mas-Balleste, R.; Que Jr., L., *J. Am. Chem. Soc.* **2007**, *129*, 15964.
185. Iwasawa, T., *Tetrahedron Lett.* **2017**, *58*, 4217.
186. Natarajan, N.; Brenner, E.; Sémeril, D.; Matt, D.; Harrowfield, J., *Eur. J. Org. Chem.* **2017**, *2017*, 6100.
187. Gibson, C.; Rebek, J., *Org. Lett.* **2002**, *4*, 1887.
188. Chavagnan, T.; Sémeril, D.; Matt, D.; Toupet, L., *Eur. J. Org. Chem.* **2017**, *2017*, 313.
189. Chavagnan, T.; Bauder, C.; Sémeril, D.; Matt, D.; Toupet, L., *Eur. J. Org. Chem.* **2017**, *2017*, 70.
190. Al-Azemi, T. F.; Vinodh, M., *RSC Advances* **2015**, *5*, 88154.
191. Canta, M.; Rodriguez, M.; Costas, M., *Top Curr Chem* **2016**, *372*, 27.
192. Cusso, O.; Ribas, X.; Costas, M., *Chem. Commun.* **2015**, *51*, 14285.
193. Lyakin, O. Y.; Ottenbacher, R. V.; Bryliakov, K. P.; Talsi, E. P., *ACS cat.* **2012**, *2*, 1196.
194. Gomez, L.; Garcia-Bosch, I.; Company, A.; Benet-Buchholz, J.; Polo, A.; Sala, X.; Ribas, X.; Costas, M., *Angew. Chem. Int. Ed.* **2009**, *48*, 5720.
195. Bryliakov, K. P.; Talsi, E. P., *Coord. Chem. Rev.* **2014**, *276*, 73.
196. Kanaura, M.; Endo, N.; Schramm, M. P.; Iwasawa, T., *Eur. J. Org. Chem.* **2016**, *2016*, 4970.
197. Krebs, C.; Fujimori, D. G.; Walsh, C. T.; Bollinger jr., J. M., *Acc. Chem. Res.* **2007**, *40*, 484.
198. Nam, W., *Acc. Chem. Res.* **2015**, *48*, 2415.
199. McDonald, A. R.; Que, L., *Coord. Chem. Rev.* **2013**, *257*, 414.
200. Hagen, K. S., *Inorg. Chem.* **2000**, *39*, 5867.
201. Macikenas, D.; Skrzypczak-Jankun, E.; Protasiewicz, J. D., *J. Am. Chem. Soc.* **1999**, *121*, 7164.
202. Iranzo, O.; Elmer, T.; Richard, J. P.; Morrow, J. R., *Inorg. Chem.* **2003**, *42*, 7737.
203. McLachlan, G. A.; Fallon, G. D.; Martin, R. L.; Moubaraki, B.; Murray, K. S.; Spiccia, L., *Inorg. Chem.* **1994**, *33*, 4663.
204. Olivo, G.; Lanzalunga, O.; Mandolini, L.; Di Stefano, S., *J. Org. Chem.* **2013**, *78*, 11508.
205. Ottenbacher, R. V.; Samsonenko, D. G.; Talsi, E. P.; Bryliakov, K. P., *Org. Lett.* **2012**, *14*, 4310.
206. Renslo, A. R.; Danheiser, R. L., *J. Org. Chem.* **1998**, *63*, 7840.

207. Füllroth, B.; Emil, H., *Helvetica Chimica Acta* **1975**, *58*, 682.

208. Kazock, J.-Y.; Taggougui, M.; Carré, B.; Willmann, P.; Lemordant, D., *Synthesis* **2007**, *2007*, 3776.

209. Milan, M.; Bietti, M.; Costas, M., *ACS Cent. Sci.* **2017**, *3*, 196.

